Dynamics of Particle Escape from a Potential Well

Zur Erlangung des akademischen Grades

Doktor der Ingenieurwissenschaften

von der KIT-Fakultät Maschinenbau

angenommene
Dissertation

von

Attila Genda

Tag der mündlichen Prüfung: 24.09.2024
Hauptreferent: Prof. Dr.-Ing. habil. Alexander Fidlin
Korreferent: Prof. Oleg Gendelman

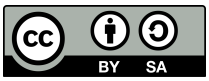

Kurzfassung

Der Schwerpunkt dieser Arbeit liegt auf der Dynamik des Entkommens (Escape) eines Partikels oder von Partikeln aus einem Potentialtopf. Dieses Problem ist entscheidend für die Beschreibung verschiedener physikalischer, chemischer und biologischer Prozesse. Das Phänomen des Escapes ist in zahlreichen Beispielen von Bedeutung, wie z.B. dem Kentern von Schiffen aufgrund äußerer Einwirkung durch Wellen, wo die Analyse der vereinfachten Schiffsdynamik ungefähre Kriterien für das Kentern liefern kann.
Escape spielt auch eine entscheidende Rolle beim Gravitationskollaps von Sternen und hat Anwendungen in der Physik und im Ingenieurwesen, insbesondere beim Josephson-Effekt und dynamischen Beulen, einem wesentlichen Aspekt der elastischen Instabilitätsphänomene. Im Bereich der mikroelektromechanischen Systeme (MEMS) hilft die Untersuchung der Escapesdynamik bei der Verbesserung von Geräten wie MEMS-Schaltern, und im Kontext der Partikelabsorption und -falle ist sie instrumental beim Einsatz von beweglichen Spiegeln und elektromagnetischen Fallen sowohl für geladene als auch für neutrale Partikel. Weitere Beispiele umfassen das Escape von Polymeren in der Chemie und die Energieerzeugung mittels bi-stabiler Potentialtöpfe.
Der theoretische Aspekt dieser Arbeit umfasst Untersuchungen zur Escapesdynamik, die durch Differentialgleichungen mit Anfangsbedingungen gesteuert werden. Die Abhängigkeit von diesen Anfangsbedingungen in Verbindung mit Erregungsparametern wie Frequenz, Amplitude und Phasenverschiebung bestimmt, ob das Escape stattfindet. Dieses binäre Ergebnis des Escapes oder kein Escapes hängt vom multidimensionalen Raum der Parameter und Anfangsbedingungen ab. Zusätzlich zur Darstellung des binären Escapesatzes kann es auch nützlich sein, die Escapesrate zu bestimmen, d.h. die Zeit, die ein Partikel benötigt, um das Potential zu verlassen.
Die Studie berücksichtigt auch die Rolle der Dämpfung in Systemen, wobei ihre Präsenz bei normal großen Anwendungen wie dem Kentern von Schiffen, ihre Abwesenheit bei atomaren und himmlischen Prozessen und die Komplexität, die sie in mäßig gedämpften Systemen hinzufügt, berücksichtigt wird. Diese Komplexität entsteht aus der Unfähigkeit, die Dämpfung vollständig zu ignorieren oder sich ausschließlich auf

stationäre Bewegungen zu verlassen, angesichts der Bedeutung von Übergangsprozessen bei Escapesphänomenen.
Die transiente Natur des Escapes, das nur einmal auftritt, stellt Herausforderungen bei der Detektion dar und erfordert präzise analytische Lösungen (oder zumindest Schätzungen), um die Bedingungen für das Escape zu bestimmen. Im Wesentlichen untersucht diese Arbeit die grundlegenden Mechanismen des Escapes, insbesondere am Beispiel des harmonischen Oszillators mit und ohne viskose Dämpfung. Es erweitert sich auf die Untersuchung der Escapesdynamik gekoppelter Partikel und erforscht das Potenzial der Nutzung des Escapes zur Steuerung von Partikeln innerhalb eines sinusförmigen Potentialtopfes. Darüber hinaus stellt die Studie mathematische Theoreme im Zusammenhang mit dem Mittelwert und der globalen Optimierung periodischer Funktionen vor, die wertvolle Werkzeuge zur Lösung von Problemen im Zusammenhang mit der Escapesdynamik bieten. Diese Elemente prägen zusammen den Kern dieser Forschung und spiegeln eine fokussierte, aber umfassende Erkundung des facettenreichen Bereichs der Escapesdynamik wider.

Abstract

The focus of this work is on the dynamics of a particle/particles escape from a potential well. This problem is crucial in describing various physical, chemical, and biological processes. The phenomenon of escape finds relevance in numerous examples, such as the capsize of ships due to external excitation by waves, where the analysis of simplified ship dynamics can provide approximate criteria for capsize.

The escape phenomenon also plays a crucial role in the gravitational collapse of stars and has applications in physics and engineering, notably in the Josephson effect and dynamic buckling, an essential aspect of elastic instability phenomena. In the realm of micro-electromechanical systems (MEMS), the study of escape dynamics aids in improving devices like MEMS switches, and in the context of particle absorption and trapping, it is instrumental in the use of moving mirrors and electromagnetic traps for both charged and neutral particles. Further examples include polymer escape in chemistry and energy harvesting using bi-stable potential wells.

The theoretical aspect of this study includes investigations into escape dynamics governed by differential equations with initial conditions. Dependence on these initial conditions, coupled with excitation parameters such as frequency, amplitude, and phase shift, determines whether escape occurs. This binary outcome of escape or non-escape depends on the multidimensional space of parameters and initial conditions. In addition to detailing the binary escape set, it may also be useful to determine the escape rate, i.e., the time required for a particle to exit the potential.

The study also considers the role of damping in systems, noting its presence in normal-sized applications such as ship capsizing, its absence in atomic and celestial-sized processes, and the complexity it adds in moderately damped systems. This complexity arises from the inability to disregard damping entirely or rely solely on stationary motion, given the significance of transients in escape phenomena.

The transient nature of escape, which occurs only once, presents challenges in detection, requiring precise analytical solutions (or at least estimates) to determine the conditions for escape.

In essence, this thesis delves into the fundamental mechanisms of escape, particularly focusing on the example of the harmonic oscillator with and without viscous damping. It extends to investigate the escape dynamics of coupled particles and explores the potential of utilizing escape for the control of particles within a sinusoidal potential well. Additionally, the study introduces mathematical theorems related to averaging and global optimization of periodic functions, providing valuable tools to address problems related to escape dynamics. These elements collectively shape the core of this research, reflecting a focused yet comprehensive exploration into the multifaceted realm of escape dynamics.

Contents

Preface

This work was made possible during my time as a research associate at the Institute for Engineering Mechanics, Dynamics/Mechatronics division of the Karlsruhe Institute of Technology (KIT).
I would like to express my deepest gratitude to Professor Dr.-Ing. habil. Alexander Fidlin for supervising this thesis, for the invaluable suggestions, and for the honest critique. The freedom to shape the topic of my dissertation according to my vision has been incredibly valuable for my personal development and the work presented herein. My thanks also go to Professor Oleg Gendelman, who served as the co-referee of this thesis.
I owe a debt of gratitude to Prof. Dr. Christian Greiner for serving as the committee chair.
I wish to pay my respects and express my thanks to my former professors in dynamics, especially to the late Professor Seemann. My appreciation also extends to Professor Proppe, Dr. Bende from the Budapest University of Technology and Economics, and Professor Stépan from the same institution.
I am grateful to the three Professors Emeritus: Professor Wauer, Wedig, and Wittenburg, for their continuous interest in the welfare of the doctoral candidates and the institute.
Additionally, I extend my gratitude to the secretaries Ms. Höllig, Ms. Gelsok, and Ms. Volz, whose diligent work behind the scenes has been the backbone of our daily academic operations, providing an organized and conducive environment for research and teaching. Their commitment to the institute's mission and their unwavering support to the faculty and students alike have been indispensable to my success.
Our research has been generously supported by the Deutsche Forschungsgemeinschaft, DFG, under project number 508244284. I am grateful for this support.
I am also grateful to Professor Lenci for welcoming me into Ancona for my research stay and for the exciting time spent on the analysis of the Lotka-Volterra model. This stay was generously funded by the Karlsruhe House of Young Scientists (KHYS), for which we are deeply grateful.

I acknowledge the assistance of AI tools, including OpenAI's ChatGPT (version GPT-4), Grammarly, and Writefull, for language editing and refinement in the preparation of this dissertation.

I am indebted to my colleagues for their cooperative and congenial work atmosphere, and for the many professional and non-professional discussions. A special mention goes to my long-standing office mate Tunc Yüzbasioglu, with whom I have had many stimulating discussions, who has managed on many occasions to offer new perspectives on my research topic, as well as on non-academic matters.

I would like to thank my friends scattered around the world for accompanying me through my studies and research phase in Karlsruhe. I consider myself very fortunate to have you in my life.

Last but certainly not least, heartfelt thanks go to my family for their unwavering support and the grounding they have provided me in the past and continue to offer. I am especially thankful to my girlfriend, whose steadfast belief and support have been a cornerstone of this journey. Her encouragement and unwavering confidence in me have been a constant source of strength and inspiration. For all the sacrifices and the tireless optimism, my deepest gratitude goes to her.

...

Karlsruhe, July 11, 2024

Attila Genda

1 Introduction

In the first chapter of this thesis, the subject is introduced and its significance established. In addition, an overview of the current state of research is provided, along with identifying existing gaps in the research. From this, the objectives and structure of the thesis are derived.

1.1 Motivation and the topic of the work

The concept of escape in dynamics forms the cornerstone of this thesis. Escape, in its fundamental sense, refers to a scenario in which a particle or a body, initially situated in a confined area around the minimum of a potential well (the basin of attraction), exits this region due to initial conditions, external excitation, or parametric excitation, and, importantly, does not return to it.
To elucidate this concept, consider the example of a rocket. Initially, the rocket resides within Earth's gravitational potential well, or its basin of attraction. However, because of propulsion, a form of excitation, the rocket leaves Earth's vicinity, embarking on a voyage to destinations like the Moon, Mars, or even further celestial bodies with no intention of returning. This departure from Earth's gravitational influence exemplifies escape.
Another pertinent example is that of the dynamics of a ship. A ship at rest in calm waters maintains a vertical position, its asymptotically stable equilibrium, due to the restoring moments and the energy dissipation provided by the water. However, periodic external excitation, such as ocean waves, induces a rolling motion in the ship. The ship oscillates due to the combined effect of potential and wave forces. In extreme cases, this oscillation can lead the ship to capsize, a point of no return where the initial assumptions and system dynamics change drastically, possibly beyond the descriptive power of the original equations of motion.
This dramatic alteration, often observed in escape scenarios, can fundamentally change the system's state, potentially involving additional variables or completely altering the system's dynamics.

Another concept related to the problem of escape is known as level crossing or first passage. This problem is similar to the escape problem, but in this case, a certain observable of the system, such as displacement, total energy, or force, crosses a predefined level. It is worth noting that the level-crossing problem encompasses a broader range of problems as compared to the escape problem, since the potential must be bounded for an escape to occur, whereas, in level-crossing problems, there is no such restriction. This suggests that escape problems are fundamentally nonlinear, whereas level-crossing problems may still be linear.

In this dissertation, we explore the theoretical aspects of escape dynamics within the framework of ordinary differential equations (ODEs). Central to our exploration are ODEs, often with uncertain initial conditions and influenced by external excitations. Our investigation primarily revolves around the system's response to harmonic excitation, characterized by its amplitude, frequency, and initial phase. This study aims to determine the precise effects of these initial conditions and excitation parameters on the phenomenon of escape, which manifests as a binary outcome, either occurring or not.

Another critical aspect of escape/level-crossing dynamics is the temporal factor, introducing the notion of 'escape time' or 'first passage time.' This element is especially critical in engineering contexts where escape is generally undesirable due to its potentially hazardous implications. In many instances, escape/level-crossing occurs rapidly. However, certain parameter combinations exhibit a more gradual process, observable both in linear and nonlinear systems. Notably, nonlinear systems introduce the additional saddle and maximum mechanisms, further complicating the escape dynamics.

The work of Professor Gendelman and his group [55, 56, 67, 68, 88], particularly their use of action-angle variables, offers significant insights into these mechanisms. This thesis extends this exploration by describing safe basins in simple dynamic problems such as harmonic and damped harmonic oscillators.

Another area of interest is the effect of coupled bodies' relative motion, for which we introduce a new averaging theorem. This theorem is particularly pertinent for systems with strong coupling between particles and fast relative motions, allowing for a simplification from multi-degree-of-freedom systems to a single-degree system in an effective potential. This simplification is not only theoretically fascinating but also offers practical advantages, significantly reducing numerical costs, particularly for large systems with high stiffness values in their differential equations.

Additionally, we examine the positioning of a strongly damped particle in a harmonic potential well, exploring the dynamic implications of such a setup. This examination naturally extends to related issues of escape, including capturing and scattering, and the intricacies of positioning. The approaches outlined in this thesis add to the dialogue on these topics, suggesting avenues for future research and potential improvements in particle positioning techniques.

1.2 Literature overview: Methods

The literature review begins by examining stochastic escape, tracing its development from *Kramers*' work to recent studies, emphasizing its role in chemistry for analyzing molecular reaction rates. It then shifts to deterministic escape, covering its initial theoretical investigations, the concept of safe basins and integrity measure, and the advancements of the recent years on escape in conservative systems. Subsequently, several problem-specific studies are summarized including the problematics of ship capsizing, dynamic pull-in of MEMS devices, and dynamic beam buckling. Further, but precisely not detailed examples are the physics of Josephson junctions [9], escape into inflation or recollapse to singularity in cosmology [16, 151], and escape and recapture of comets and asteroids in celestial mechanics [44].
This review aims to provide an impression of the importance of both stochastic and deterministic escape dynamics, combining historical context with current theoretical developments.

1.2.1 Stochastic Escape

In his landmark study, *Kramers* investigated the Brownian motion of particles in a potential well, providing a diffusion model that was instrumental in calculating the escape rate of particles, analogous to chemical reactions [94]. *Kramers*' model was elegant in its simplicity, employing a one-dimensional potential to draw parallels between the stochastic motion of particles and reaction kinetics. His findings demonstrated that, across a vast viscosity range, the escape probabilities deduced from the diffusion equation were consistent with those predicted by the transition state theory, thus validating his theoretical approach.
Kramers' work transcended its immediate field, influencing various areas, including nuclear physics, as evidenced by its relevance to the fission processes discussed by *Bohr* and *Wheeler*. *Kramers* set the stage for decades of research into thermally activated processes and stochastic dynamics by presenting a unifying framework that linked Brownian motion with chemical reaction rates. His diffusion model remains a cornerstone in the study of chemical kinetics.
The works of *Chandrasekhar* on stochastic processes in physics and astronomy [32], *Wang* and *Uhlenbeck* on the theory of Brownian motion [209], and *Brown Jr.* on thermal fluctuations of ferromagnetic particles [86] were all influenced by the foundational insights provided by *Kramers*' work.
Benzi et al. contributions [13–15] explore stochastic resonance and system complexity, with his 1981 paper emphasizing the resonance in systems subjected to both periodic and random perturbations. *Arecchi et al.*, in their 1984 paper [5] focus on first passage times in

stochastic processes, a quantity of interest similar to escape time, which we will further elucidate in the theory section. In 1986, *Fonseca et al.* [64] investigated non-Gaussian and non-Markovian dynamics in liquids. They connected these dynamics to escape processes from potential wells and activated rate processes in pumped systems.
The paper authored by *Soliman et al.* in 1990 [184] examines the escape dynamics of an oscillator that is sinusoidally driven from a cubic potential well. The study finds that the optimal escape occurs at around 80% of the natural frequency of the oscillator linearized around its bottom stable equilibrium. The research also introduces a stochastic integrity measure. It establishes a connection between this measure and changes in the deterministic basin of attraction's geometry.
The 1993 book 'Activated Barrier Crossing,' edited by *Fleming and Hanggi* [63], focuses on noise-driven escape from metastable states and reactive processes in various environments. It discusses transition-state theory and Kramer's theory, emphasizing the effects of environmental coupling on reactions. The book also touches on recent developments in ultrafast spectroscopy and their impact on barrier-crossing dynamics.
'New Trends in *Kramer*'s Reaction Rate Theory,' a 1995 book edited by *Talkner and Hanggi* [193], extends these discussions covering the concept of escape from metastable states, reviewing foundational theories and introducing recent advancements. The book highlights applications in diffusion, chemical reactions, nucleation, and biological processes.
The paper from 2006 by *Kalmykov et al.* [87] discusses the rate at which a Brownian particle escapes from a double-well potential due to thermal activation. The study explores the escape rates and position correlation times for different dissipation levels. It provides analytical equations for low-barrier scenarios in various damping regimes.
Further research on stochastic escape includes the effect of time-derivative Ornstein-Uhlenbeck noise [7], initial conditions [34], mean escape time [28], and control of the escape rate by combining vortex flow with magnetic fields [2].

1.2.2 Deterministic Escape

Undertaking the exploration of the complex topic of escape, we explore the domain of deterministic escape, distinct from its stochastic counterpart.

Early theoretical advancements

In 1970, *Subramanian* published his Ph.D. dissertation at Harvard University [188], titled 'Escape from a potential well.' This study explores the dynamics of escaping from potential wells in elastic structure buckling and galactic models. Drawing inspiration from *Budiansky*'s dynamic buckling criteria in elastic structures, the dissertation extends to examine conservative two-degree-of-freedom systems. It proposes a model where a

particle is trapped at the bottom of a double-well potential energy function, focusing on the kinetic energy needed to transition to the second well, especially the energy surpassing the saddle point. The dissertation introduces a Hamiltonian for a two-coordinate system with a time-independent potential function and an axis of symmetry, significant in galactic models for analyzing trapped motions. The study also considers a nonlinear coordinate coupling. The results provide insight into escape conditions from potential wells, influencing structural design against buckling and enhancing our understanding of galactic dynamics in gravitational wells.

Later, in his seminal 1979 work [78], *Holmes* investigated the complex behaviors of a nonlinear oscillator under harmonic forcing in a double-welled Duffing potential. The study delves into the bifurcation phenomena that occur as the amplitude of the external force varies. Holmes finds that the system's responses are predictable for small and large force amplitudes and align with established averaging theories. However, at intermediate force levels, the oscillator exhibits complex and unexpected behavior known as strange attractors or chaotic oscillations, a concept previously identified in higher-dimensional autonomous ordinary differential equations. The underlying potential is significant, as it is one of the simplest to model an escape.

The book by *Guckenheimer* and *Holmes* [73] offers a comprehensive examination of nonlinear oscillations, dynamical systems, and bifurcations of vector fields including a systematic analysis of the double-well potential given by the Duffing equation.

In 1985, the same potential well was investigated by *Moon et al.* [135]. The authors report on chaotic motions, emphasizing the fractal nature of the system's basins of attraction and their correlation with homoclinic orbits.

In their paper from 1987, *Ueda et al.* observed subharmonic motions while simulating a particle's dynamics in the two-welled Duffing potential [203], which sheds light on nonlinear resonance and the role of period-doubling bifurcation in the emergence of strange attractors.

In 1991, a paper by *Thompson* [200], titled 'Chaotic Phenomena Triggering the Escape from a Potential Well,' explored the dynamics of a damped, driven mechanical oscillator in a quadratic-cubic potential well, representing a metastable system near a fold. The paper aims to demonstrate how dynamic elements such as saddle nodes, folds, and period doublings combine to form complex response structures, such as hierarchies of cusps and incomplete Feigenbaum trees. A key focus is on the basin of attraction and the loss of engineering integrity caused by a homoclinic tangle, which analysis can precisely forecast. The paper also examines chaotic transients, aligning with scaling laws and disproving common predictions made by harmonic balance analysis about flips and folds. Melnikov's analysis is employed to demonstrate the presence of chaos analytically, showing a good correlation between the generated curve and the numerical data. The paper then shifts focus to 'safe basins,' identifying initial conditions that

lead to escape versus those that do not. The safe basin area is seen to shrink with increasing excitation, a phenomenon called the 'Dover Cliff,' where the safe basin area decreases minimally at first, followed by a drastic reduction, explained through homoclinic tangency. The current dissertation will provide an alternative explanation of the 'Dover Cliff' phenomenon, showing that the typical erosion profile can also be created in linear systems.

Neishtadt 's 1991 paper [145] examines the effects of small or slow perturbations on a Hamiltonian system with one degree of freedom. It focuses on how the phase plane of the unperturbed system, divided by separatrices, behaves under perturbations that enable phase points to cross these separatrices. The paper describes various probabilistic phenomena arising from these separatrix crossings. These include scattering of trajectories, random jumps in the values of adiabatic invariance, and adiabatic chaos. These phenomena are significant both in theoretical problems of classical mechanics and in practical contexts like planetary science and plasma physics.

In 1992, *Gottwald et al.* published a paper on the experimental mimicry of Duffing's equation [72]. Before his work, Duffing's equation was extensively studied analytically and numerically. Nevertheless, experimental work in mechanics has been more limited. *Gottwald*'s work describes a novel experimental approach in which a particle or a rigid body mimics the behavior of Duffing's equation. The study investigates free and forced oscillations, illustrating familiar nonlinear dynamic features such as competing steady-state attractors, hysteresis, sensitivity to initial conditions, subharmonic oscillation, and chaos. The experiment uses a setup similar to a ball rolling on a double-walled potential energy surface, offering insights into Duffing's oscillator.

Quinn 's 1997 paper [162], 'Transition to Escaping System of Coupled Oscillators,' explores a Hamiltonian system derived from two forced pendulums connected by a torsional spring. The paper focuses on a coupled oscillator system's confined motions at intermediate energy levels. These motions, unbounded over time but oscillating within the bounds of the homoclinic orbit of the unperturbed system for a significant duration, are analyzed through equipotential surfaces. These surfaces are closed at lower energies but open up at higher energy levels. The trajectories from a stochastic phase-space region remain confined for extended periods before eventually escaping through the opening in equipotential curves and proceeding to infinity.

In 1999, *Sanjuan* published a paper exploring the effect of nonlinear damping on the universal escape oscillator [175], the first study to investigate the impact of velocity-power proportional damping on escape dynamics. It described a range of nonlinear phenomena, including period-doubling bifurcations and chaos. The research demonstrated that increasing the nonlinear damping power had a similar effect to reducing the damping coefficient in linearly damped systems. The theoretical findings based on the Melnikov

analysis were supported by numerical results, focusing on how the varying excitation amplitude and damping power affected the system's behavior.

Basins of attraction and integrity measures

Over the past four decades, the field of nonlinear dynamics has made significant advancements in understanding the phenomena of particle escape from a potential well, which is strongly related to the concept of the basin of attraction and its integrity measures. Safe basins are areas in the phase space where the system's behavior is dynamically acceptable, including scenarios such as the convergence towards attractors or maintaining stability within a potential well. The integrity of these basins is paramount in studying nonlinear mechanical oscillators, especially concerning the concept of escape from potential wells, as it ensures the system's reliability under variable conditions. [163]
Integrity measures are a quantitative tool to assess the robustness and size of safe basins. The Global Integrity Measure (GIM) and the Integrity Factor (IF) are two primary metrics used in this context [163]. The GIM measures the normalized hyper-volume of the safe basin, offering a straightforward indication of its overall size. On the other hand, the IF assesses the radius of the largest hyper-sphere fully encompassed by the safe basin, focusing on its compact and non-fractal aspects, which are vital for maintaining dynamical integrity.
The concept of basin erosion is central to understanding the dynamics of escape. Erosion refers to the diminishing integrity of safe basins due to changes in system parameters, particularly excitation amplitude. This erosion is a critical indicator of a system's weakening ability to stay within safe operational limits, directly impacting the potential for escape from a well.
Control methods are used to mitigate the effects of basin erosion and maintain dynamical integrity. These methods involve adjusting system parameters or modifying excitation characteristics to delay or prevent the erosion of safe basins. Such strategies are essential to avoid abrupt system failures, especially in environments with uncertainties or external disturbances.
In essence, safe basins and integrity measures are essential to analyzing and controlling the dynamics in nonlinear mechanical oscillators. They are vital to ensuring the reliability of the system and preventing escape from potential wells, with a focus on monitoring and controlling the erosion process.
The following section provides a historical overview of the research on this topic.
In 1989, *Thompson* initiated this exploration focusing on chaotic phenomena that trigger escape from a potential well [198]. His study explored mechanical oscillators and their dynamics, focusing on saddle-node folds, period-doubling flips, and chaos that influence

escape dynamics. *Thompson* 's work was instrumental in highlighting the significance of the basin of attraction and its erosion due to homoclinic tangling, a phenomenon precisely predicted using Melnikov analysis. This foundation was essential to setting the stage for subsequent explorations of the integrity and stability of dynamical systems. Parallel to this, *Soliman and Thompson*, in the same year, advanced the understanding of system stability by introducing the concept of integrity measures to quantify the erosion of both smooth and fractal basins of attraction [183]. Their research explored how attractor basins evolve under varying control parameters, deepening the understanding of system responses to external influences.
Further expanding this field, *Szemplinska-Stupnicka* in 1992 explored the phenomena of cross-well chaos and escape in driven oscillators. Her research offered insights into common behaviors among various dissipative softening-type oscillators, integrating computational simulations and analytical approximations. This work enriched the understanding of how systems transition from regular, periodic responses to more complex, chaotic motions, providing valuable formulae for predicting these transitions [190].
The early 1990s also saw significant contributions from *Lansbury, Thompson* and *Stewart*. Their 1992 study on basin erosion in the twin-well Duffing oscillator unveiled two distinct bifurcation scenarios. This research was essential in understanding how basin boundaries develop fractal structures and how this is related to the dynamics of homoclinic tangencies, further illuminating the complexities of system stability and response under varied conditions [104].
In a series of papers, *Lenci* and *Rega* explored control strategies for nonlinear dynamics in various systems, including two-well impact systems, rocking blocks, and thermoelastic electrically actuated microbeams. Their work combined theoretical treatment and practical applications to provide insights into optimal control strategies aimed at mitigating safe basin erosion and controlling homoclinic bifurcations, thus improving system stability and predictability [109–118].

Escape in conservative systems

Previously, the exploration of escape dynamics through analytical methods has predominantly focused on damped systems, where the assumption of transient decay holds, allowing the application of methods such as harmonic balance [206–208]. Another commonly used technique, Melnikov analysis, does not focus on the solution. Instead, it describes the homoclinic tangency and assesses chaotic behavior, which is then linked to escape [113, 198]. In conservative systems, the decay of transients cannot be assumed, and the impact of initial conditions is preserved throughout the motion, seemingly complicating the situation. However, freely oscillating conservative systems have the

advantage of conserving total energy. Moreover, adiabatic invariants can be identified using action-angle variables, which retain their value throughout the system's motion, even if it is subjected to some excitation [103].

Action-angle variables in classical mechanics are a set of canonical coordinates used in integrable systems. These variables are particularly useful for characterizing the nature of flows within a system when energy levels are conserved, and the space of these energy levels is compact. In essence, they provide a means to understand the frequencies of oscillatory or rotational motions in a system without directly solving its equations of motion, which is especially valuable in systems where the Hamilton–Jacobi equation is entirely separable. Action-angle variables are applicable only when a system is completely integrable, meaning there is a maximal number of independent Poisson commuting invariants, and the conserved energy surface is compact. These variables are instrumental in simplifying the analysis of such systems, making them integral to understanding their dynamics [70, 159, 176].

The 2018 paper by *Gendelman* examines the escape of a classical particle from a one-dimensional conservative potential well using action-angle variables [67]. This approach yields a nontrivial conservation law, enabling efficient analytic methods to predict the minimal forcing amplitude for escape. The study finds a sharp minimum in this amplitude at an intermediate frequency, corroborating previous models relevant to the capsize of ships and microelectromechanical systems.

The research utilizes a cosine hyperbolic potential, uniquely allowing for exact calculations of the action-angle variables. This leads to the identification of two escape mechanisms: the direct maximum mechanism and the subtler saddle mechanism.

Gendelman and *Karmi* in their 2019 paper extend these concepts to other potentials, including truncated quadratic and quadratic-quartic wells. It is possible to find the exact solution in the first case. However, describing the critical force and its dependence on the excitation frequency and the initial phase is not straightforward, especially when dealing with a commensurable ratio of the natural frequency of the well and the excitation frequency. This issue will be later clarified in Chapter 3 describing the dynamics of forced escape from an asymmetrically truncated quadratic potential well based on [224]. The analysis of the quadratic-quartic potential, incorporating elliptic functions, re-encounters the two distinct escape scenarios, allowing a conjecture for the more general case: that the sharp minimum of the critical force at specific frequencies signifies a universal 'fingerprint' of escape dynamics under periodic forcing for a wide variety of weakening potentials.

The 2019 study by *Naiger* and *Gendelman*, [137], represents an important development in the field. This research introduced viscous damping into the model, diverging from the traditional Hamiltonian approach. The paper investigates the averaged transient dynamics by focusing on the primary 1:1 resonance. The study's analytical approach

determines the minimum force necessary to escape, considering the excitation frequency and damping coefficients. The results show consistency with the theoretical predictions, with some deviations at very low frequencies.

Farid's 2020 paper [55] further explores this field by examining asymmetric potential wells. Using two different models, Farid's study contributes to understanding the nuances of transient escape dynamics. The findings demonstrate the uniformity of escape mechanisms in various well structures, even with minor damping, complementing the earlier findings on symmetric wells.

Farid expanded the scope of escape dynamics studies by examining a particle's behavior in a purely nonlinear truncated quartic potential well under harmonic excitation [57]. This work deviates from earlier models that approximated potential wells linearly for small perturbations. The paper highlights the inadequacy of traditional analytical methods when addressing systems with strong nonlinearity, such as pre-tensioned metal wires and polymer-based structural components. Instead, it employs a canonical transformation to action–angle variables within the framework of isolated resonance approximation. This approach allows for an analytic formulation of the escape envelope, revealing that even in such a nonlinear context, a sharp minimum exists in the forcing amplitude for escape, indicative of intersecting escape mechanisms. Notably, Farid identifies three mechanisms: two gradual 'maximum' mechanisms, corresponding to a steady increase in response with excitation intensity, and a 'saddle' mechanism that leads to an abrupt response, which could pose a significant risk due to its sudden nature. The analysis uses energy-based response curves to predict the maximal transient energy over a range of excitation parameters, illustrated by iso-energy contours. These theoretical predictions align well with numerical simulations, offering a comprehensive understanding of escape dynamics in purely nonlinear systems.

Furthering this line of inquiry, *Farid* and *Gendelman* 's joint paper in 2021, [56], investigates the escape dynamics from a weakly nonlinear truncated potential well under the influence of viscous damping. Prioritizing the primary 1:1 resonance, this study is notable for considering the effects of damping in the context of transient behavior, drawing a parallel to a 2019 paper by *Naiger* and *Gendelman* [137]. The researchers employ a multiple-scales analysis to tackle the non-integrable slow-flow equations introduced by damping, demonstrating the significant divergence in escape dynamics between linear and weakly nonlinear systems. This paper uniquely quantifies the damping's impact on the escape threshold through an explicit analytical expression. Their findings underscore the intricacies of slow-flow dynamics and provide an understanding of how damping alters escape mechanisms, thus refining the conceptual framework for studying escape phenomena in damped systems.

Advancing the study of escape dynamics, the work of *Kravetc and Gendelman* in 2022, [95], revisits the classic problem of a particle's escape from a potential well under harmonic

forcing. This paper addresses the challenge of applying action–angle variables to model potentials, which is traditionally possible for only a limited number of potential functions. They propose a method to approximate realistic generic potentials with low-order polynomial functions suitable for the action-angle transformation. To demonstrate their method's effectiveness, they applied it to the isolated resonant approximation for a generic quartic potential. The implications of this approach are particularly relevant to the study of pull-in instabilities in MEMS, including the analysis of a single-degree-of-freedom model of a capacitive micromachined ultrasonic transducer. By approximating the electrostatic potential in MEMS with quartic polynomials, they assessed the accuracy of escape threshold predictions, finding that a global L^2-optimal heuristic approximation yields the most precise results.

In a 2023 study by *Kravetc, Gendelman* and *Fidlin*, [96], the resonant escape under finite-time harmonic excitation in nonlinear systems with damping is explored. Their approach establishes the critical forcing for resonant escape within a finite timeframe. Subsequently, they adapt the isolated resonance approximation (AIR) method to estimate the escape time, offering insight into the escape process's temporal aspect. Their analysis uncovers a fractal-like boundary demarcating the finite-time escape region, elucidating the limitations of the AIR method and the high sensitivity of escape dynamics to the duration of numerical simulations. This discovery is significant for comprehending the intricacies of escape phenomena in practical applications where time constraints are critical.

Shifting the focus from the role of excitation parameters to the influence of initial conditions on escape dynamics, *Karmi, Kravetc* and *Gendelman* in 2021 presented an analytical exploration of safe basins in the context of a classical particle's escape from a potential well under harmonic forcing [88]. The study utilizes the approximation of isolated resonance, simplifying the dynamics to a conservative flow on a two-dimensional resonance manifold. This simplification enables a clear demarcation of SB boundaries, the initial conditions that do not lead to escape. The research used a parabolic-quartic well as a benchmark and provided accurate predictions of SB boundaries for lower forcing amplitudes. The analysis revealed the decomposition of SBs into disjoint zones for specific parameter ranges linked to two distinct escape mechanisms on the resonance manifold. For higher forcing amplitudes, the analytic predictions lose some accuracy due to the limitations of the isolated resonance approximation and the complex nature of secondary resonances. Nevertheless, the findings offer valuable insights into the SB boundaries.

Additional details are available in *Karmi* 's 2022 dissertation on the analytic prediction of safe basins, examining three benchmark potential wells and their transient dynamics [89]. The study presents an in-depth analysis of escape behavior, especially under conditions of principal 1:1 resonance, examining the shift in minimal forcing for

different frequencies and providing explicit evaluations of the critical force values. The dissertation highlights the two earlier found distinct escape scenarios in a strongly nonlinear well, differentiated by their approach to the escape transition. This research provides an analytical framework for predicting SBs, even with strong nonlinearities. It marks an advancement in understanding the influence of initial conditions on escape dynamics. The study highlights the potential for using these predictions as preliminary estimates for more detailed numerical computations.

The 2024 study conducted by *Kravetc et al.* [97] advances our understanding of dynamical integrity and safe basins in systems undergoing forced escape. The 'approximation of isolated resonance' method was used to determine and analyze safe basins in escape scenarios from potential wells. The authors' approach features precise identification and characterization of SBs, including the establishment of erosion profiles. A notable contribution is the introduction of the concept of 'true' safe basins, which are characterized by their invariance to phase shifts, a crucial consideration in real-world applications. The study uses a cubic polynomial potential as a benchmark model to demonstrate the effectiveness of their method.

Building on the foundation of escape dynamics in single-degree-of-freedom systems, recent studies by *Engel, Ezra, Gendelman* and *Fidlin* have expanded analytical investigation into two-degree-of-freedom dynamical systems. In their 2023 paper, *Engel et al.* explored the escape mechanisms of a system consisting of two coupled particles via a spring from a potential well [50]. By examining three distinct potential wells with varying topologies, the study aims to uncover the fundamental escape mechanisms within different regions of parameter space. Employing both numerical and analytical methods, the researchers map out escape mechanisms across a range of initial conditions, proposing analytic criteria to predict system behavior.

In a related study by *Engel, Gendelman* and *Fidlin*, the scope of analytical research is expanded to include the escape of a single particle from a two-dimensional potential well [51]. This research is focused on scenarios with zero initial velocities, analyzing the escape basins on the configuration plane. To achieve this, the study develops two complementary analytic approaches. The first approach examines the gradient system linked to the well's potential relief, while the second modifies the isolated resonance approximation to suit the two-dimensional context. Together, these methods delineate an outer boundary of the stability basin. Additionally, the erosion of this boundary by secondary resonances is numerically investigated, providing insight into the destabilizing effects that these resonances can have on escape dynamics.

1.3 Literature overview: Applications

The previous sections have articulated the importance of the escape phenomenon in nonlinear dynamics, a concept integral to numerous applications. The following section will present specific engineering cases that emphasize the role of escape. Through these cases, we will see how understanding escape dynamics is a critical element in the design and functionality of various engineering systems.

Ship capsize

A ship can capsize when external forces, such as waves, wind, or uneven weight distribution, cause it to tip beyond its angle of positive static stability. This tipping point is comparable to a particle escaping a potential well where enough energy is received to cross the boundary. The dynamics of a ship capsize is governed by the interplay of these forces, the vessel's design, and its initial stability, determining whether it can recover or not.

The 1987 paper authored by *Virgin* [205] significantly contributes to understanding nonlinear ship rolling motion. The paper proposes a semi-empirical, nonlinear differential equation that models the rolling motion of a ship. The equation incorporates experimental data to model nonlinear damping and righting lever characteristics, and the comparison with observed behavior is reasonably good. The article describes a numerical phenomenological approach that analyzes this type of behavior.

In his 1989 paper, *Virgin* introduces a safety criterion to prevent the capsize of floating vessels [206]. The criterion is based on the total energy of the steady-state solution of a harmonically driven oscillator. Should the energy level reach a certain percentage of the energy corresponding to the saddle energy, the ship enters a critical region where its operation is unsafe. For analytical purposes, the softening Duffing oscillator is used with some additional damping.

Virgin's safety criterion is elaborated through the harmonic balance method, which approximates the steady-state amplitudes for velocity and displacement, leading to an evaluation of escape conditions. The paper also extends this analysis to biased systems, where additional constant forces, such as wind, result in asymmetric potentials and modified escape dynamics. The research validates the safety criterion through comparisons with numerical simulations, noting its conservative estimates in predicting the required forces for escape. The conclusion emphasizes the practical significance of the criterion in marine design, offering a straightforward, adaptable method for enhancing the safety and stability of floating vessels.

Related to *Virgin*'s 1989 investigation of the double-well Duffing oscillator, *Nayfeh et al.* study the bifurcations in a forced softening Duffing oscillator, providing a complementary analytical perspective [140]. Similarly, the behavior of a damped

Duffing oscillator with softening characteristics was analyzed, taking into account the impact of harmonic excitation's frequency and amplitude with the novelty in the methodology combining second-order perturbation solutions and Floquet analysis to construct bifurcation diagrams. This approach successfully predicts complex system behaviors such as symmetry breaking, period-doubling bifurcations, and jumps between bounded and unbounded motions, which are corroborated by computer simulations exhibiting chaos and unbounded motions, among other behaviors.
The subsequent note from 1991 by *Virgin et al.* links directly to *Nayfeh* and *Sanchez*'s findings by contrasting the multiple-scale method with the harmonic balance approach in analyzing escape dynamics from a potential well [207]. This comparison, underpinned by stability investigations via Floquet theory and the Routh-Hurwitz criterion, further elucidates the capsize mechanisms outlined in the softening-spring Duffing oscillator model.
In 1992, *Virgin et al.* continued this line of inquiry with a focus on predicting escape from potential wells under harmonic excitation [208]. The study extends the application of the harmonic balance method to assess the critical forcing amplitudes against potential barriers in nonlinear systems with damping. The paper presents findings for both single and coupled two-degree-of-freedom systems, showing close alignment with numerical integration results, albeit with some discrepancies. This progression of research, initiated by *Virgin*'s work, develops a more nuanced understanding of the nonlinear dynamical systems relevant to marine safety and design.
The 1992 paper by *Thompson et al.*, parallel to *Virgin*'s work, delves into the dynamics of a capsizing ship by deriving equations of motion for a vessel experiencing heaving, swaying, and rolling in varying wave conditions [201]. It adopts a first-principles approach, allowing for a broad application to different sea states. It also introduces a novel method for approximating hydrodynamic pressure using an expansion in circular harmonics. By assuming a static balance in heave, *Thompson* simplifies the analysis to focus on a single roll equation. This equation accounts for both direct and parametric excitation. The numerical and transient state analysis of a biased boat model upholds the earlier findings about basin erosion and emphasizes the significance of transient capsize phenomena, particularly under realistic levels of parametric excitation.
The paper published by *Spyrou et al.* in 2000 reviews the progress made in nonlinear dynamics within naval architecture in recent years, providing a comprehensive analysis of ship dynamics [186]. The paper focuses on the advancements made since the 1970s, highlighting key topics such as ship capsize mechanisms and broaching, particularly in the context of their nonlinear behavior. The authors also discuss how these insights were integrated with numerical ship hydrodynamics, representing a significant shift in understanding ship motion instabilities. This review showcases the importance

of nonlinear dynamics in addressing complex challenges in naval architecture and improving marine safety and ship design.
A similar message is found in the book by *Belenky et al.* from 2007. The book comprehensively covers stochastic and deterministic differential equations that describe ship motion [11]. This book emphasizes the importance of nonlinear dynamics and stochastic processes in ship motion, particularly in waves. It evaluates the limitations of conventional dynamic stability assessment methods for modern naval and commercial ships. The book also discusses contemporary solutions and various stability failures, including capsizing, surf riding, broaching, parametric resonance, and instability at wave crests.

Dynamic buckling

Dynamic buckling is a failure mechanism of elastic structures under time-dependent loads, which has been extensively analyzed in the works of *Budiansky* [21–23, 82] and by others [65, 71, 77, 80, 92]. This concept is particularly relevant in structures sensitive to initial imperfections and subjected to variable loading conditions. *Budiansky* 's research provides criteria and estimates for the dynamic buckling strength of such structures.
The subject of dynamic buckling is further explored in the work of *Thompson et al.* [196], which discusses the broader spectrum of elastic instability phenomena, including buckling. This approach provides a framework for understanding the boundary conditions and constraints contributing to such instabilities.
The phenomenon of dynamic buckling can be observed in various structural forms under different loading scenarios. For instance, the study by *Vasilikis and Karamanos* [204] investigates the behavior of thin-walled cylinders under external pressure, focusing on buckling and post-buckling characteristics. This research is significant for practical engineering applications, such as the stability of buried pipelines. Another example is provided by *Sadighi et al.* [172], where the dynamic buckling of axially half-corrugated thin-walled tubes under axial loading is examined. Their work emphasizes the influence of structural geometry on the buckling process.
The study by *Buratti and Tavano* [24] on the dynamic buckling of anchored steel tanks in seismic conditions further illustrates the relevance of dynamic buckling in structural engineering. This research highlights the interaction between structural dynamics and external loading. The foundational texts by *Simitses and Hodges* [182], and *Bushnell* [26] provide a broader context to understand dynamic buckling in various engineering scenarios.
Dynamic buckling can be conceptually linked to the 'escape from a potential well' problem. In this analogy, the structure in a stable equilibrium state is akin to a particle in a potential well. Under dynamic loading, the stability of the structure is challenged,

similar to that of a particle that receives energy to escape the well. The critical point of dynamic buckling, where the structure loses stability, parallels the particle's escape point from the potential well.
Further expansion of the topic is seen in the work of *Champneys et al.* [31], which explores elastic instability, particularly in structures that lose stability subcritically without a nearby stable post-buckled state. This work underscores the challenges of designing structures susceptible to buckling due to imperfections or external shocks. It also emphasizes the concept of the Maxwell load, where the energy levels of the unbuckled and buckled states are equivalent.

Dynamic pull-in

The following overview is based on the comprehensive summary of *Zhang et al.* [220]. Electrostatic actuation is a leading mechanism in micro/nanoelectromechanical systems (MEMS/NEMS), chosen for its numerous advantages. This method has spurred the development of various electrostatic actuators employed in applications such as micro/nanomotors, switches, relays, resonators, mirrors, pumps, valves, and filters [10, 27, 35, 42, 52, 121, 124, 149, 150, 160, 194, 218]. [220] categorizes these devices by:

- Input condition: encompassing displacement, torsional, and general type actuators [59, 85, 105, 106, 108, 146, 157, 211].
- Designated motion: consisting of parallel-plate (horizontal and vertical movement types) and comb-drive (lateral, vertical, rotational, torsion bar types) actuators [59, 185, 194, 211, 212].
- Element configuration: incorporating beam-type (such as cantilever, fixed-fixed, curved, bridge-type beams) [157, 213], plate-type [105], membrane-type [85], and specialized forms (S-shaped [187], tulip-shaped [178], stacked [90], U-shaped [161], multi-layer [147, 170], etc.).

Electrostatic MEMS/NEMS are particularly advantageous because of the intense interaction between different energy domains at the micro- and nanoscales. However, this actuation method inherently introduces nonlinear dynamics, notably leading to a 'pull-in' instability. This pull-in phenomenon is analogous to the problem of a particle escaping from a potential well, both illustrating critical behaviors in their respective systems. Pull-in instability significantly limits the operational range of these systems, as it occurs when the electrostatic force increases more rapidly than the corresponding spring force, causing a crucial performance limitation [189]. Instability here refers to the loss of stability and the post-critical behavior of the system, including both static

and dynamic aspects. *Bolotin* [18] offers an in-depth look at dynamic instabilities in structural mechanics, which is essential for understanding pull-in instability.
The groundwork on pull-in phenomena was laid by *Nathanson et al.* [138] and *Taylor* [195] in the late 1960s, leading to a rich body of research on this nonlinear behavior. Various modeling and simulation approaches have been developed for pull-in analysis, including lumped capacitor-mass-spring systems [126], simplified geometrical analytical models [17, 170], reduced order models [33, 143, 215], Full-Lagrangian methods [40, 41], Lyapunov exponent methods [100], and molecular dynamics modeling for carbon nanotubes [53]. Comprehensive reviews on these models and simulations are available from authors such as *Pelesko* and *Bernstein* [156], *Lin* and *Wang* [120], *Batra et al.* [10], *Zhang et al.* [218], and *Chuang et al.* [35]. Pull-in analysis is generally divided into two categories: one using quasistatic assumptions and the other focusing on dynamic pull-in [54].
In addition to electrostatic forces, factors such as geometrical and material characteristics, surface effects [4, 12, 47, 48, 58, 127], temperature variations [192, 214], size-dependent effects [1, 6, 66, 171], gas squeeze film effects [8, 119, 217], fluid loadings [165, 180], mechanical shocks and noise impacts [3, 38, 83, 153, 216, 219] also play a role in pull-in instability. Researchers such as *Luo* and *Wang* [126], *Zhao et al.* [143], *Krylov* and *Maimon* [99], and *Neilson* and *Barbastathis* [148] have made significant contributions to understanding pull-in dynamics in MEMS/NEMS.
Furthermore, the pull-in phenomenon is not only limited to electrostatic actuators but also occurs in magnetostatic [41, 146, 194] and dielectric elastomer actuators [39, 76, 91, 136], often leading to failures. The rapid development of MEMS/NEMS has heightened interest in reliability analysis, prediction, and testing of pull-in-induced failures [35, 37, 124, 125]. The degree of frequency adjustment in these systems is also constrained by pull-in effects [49, 54, 144, 154, 155]. Furthermore, recent attention has been drawn to pull-in instabilities in nano-switches [191] and graphene membranes [123].
The pull-in instability in electrostatic MEMS/NEMS devices has received significant attention due to its widespread impact on device performance, as highlighted by *Zhang et al.* [220]. Strategies to mitigate pull-in instability, improve operational range, and harness the phenomenon for practical applications have become focal points in MEMS/NEMS research. Numerous studies have proposed various approaches, including mechanical modifications [25, 81, 164] and control strategies [30, 131, 179], to extend the travel range and improve the stability of these devices.
Rocha et al. [167] have contributed to this discourse by comparing different methodologies to expand the travel range of electrostatic actuators on parallel plates. Despite the general perception of pull-in as an undesirable effect, its control, especially in the context of dispersive forces, has been a subject of considerable research [101, 102, 107]. *Borovic et*

al.[19] and *Shirazi et al.* [181] have provided insightful analyses of existing open-loop and closed-loop control strategies for gap-closing MEMS electrostatic actuators.
Although pull-in instability is typically seen as a negative aspect in most MEMS/NEMS devices, it is also ingeniously utilized as a sensor mechanism in some cases, creating actuators capable of generating significant force. Devices such as MEMS switches and accelerometers [46, 85, 161, 168] are examples where pull-in instability is not merely managed but is effectively employed as a functional characteristic. Additionally, the pull-in phenomenon serves as a test mechanism to extract crucial material parameters such as Young's modulus, interlayer shear effect, and residual stress [122, 152, 169–171].

Particle positioning

The manipulation of particles from the microscale down to the nanoscale with precision and efficiency is becoming increasingly significant, especially in fields such as rapid prototyping and biomedicine. While optical manipulation techniques have traditionally dominated this area, there has been a shift towards utilizing acoustic forces for assembling particles. This approach eliminates the requirement for chemical agents, including photoinitiators, as noted in the works of [128, 134].
In Chapter 6, we focuses on the dynamics of a strongly damped particle in a cosine potential, analogous to the system of a damped-driven pendulum, which has been extensively studied in the literature. In his 1922 publication, *Hamel* [75] investigated the undamped forced oscillations of a pendulum at considerable amplitudes, examining the presence and characteristics of periodic solutions. Later, *Hubbard* [79] investigated the chaotic dynamics of the forced damped pendulum, illuminating the complexity and control opportunities within such systems. Thanks to *Coullet et al.* [158], recent advances have been made in understanding the dynamics of the damped driven pendulum subjected to a constant torque. Further contributions were made by *Boscaggin et al.* [20], who studied subharmonic solutions, and *Salas et al.* [173], who offered closed-form solutions for the dynamics of forced damped rotational pendulum oscillators.

Further examples

In the following, some further examples on the importance of the escape phenomena are given.
A significant paper from *Bethe et al.* from 1979, investigates the gravitational collapse of stars [16]. This paper offers insights into the equation of state during stellar collapse. The authors discuss the transformation of nuclei and particles at various densities, electron capture by nuclei, and the adiabatic journey to higher densities. The paper contributes significantly to our understanding of stellar phenomena, particularly in the context of the equation of state.

The book by *Barone et al.* [9] is a significant study on the physics and applications of the Josephson junction, where the tunneling of electrons can be understood as an escape.
The paper by *Castagnino and Ferraro* [29], published in 1984, provides a detailed analysis of the phenomenon of the capture of charged particles by an electric field. The study examines the behavior of a massless scalar quantized field in two-dimensional flat space-time, with one mirror exhibiting in-out motion. This analysis sheds new light on the creation of particles and the spectrum of such particles.

1.3.1 Objective of the Work

The primary aim of this research is to make a modest contribution to the field of oscillator dynamics, with a particular focus on understanding escape dynamics in various systems. Our approach is structured around three key objectives:

1. **Exploring under-researched areas in harmonic oscillators related to escape**: We recognize the gaps in current literature, especially in studying the harmonic oscillator, where excitation and natural frequencies are commensurable. This aspect of our research seeks to build on and extend the existing knowledge base, addressing topics that have not been fully resolved in previous studies. Additionally, we aim to broaden the understanding of transient processes in harmonic oscillators involving both damping and excitation, areas that seem to be less covered in existing research.

2. **Advancing the understanding of the escape of multiparticle chains**: A significant part of our research is dedicated to exploring the escape of strongly coupled chains under poly-harmonic excitation. We develop and analyze models for two and more complex n-body systems.

3. **Exploring the mechanisms of escape**: Our objective is to enhance our understanding of the escape mechanisms in oscillator systems. This involves a thorough analysis of the maximum and saddle mechanisms described by *Gendelman*, as well as the interaction of the concurring fast and slow mechanisms that emerge as a result of initial conditions and from the interplay between free and forced oscillations.

Furthermore, our research incorporates a newly developed averaging method based on classical probability density functions. This method is intended to offer an alternative to our study's analytical and numerical analysis processes, facilitating a more efficient calculation of the averaging integral.
In summary, this research aims to contribute to understanding the dynamics of escape by studying less-explored areas, enhancing the understanding of multiparticle chains,

and elucidating escape mechanisms to add valuable insights to the field of dynamical systems.

1.3.2 Structure of the Work

This dissertation is structured as follows. In Chapter 2, the development of averaging methods and their applications to describe nonlinear escape dynamics is performed. Linear and nonlinear escape problems are investigated in Chapter 3, respectively, from a safety perspective focusing on safe basins of escape. In contrast, Chapter 4 focuses on the case where escape is desired, exploring the effects of excitation parameters on escape. Chapter 5 investigates escaping multiparticle chains and reducing their dynamics, whereas Chapter 6 offers a perspective for controlling escape. The final chapter provides a summary and an outlook on future research directions.

Chapter 2: Methods
This chapter introduces the mathematical methods used throughout the dissertation. It begins with a discussion of averaging techniques and an exploration of cross-correlation-based averaging. The chapter concludes by examining the global optimization of the sum of sines, which sets the stage for more sophisticated analyses in subsequent chapters.

Chapter 3: Safe basins of escape in the linear case
The focus shifts to examining safe basins of escape in linear systems. For that, various definitions of escape are introduced in this chapter. Furthermore, the undamped-driven harmonic oscillator and its extension to a damped-driven harmonic oscillator are analyzed.

Chapter 4: Critical forcing of escape
This chapter parallels the structure of Chapter 3. However, it focuses on critical forcing scenarios in both undamped and damped-driven harmonic oscillators. The investigation is extended to small-nonlinearities in conservative harmonically driven systems. Finally, an experimental validation of the results is performed.

Chapter 5: Escape of multiparticle chains with different time-scales
Here, the dissertation expands to multiparticle chains, exploring the escape of a two-particle chain under biharmonic excitation, an n-particle chain under polyharmonic excitation, and a chain of two colliding particles under biharmonic excitation, providing a comprehensive view of escape dynamics across various system complexities.

Chapter 6: Controlling escape
The penultimate chapter addresses control strategies for escape dynamics, focusing on particle positioning in overdamped systems. This chapter bridges the theoretical aspects of the dissertation with practical control applications.

Chapter 7: Summary and outlook

The final chapter summarizes the key findings of the dissertation and discusses open questions and potential future applications of the models and methods developed throughout the work.

2 Fundamentals

In the field of nonlinear dynamics, obtaining exact analytical solutions can be challenging or even impossible, leading to the need for approximations and simplifications. These approximation methods must be consistent and yield the known solution of the linear system for diminishing nonlinearities. Such methods are referred to as asymptotic methods.

Among the leading asymptotic approaches are perturbation theory (with the Lindstedt-Poincaré method noted for its prominence [141]), averaging techniques [174], and the method of multiple scales [142]. Which method is used depends on the problem at hand and the depth of knowledge that the researcher has. Perturbation theory is the most basic and commonly used of these methods, giving direct approximations for the paths that state variables follow. In contrast, averaging and multiple-scale methods start by transforming the system's coordinates, to simplify the process of finding and analyzing both stable and unstable equilibrium solutions. These methods enable one to identify slow manifolds and to separate dynamics on these manifolds and oscillations around them. Then, all kinds of motion on these manifolds can be investigated much more easily. For example, periodic motions of the original system appear as equilibria on the slow manifold. Transient motions on the slow manifold are easy to integrate numerically since they are slow and allow for significantly larger time steps.

Other methods focus only on long-term steady-state solutions. One of the most famous representative of such methods is the method of harmonic balance. To analyze the dynamics of the forced-damped pendulum, we employ the harmonic balance method, a proven analytical technique in various scientific and engineering fields, including but not limited to electrical circuits, fluid dynamics, and mechanical systems, as extensively documented in the literature [69, 74, 93, 139, 177].

In this chapter, we describe a specific form of the averaging method utilized throughout the dissertation. Calculating the average of a function includes an integral over a time period, which is often not straightforward, especially in piecewise smooth problems. Therefore, an alternative method developed by *Genda et al.* is also described briefly [227].

Finally, at the end of this chapter, a theorem is presented to approximate the global extrema of the sum of two sinusoidal functions. This theorem is necessary to handle one of the simplest oscillatory systems capable of escape: a harmonically driven particle in a truncated quadratic potential well. If the particle is in the well, the solution in the non-resonant case is the sum of two harmonics. However, to determine whether the particle will reach the boundary of the well, we need to find the global optima of the solution. This problem results in significant algebraic difficulties, so an approximation needs to be developed.

2.1 The method of harmonic balance

The following section is based on [84][1].

The method of harmonic balance facilitates the approximation of periodic solutions to nonlinear systems up to any desired order. This approach is particularly valuable in identifying limit cycles within a system. Unlike perturbation method solutions, the harmonic balance method is not limited to small nonlinearities. However, the term 'harmonic balance' is not consistently defined across the literature. Typically, 'harmonic balance' refers to a first-order approximation. Some authors use the term to denote an 'equivalent linearization,' while in control theory, this concept is related to the describing function of a nonlinear element. Assuming a periodic solution, the nonlinear equation is harmonically linearized, thus representing a first-order approximation technique. This results in a linear differential equation with amplitude-dependent coefficients that reflect the nonlinearity of the original system. A slightly modified version involves inserting a harmonic function with the problem's fundamental frequency into the nonlinear differential equation and performing a coefficient comparison. Instead of the harmonically linearized system equation, this yields a direct first-order approximation solution. For higher-order approximations, the harmonic balance method can be employed as a Galerkin method [129].

2.1.1 Harmonic balance as equivalent linearization

Consider the following nonlinear equation:

$$\ddot{x} + f(x, \dot{x}) = g(t). \tag{2.1}$$

[1] The original German text has been translated by the author.

We seek periodic solutions. Assume that $f(x, v)$ is symmetric and lacks a constant component. The objective is to transform the equation into the following form:

$$\ddot{x} + b^*\dot{x} + a^*x = g(t). \tag{2.2}$$

This can be achieved by assuming sinusoidal vibration responses:

$$x = \hat{x}\cos\omega t \tag{2.3}$$

$$\dot{x} = v = -\hat{x}\omega\sin\omega t \tag{2.4}$$

These expressions are substituted into $f(x, v)$. Since a periodic solution is sought, $f(x, v)$ is also periodic and can be expressed as a Fourier series, considering only the fundamental frequency ω components (first-order approximation).

$$\begin{aligned} f(\hat{x}\cos\omega t, -\hat{x}\omega\sin\omega t) &= a_0 + \sum_{k=1}^{\infty}(a_k\cos k\omega t + b_k\sin k\omega t) \\ &\approx a_1\cos\omega t + b_1\sin\omega t \\ &\approx a_1\frac{x}{\hat{x}} + b_1\frac{\dot{x}}{-\hat{x}\omega} \\ &\approx a^*x + b^*\dot{x} \end{aligned} \tag{2.5}$$

with coefficients

$$a^* = \frac{\omega}{\pi\hat{x}}\int_0^{\frac{2\pi}{\omega}} f(\hat{x}\cos\omega t, -\hat{x}\omega\sin\omega t)\cos\omega t\,\mathrm{d}t \tag{2.6}$$

$$b^* = -\frac{1}{\pi\hat{x}}\int_0^{\frac{2\pi}{\omega}} f(\hat{x}\cos\omega t, -\hat{x}\omega\sin\omega t)\sin\omega t\,\mathrm{d}t \tag{2.7}$$

This process linearizes the original equation. The coefficients a^* and b^* depend on the amplitude $\hat{x}$.

2.1.2 Harmonic balance as a weighted residuals method

This is a Galerkin method that employs harmonic functions as both ansatz and weight functions. Consider the following nonlinear equation:

$$\ddot{x} + f(x, \dot{x}) = g(t). \tag{2.8}$$

The solution is expressed as a Fourier series:

$$x_h(t) \approx C_0 + \sum_{k=1}^{N} (C_k \cos k\omega t + S_k \sin k\omega t). \tag{2.9}$$

The approach involves defining a residual with the approximation x_h and minimizing this residual. We define an error (the residual) as:

$$r = \ddot{x}_h + f(x_h, \dot{x}_h) - g(t). \tag{2.10}$$

If the residual itself is expanded into a Fourier series

$$r_h(t) = \alpha_0 + \sum_{k=1}^{\infty} (\alpha_k \cos k\omega t + \beta_k \sin k\omega t), \tag{2.11}$$

the residual is minimized when the coefficients of the Fourier series up to order N (the order of the approximation x_h) vanish:

$$\alpha_0 = \frac{1}{T} \int_0^T r_h(t) \mathrm{d}t = 0 \tag{2.12}$$

$$\alpha_k = \frac{2}{T} \int_0^T r_h(t) \cos(k\omega t) \mathrm{d}t = 0, \quad k = 1, \ldots, N \tag{2.13}$$

$$\beta_k = \frac{2}{T} \int_0^T r_h(t) \sin(k\omega t) \mathrm{d}t = 0, \quad k = 1, \ldots, N \tag{2.14}$$

This produces $2N + 1$ equations to solve for the $2N + 1$ unknowns ($C_0, C_1, \ldots, C_N$, $S_1, \ldots, S_N$). Being a Galerkin method, it yields the best possible solution with the given ansatz functions. By minimizing the residual, the distance between the linear combination of the basis functions and the actual solution is minimized.

2.2 The averaging method

In what follows, the averaging method is briefly described based on the book of *Sanders et al.* [174].

2.2.1 Transformation to standard form

In the analysis of nonlinear dynamical systems, it is practical to express the system in a standard form. This step makes using perturbation methods more straightforward to

analyze the system's behavior. Consider a system subject to a perturbation given by the equation

$$\dot{\mathbf{x}} = \mathbf{f^0}(\mathbf{x}, t) + \varepsilon \mathbf{f}^1(\mathbf{x}, t, \varepsilon), \qquad \mathbf{x}(0) = \mathbf{a}, \tag{2.15}$$

and the corresponding unperturbed system

$$\dot{\mathbf{z}} = \mathbf{f}^0(\mathbf{z}, t), \qquad \mathbf{z}(0) = \mathbf{a}. \tag{2.16}$$

We assume that the initial condition-dependent solution to the unperturbed system $\mathbf{z}(\mathbf{a}, t)$ is known. Using the method of variation of integration constants, we define a transformation $\mathbf{z} = \mathbf{z}(\zeta, t)$, with $\mathbf{z}(\zeta, 0) = \zeta$ and $\zeta \in \mathbb{R}^n$.
The perturbed solution can be expressed as $\mathbf{x} = \mathbf{z}(\zeta, t)$ after the transformation. We then derive a differential equation for ζ that combines the original perturbed system with the unperturbed solution:

$$\frac{\partial \mathbf{z}(\zeta, t)}{\partial t} + \mathrm{D}_\zeta \mathbf{z}(\zeta, t) \cdot \frac{d\zeta}{dt} = \mathbf{f}^0(\mathbf{z}(\zeta, t), t) + \varepsilon \mathbf{f}^1(\mathbf{z}(\zeta, t), t, \varepsilon), \tag{2.17}$$

with $\mathrm{D}_\zeta(\mathbf{z})$ denoting the Jacobian of the vector $\mathbf{z}$ with respect to ζ. Realizing that the unperturbed function $\mathbf{z}$ satisfies its differential equation, we simplify to find an equation for $\dot{\zeta}$, assuming that the Jacobian $\mathrm{D}_\zeta \mathbf{z}(\zeta, t)$ is invertible and sufficiently smooth:

$$\dot{\zeta} = \varepsilon \left(\mathrm{D}_\zeta \mathbf{z}(\zeta, t)\right)^{-1} \cdot \mathbf{f}^1(\mathbf{z}(\zeta, t), t, \varepsilon). \tag{2.18}$$

Under the above assumptions on the Jacobian $\mathrm{D}_\zeta \mathbf{z}(\zeta, t)$, the equation for ζ, with the initial condition $\zeta(0)$, is the system in its standard form. While the transformation is theoretically simple, it can be complex and impractical in practice. However, the standard form works well in the case of quasilinear perturbation problems. We consider the perturbation problem to be quasilinear when the system can be expressed as:

$$\dot{\mathbf{x}} = A(t)\mathbf{x} + \varepsilon \mathbf{f}^1(\mathbf{x}, t, \varepsilon), \tag{2.19}$$

where $A(t)$ is a matrix function that varies continuously with time. The unperturbed equation is represented by $\dot{\mathbf{y}} = A(t)\mathbf{y}$, which has a complete set of independent solutions that construct the fundamental matrix solution $\Phi(t)$. This fundamental matrix is chosen to satisfy $\Phi(t_0) = I$. With this, the variable transformation is applied:

$$\mathbf{x} = \Phi(t)\mathbf{z}, \tag{2.20}$$

leading to the perturbed equation in the transformed variables:

$$\dot{\mathbf{z}} = \varepsilon \Phi^{-1}(t)\mathbf{f}^1(\Phi(t)\mathbf{z}, t, \varepsilon) \tag{2.21}$$

under the assumption that $\Phi^{-1}(t)$ is invertible for all nonnegative t. If $A(t)$ is constant, the fundamental matrix becomes $\Phi(t) = e^{A(t-t_0)}$, and the standard form is expressed as:

$$\dot{\mathbf{z}} = \varepsilon e^{-A(t-t_0)}\mathbf{f}^1(e^{A(t-t_0)}\mathbf{z}, t, \varepsilon). \tag{2.22}$$

This form is particularly useful when the eigenvalues of A are all purely imaginary. If not, the situation can still be challenging even if f^1 is bounded.
An illustrative example is provided by an oscillatory system subject to a perturbed initial value problem:

$$\ddot{x} + \omega^2 x = \varepsilon g(x, \dot{x}, t, \varepsilon), \tag{2.23}$$
$$x(0) = a_1, \tag{2.24}$$
$$\dot{x}(0) = a_2. \tag{2.25}$$

For the unperturbed scenario $\ddot{y} + \omega^2 y = 0$, we adopt a transformation from the variation of constants:

$$x = z_1 \cos(\omega(t - t_0)) + \frac{z_2}{\omega} \sin(\omega(t - t_0)), \tag{2.26}$$
$$\dot{x} = -z_1 \omega \sin(\omega(t - t_0)) + z_2 \cos(\omega(t - t_0)). \tag{2.27}$$

This transformation enables us to recast the perturbed system as:

$$\dot{z}_1 = -\frac{\varepsilon}{\omega} \sin(\omega(t - t_0)) g(\cdot, \cdot, t, \varepsilon), \tag{2.28}$$
$$\dot{z}_2 = \varepsilon \cos(\omega(t - t_0)) g(\cdot, \cdot, t, \varepsilon), \tag{2.29}$$
$$z_1(t_0) = a_1, \tag{2.30}$$
$$z_2(t_0) = a_2. \tag{2.31}$$

To elucidate the system's behavior further, we introduce a transformation to amplitude r and phase ϕ variables:

$$\mathbf{x} = \begin{bmatrix} r \sin(\omega t - \phi) \\ r\omega \cos(\omega t - \phi) \end{bmatrix}, \qquad \dot{\mathbf{x}} = \begin{bmatrix} r\omega \cos(\omega t - \phi) \\ -r\omega^2 \sin(\omega t - \phi) \end{bmatrix}. \tag{2.32}$$

Through this transformation, we derive the equations governing the evolution of r and ϕ:

$$\dot{r} = \varepsilon \cos\big(\omega t - \phi\big) g(\cdot, \cdot, t, \varepsilon), \tag{2.33}$$

$$\dot{\phi} = -\frac{\varepsilon}{r\omega} \sin\big(\omega t - \phi\big) g(\cdot, \cdot, t, \varepsilon). \tag{2.34}$$

The initial conditions for r and ϕ are extracted from the initial state of x and $\dot{x}$. This transformation will be frequently used in this work to transform nonlinear escape problems with a single degree of freedom into the standard form to analyze them further.

2.2.2 Periodic averaging in perturbation analysis

Periodic averaging is applied to perturbation problems in the standard form where the function to be averaged is periodic. For a system described by

$$\dot{\mathbf{x}} = \varepsilon \mathbf{f}^1(\mathbf{x}, t) + \varepsilon^2 \mathbf{f}^2(\mathbf{x}, t, \varepsilon), \tag{2.35}$$

$$\mathbf{x}(0) = \mathbf{a}, \tag{2.36}$$

with $\mathbf{f}^1$ and $\mathbf{f}^2$ being T-periodic in t, the averaged equation is obtained by integrating $\mathbf{f}^1$ over one period and neglecting the ε^2 term:

$$\dot{\mathbf{z}} = \varepsilon \bar{\mathbf{f}}^1(\mathbf{z}), \tag{2.37}$$

$$\mathbf{z}(0) = \mathbf{a}, \tag{2.38}$$

where

$$\bar{\mathbf{f}}^1(\mathbf{z}) = \frac{1}{T} \int_0^T \mathbf{f}^1(\mathbf{z}, s)\, ds =: \left\langle \mathbf{f}^1(\mathbf{z}, t) \right\rangle. \tag{2.39}$$

This method ensures that the solution $\mathbf{x}(t)$ stays within a bound of $\mathbf{z}(t)$, of magnitude ε, for $0 \leq t \leq L/\varepsilon$, which was first shown by *Bogoliubov* [98]. The reader is referred to [174] for the proof of first-order periodic averaging. The method can be enhanced to incorporate the higher-order terms $\varepsilon^2, \varepsilon^3, \ldots$
An example is given in the following to demonstrate the application of periodic averaging.

Example 2.2.1 (Van der Pol Oscillator)**.** *The Van der Pol oscillator, with nonlinearity of $O(\varepsilon)$, is expressed as:*

$$\ddot{x} - \varepsilon(1 - x^2)\dot{x} + x = 0, \qquad x(0) = x_0, \qquad \dot{x}(0) = u_0, \tag{2.40}$$

where the function $g(x, \dot{x})$ from Eq. (2.23) corresponds to $\varepsilon(1-x^2)\dot{x}$, a nonlinear damping term. Implementing the standard amplitude-phase transformation, we consider:

$$x = r\sin\big(t-\phi\big), \tag{2.41}$$
$$\dot{x} = r\cos\big(t-\phi\big). \tag{2.42}$$

Substituting into the Van der Pol equation yields the equations in the standard form for the amplitude r and phase shift ϕ:

$$\dot{r} = \varepsilon r\left(1-r^2\cos^2(t+\phi)\right)\sin^2(t+\phi), \qquad r(0)=r_0, \tag{2.43}$$
$$\dot{\phi} = \varepsilon\left(1-r^2\cos^2(t+\phi)\right)\sin\big(t+\phi\big)\cos\big(t+\phi\big), \qquad \phi(0)=\phi_0, \tag{2.44}$$

where r_0 and ϕ_0 are to be obtained from x_0 and u_0. These equations can be averaged over one period to determine the change in r and ϕ due to the perturbation:

$$\bar{f}_r^1(r) = \frac{\varepsilon}{2\pi}\int_0^{2\pi}\varepsilon r\left(1-r^2\cos^2(t+\phi)\right)\sin^2(t+\phi)\,\mathrm{d}s = \frac{1}{8}\varepsilon r(4-r^2), \tag{2.45}$$
$$\bar{f}_\phi^1(r) = -\frac{\varepsilon}{2\pi r}\int_0^{2\pi}\left(1-r^2\cos^2(t+\phi)\right)\sin\big(t+\phi\big)\cos\big(t+\phi\big)\,\mathrm{d}s = 0. \tag{2.46}$$

Furthermore, we introduce the averaged amplitude $A := \langle r\rangle$ and the averaged phase shift $\varphi := \big\langle\phi\big\rangle$. Their differential equations are given by

$$\dot{A} = \frac{1}{8}\varepsilon A(4-A^2), \qquad A(0)=r_0, \tag{2.47}$$
$$\dot{\varphi} = 0, \qquad \varphi(0)=\phi_0, \tag{2.48}$$

Solving the averaged system approximates the system's response under the perturbation, revealing the slow evolution of the amplitude and phase.

$$A(t) = \frac{2e^{\frac{\varepsilon t}{2}}}{\sqrt{e^{\varepsilon t}+\frac{4}{r_0^2}-1}}, \qquad \varphi(t)=\phi_0. \tag{2.49}$$

Specifically, for small ε, in the first-order approximation, the amplitude A converges to a constant value, leading to a limit cycle, while the phase shift φ remains constant.

2.3 Cross-correlation-based averaging

In practice, the averaging integral, given in Eq. (2.39), is not always as straightforward to evaluate as in Eqs. (2.45)-(2.46). Specifically, integrals of the form

$$\bar{f}(x) = \langle f(x + g(t)) \rangle = \frac{1}{T} \int_0^T f(x + g(t))\, \mathrm{d}t \tag{2.50}$$

can become difficult to handle analytically. Challenging cases include when $f(x)$ is defined piecewise or simply the antiderivative of $f(x_S + g(t))$ is not available analytically. In [227], *Genda et al.* offer an alternative method, which is based on the classical probability density (CPD) function of the function $g(t)$. The following text and figures are adapted from [227] and [228].

Definition 2.3.1. *Let $g_i : (a, b) \to \mathbb{R}$ be either a strictly monotonically increasing C^1 function with the parameter $d_i = 0$ when the sign of its derivative is positive or a strictly monotonically decreasing C^1 function with the parameter $d_i = 1$ when the sign of its derivative is negative. Then, its CPD is defined [45] by*

$$\rho_i : \begin{cases} \mathbb{R} & \to \mathbb{R}^{0+} \\ x & \mapsto \frac{(-1)^{d_i}}{g_i'[g_i^{-1}(x)]} \frac{1}{b-a} \mathbf{1}_{(g_i(a), g_i(b))}(x), \end{cases} \tag{2.51}$$

where slightly abusing the notation to set the value of ρ_i to 0 outside $(g_i(a), g_i(b))$, we use the indicator function defined as

$$\mathbf{1}_X(x) = \begin{cases} 1 & x \in X, \\ 0 & \textit{otherwise}. \end{cases} \tag{2.52}$$

Note that the strict monotony guarantees the existence of the inverse. If the function $g_i(x) = C_i$ is constant on $x \in (a, b)$, its CPD is given by

$$\rho_i(x) = \delta(x - C_i), \tag{2.53}$$

where $\delta(\cdot)$ denotes the Dirac distribution.

Definition 2.3.2. *Let g be a piecewise, continuously differentiable, periodic function with the time period T defined by*

$$g : \begin{cases} (t_{i-1}, t_i) & \to \mathbb{R} \qquad \textit{for } i = 1 \dots n, \\ x & \mapsto g_i(x), \end{cases} \tag{2.54}$$

with $t_0 = 0$ and $t_n = T$ such that all g_i are either strictly monotonously increasing, decreasing, or constant on its domain of definition. We further define $\Delta T_i := t_i - t_{i-1}$. Then, the CPD of g is defined by the weighted average

$$\rho(x) := \frac{1}{T} \sum_{i=1}^{n} \Delta T_i \rho_i(x). \tag{2.55}$$

Theorem 2.3.3. *For a bounded function f and an at least piecewise continuously differentiable periodic function g with period T, the averaging operator*

$$\bar{f}(x) = \langle f(x + g(t)) \rangle = \frac{1}{T} \int_0^T f(x + g(t)) \, \mathrm{d}t \tag{2.56}$$

is equivalent to the cross-correlation integral

$$(\rho \star f)(x) = \int_{-\infty}^{\infty} f(y) \rho(y - x) \, \mathrm{d}y, \tag{2.57}$$

if $\rho(x)$ is chosen as the CPD of the 'fast' variable $g(t)$.

For the proof of Theorem 2.3.3, we refer to [227].

Remark 2.3.4. *In practical technical scenarios, 'fast' almost periodic motions frequently occur. An example is the summation of two sine functions with incommensurable frequencies. The selection of interval boundaries impacts the outcome when averaging these functions over a finite duration. Since $g(t)$ is almost periodic, it lacks a specific time period. Nevertheless, one can consider $T \longrightarrow \infty$ to achieve a uniquely determined integral.*

Based on Eq. (2.57), a second, moment-based theorem can be derived, further reducing calculation complexity for many practical cases.

Definition 2.3.5. *The k^{th} moment of a CPD $\rho(x)$ is defined by*

$$m_k = E(X^k) = \int_{-\infty}^{\infty} x^k \rho(x) \, \mathrm{d}x. \tag{2.58}$$

For the specific values of several CPDs, refer to [227].

Theorem 2.3.6. *Assume that $f(x)$ is a real analytic function and has the domain of convergence $D(y) = (y + R_l(y), y + R_u(y))$ when expanded into Taylor series around y with the non-positive valued function $R_l(y)$ and the non-negative valued one $R_u(y)$. Furthermore, assume that the range of the 'fast' variable $g(t)$ is $[x_l, x_u]$, that is, $\sup g(t) = x_u$ and $\inf g(t) = x_l$. Without loss of generality, we assume $m_1 = 0$, and thus $x_l \leq 0 \leq x_u$. We define the set*

$$D_\rho = \{(y \in \mathbb{R} | (R_l(y) < x_l) \wedge (x_u < R_u(y))\}, \tag{2.59}$$

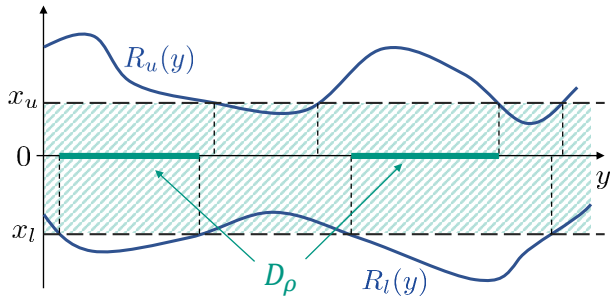

Figure 2.1: Visual interpretation of the definition of D_ρ. Figure adapted from [227]

i.e., the set of points around which the convergence radius of $f(x)$ is large enough that the support of $\rho(x)$ fits into it (cf. Fig. 2.1). Then, the following holds.

$$\bar{f}(x) = \int_{-\infty}^{\infty} f(y)\rho(y-x)\,\mathrm{d}y = \sum_{k=0}^{\infty} m_k \frac{f^{(k)}(x)}{k!} \quad \text{for } x \in D_\rho, \tag{2.60}$$

where $(\cdot)^{(k)}(x)$ denotes the k^{th} derivative.

For the proof of Theorem 2.3.6, we refer to [227].

Theorem 2.3.6 is of particular significance in two specific instances: a) when the target function is a polynomial, which implies that a finite set of moments suffices to compute the average, and b) when the support of ρ is limited, leading to $m^k \to 0$ as $k \to \infty$.
In the following, we demonstrate how to obtain the CPD of complex motions consisting of the sum of individual periodic motions with incommensurable frequencies. For that end, we generalize the concept of incommensurability for more than two frequencies.

Definition 2.3.7 (Linear independence over $\mathbb{Q}$)**.** *The frequencies $\omega_1, \ldots, \omega_P \in \mathbb{R}$ are linearly independent over $\mathbb{Q}$ if*

$$\sum_{i=1}^{P} r_i \omega_i \neq 0, \tag{2.61}$$

holds for any set of rational numbers $r_i \in \mathbb{Q}$, except $r_1 = r_2 = \ldots = r_P = 0$.

Weyl established that the P-dimensional flow on a torus $\mathbb{T}^P = \mathbb{R}^P/\mathbb{Z}^P$ is equidistributed [210], meaning a particle starting at $\boldsymbol{x_0} = [x_{0,1}, \ldots, x_{0,P}]^\top \in \mathbb{T}^P$ and traversing with uniform velocity in direction $\boldsymbol{\omega} = [\omega_1, \ldots, \omega_P]^\top \in \mathbb{R}^P$ on $\mathbb{T}^P$, such that

$$\mathbf{x}(t) = (\mathbf{x}_0 + \boldsymbol{\omega} t) \bmod 1 = \Big(\{x_{0,1} + \omega_1 t\}, \{x_{0,2} + \omega_2 t\}, \ldots, \{x_{0,P} + \omega_P t\}\Big)^\top, \tag{2.62}$$

spends a relative dwell time in any volume element V proportional to the element's hypervolume $|V|$, if and only if the frequencies $\omega_1, \ldots, \omega_P$ are linearly independent over $\mathbb{Q}$.

Here, $\{\cdot\}$ denotes the fractional part function, and 'relative dwell time' refers to the ratio $\lim_{t\to\infty} t_V/t$, where t_V is the time spent within volume element V over the total observation period t. This aligns with the notion that flow on a P-dimensional torus is ergodic with respect to the Haar measure on $\mathbb{T}^P$ [36].

Thus, sampling particle positions at uniformly distributed random time points within $[0, T]$, as $T \to \infty$, will yield a uniform multivariate distribution in $\mathbb{T}^P$. These sampled positions can be viewed as outcomes of a P-dimensional random variable $\mathbf{X} = [X_1, \ldots, X_P]^\top$, with each scalar component uniformly distributed in $[0, 1]$ and independent of others. This interpretation allows for the computation of the CPD for polyharmonic excitation as described.

Theorem 2.3.8. *Assuming the frequencies $\omega_1, \ldots, \omega_P$ are linearly independent over $\mathbb{Q}$, the CPD of*

$$z(t) = \sum_{i=1}^{P} A_i \sin(\omega_i t + \beta_i) \tag{2.63}$$

is obtained through

$$\rho(x) = (\rho_1 * \rho_2 * \ldots * \rho_P)(x), \tag{2.64}$$

where $\rho_1 * \rho_2 * \ldots * \rho_P$ denotes the convolution of $\rho_1, \rho_2, \ldots, \rho_P$, each characterized by the arcsine distribution

$$\rho_i(x) = \frac{1}{\pi\sqrt{A_i^2 - x^2}}. \tag{2.65}$$

Proof. The ergodic nature of the line on $\mathbb{T}^P$, parameterized by the sines' arguments, implies that the flow of these arguments on $\mathbb{T}^P$ is uniform. Sampling this flow at uniformly random intervals equates statistically to sampling from a P-dimensional uniform distribution on the torus, indicating that Eq. (2.63)'s sum mirrors the probability distribution of the sum of P uniformly distributed random variables on $[0, 2\pi]$ after the transformation $A_i \sin(\Omega_i X_i + \beta_i)$ is applied.

As per [227], the CPD of a simple harmonic term $A_i \sin(\Omega_i t + \beta_i)$ is represented by Eq. (2.65). CPDs and PDFs share equivalent statistical properties, and the PDF of the sum of independent variables is the convolution of their individual PDFs, as outlined in Eq. (2.64), thus concluding the proof. □

Remark 2.3.9. *The commutative property of convolution implies the sequence of operations is irrelevant.*

Remark 2.3.10. *The moments of the centered arcsine distribution with half-width A are provided by [227] as follows:*

$$m_K = \begin{cases} A^K \frac{1}{2^K} \binom{K}{K/2} & \text{if } K \text{ is even}, \\ 0 & \text{if } K \text{ is odd}, \end{cases} \quad \text{for } K \geq 0. \tag{2.66}$$

Theorem 2.3.11. *Let m_{j,j_i} denote the j_i^{th} moment of the j^{th} term's CPD from Eq. (2.63), where $j_i \in \mathbb{N}^+$ for all $j = \{1, \ldots, P\}$. The K^{th} moment of $\rho(x)$, as indicated in Eq. (2.64), is expressed as*

$$m_K = \left(\sum_{\left(\sum_{j=1}^{P} j_i\right)=K} \prod_{j=1}^{P} \frac{m_{j,j_i}}{j_i!} \right) K! \tag{2.67}$$

Proof. The moment-generating function of a random variable X is represented by

$$M_X(t) = \sum_{K=0}^{\infty} \frac{m_K}{K!} t^K. \tag{2.68}$$

It is a well-established fact that the product of the moment-generating functions of independent random variables $X_1, X_2, \ldots, X_P$ results in the moment-generating functions of their sum, $X = \sum_{i=1}^{P} X_i$:

$$M_X(t) = M_{X_1}(t) M_{X_2}(t) \ldots M_{X_P}(t). \tag{2.69}$$

Given that moment-generating functions are power series, the Cauchy product rule is applicable, resulting in Eq. (2.67). □

In the following, we demonstrate the application of the above theorems.
Fig. 5.5 gives an example for the CPD of a biharmonic function. In Fig. 2.2a, the function is periodic, thus the linear independency of the frequency components over $\mathbb{Q}$ is not fulfilled. As a result, the CPD differes significantly from the CPD of an aperiodic function, represented in Fig. 2.2b.

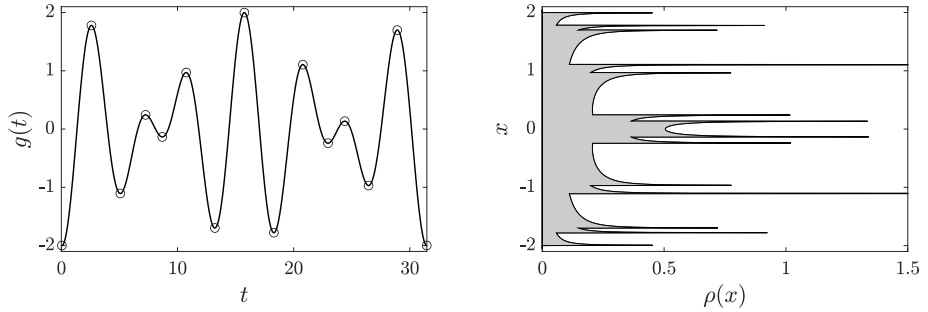

(a) Periodic bi-harmonic motion given by $g(t) = -\cos(t) - \cos(1.4t - 0.1)$ and its numerically obtained CPD

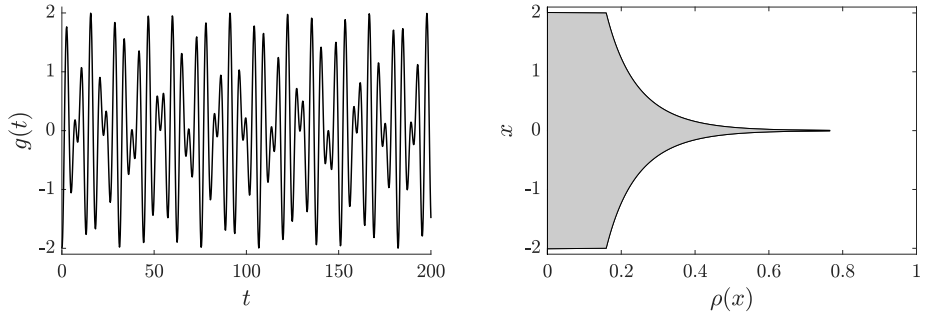

(b) Aperiodic bi-harmonic motion given by $g(t) = -\cos(t) - \cos\left(\sqrt{2}t - 0.1\right)$ and its analytically obtained CPD

Figure 2.2: Effects of commensurability on the CPD. Figures adapted from [227]

Example 2.3.12 (Escape of a pair of coupled particles)**.** *Consider the scenario where two particles are coupled by a strong linear spring of stiffness $k \gg 1$, located in a quadratic-quartic potential well given by $V(x) = x^2/2 - x^4/4$ (cf. Fig. 2.3). The equations of motion are:*

$$\ddot{x}_1 + V'(x_1) + k(x_1 - x_2) = 0, \tag{2.70}$$

$$\ddot{x}_2 + V'(x_2) + k(x_2 - x_1) = 0, \tag{2.71}$$

$$x_1(0) = x_2(0) = 0, \tag{2.72}$$

$$\dot{x}_1(0) = -v_0, \tag{2.73}$$

$$\dot{x}_2(0) = v_0. \tag{2.74}$$

The stability of the solution is sought in dependence of the parameters k and v_0. By introducing the center of mass and relative displacement as new variables

$$\eta = \frac{x_1 + x_2}{2}, \qquad \textit{and} \qquad y = x_2 - x_1, \tag{2.75}$$

the following equations are derived:

$$\ddot{\eta} + \frac{V'\left(\eta - \frac{y}{2}\right) + V'\left(\eta + \frac{y}{2}\right)}{2} = 0, \tag{2.76}$$

$$\ddot{y} + \left(2k + 1 - 3\eta^2\right) y - \frac{y^3}{4} = 0, \tag{2.77}$$

$$\eta(0) = \dot{\eta}(0) = 0, \tag{2.78}$$

$$y(0) = 0, \tag{2.79}$$

$$\dot{y}(0) = 2v_0. \tag{2.80}$$

Given that $V'(x)$ is an even function, one solution is $\eta(t) = 0$. However, its stability depends on the values of v_0 and k. Substituting $\eta(t)$ in Eq. (2.77) simplifies the problem to a softening Duffing oscillator. The total energy is given by

$$E_0 = \frac{1}{2}\dot{y}^2(0) = 2v_0^2, \tag{2.81}$$

which helps in determining the amplitude of oscillations

$$A = 2\sqrt{2k+1}\sqrt{1 - \sqrt{1 - \frac{2v_0^2}{(2k+1)^2}}}. \tag{2.82}$$

With $k \gg 1$, the oscillations in y are rapid, allowing for the averaging of Eq. (2.76) [60]. By Theorem 2.3.3, an exact determination of $y(t)$ is unnecessary; its CPD suffices. Theorem 2.3.6 indicates that only the first three moments are relevant in the averaging, as $V'(x)$ is a third-degree polynomial. The symmetry of $y(t)$ nullifies the odd moments, leaving only the second moment (other than the trivial zeroth one). The linear force being significantly larger than the nonlinear cubic force, the motion is closely akin to harmonic motion, with the second moment

$$m_{y,2} = \frac{A^2}{2}. \tag{2.83}$$

The averaged center of mass is denoted as $\xi := \langle \eta \rangle$. After rescaling the moment due to the factor $1/2$ and inserting it into Eq. (2.83), we get

$$\left\langle V'\left(\eta - \frac{y(t)}{2}\right)\right\rangle = \left\langle V'\left(\eta + \frac{y(t)}{2}\right)\right\rangle = V'(\xi) + \frac{1}{8}V'''(\xi)m_{y,2} = \left(1 - \frac{3}{8}A^2\right)\xi - \xi^3, \tag{2.84}$$

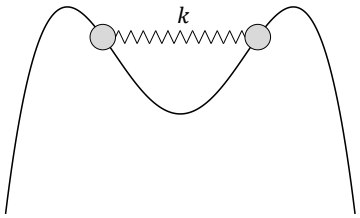

Figure 2.3: Configuration of two coupled particles in a quadratic-quartic potential well. Figure adapted from [227]

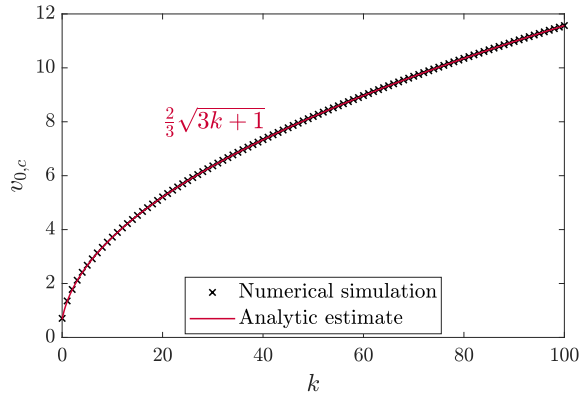

Figure 2.4: Graphical representation of the critical initial velocity $v_{0,c}$ in relation to the stiffness parameter k of the linear spring. Figure adapted from [227]

resulting in an averaged differential equation

$$\ddot{\xi} + \left(1 - \frac{3}{8}A^2\right)\xi - \xi^3 = 0. \tag{2.85}$$

Linear stability analysis results in the stability condition

$$\frac{8}{3} \overset{!}{>} A^2, \tag{2.86}$$

which translates to

$$v_0 \overset{!}{<} v_{0,c} := \frac{2}{3}\sqrt{3k+1}. \tag{2.87}$$

The comparison between this analytical estimate and direct numerical simulations is depicted in Fig. 2.4. The simulations were conducted by slightly altering the initial conditions to $\eta(0) = 0.005$ *and integrating the system for up to 1000 time units. The particle pair's escape classifies the solution* $\eta(t) = 0$ *as unstable.*

2.4 Global optimization of the sum of two harmonics

In investigating escape problems, it is paramount to determine the maximum displacement of the particle during its course, as it is a helpful indicator of escape. The escape condition is often simplified as follows: if some quantity related to the particle's motion (total energy, displacement, force) crosses a certain level, the case is classified as escape

[225, 68]. The following section assists in investigating a specific case by working with the exact motion of the underlying system.
Undamped linear differential equations give rise to harmonics in their solutions. When a single-degree-of-freedom undamped harmonic oscillator is subjected to harmonic excitation with different natural and excitation frequencies, the resulting motion can be represented as the sum of two sine functions. However, finding the maximum of such a function with general frequency, phase, and amplitude values is not straightforward and, in most cases, can only be done numerically, especially if the excitation and natural frequencies are commensurable.
However, reasonable estimates can be given even for those cases. The following text and figure are adapted from the work of *Genda et al.* [224].

We seek to find the supremum of a function f with respect to time $\tilde{t}$, which is represented by

$$\sup_{\tilde{t}} f(\tilde{t}) = \sup_{\tilde{t}} \left(A\cos\left(\Omega_A \tilde{t} + \alpha_A\right) + B\cos\left(\Omega_B \tilde{t} + \alpha_B\right)\right) \tag{2.88}$$

where $A, B, \Omega_A, \Omega_B > 0$ and $\alpha_A, \alpha_B \in [0, 2\pi)$. Through the transformation of coordinates

$$t := \Omega_A \tilde{t} + \alpha_A \tag{2.89}$$

and defining

$$\Omega_{\text{ratio}} := \frac{\Omega_B}{\Omega_A}, \qquad \alpha_{\text{shift}} := -\frac{\Omega_B \alpha_A}{\Omega_A} + \alpha_B, \tag{2.90}$$

we can reformulate the problem as

$$f_{\text{sup}} := \sup_t f(t) = \sup_t \left(A\cos t + B\cos(\Omega_{\text{ratio}} t + \alpha_{\text{shift}})\right). \tag{2.91}$$

Theorem 2.4.1. *If Ω_{ratio} is a non-rational real number, the supremum of Eq. (2.91) is*

$$f_{sup,Irr} := A + B. \tag{2.92}$$

In contrast, if Ω_{ratio} is rational, denoted as $\Omega_{ratio} = N/M$ for some $N, M \in \mathbb{N}$, the supremum of $f(t)$ can be approximated by

$$f_{sup,Rat} := A\left(1 - 2\pi^2 \left(\frac{B\Omega_{ratio}}{A + B\Omega_{ratio}^2}\right)^2 |y_0|^2\right) + B\left(1 - 2\pi^2 \left(\frac{A}{A + B\Omega_{ratio}^2}\right)^2 |y_0|^2\right), \tag{2.93}$$

with

$$\Delta E = \frac{\gcd(M,N)}{M}, \tag{2.94}$$

$$y_{shift} = \frac{\alpha_{shift}}{2\pi} + \left\lfloor -\frac{\alpha_{shift}}{2\pi\Delta E} \right\rfloor \Delta E, \tag{2.95}$$

$$|y_0| = \min\{-y_{shift}, \Delta E + y_{shift}\} = -\left| y_{shift} + \frac{\Delta E}{2} \right| + \frac{\Delta E}{2}. \tag{2.96}$$

where the relative error due to α_{shift} is of the fourth order. '$\gcd(M,N)$' denotes the greatest common divisor of M and N. $\{x\} = x - \lfloor x \rfloor$ denotes the fractional part, with $\lfloor \cdot \rfloor$ representing the floor function.

For the proof of Theorem 2.4.1, we refer to [224].

Remark 2.4.2. *For improved precision in the results ($\epsilon_{rel} = O(\alpha_B^6)$, see Fig. 2.5), the following formula is recommended*

$$f_{max,T} = A\cos\left(-2\pi\frac{B\Omega_B y_0}{A + B\Omega_B^2}\right) + B\cos\left(2\pi\frac{A y_0}{A + B\Omega_B^2}\right) \tag{2.97}$$

$$= A\cos\left(2\pi\frac{B\Omega_B}{A + B\Omega_B^2}|y_0|\right) + B\cos\left(2\pi\frac{A}{A + B\Omega_B^2}|y_0|\right), \tag{2.98}$$

where the latter equality emerges due to the symmetric property of the cosine function.

For more on the derivation of Eq. (2.97), see [224].
In Fig. 2.5, the logarithmic values of relative errors for maximum estimates as per Eqs. (2.92), (2.93), and (2.97) are represented against the logarithm of the phase shift, specifically α_B, for

$$\max_{t\in(0,4\pi)} \cos(t) + \cos\left(\frac{1}{2}t + \alpha_B\right). \tag{2.99}$$

Within the α_B range of $(0.01, \frac{\pi}{6})$, the relative errors for the estimates (2.92), (2.93), and (2.97) are of the second, fourth, and sixth order respective to α_B.

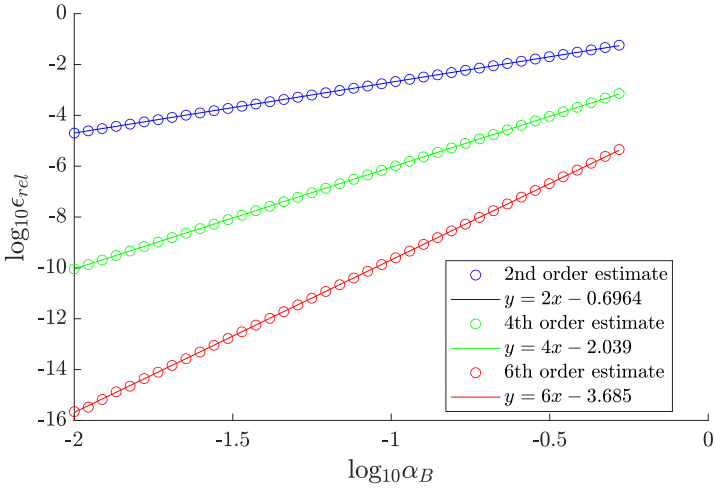

Figure 2.5: Logarithmic representation of the relative error, $\epsilon_{\text{rel}} := \frac{|\hat{f}\max - f\max|}{f\max}$ for three different estimates of $\max_{t\in(0,4\pi)} \cos(t) + \cos\left(\frac{1}{2}t + \alpha_B\right)$, plotted against the logarithm of $\alpha_B \in (0.01, \frac{\pi}{6})$. The 2^{nd} order estimate is obtained by $A + B$, the 4^{th} order one by Eq. (2.93), and the 6^{th} order one by Eq. (2.97). The linear fits with one parameter align precisely with the numerically derived data. Figure adapted from [224]

3 Safe basins of level crossing in the linear case

The following chapter deals with the topic of preventing escape. The main focus is identifying the safe basins of escape, which are the initial conditions for which the particle remains within the potential well under a given excitation. The escape is not defined if the problem is linear, as the underlying potential well is infinitely deep. To address this, some authors propose truncating the quadratic well and replacing the cut-off part with a constant value [57, 68, 89], resulting in zero restoring force in that area.
An alternative method of analyzing a problem without truncating the data involves examining the first passage or level crossing. This approach determines whether a particle reaches a specific displacement value during its course.
However, to analyze the escape dynamics of a particle, it is necessary to define what escape is and what a potential well is. In simple terms, a potential well is the region surrounding a local minimum of potential energy $V(x)$. However, it is essential to specify the exact boundaries of this area. To do so, we use the concept of drainage basins in geology, adapting it to dynamic systems.

Definition 3.0.1 (Potential Well)**.** *Let $V : \mathbb{R}^n \to \mathbb{R}$ be a potential function. The largest subset $W \subseteq \mathbb{R}^n$ is called a potential well if for every $\mathbf{x}_0 \in W$, the trajectory $\mathbf{x}(t)$ governed by the differential equation*

$$\begin{aligned} \dot{\mathbf{x}} &= -\nabla V(\mathbf{x}), \\ \mathbf{x}(0) &= \mathbf{x}_0, \end{aligned} \tag{3.1}$$

converges to $\mathbf{x}_W$ as $t \to \infty$, where $\mathbf{x}_W \in W$ (or $\mathbf{x}_W \subseteq W$ for a set of local minima) denotes a local minimum of $V(\mathbf{x})$ associated with W.

Remark 3.0.2. *Eq. (3.1) corresponds to the motion of a damped particle of negligible mass, such as a drop of water on a non-absorbing surface.*

Def. 3.0.1 allows us to define particle escape.

Definition 3.0.3 (Escape of a particle)**.** *Let $V : \mathbb{R}^n \to \mathbb{R}$ be a potential energy function with a local minimum $\mathbf{x}_W$ and its corresponding potential well $W \subseteq \mathbb{R}^n$. A particle escapes from the well W, if $\exists\, t_E \in \mathbb{R}^+$ such that $\forall t > t_E$, $\mathbf{x}(t) \notin W$.*

Remark 3.0.4. *Although Def. 3.0.3 is an accurate definition in most cases, it is impractical for both numerical and analytical calculations because knowledge of the solution is required at all times.*

A more convenient definition for numerical purposes is stated below.

Definition 3.0.5 (Numerical escape criterion)**.** *Let $V : \mathbb{R}^n \to \mathbb{R}$ be a potential energy function with a local minimum $\mathbf{x}_W$ and its corresponding potential well $W \subseteq \mathbb{R}^n$. A particle escapes from the well W, if $\forall t \in (t_E, T]$, $\mathbf{x}(t) \notin W$ and $\frac{T-t_E}{T} \in \mathcal{O}(1)$. Here, $1 \ll T \in \mathbb{R}^+$ denotes the upper limit of the simulation time interval.*

Remark 3.0.6. *Def. 3.0.5 gives a weaker condition than Def. 3.0.3; thus, the set of non-escaping points in the latter case is at least as large as in the case of Def. 3.0.3.*

Remark 3.0.7. *The condition $\frac{T-t_E}{T} \in \mathcal{O}(1)$ is necessary to ensure that the particle leaves W not only temporarily, but that escape indeed occurs.*

This definition is appropriate for numerical studies; however, its application in analytics is still cumbersome. Therefore, an even weaker escape definition is given below.

Definition 3.0.8 (Analytical escape criterion)**.** *Let $V : \mathbb{R}^n \to \mathbb{R}$ be a potential energy function with a local minimum $\mathbf{x}_W$ and its corresponding potential well $W \subseteq \mathbb{R}^n$. A particle escapes from the well W, if $\exists\, t_E \in \mathbb{R}^+$ such that $\mathbf{x}(t_E) = \partial W$, i.e., the particle reaches the potential well's boundary.*

This definition can be generalized for quantities other than the displacement of particles. An extension to other values related to the particle's motion is given in the following.

Definition 3.0.9 (Level crossing in dynamical systems)**.** *In a dynamical system defined by $\dot{\mathbf{x}} = \mathbf{f}(\mathbf{x}(t)) \in \mathbb{R}^n$ with observable $g : \{\mathbf{x}(t) \mid t \in [0, \infty)\} \to \mathbb{R}$, a level crossing occurs at time t_{LC} if $g(\mathbf{x}(t_{LC})) = G$, for some predefined threshold value $G \in \mathbb{R}$. The first level-crossing time (also called first-passage time) is the smallest positive time for which $g(\mathbf{x}(t)) = G$ holds.*

Remark 3.0.10. *The criterion given by Def. 3.0.8 is based on the criterion given by Def. 3.0.9 when choosing the observable as the distance of the particle from ∂W and setting $G := 0$.*

Alternatively, one might choose other observables as in [67, 68], where the average action and total energy are the relevant values. Def. 3.0.9 allows for the investigation of a wide variety of problems within the framework of generalized escape, as the observable $g(\mathbf{x}(t))$ can be any functional related to the system's temporal evolution.

Definition 3.0.11 (Safe basins of escape)**.** *The safe basin is the set of initial conditions for which a particle, with given parameter values and excitation, does not escape.*

In the specific case of a single harmonic excitation, there are three forcing parameters: excitation amplitude, frequency, and initial phase. Amplitude and frequency are of equal importance and are well-controllable in experiments. However, the impact of the initial phase on escape is often secondary and results solely in the dislocation of the safe basins in the initial condition plane. Furthermore, controlling the initial phase is also difficult in experimental settings. In [97], *Kravetc et al.* introduced the concept of 'true' safe basins; the set of initial conditions that do not escape under variation of the excitation's initial phase.

Definition 3.0.12 (True safe basins of escape)**.** *The true safe basin refers to a set of initial conditions for a particle with given system parameters, excited with a harmonic excitation of given amplitude and frequency, with which the particle does not escape for any initial phase value.*

Remark 3.0.13. *The size of the true safe basin is always less than the size of the safe basin with a specific initial phase.*

Our investigation of the escape problem in an asymmetrically truncated quadratic potential well uses Def. 3.0.8 for analytical purposes and Def. 3.0.5 for numerical ones. The following text and figures are adapted from the work of *Genda et al.* [224].

3.1 Undamped driven harmonic oscillator

The equations of motion of an undamped harmonically driven particle in an asymmetrically truncated quadratic potential are given as follows,

$$m\ddot{x} + mV'(x) = F\sin(\Omega_x\tau + \beta), \tag{3.2}$$

$$x(0) = \tilde{x}_0, \tag{3.3}$$

$$\dot{x}(0) = \tilde{u}_0, \tag{3.4}$$

with the potential function defined as

$$V(x) = \begin{cases} -\frac{\Omega_0^2}{2}r_B^2 + \frac{\Omega_0^2}{2}x^2 & \text{for } x_l \le x \le x_u, \\ \frac{-r_B^2+x_l^2}{2}\Omega_0^2 & \text{for } x < x_l, \\ \frac{-r_B^2+x_u^2}{2}\Omega_0^2 & \text{for } x_u < x, \end{cases} \tag{3.5}$$

Here, $\Omega_x \in [0, \infty)$ represents the angular frequency, $\beta \in [-\pi, \pi)$ the phase, and $F \in [0, \infty)$ the amplitude of the excitation. $\Omega_0 \in (0, \infty)$ denotes the natural angular frequency of

the potential well and $m \in (0, \infty)$ is the mass of the particle. The left and right potential boundaries around the origin are denoted by $x_l \in (-\infty, 0)$ and $x_u \in (0, \infty)$, respectively. Using Def. 3.0.1, it is clear that $W = (x_l, x_u)$. We introduce

$$r_B := \min\{-x_l, x_u\} \tag{3.6}$$

to represent the minimum distance from the deepest point of the potential to its nearest boundary. Figure 3.1 gives a graphical representation of $V(x)$. Introducing

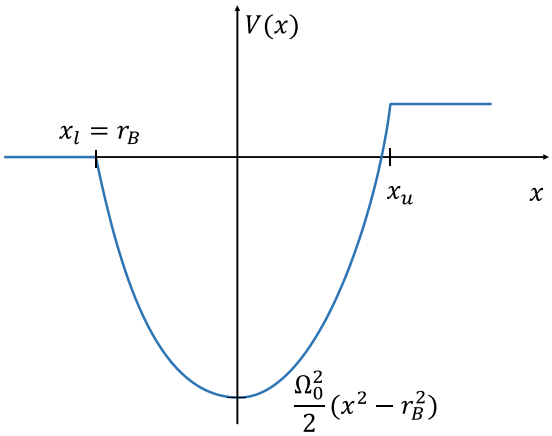

Figure 3.1: Asymmetrically truncated quadratic potential $V(x)$. Figure adapted from [224]

nondimensional parameters such as the nondimensional time $t := \Omega_0 \tau$, excitation amplitude $f := F/m$, and excitation frequency $\omega := \Omega_x/\Omega_0$, the equation of motion can be reformulated as:

$$\ddot{x} + \tilde{V}'(x) = f \sin(\omega t + \beta), \tag{3.7}$$

$$x(0) = x_0 := \tilde{x}_0, \tag{3.8}$$

$$\dot{x}(0) = u_0 := \frac{\tilde{u}_0}{\Omega_0}, \tag{3.9}$$

alongside the adjusted potential function:

$$\tilde{V}(x) = \begin{cases} -\frac{r_B^2}{2} + \frac{x^2}{2} & \text{for } x_l \le x \le x_u, \\ \frac{-r_B^2 + x_l^2}{2} & \text{for } x < x_l, \\ \frac{-r_B^2 + x_u^2}{2} & \text{for } x_u < x. \end{cases} \tag{3.10}$$

Using the analytic escape condition from Def. 3.0.8, the calculation of the motion is confined to the range $x_l < x < x_u$. The differential equation becomes linear, allowing for an explicit analytic solution. For $\omega \neq 1$ (excluding the resonance and escape scenario for any initial condition), the solution is expressed as:

$$x(t) = R\sin(t + \alpha) + P\sin(\omega t + \beta), \tag{3.11}$$

with

$$P = \frac{f}{1-\omega^2}, \tag{3.12}$$

$$R = \sqrt{(x_0 - P\sin\beta)^2 + (u_0 - P\omega\cos\beta)^2}, \tag{3.13}$$

$$\alpha = \operatorname{atan2}\left((x_0 - P\sin\beta), u_0 - P\omega\cos\beta\right). \tag{3.14}$$

3.1.1 Safe basins of quasi-periodic motions

The relationship between the excitation frequency and the natural frequency of a potential well plays a crucial role in determining the periodicity of motion. In [89], an extensive investigation was carried out for the simpler scenario of $\omega \in \mathbb{R}\backslash\mathbb{Q}$, indicative of a quasi-periodic motion. An effective approach to estimate the upper limit of the absolute displacement, $r_{\text{sup}} := \max_t |x(t)|$, is given by Theorem 2.4.1 as

$$r_{\max} = R + |P|. \tag{3.15}$$

Implementing the values of $|P|$ and R from Eqs. (3.12)-(3.13) in Eq. (3.15), and ensuring that $r_{\max} < r_B$ to maintain a non-escape scenario, we derive:

$$r_B > R + |P|, \tag{3.16}$$

$$r_B - |P| > R. \tag{3.17}$$

In cases where $|P| \geq r_B$, no initial conditions can satisfy this inequality since R is always nonnegative. Consequently, based on this estimation, for an excitation amplitude

$$f \geq r_B|1-\omega^2|, \tag{3.18}$$

the particle will inevitably escape from the well for any initial condition. Conversely, if $|P| < r_B$, squaring both sides of Eq. (3.17) yields:

$$D_P: \qquad (r_B - |P|)^2 > (x_0 - P\sin\beta)^2 + (u_0 - P\omega\cos\beta)^2, \tag{3.19}$$

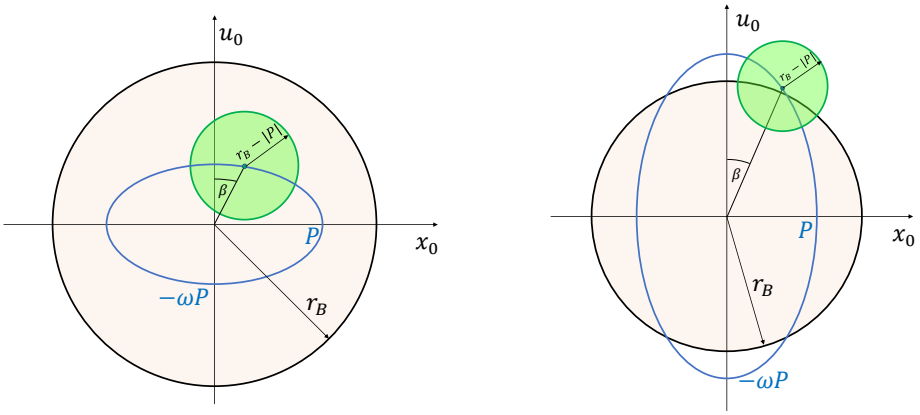

(a) $\omega < 1$ **(b)** $\omega > 1$

Figure 3.2: The location of the safe basin D_P on the $x_0 - u_0$ plane. Figure adapted from [224]

indicating the interior of a circular disk centered at $(P \sin\beta, P\omega \cos\beta)$ with radius $R_D = r_B - |P|$.
The largest possible disk, denoted by D_0, is realized when $|P| = 0$ (i.e., $F = 0$), implying no external excitation. This results in a disk centered at the origin with radius r_B:

$$D_0 : \qquad r_B^2 > x_0^2 + u_0^2, \tag{3.20}$$

covering a total area of:

$$A_0 = \pi r_B^2. \tag{3.21}$$

A notable distinction arises between the cases where $\omega < 1$ and $\omega > 1$. For $\omega < 1$, the circular disk defined by Eq. (3.19) remains entirely within D_0. However, for $\omega > 1$, parts or the entire disk area D_P may extend beyond D_0. Figure 3.2 visually represents the non-escaping set. In both scenarios, the total area of the safe basin also called the global integrity measure (GIM), is calculated as:

$$A_P = \pi(r_B - |P|)^2. \tag{3.22}$$

Although these observations on the safe basin area may seem straightforward, they have significant practical value. Due to the lack of precise control over the particle's initial conditions, having a reference case is essential for comparing results and investigating non-escaping sets of initial conditions from nonquadratic potentials. Understanding the impact of system parameters and excitation on the global integrity measure allows one to characterize other potentials with respect to their erosion properties.

Remarks

Throughout this dissertation, we will explore the concept of escape and how it involves competing mechanisms. Even in the simple case of the harmonically driven undamped harmonic oscillator, we can identify two mechanisms for moderate values of f. The first mechanism involves the impact of initial conditions on escape. If (x_0, u_0) is chosen outside the circle with radius r_B, the particle is already out of the potential or will be during the first period of its oscillation. This is because its initial energy is so large that it alone is sufficient for escape. This mechanism causes escape rapidly, and we term it the 'fast' mechanism.
The second mechanism involves the excitation driving the particle out of the well, even if the particle's initial energy is not sufficient for escape. This mechanism is slower and requires time and several excitation periods, particularly if the force amplitude f is moderate. We call this mechanism the 'slow' mechanism. It is a beat-like phenomenon when the excitation frequency and the natural frequency of the well are close to each other.
The importance of these two competing mechanisms will be discussed in detail for the damped driven harmonic oscillater in Sect. 3.2.

True safe basins

In the simple case of the driven undamped harmonic oscillator, where the excitation frequency and the natural frequency of the well are incommensurable, the calculation of the true safe basins (see Def. 3.0.12) is possible. With initial conditions from this non-escaping set, for arbitrary values of the initial excitation phase, the particle does not escape. Thus, we can define the set as follows:

$$TSB: \qquad (r_B - |P|)^2 > \max_{\beta\in[0,2\pi)} (x_0 - P\sin\beta)^2 + (u_0 - P\omega\cos\beta)^2 \,. \tag{3.23}$$

With simple geometrical considerations based on Fig. 3.2, we can derive the existence condition of true safe basins

$$|P| < \begin{cases} \frac{r_B}{2} & \text{for } \omega < 1, \\ \frac{r_B}{1+\omega} & \text{for } \omega > 1. \end{cases} \tag{3.24}$$

In order to determine the size of the set of initial conditions that satisfy the inequality (3.23), we have to solve the following optimization problem first:

$$\beta^*(x_0, u_0) = \underset{\beta\in[0,2\pi)}{\arg\max} (x_0 - P\sin\beta)^2 + (u_0 - P\omega\cos\beta)^2 \,. \tag{3.25}$$

Then, we can insert $\beta^*(x_0, u_0)$ in Eq. 3.19, and find the true safe basin. Since the objective function is smooth, we can calculate its derivative to find the optimal β value. We have

$$2(P\sin\beta - x_0)P\cos\beta - 2(P\omega\cos\beta - u_0)P\omega\sin\beta = 0 \qquad \vdots$$
$$\frac{P(1-\omega^2)}{x_0}\sin\beta + \frac{\omega u_0}{x_0}\tan\beta = 1. \tag{3.26}$$

Eq. (3.26) allows for an analytical solution. Further manipulating the equation results in the following fourth-order polynomial in $\sin\beta$:

$$a^2\sin^4\beta - 2a\sin^3\beta + (1+b^2)\sin^2\beta + 2a\sin\beta - 1 = 0 \tag{3.27}$$

where

$$a = \frac{P(1-\omega^2)}{x_0}, \qquad b = \frac{\omega u_0}{x_0} \tag{3.28}$$

have been introduced for brevity. The four solutions for $\sin\beta$ can be determined by Ferrari's method. However, they are very lengthy expressions, with which further calculations are impractical.
Nevertheless, when limiting our scope to $\omega \approx 1$, we can introduce the small parameter $\varepsilon := 1 - \omega^2$ and look for the solution in terms of a series by ε described by the small-parameter perturbation method for algebraic expressions:

$$\beta = \beta_0 + \varepsilon\beta_1 + \dots. \tag{3.29}$$

Furthermore, we rewrite ω as follows:

$$\omega = \sqrt{1-\varepsilon} \approx 1 - \frac{\varepsilon}{2} + O(\varepsilon^2). \tag{3.30}$$

To handle the trigonometric expressions $\sin\beta$ and $\tan\beta$ in Eq. (3.26), we rewrite them in Taylor series around β_0 as follows:

$$\sin\beta = \sin\beta_0 + \cos(\beta_0)(\varepsilon\beta_1 + \varepsilon^2\beta_2 + \dots) - \sin(\beta_0)(\varepsilon\beta_1 + \varepsilon^2\beta_2 + \dots)^2 + \dots \tag{3.31}$$
$$= \sin\beta_0 + \cos(\beta_0)\beta_1\varepsilon + O(\varepsilon^2) \tag{3.32}$$

and

$$\tan\beta = \tan\beta_0 + \frac{1}{\cos^2\beta_0}\beta_1\varepsilon + O(\varepsilon^2). \tag{3.33}$$

Inserting Eqs. (3.29)-(3.33) in Eq. (3.26), we obtain

$$\frac{P\varepsilon}{x_0}(\sin\beta_0 + \cos\beta_0\varepsilon\beta_1) + \left(1 - \frac{\varepsilon}{2}\right)\frac{u_0}{x_0}\left(\tan\beta_0 + \frac{\varepsilon\beta_1}{\cos^2\beta_0}\right) = 1. \tag{3.34}$$

Collecting terms of ε^0 yields the following.

$$\frac{u_0}{x_0}\tan\beta_0 = 1, \tag{3.35}$$

which has its solutions at

$$\beta_0 = \arctan\left(\frac{x_0}{u_0}\right) + k\pi, \quad \text{with } k \in \{0, 1\}. \tag{3.36}$$

It turns out that for $P > 0$, $k = 0$ is a minimum and $k = 1$ is a maximum, and for $P < 0$ vice versa. We limit our focus to the case with $P > 0$ and note that the calculation is analogous for $P < 0$. Then, we have

$$\beta_0^* = \arctan\left(\frac{x_0}{u_0}\right) + \pi. \tag{3.37}$$

Now, we collect the terms of ε^1 in Eq. (3.34):

$$\frac{P\sin\beta_0}{x_0} + \frac{u_0}{x_0}\left(\frac{\beta_1}{\cos^2\beta_0} - \frac{\tan\beta_0}{2}\right) = 0, \tag{3.38}$$

resulting in

$$\beta_1^* = \left(\frac{\tan\beta_0}{2} - \frac{P\sin\beta_0}{u_0}\right)\cos^2\beta_0 = \frac{x_0u_0}{x_0^2 + u_0^2}\left(\frac{1}{2} + \frac{P}{\sqrt{x_0^2 + u_0^2}}\right), \tag{3.39}$$

where the last equation results from the insertion of β_0^*. Thus, the solution is estimated by

$$\beta^* \approx \arctan\left(\frac{x_0}{u_0}\right) + \pi + \varepsilon\frac{x_0u_0}{x_0^2 + u_0^2}\left(\frac{1}{2} + \frac{P}{\sqrt{x_0^2 + u_0^2}}\right). \tag{3.40}$$

In the following, we use the less precise estimate $\beta^* \approx \beta_0^*$. Inserting it into Eq. (3.23), we estimate the true safe basin by

$$(r_B - P)^2 \geq \left(x_0 + \frac{P x_0}{\sqrt{x_0^2 + u_0^2}} \right)^2 + \left(u_0 + \frac{P \omega u_0}{\sqrt{x_0^2 + u_0^2}} \right)^2 \tag{3.41}$$

$$= x_0^2 \left(1 + \frac{P}{\sqrt{x_0^2 + u_0^2}} \right)^2 + u_0^2 \left(1 + \frac{P\omega}{\sqrt{x_0^2 + u_0^2}} \right)^2 . \tag{3.42}$$

The comparison between the numerically obtained exact boundary and the estimate in Eq. (3.42) is shown in Fig. 3.3. Even for non-small frequency discrepancies ($\omega = \sqrt{2}$), the estimated boundary remains reasonably close to the numerically obtained one.
At the boundary of TSB, the equality in inequality (3.41) holds. We introduce the polar coordinates (r, φ) and reparametrize ∂TSB as

$$x_0 = r \cos \varphi, \qquad u_0 = r \sin \varphi. \tag{3.43}$$

Insertion in Eq. (3.42) yields

$$(r_B - P)^2 = r^2 \left(\cos^2(\varphi) \left(1 + \frac{P}{r} \right)^2 + \sin^2(\varphi) \left(1 + \frac{P\omega}{r} \right)^2 \right) \tag{3.44}$$

$$= \cos^2(\varphi)(r + P)^2 + \sin^2(\varphi)(r + P\omega)^2, \tag{3.45}$$

from which we can express ∂TSB as

$$r(\varphi) = \sqrt{P^2(\omega - 1)^2 \cos^4 \varphi - P^2(\omega - 1)^2 \cos^2 \varphi + (P - r_B)^2} + P(\omega - 1) \cos^2 \varphi - P\omega. \tag{3.46}$$

The area of the true safe basin is given by the integral

$$\text{Area} = \int_0^{2\pi} \frac{r^2(\varphi)}{2} \mathrm{d}\varphi \tag{3.47}$$

$$= \frac{\pi}{4} \left(\left(\omega^2 + 2\omega + 5 \right) P^2 - 8 r_B P + 4 r_B^2 \right) - 2P(r_B - P)(1 + \omega) E\left(\frac{(\omega - 1)^2 P^2}{4(r_B - P)^2} \right), \tag{3.48}$$

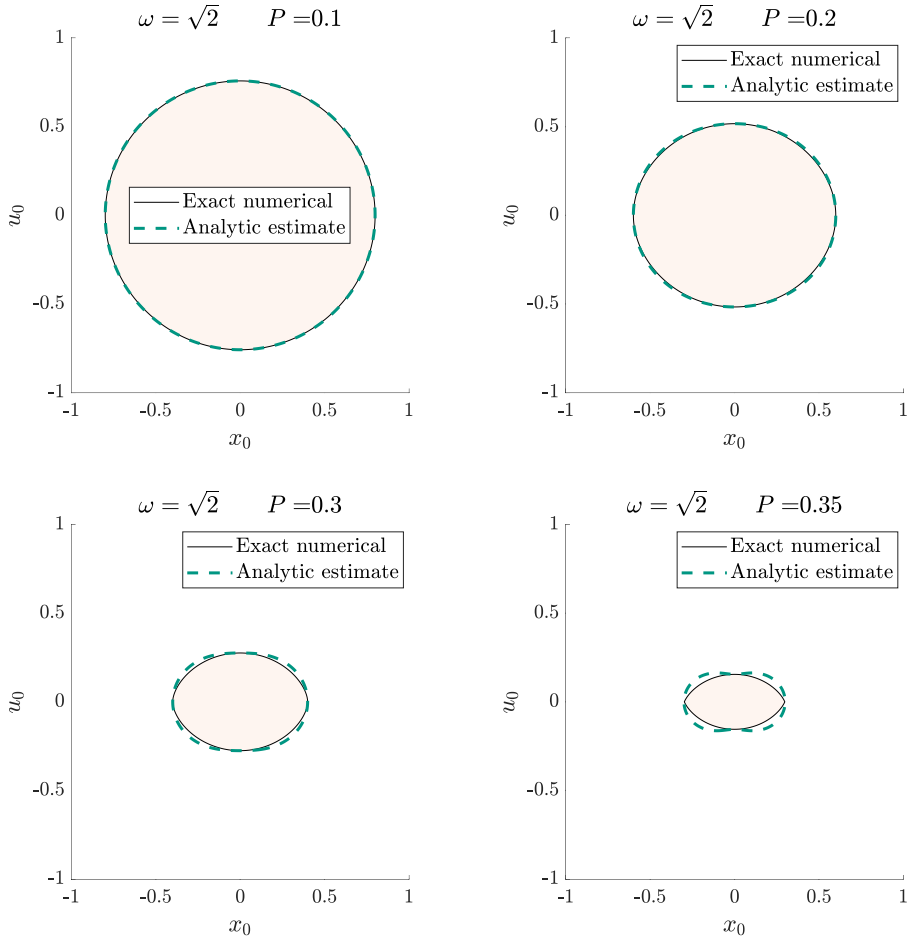

Figure 3.3: True safe basins on the $x_0 - u_0$ plane for large frequency discrepancy $\omega = \sqrt{2}$, resulting in $\varepsilon = -1$, and for various values of P. With increasing values of P, the boundary estimate becomes less accurate. This is due to Eq. (3.26), where for small P, the first term of the left-hand side remains small, even though $1 - \omega^2$ is large

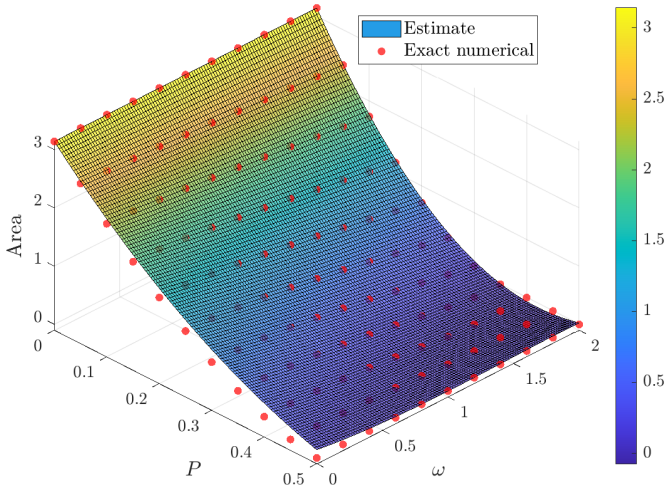

Figure 3.4: Exact numerical area (red dots) vs. analytically estimated area (color scale) of the true safe basins depicted against the parameter values ω and P. It is important to note that the values are only valid for irrational values of ω. For rational ω values, the true safe basin may be larger

where $E(m)$ denotes the complete elliptic integral of the second kind with the parameter m. Since the estimate is valid for small ε, we can further simplify Eq. (3.48). Substituting $\omega^2 = 1 - \varepsilon$ and $\omega = 1 - \varepsilon/2$, we obtain

$$\text{Area} = \pi \left((r_B - 2P)^2 + \varepsilon \frac{P(r_B - 2P)}{2} \right) = \pi \left((r_B - 2P)^2 - (\omega - 1)P(r_B - 2P) \right), \quad (3.49)$$

resulting in a small influence of the excitation frequency on the true safe basins. In fact, the estimate (see Fig. 3.4) showed good agreement with the numerically found area of the set determined by Eq. (3.23).
For $P < 0$, $|P|$ is to be inserted everywhere in Eqs. (3.48) and (3.49).
The estimates (3.48)-(3.49) could be further improved by applying $\beta^* = \beta_0^* + \varepsilon\beta_1^*$. However, this would result in much more complicated expressions for ∂TSB, possibly leading to inexpressible $r(\varphi)$.

3.1.2 Safe basins of periodic motions represented as a sum of two harmonics with commensurable frequencies

In the previous section, we analyzed the size and location of safe basins of oscillations consisting of two harmonics with incommensurable frequencies. Now, we focus our

attention on the more complicated commensurable case. In this case, the frequency ratio is given by the fraction of two positive integers $\omega = N/M$.
The function $x(t; x_0, u_0, f, \omega, \beta)$, as stated in Eq. (3.11), depends on time and several parameters. If we consider time, initial position, and velocity as variables, Eq. (3.11) transforms into $x(t, x_0, u_0; f, \omega, \beta)$, a function of three variables. Determining

$$x_{\min}(x_0, u_0) := \min_{\tilde{t}\geq 0} x(\tilde{t}, x_0, u_0) \tag{3.50}$$

and

$$x_{\max}(x_0, u_0) := \max_{\tilde{t}\geq 0} x(\tilde{t}, x_0, u_0) \tag{3.51}$$

yields the largest negative and positive displacements as functions of two variables, given a set of fixed parameters. The escape condition from Def. 3.0.8 is applied to define safe basins:

$$SB: \qquad \big(x_l < x_{\min}(x_0, u_0)\big) \quad \cap \quad \big(x_{\max}(x_0, u_0) < x_u\big). \tag{3.52}$$

To evaluate $x_{\max}(x_0, u_0)$ according to Theorem 2.4.1, the optimization problem

$$\max_{\tilde{t}\geq 0} x(\tilde{t}) = \max_{\tilde{t}\geq 0}(R\sin\big(\tilde{t}+\alpha\big) + P\sin\big(\omega\tilde{t}+\beta\big)), \tag{3.53}$$

is reformulated to the standard form:

$$\max_{t\geq 0} x(t) = \max_{t\geq 0}(R\cos t + P\cos(\omega t + \alpha_{B,\max})) \tag{3.54}$$

with the transformation

$$t = \tilde{t} + \alpha - \frac{\pi}{2}. \tag{3.55}$$

The new phase shift is thus:

$$\alpha_{B,\max} = \frac{\pi}{2}(\omega - 1 + 2\sigma(-P)) - \omega\alpha + \beta, \tag{3.56}$$

where the Heaviside function is applied:

$$\sigma(x) = \begin{cases} 1 & x \geq 0, \\ 0 & x < 0, \end{cases} \tag{3.57}$$

to include the case where $P < 0$. The minimum value $x_{\min}(x_0, u_0)$ can be found similarly, using the fact that all minimization problems can be converted to maximization ones,

$$x_{\min}(x_0, u_0) = -\max_{\tilde{t}\geq 0}(R\sin(\tilde{t} + \alpha + \pi) + P\sin(\omega\tilde{t} + \beta + \pi)), \tag{3.58}$$

and then transforming it into:

$$x_{\min}(x_0, u_0) = -\max_{t\geq 0}(R\cos t + |P|\cos(\omega t + \alpha_{B,\min})), \tag{3.59}$$

using:

$$t = \tilde{t} + \alpha + \frac{\pi}{2}, \tag{3.60}$$

$$\alpha_{B,\min} = \frac{\pi}{2}(1 - \omega + 2\sigma(-P)) - \omega\alpha + \beta. \tag{3.61}$$

The application of Theorem 2.4.1 leads to the estimation:

$$\hat{x}_{\max}(x_0, u_0) = R(1 - 2\pi^2\tilde{x}_{\max}^2) + |P|(1 - 2\pi^2\tilde{y}_{\max}^2), \tag{3.62}$$

$$\hat{x}_{\min}(x_0, u_0) = -R(1 - 2\pi^2\tilde{x}_{\min}^2) - |P|(1 - 2\pi^2\tilde{y}_{\min}^2), \tag{3.63}$$

or, based on Remark 2.4.2, more accurately:

$$\hat{x}_{\max}(x_0, u_0) = R\cos(2\pi\tilde{x}_{\max}) + |P|\cos(2\pi\tilde{y}_{\max}), \tag{3.64}$$

$$\hat{x}_{\min}(x_0, u_0) = -R\cos(2\pi\tilde{x}_{\min}) - |P|\cos(2\pi\tilde{y}_{\min}), \tag{3.65}$$

with:

$$\tilde{x}_{\max/\min} = \frac{\omega|P||y_{0,\max/\min}|}{R + \omega^2|P|}, \tag{3.66}$$

$$\tilde{y}_{\max/\min} = \frac{R|y_{0,\max/\min}|}{R + \omega^2|P|}, \tag{3.67}$$

$$|y_{0,\max/\min}| = -\left|y_{N,\max/\min} + \frac{\Delta E}{2}\right| + \frac{\Delta E}{2}, \tag{3.68}$$

$$y_{N,\max/\min} = \frac{\alpha_{B,\max/\min}}{2\pi} + L_{0,\max/\min}\Delta E, \tag{3.69}$$

$$L_{0,\max/\min} = \left\lfloor -\frac{\alpha_{B,\max/\min}}{2\pi\Delta E}\right\rfloor, \tag{3.70}$$

$$\Delta E = \frac{\gcd(M, N)}{M}, \tag{3.71}$$

where the notation 'max\min' is used to denote both cases concisely. The deviation in $\hat{x}_{\max}(x_0, u_0)$ and $\hat{x}_{\min}(x_0, u_0)$ arises from different values of $\alpha_{B,\max}$ and $\alpha_{B,\min}$. Assuming that M and N are relative primes, we have $\Delta E = 1/M$, simplifying Eqs. (3.68)-(3.70) to:

$$|y_{0,\max}(\alpha_{B,\max\backslash\min})| = -\left|\frac{\alpha_{B,\max\backslash\min}}{2\pi} - \frac{1}{M}\left\lfloor\frac{M\alpha_{B,\max\backslash\min}}{2\pi}\right\rfloor - \frac{1}{2M}\right| + \frac{1}{2M}. \tag{3.72}$$

For every pair of coordinates (x_0, u_0) located within the safe basin, (x_0, u_0) belongs to both SB_u and SB_l. Therefore, we can assert that (x_0, u_0) is a member of the intersection $SB_u \cap SB_l$, where SB_u and SB_l are defined as

$$SB_u := \{(x_0, u_0) \in \mathbb{R}^2 | \hat{x}_{\max}(x_0, u_0) < x_u\}, \tag{3.73}$$

$$SB_l := \{(x_0, u_0) \in \mathbb{R}^2 | x_l < \hat{x}_{\min}(x_0, u_0)\}. \tag{3.74}$$

Determining the boundaries of this set using analytical methods is a complex task (see Figures 3.5a and 3.5c). However, in specific scenarios, the complexity can be significantly reduced, such as when $(-x_l = x_u)$ is a symmetric potential or when SB_l is a subset of SB_u (or vice versa) for all values of f and β as illustrated in Figs. 3.5c and 3.5d.
In cases where $N + M$ is an even number, we find that Eq. (3.72) is periodic with a period of $\frac{2\pi}{M}$:

$$|y_{0,\max}(x)| = \left|y_{0,\max}\left(x + \frac{2\pi}{M}\right)\right|, \tag{3.75}$$

and by evaluating

$$\alpha_{B,\max} - \alpha_{B,\min} = (\omega - 1)\pi = \frac{N - M}{M}\pi, \tag{3.76}$$

we can confirm this periodic nature. Therefore, $x_{\max}(x_0, u_0)$ is equivalent to $x_{\min}(x_0, u_0)$ when $N + M$ is an even number. Subsequently, an analytical estimate for the boundary of the safe basin is provided for the cases mentioned above.

Case 1: $|x_l| \gg x_u$ **or** $N + M$ **even**

This section addresses situations where one of the potential well's boundaries is substantially farther from the center than the other or when the sum of N and M is even.

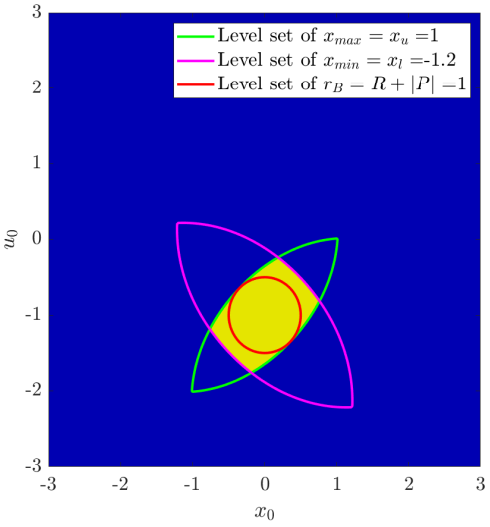

(a) $N = 2$ and $M = 1$ with $|P| = 0.5$

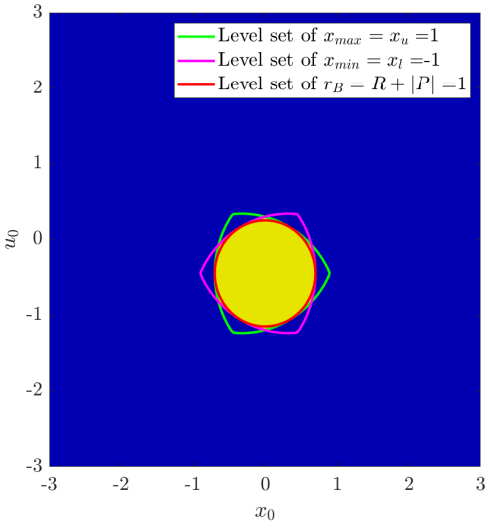

(b) $N = 3$ and $M = 2$ with $|P| = 0.3$

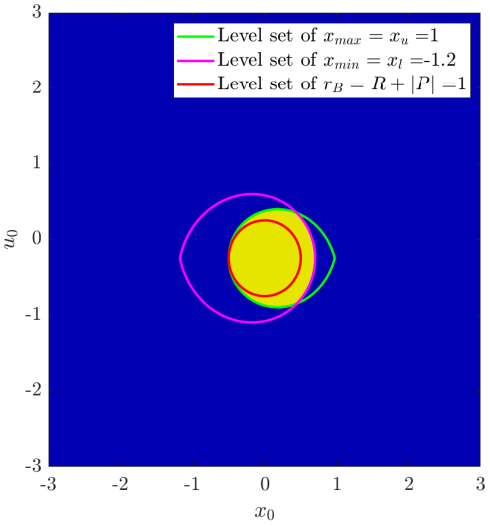

(c) $N = 1$ and $M = 2$ with $|P| = 0.5$

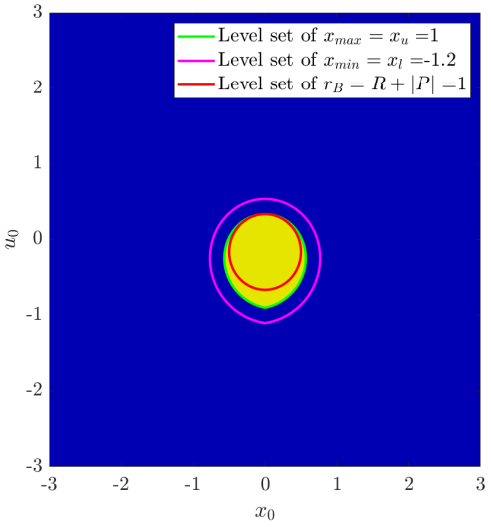

(d) $N = 1$ and $M = 3$ with $|P| = 0.5$

Figure 3.5: Analytically derived estimates for the safe basin (yellow region), relevant to escape scenarios in the initial condition plane for varying $\omega = \frac{N}{M}$. The level sets of $x_{\max}(x_0, u_0) = x_u$ and $x_{\min}(x_0, u_0) = x_l$ are colored green and pink, respectively. The circular disk, defined by Eq. (3.19), is colored red. The intersecting areas of the level sets (SB_u and SB_l) demarcate the region of no escape (SB). Figure adapted from [224]

In cases where the difference between the potential boundaries is significant, the particle tends to escape towards the nearer boundary. Therefore, the level set related to this closer boundary gains importance.
Assuming $|x_l| \gg x_u$, it implies that SB_u is a subset of SB_l (otherwise, we consider an analogous calculation for $\hat{x}_{\min}(x_0, u_0)$). To investigate the structure of the safe basin, which is influenced by the parameters f, M and N (noting that β acts as a rotational factor in the initial condition plane), the escape criterion 3.0.8 is applied to the more manageable, although less accurate, estimate given in Eq. (3.62), resulting in the following:

$$\hat{x}_{\max}(x_0, u_0) = R + |P| - \frac{2\pi^2 R|P||y_{0,\max}|^2}{R + \omega^2|P|} \stackrel{!}{=} x_u. \tag{3.77}$$

Given that R and $|y_{0,\max}|$ depend on x_0 and u_0, we can define a polar coordinate function centered at $(P\sin\beta, P\omega\cos\beta)$. This function determines the boundary's distance based on the angle, denoted as $R(\varphi)$. For this purpose, $|y_{0,\max}|$ is redefined as:

$$g(\varphi) := |y_{0,\max}(\varphi)| = -\left|\frac{N}{M}\frac{\varphi}{2\pi} - \frac{1}{M}\left\lfloor\frac{N\varphi}{2\pi}\right\rfloor - \frac{1}{2M}\right| + \frac{1}{2M}, \tag{3.78}$$

with the angular coordinate φ being:

$$\varphi := -\frac{\alpha_{B,\max}}{\omega} = \alpha - \frac{\beta}{\omega} - \frac{\pi}{2\omega}(\omega - 1 + 2\sigma(-P)), \tag{3.79}$$

forming a triangle wave with a period of $2\pi/N$, an amplitude of $1/(4M)$, and a positive shift of $1/(4M)$. The escape condition (3.77) is then modified to:

$$R^2 + \left((\omega^2 + 1 - 2\pi^2 g^2(\varphi))|P| - x_u\right) R + \omega^2|P|(|P| - x_u) = 0, \tag{3.80}$$

and resolved for R, resulting in:

$$R(\varphi) = \frac{x_u - \left(1 + \omega^2 - \pi^2 g^2(\varphi)\right)|P|}{2} \pm \frac{\sqrt{4g^4(\varphi)\pi^4|P|^2 - 4\pi^2\left((\omega^2+1)|P| - x_u\right)|P|g^2(\varphi) + \left((\omega^2-1)|P| - x_u\right)^2}}{2}, \tag{3.81}$$

where, for $|P| < x_u$, the positive solution uniquely defines the safe basin's boundary (illustrated by the green curve in Fig. 3.7a). At the points where $g(\varphi) = 0$, occurring N times within $\varphi \in [0, 2\pi)$, the solution simplifies to $R = x_u - |P|$, signifying that the shape from Eq. (3.77) intersects the circle from Eq. (3.19). For values of φ other than $\frac{n}{2\pi}$ (with

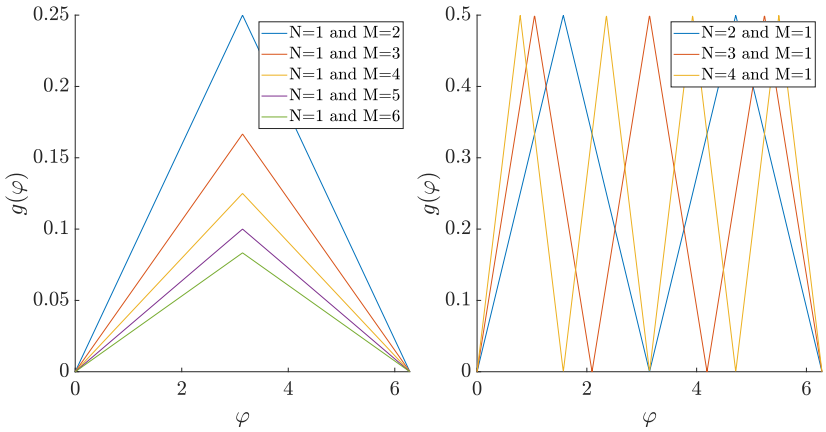

(a) $N = 1, M = 1, 2, 3, \ldots$ **(b)** $N = 1, 2, 3, 4, M = 1$

Figure 3.6: Representation of the triangle wave function for various M and N values. Figure adapted from [224]

$n = 0, 1, \ldots, N-1$), where $R(\varphi) > x_u - |P|$, the circle in Eq. (3.19) becomes inscribed within the shape in Eq. (3.77). A notable situation arises when $N = 1$, where a potential safe basin may exist for $x_u < |P| < P_{\text{crit}}$, despite the absence of the circle, and yet $|P|$ remains below the critical threshold P_{crit}, beyond which no safe basin can be formed. In this case, the origin of the polar coordinates $(x_0, u_0) = (P \sin\beta, P\omega \sin\beta)$ shifts outside the safe basin, leading to some values of φ yielding negative $R_{1,2}(\varphi)$, which lack physical significance. However, for other values of φ, there are two positive roots $R_{1,2}(\varphi)$ that define the safe basin (blue curve in Fig. (3.7a)).

An upper limit for P_{crit} can be obtained by noting that safe basins vanish when the square root term in Eq. (3.81) becomes zero. At this point, the safe basin reduces to a single point in the direction of the angle, at $\varphi = \pi$, where $g(\varphi)$ takes its maximum, namely $g(\varphi) = \frac{1}{2M}$ (see Fig. 3.6). Given $N = 1$, we get $\omega = 1/M$. Thus, the discriminant in Eq. (3.80)

$$\left(\omega^2 + 1 - 2\pi^2 g^2(\varphi))|P| - x_u\right)^2 - 4\left(\omega^2|P|^2 - x_u|P|\omega^2\right) = 0 \tag{3.82}$$

reaches zero at

$$P_{\text{crit}} = \frac{2\left(2M^2 - 2\sqrt{2}\,\pi - \pi^2 - 2\right)M^2}{(2M^2 - \pi^2 + 4M + 2)\,(2M^2 - \pi^2 - 4M + 2)}\,x_u. \tag{3.83}$$

Figure 3.8 presents the calculated values for the scaled critical forcing $\frac{|P|}{x_u}$ when $N = 1$ and either $SB_u \subseteq SB_l$ or the reverse holds, for various values of M.

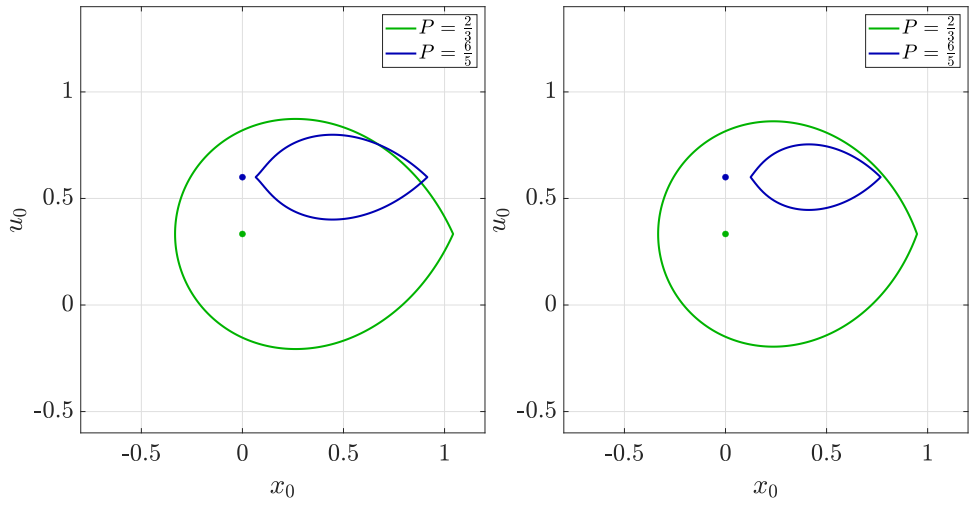

(a) Employing the approximation in Eq. (3.62) **(b)** Employing the approximation in Eq. (3.64)

Figure 3.7: Illustration of the boundaries of the safe basin in the initial condition plane for $\omega = \frac{N}{M} = \frac{1}{2}, \beta = 0$, $x_l = -\infty$, and $x_u = 1$, considering various values of P and the approximations in Eqs. (3.62) and (3.64). The existence of a safe basin is indicated by the blue curve for $P > x_u$. The origins of the polar coordinates $(P \sin\beta, P\omega\cos\beta)$, with respect to which the curve in Eq. (3.81) delineates the basin boundary, are marked as dots. The safe basin estimates on the left-hand side are higher due to $f_{sup,Rat} \leq f_{sup,T}$ (cf. Eqs. (2.93) and (2.97)). Figure adapted from [224]

For $N \geq 2$, we cannot observe that $P_{\text{crit}} > x_u$ occurs, as it would imply the presence of N disjoint, non-escaping basins (resulting from the N-fold rotational symmetry), centered at $(P \sin\beta, P\omega\cos\beta)$. Hence, the analytically deduced safe basin vanishes in these instances if $|P| > 1$.
To approximate the area within the level set $x_{\max}(x_0, u_0) = x_u$, one must compute the following integral:

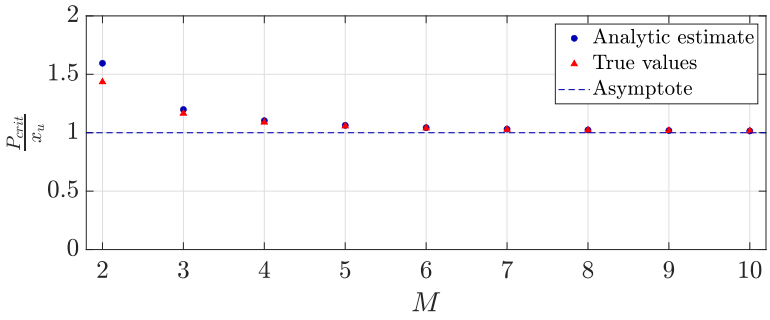

Figure 3.8: The trend of P_{crit}/x_u approaching 1 as the value of M increases, keeping $N = 1$ constant. Figure adapted from [224]

$$A_{\max} = \int_0^{2\pi} \frac{R^2(\varphi)}{2} \mathrm{d}\varphi, \tag{3.84}$$

which simplifies to

$$A_{\max} = N \int_0^{\frac{\pi}{N}} R^2(\varphi) \mathrm{d}\varphi, \tag{3.85}$$

due to the N-fold rotational and the mirror symmetry. Eq. (3.85) results in elliptic integrals that require extensive calculations. Nevertheless, for an estimate, the Taylor series of $R^2(\varphi)$ around $\varphi = 0$ up to the fifth order yields

$$\begin{aligned} R^2(\varphi) = (x_u - |P|)^2 &+ \frac{(x_u - |P|)^2 |P| \omega^2}{|P|(\omega^2 - 1) + x_u} \varphi^2 \\ &+ \frac{(x_u - |P|)^2 |P|^2 \left((3\omega^2 - 1)|P| + x_u\right) \omega^4}{4\left((\omega^2 - 1)|P| + x_u\right)^3} \varphi^4 + O(\varphi^6). \end{aligned} \tag{3.86}$$

Integration and insertion of $\omega = N/M$ leads to

$$A_{\max,\mathrm{T}} = \left(x_u - |P|\right)^2 \pi \left(1 + \frac{\pi^2}{3\left(N^2 + M^2\left(\frac{x_u}{|P|} - 1\right)\right)} + \frac{\left(3N^2 + M^2\left(\frac{x_u}{|P|} - 1\right)\right)\pi^4}{20\left(N^2 + M^2\left(\frac{x_u}{|P|} - 1\right)\right)^3}\right). \tag{3.87}$$

The denominators remain positive considering that $x_u > |P|$. For large N and M, the higher-order terms in the expansion diminish, leading the safe basin to approach a circular disk as described in Sect. 3.1.1. Fig. 3.9 compares Eq. (3.87) with direct numerical simulation and semianalytic estimates based on numerical integration of sublevel sets defined by $\hat{x}_{\max(x_0,u_0)} < x_u$, where $\hat{x}_{\max(x_0,u_0)}$ is derived from Eq. (3.64) and Eq. (3.62) respectively. For the smallest values M and N, that is, $N = 1$ and $M = 2$ or $N = 2$ and $M = 1$, the analytic approximations are less precise. However, for higher values of N and M, the estimate of GIM becomes more accurate. Direct simulation indicates the persistence of safe basins even for $|P| > x_u$. However, their prediction is not feasible with the methodology mentioned above due to the restrictive escape condition 3.0.8: the particle exits the potential each excitation period, but it returns due to the high excitation amplitude and essential nonlinearity at the potential's edge. Increasing excitation amplitudes results in nonlinear effects, as evidenced in Fig. 3.10 with a relatively smooth boundary and Fig. 3.11 showing a fractal-like boundary with period tripling.

$x_u = -x_l$ **with** $N + M$ **odd**

In cases where the potential is symmetric and the sum of N and M forms an odd number, the safe basin exhibits a rotational symmetry of $2N$-fold and mirror symmetry, allowing the computation of its area as

$$A_{\max} = 2N \int_0^{\frac{\pi}{2N}} R^2(\varphi) \mathrm{d}\varphi. \tag{3.88}$$

Applying the Taylor series expansion for $R^2(\varphi)$ as specified in Eq. (3.86), we deduce the expression for

$$A_{\max,\mathrm{T}} = \left(x_u - |P|\right)^2 \pi \left(1 + \frac{\pi^2}{12\left(N^2 + M^2\left(\frac{x_u}{|P|} - 1\right)\right)} + \frac{\left(3N^2 + M^2\left(\frac{x_u}{|P|} - 1\right)\right)\pi^4}{320\left(N^2 + M^2\left(\frac{x_u}{|P|} - 1\right)\right)^3} \right). \tag{3.89}$$

A graphical example of Eq. (3.89) for $N = 2$ and $M = 1$ is provided in Fig. 3.9c.

3.1.3 Comparison with numerical results

This section compares the analytically derived results with their numerical counterparts, considering various parameter selections. For numerical simulations, the escape condition 3.0.5 was used.
Fig. 3.9 compares the analytical and numerical findings for the global integrity measure (GIM), specifically the safe basin area, under varying parameters.
Fig. 3.10 shows a wedge-shaped safe basin for a supercritical forcing value $\frac{|P|}{x_u} = 1.3$ ($N = 2$, $M = 1$ and $x_l = -\infty$), unanticipated by the stated model. However, the safe basin boundary is smooth and lacks fractal characteristics.
Fig. 3.11 illustrates a fractal-like non-escaping set under a high excitation amplitude of $\frac{|P|}{x} = 1.6$ ($N = 2$, $M = 1$ and $x_l = -\infty$). The substantial amplitude and the problem's strong nonlinearity at the boundary cause fractal-like edges for the safe basin.

3.1.4 Concluding remarks

The safe basins of a particle in an asymmetrically truncated quadratic potential well subjected to harmonic excitation are significantly impacted by a commensurable frequency ratio $\frac{N}{M}$. The size of the safe basins increases significantly when the ratio of the excitation frequency to the natural frequency is a ratio of small integers.
In a system close to $1 : M$ frequency ratio, safe basins may not appear when the system is perturbed. On the contrary, they may be present if the ratio is exactly $1 : M$, emphasizing

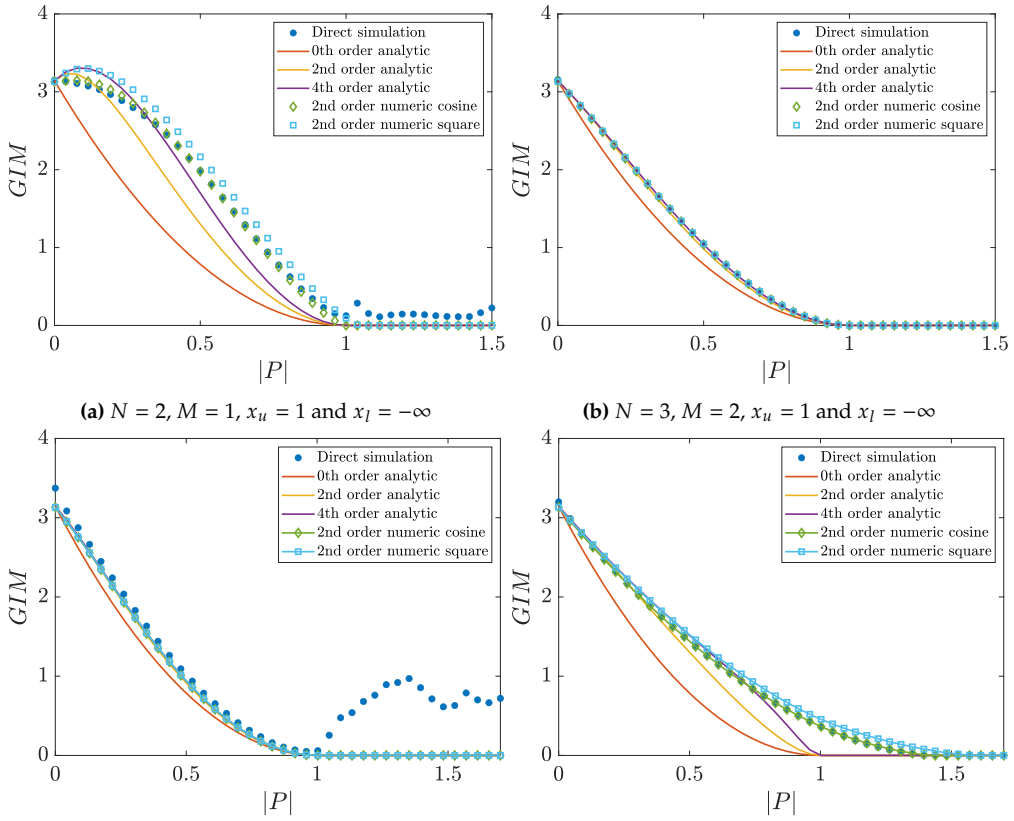

(a) $N = 2$, $M = 1$, $x_u = 1$ and $x_l = -\infty$

(b) $N = 3$, $M = 2$, $x_u = 1$ and $x_l = -\infty$

(c) $N = 2$, $M = 1$, $x_u = 1$ and $x_l = -1$

(d) $N = 1$, $M = 2$, $x_u = 1$ and $x_l = -\infty$

Figure 3.9: Variation in the global integrity measure (GIM) in response to the excitation amplitude for different excitation frequency values (shown in deep blue dots). The analytic estimates, indicated by red, yellow, and purple lines, are based on Eq. 3.87. The numerical integration of the area of the sublevel set, defined by $\hat{x}_{\max(x_0,u_0)} < x_u$ and denoted by green diamonds and light blue squares, is also depicted. Here, $\hat{x}_{\max(x_0,u_0)}$ is determined by Eqs. (3.64) and (3.62). In particular, Fig. 3.9d shows that the Taylor series expansion of Eq. (3.81) offers estimations only for $|P| < x_u$, yet the semianalytic approach, marked with green diamonds, still yields qualitatively correct results. Figures adapted from [224]

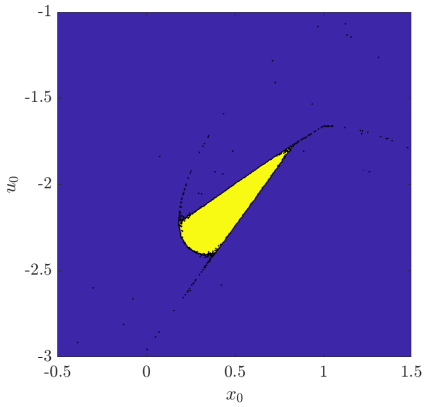

(a) Safe basin on the initial condition plane

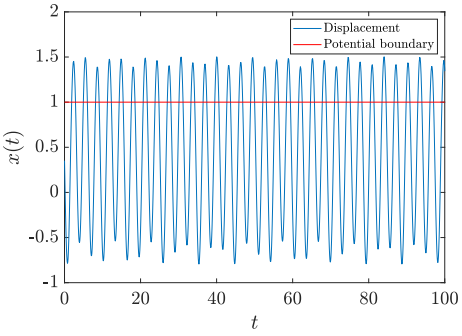

(b) Time evolution of the solution for $x_0 = 0.352$, $u_0 = -2.224$

Figure 3.10: The wedge-shaped safe basin (yellow region) for $P_{\text{crit}} < |P| = 1.3$ with $N = 2$, $M = 1$, $x_{\text{l}} = -\infty$ and $x_{\text{u}} = 1$, after 50 excitation periods. Selected initial conditions within the safe basin show that the particle leaves the potential well in each excitation period, but the strong force returns it; thus, a safe basin is maintained for supercritical forcing. Observations suggest that this non-escaping mechanism is feasible only for excitation frequencies exceeding the well's natural frequency ($\omega > 1$). The prediction of these basins using the analytical method of this study is not feasible. Figures adapted from [224]

the dependence of safe basins on frequency ratios. In the case of the frequency ratio $N : M$, a safe basin can be divided into two parts: a stable and long-lasting part unaffected by minor frequency changes and a temporary and illusory part that disappears even with slight disturbances in the frequency ratio. Safe basins that disappear under the slightest disturbance are dangerous in applications, as they give the false illusion of a safe operation.

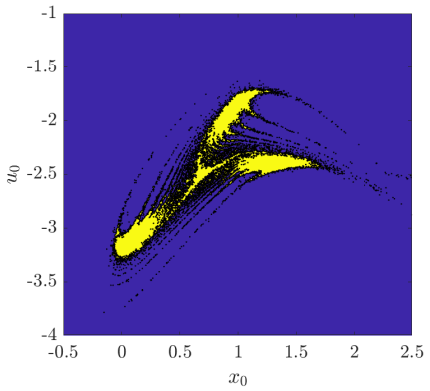

(a) Safe basin on the plane of initial conditions

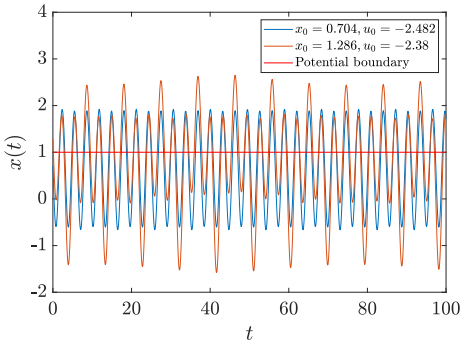

(b) Temporal progression of the solution for initial conditions $x_0 = 1.286$, $u_0 = -2.38$ and for $x_0 = 0.704$, $u_0 = -2.482$.

Figure 3.11: The fractal characteristics of safe basin (yellow region) at $P_{\text{crit}} < |P| = 1.6$ with parameters $N = 2$, $M = 1$, $x_{\text{l}} = -\infty$, and $x_{\text{u}} = 1$. The integration was carried out over 100 periods of excitation. The particle displacement's temporal evolution can be periodic or experience periodic tripling, contingent on the chosen initial condition. Figures adapted from [224]

3.2 Damped-driven harmonic oscillator

This section extends our previous model of a driven harmonic oscillator with a viscous damping force, which is essential in realistic engineering models. The model is suitable for a broad range of engineering, physics, and natural sciences systems because it represents the standard form of a damped, driven single degree-of-freedom mechanical system after linearization around a stable equilibrium.
We focus on the level-crossing problem of this system. This focus allows us to minimize the secondary effects of truncating a potential, which often introduces significant nonlinearities, as seen in the previous section. Additionally, abrupt force changes, typical in truncated systems, are rare in natural or technical systems, confirming the appropriateness of choosing the level-crossing problem.

3.2.1 Problem setting

This section focuses on safe basins regarding the level crossing of a classical particle, denoted as m, under the influence of a linear spring with stiffness k and viscous damping characterized by c. The absolute magnitude of the critical displacement is represented by r_B. Once the particle crosses this boundary, it enters an unsafe zone. The undamped natural frequency is defined as

$$\Omega_0 = \sqrt{\frac{k}{m}}. \tag{3.90}$$

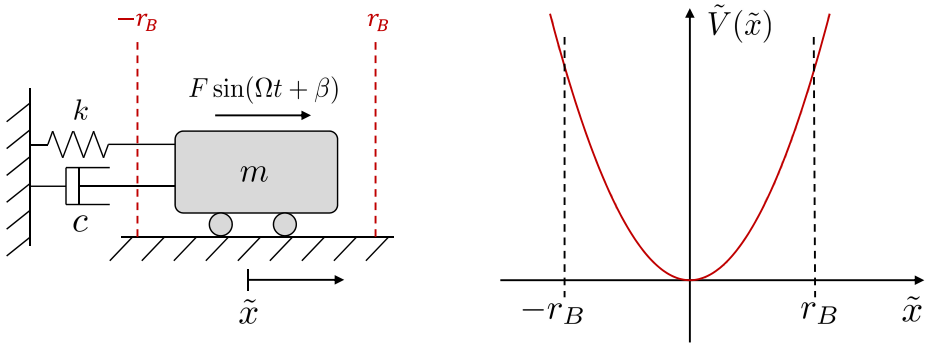

(a) Equivalent mechanical model of the problem **(b)** Crossing of the symmetric boundary at r_B

Figure 3.12: Illustration of problem settings. Figures adapted from [225]

A sinusoidal force characterized by an amplitude F, an angular frequency Ω, and an initial phase β excites the particle. The initial conditions are given by $(\tilde{x}_0, \tilde{u}_0)$. The illustration of this problem setting is shown in Fig. 3.12.

3.2.2 Equations of motion

Then, the equation of motion is expressed by

$$m\tilde{x}'' + c\tilde{x}' + m\Omega_0^2\tilde{x} = F\sin(\Omega t + \beta), \tag{3.91}$$

$$\tilde{x}(t=0) = \tilde{x}_0, \tag{3.92}$$

$$\tilde{x}'(t=0) = \tilde{u}_0, \tag{3.93}$$

with $\square' := \mathrm{d}\square/\mathrm{d}t$. After division by m and the introduction of the dimensionless displacement $x := \tilde{x}/r_B$ and dimensionless time $t := \Omega_0\tau$, the equation transforms to

$$\ddot{x} + \frac{c}{\Omega_0 m}\dot{x} + x = \frac{F}{r_B m}\sin\left(\frac{\Omega}{\Omega_0}\tau + \beta\right), \tag{3.94}$$

$$x(\tau=0) = x_0 := \frac{\tilde{x}_0}{r_B}, \tag{3.95}$$

$$\dot{x}(\tau=0) = u_0 := \frac{\tilde{u}_0}{\Omega_0 r_B}, \tag{3.96}$$

where $\dot{\square}$ denotes the derivative concerning the dimensionless time τ. Defining

$$D := \frac{c}{2\Omega_0 m}, \qquad f := \frac{F}{r_B m}, \qquad \omega := \frac{\Omega}{\Omega_0}, \tag{3.97}$$

leads to the non-dimensional equation of motion of a driven damped harmonic oscillator

$$\begin{aligned} \ddot{x} + 2D\dot{x} + x &= f\sin(\omega\tau + \beta), \\ x(\tau = 0) &= x_0, \\ \dot{x}(\tau = 0) &= u_0. \end{aligned} \tag{3.98}$$

The procedure to solve Eq. (3.98) is standard and is not elaborated here. The solution takes the form

$$x(\tau) = Re^{-D\tau}\sin(\omega_0\tau + \alpha) + P\sin(\omega\tau + \beta + \gamma), \tag{3.99}$$

with

$$\omega_0 := \sqrt{1 - D^2}, \tag{3.100}$$

$$P := \frac{f}{\sqrt{(1-\omega^2)^2 + 4D^2\omega^2}}, \tag{3.101}$$

$$\gamma := \operatorname{atan2}(-2D\omega, 1 - \omega^2), \tag{3.102}$$

$$C_1 := x_0 - P\sin(\beta + \gamma), \tag{3.103}$$

$$C_2 := u_0 - P\omega\cos(\beta + \gamma), \tag{3.104}$$

$$R := \sqrt{\frac{C_1^2 + 2DC_1C_2 + C_2^2}{1 - D^2}}, \tag{3.105}$$

$$\alpha := \operatorname{atan2}(\omega_0 C_1, DC_1 + C_2), \tag{3.106}$$

where $\operatorname{atan2}(y, x)$ denotes the '2-argument arctangent'. By assuming the excitation frequency is close to ω_0, the small parameter

$$\varepsilon := \omega - \omega_0 \tag{3.107}$$

is introduced. The determination of the level-crossing time involves identifying the smallest positive τ_{LC} satisfying

$$x(\tau_{\mathrm{LC}}) \stackrel{!}{=} \pm 1. \tag{3.108}$$

According to Eq. (3.99), two distinct level-crossing cases emerge: 'fast' and 'slow' level crossing. In the 'fast' scenario, the particle attains the critical distance within the initial excitation period, implying that the level crossing is predominantly influenced by the initial conditions, as a small excitation amplitude cannot significantly alter the particle's trajectory in such a brief interval. On the contrary, in the 'slow' scenario, the particle

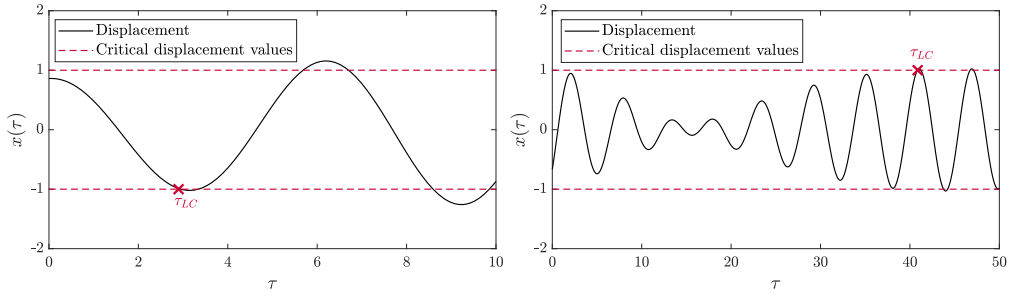

(a) 'Fast' level crossing ($x_0 = 0.86$, $u_0 = 0.045$) **(b)** 'Slow' level crossing ($x_0 = -0.665$, $u_0 = 0.945$)

Figure 3.13: Illustrative cases of level crossing with $D = 0.02$, $f = 0.15$, $\omega = 1.1$, $\beta = \pi$. Figures adapted from [225]

initially lacks the total energy necessary for level crossing. However, the harmonic force gradually drives the particle closer to the critical displacement value until it is finally achieved (see Fig. 3.13).
In each scenario, the plane of the initial conditions is divided into safe (S_F, S_S) and unsafe regions (U_F, U_S), classified by the type of level crossing. If the particle is within S_F and S_S, it will not cross the critical distance, making the ultimate safe region the intersection of these two conditions ($S := S_F \cap S_S$).

3.2.3 Criteria for level crossing

This section explores the configurations of the safe basins shaped by both the 'fast' and 'slow' crossing mechanisms.

'Fast' level crossing

Initially, we discuss the 'fast' level-crossing mechanism, predominantly influenced by the initial conditions. At the boundary of the 'fast' safe region S_F, the condition is that the first local extremum of the particle's displacement, denoted by $x(\tau_F)$, equals plus or minus one:

$$\partial S_F := \{(x_0, u_0) \in \mathbb{R}^2 | x(\tau_F; x_0, u_0) = \pm 1\}, \tag{3.109}$$

accompanied by the time of level crossing

$$\tau_F(x_0, u_0) := \{\min \tau | \dot{x}(\tau; x_0, u_0) = 0 \text{ and } \tau \geq 0\}. \tag{3.110}$$

To accurately determine the value and timing of the first local extremum of $x(\tau)$, one must solve the transcendental equation $\dot{x}(\tau) = 0$, which generally lacks an analytical

solution. However, the regular perturbation technique for algebraic equations can provide a reasonable approximation of τ_F: expanding in terms of the small parameter ε generates solvable equations in sequence to estimate the time of the first extremum of Eq. (3.99). A first-order approximation in ε is sufficiently precise (see the green line in Figs. 3.15 and 3.17), allowing us to represent time as

$$\tau = \tau_0 + \varepsilon\tau_1 + O(\varepsilon^2). \tag{3.111}$$

Similarly, $x(\tau)$ is reformulated as

$$x(\tau) = x_0(\tau) + \varepsilon x_1(\tau) + O(\varepsilon^2). \tag{3.112}$$

Setting $D = D^*|\varepsilon|$, with $D^* = O(1)$, and $\omega = \omega_0 + \varepsilon$, reduces the problem, and the only small parameter ε remains. A Taylor series expansion to the first order in ε gives

$$\begin{aligned} x(\tau) \approx & R\sin(\omega_0\tau_0 + \alpha) + P\sin(\omega_0\tau_0 + \beta + \gamma) \\ & + (R\left[\cos(\omega_0\tau_0 + \alpha)\omega_0\tau_1 - \sin(\omega_0\tau_0 + \alpha)D^*\tau_0\right] \\ & + P\cos(\omega_0\tau_0 + \beta + \gamma)(\tau_0 + \omega_0\tau_1))\varepsilon. \end{aligned} \tag{3.113}$$

By defining

$$Q := \sqrt{R^2 + 2RP\cos(\alpha - \beta - \gamma) + P^2}, \tag{3.114}$$

$$\nu := \operatorname{atan2}(R\sin\alpha + P\sin(\beta + \gamma), R\cos\alpha + P\cos(\beta + \gamma)), \tag{3.115}$$

Eq. (3.113) can be rewritten as

$$\begin{aligned} x(\tau) = & Q\sin(\omega_0\tau_0 + \nu) \\ & + \varepsilon\left(\tau_0(P\cos(\omega_0\tau_0 + \beta + \gamma) - D^*R\sin(\omega_0\tau_0 + \alpha)) + Q\tau_1\omega_0\cos(\omega_0\tau_0 + \nu)\right). \end{aligned} \tag{3.116}$$

$\dot{x}(\tau) = 0$ is satisfied at the local extrema points. The derivative with respect to τ (similar as in the method of multiple scales) is expressed as

$$\frac{\mathrm{d}\square}{\mathrm{d}\tau} = \frac{\partial\square}{\partial\tau_0} + \varepsilon\frac{\partial\square}{\partial\tau_1}, \tag{3.117}$$

which, upon disregarding higher-order terms than $O(\varepsilon)$, leads to

$$\begin{aligned} \dot{x}(\tau) = & Q\omega_0\cos(\omega_0\tau_0 + \nu) + \varepsilon\big(-Q\tau_1\omega_0^2\sin(\omega_0\tau_0 + \nu) + P(\cos(\omega_0\tau_0 + \beta + \gamma) \\ & - \tau_0\omega_0\sin(\omega_0\tau_0 + \beta + \gamma)) - D^*R(\sin(\omega_0\tau_0 + \alpha) + \tau_0\omega_0\cos(\omega_0\tau_0 + \alpha))\big). \end{aligned} \tag{3.118}$$

Based on condition (3.110), the terms involving ε^0 and ε^1 have to cancel out. While there are numerous solutions for τ_F, our interest lies in the smallest positive one, which is given as follows:

$$\tau_0^*(x_0, u_0) = \frac{\operatorname{mod}\left(\frac{\pi}{2} - \nu, \pi\right)}{\omega_0}, \tag{3.119}$$

$$\begin{aligned}\tau_1^*(x_0, u_0) = &\frac{P(\cos(\omega_0\tau_0^* + \beta + \gamma) - \tau_0^*\omega_0 \sin(\omega_0\tau_0^* + \beta + \gamma))}{Q\omega_0^2 \sin(\omega_0\tau_0^* + \nu)} \\ &- \frac{D^*R(\sin(\omega_0\tau_0^* + \alpha) + \tau_0^*\omega_0 \cos(\omega_0\tau_0^* + \alpha))}{Q\omega_0^2 \sin(\omega_0\tau_0^* + \nu)},\end{aligned} \tag{3.120}$$

$$\tau_F(x_0, u_0) := \tau_0^* + \varepsilon\tau_1^*. \tag{3.121}$$

Then, it is possible to insert the value of $\tau_F(x_0, u_0)$ in Eq. (3.109) and depict the boundary of the 'fast' safe region ∂S_F as a function implicitly dependent on (x_0, u_0) (see Figs. 3.15 and 3.17). Although the analytical evaluation of Eq. (3.109) outlining the 'fast' boundary ∂S_F is too complicated, its numerical computation is significantly more efficient than the direct numerical simulation of Eq. (3.98) (cf. Sect. 3.2.5).
It is important to note that using only $\tau_F(x_0, u_0) \approx \tau_0^*(x_0, u_0)$ in Eq. (3.121) produces a result that is less precise, but still valuable and significantly simpler than including the term of $O(\varepsilon)$.
The green line in Figs. 3.15 and 3.17 illustrates the boundary of 'fast' level crossing. Without excitation (see Fig. 3.15a), level crossing can occur only due to the initial conditions. Given that the potential is symmetric, and the motion is damped and one-dimensional (though in cases of two-dimensional motions, this may not hold due to coupling terms), its maximum is achieved during the initial half-period of the motion. Consequently, the 'fast' boundary ∂S_F plays a pivotal role in defining the safe basin of the particle. With increasing damping, the area of the safe basin also increases. When the values of D are moderate, the analytical prediction shows remarkable agreement with the numerical data.
The transient motion persists indefinitely in scenarios with excitation but no damping (see Fig. 3.15b). Here, the interplay between the particular and homogeneous solutions (the beating motion) governs the safe basin. The 'slow' boundary ∂S_S defines the safe basin in such instances. The resulting safe basin forms a circular disk when the frequency ratio between the particular and homogeneous solutions is irrational. In contrast, a rational frequency ratio leads to a safe basin of a different shape, as discussed in Sect. 3.1. However, even in these scenarios, the 'fast' boundary accurately represents the set of initial conditions where level crossing occurs within the first half-period of excitation, as shown in the deep-blue region in Fig. 3.15b.

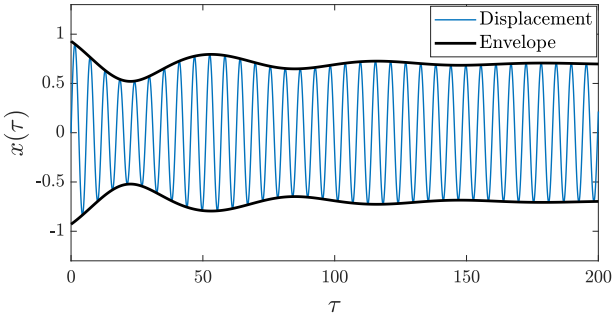

Figure 3.14: The precise solution and its envelope determined by Eq. (3.125) for $D = 0.02$, $f = 0.15$, $\omega = 1.1$, $\beta = \pi$, $x_0 = 0$ and $u_0 = 1$. Figure adapted from [225]

In situations involving both damping and excitation (see Fig. 3.17), both the 'fast' and 'slow' boundaries gain significance and outline a segment of the safe basin boundary.

'Slow' level crossing

To determine the boundary of the safe region for the 'slow' crossing mechanism, the envelope of $x(\tau)$ is analyzed. This envelope can be approximated using the total energy of the particle. Therefore, we calculate:

$$2E = x^2 + \dot{x}^2. \tag{3.122}$$

By differentiating Eq. (3.99) and inserting it into Eq. (3.122), we derive the expression:

$$\begin{aligned} 2E = {} & R^2 e^{-2D\tau} + P^2 + 2RPe^{-D\tau}\cos(\varepsilon\tau - \alpha + \beta + \gamma) \\ & + (\omega_0^2 - 1)R^2 e^{-2D\tau}\cos^2(\omega_0\tau + \alpha) + P^2(\omega^2 - 1)\cos^2(\omega\tau + \beta + \gamma) \\ & + 2RP(\omega\omega_0 - 1)e^{-D\tau}\cos(\omega_0\tau + \alpha)\cos(\omega\tau + \beta + \gamma) + D^2R^2e^{-2D\tau}\sin^2(\omega_0\tau + \alpha) \\ & - 2DR^2\omega_0 e^{-2D\tau}\sin(\omega_0 + \tau)\cos(\omega_0\tau + \alpha) \\ & - 2DRP\omega e^{-D\tau}\sin(\omega_0\tau + \alpha)\cos(\omega\tau + \beta + \gamma). \end{aligned} \tag{3.123}$$

We can observe that in Eq. (3.123) from the second line onward, each term is of $O(\varepsilon)$. Hence, disregarding these, we simplify to

$$2\tilde{E} := R^2 e^{-2D\tau} + P^2 + 2RPe^{-D\tau}\cos(\varepsilon\tau - \alpha + \beta + \gamma), \tag{3.124}$$

and the envelope is approximated by

$$A(\tau) = \pm\sqrt{2\tilde{E}}. \tag{3.125}$$

The envelope's peak, $A_{\max}$, and the instance of the first level crossing cannot be explicitly determined (for numerical instances, see Figs. 3.15b, 3.17, and 3.18). However, a reasonable approximation for the envelope's maximum is achievable, considering that it occurs at the beginning of the motion ('fast' level crossing) or around the time when the cosine term in Eq. (3.124) first equals 1 ('slow' level crossing), that is,

$$\tau_S = \operatorname{mod}\left(\frac{\alpha - \beta - \gamma}{\varepsilon}, \frac{2\pi}{|\varepsilon|}\right). \tag{3.126}$$

Therefore,

$$A_{\max}^2 = (P + Re^{-D\tau_S})^2. \tag{3.127}$$

Hence, the boundary of the 'slow' safe region is defined by

$$\partial S_S := \{(x_0, u_0) | A_{\max}(x_0, u_0) = 1\}. \tag{3.128}$$

The interior of S_S (illustrated in Fig. 3.17) is characterized by

$$-1 < P + Re^{-D\tau_S} < 1. \tag{3.129}$$

The left-hand side of the inequality is inherently satisfied. The right side leads to

$$Re^{-D\tau_S} < 1 - P, \tag{3.130}$$

implying a condition for a non-escaping set:

$$P \overset{!}{<} 1. \tag{3.131}$$

Taking the exponential term to the opposite side and squaring both sides in Eq. (3.130) results in

$$R^2 < e^{2D\tau_S}(1 - P)^2. \tag{3.132}$$

Substituting R^2 from Eq. (3.105) and reorganizing, we get

$$\frac{C_1^2 + 2DC_1C_2 + C_2^2}{(1 - D^2)(1 - P)^2} < e^{2D\tau_S}. \tag{3.133}$$

The equation's left-hand side delineates level sets of ellipses rotated by 45° and centered at $(P\sin(\beta + \gamma), P\omega\cos(\beta + \gamma))$. The right side is a function that varies with the initial conditions through $\tau_S(x_0, u_0)$. Our objective is to determine the nature of the level

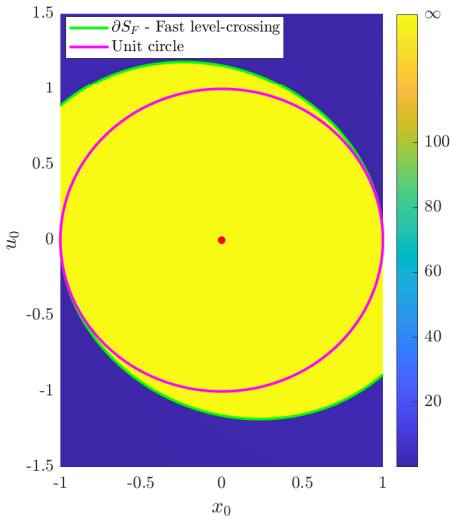

(a) As the damping increases ($D = 0.1$) with no excitation applied ($f = 0$, ω and β irrelevant), the safe basin's area (yellow surface) enlarges compared to the unit circle (solid magenta line). The 'slow' level-crossing mechanism is not applicable here since the envelope (cf. Eq. (3.125)) possesses no other local maxima aside from the initial one

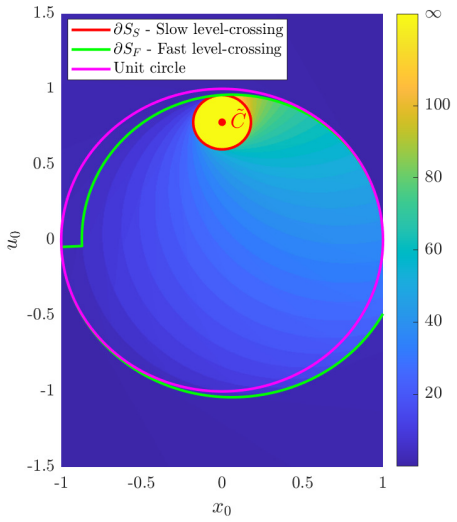

(b) The influence of exciting force ($f = 0.08$) on the boundary as predicted by the 'fast' level-crossing mechanism (solid green line) in the absence of damping ($D = 0$), $\omega = 0.95$ and $\beta = 0$. The absence of D means that the logarithmic spiral remains constant, forming a circle

Figure 3.15: Damping and excitation effects on the 'fast' level-crossing boundary within the initial condition plane. Analytical calculations ignore both influences. The color scale indicates the time required for level crossing (∞ denotes no crossing). Figures adapted from [225]

sets of $e^{2D\tau_S(x_0,u_0)}$. To achieve this, we first consider the parameter ranges $\alpha \in (-\pi, \pi]$, $\beta \in (-\pi, \pi]$, and $\gamma \in (-\pi, 0]$. We then have:

$$\tau_S = \begin{cases} \frac{\alpha-\beta-\gamma+2\pi}{\varepsilon} & \text{if } \alpha-\beta-\gamma < 0, \\ \frac{\alpha-\beta-\gamma}{\varepsilon} & \text{if } 0 \le \alpha-\beta-\gamma \le 2\pi, \\ \frac{\alpha-\beta-\gamma-2\pi}{\varepsilon} & \text{if } 2\pi < \alpha-\beta-\gamma, \end{cases} \tag{3.134}$$

where α is the only parameter dependent on the initial conditions. The domain length of τ_S exceeds 2π when all parameters vary. However, when altering only the initial conditions (as seen when the time of level crossing is plotted in the plane of initial conditions, cf. Fig. 3.17) and fixing the values of f, D, ω, and β, only α changes. Given the range of α as $(-\pi, \pi]$ and the fixed values of β and γ, at most two definition domains of Eq. (3.134) can be active. For certain ranges of x_0 and u_0, the middle case in Eq. (3.134)

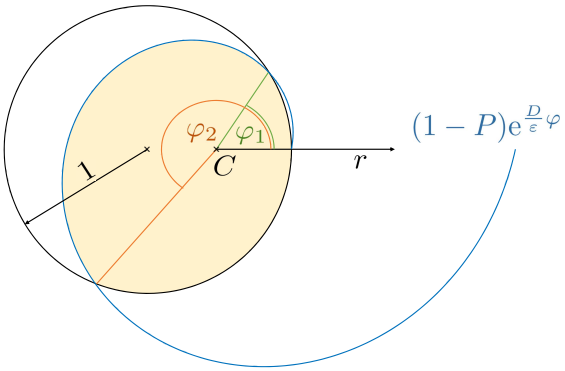

Figure 3.16: Change to polar coordinates. The black unit circle replaces ∂S_F, while the blue logarithmic spiral represents ∂S_S. The beige area, bounded by these curves, symbolizes the analytic approximation of the safe basin (here $\varepsilon < 0$). Figure adapted from [225]

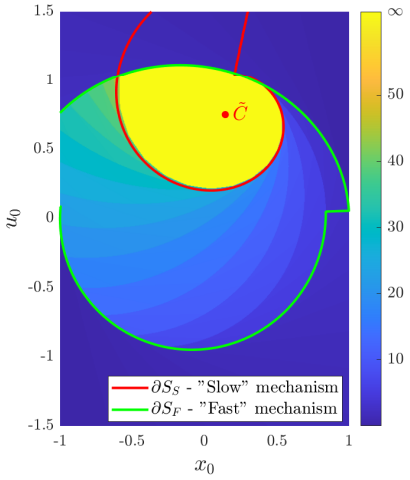

Figure 3.17: Numerically obtained level-crossing time (color scale) and safe basin (yellow area, ∞ indicates no crossing) on the $x_0 - u_0$ initial condition plane for $D = 0.02$, $f = 0.15$, $\omega = 1.1$, and $\beta = \pi$. The analytical approximation of the safe basin is represented by the intersection of curves ∂S_S and ∂S_F. Lines of constant τ_S originate from the point $\tilde{C}$, with τ_S increasing linearly with the angle in the clockwise direction. Each color change represents a peak in the solution $x(\tau)$ (see Fig. 3.13b). Figure adapted from [225]

will always be valid regardless of the values of f, D, ω, and β; however, only the first or third case can occur for other values of x_0 and u_0.

Next, we identify the subsets where τ_S remains constant, representing the level sets on the right-hand side of the equation. This observation implies that, along these sets, α also maintains a constant value, denoted as α_0. Hence, by defining α in Eq. (3.106), we establish:

$$\alpha_0 = \operatorname{atan2}\left(C_1\sqrt{1-D^2}, DC_1 + C_2\right) = \text{const.}, \tag{3.135}$$

$$C_2 = \left(\frac{\sqrt{1-D^2}}{\tan\alpha_0} - D\right) C_1. \tag{3.136}$$

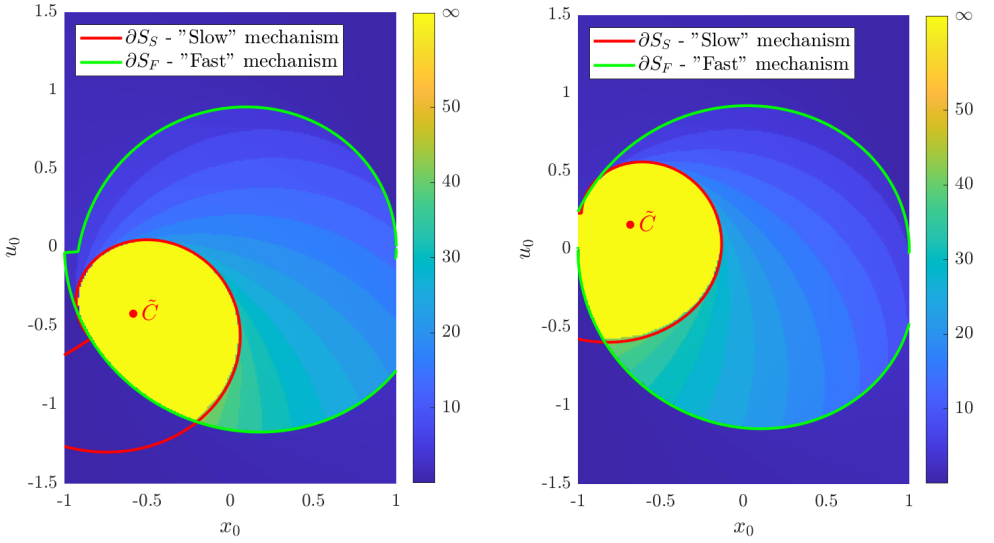

(a) $\beta = \pi/4$ **(b)** $\beta = \pi/2$

Figure 3.18: Numerical visualization of level-crossing time (color scale) and safe basin (yellow area, ∞ denotes no crossing) on the $x_0 - u_0$ plane of initial conditions for $D = 0.02$, $f = 0.15$, $\omega = 1.1$, and $\beta = \{\pi/4, \pi/2\}$. Lines of constant τ_S originate from the point $\tilde{C}$, with τ_S linearly increasing with angle clockwise. These graphs, together with Fig. 3.17, suggest that although the initial excitation phase β minimally affects the size of the safe basin, it primarily influences its orientation. Figures adapted from [225]

When the values of C_1 and C_2 from Eqs. (3.103)-(3.104) are substituted, the equation is reduced to:

$$u_0 - P\omega\cos(\beta+\gamma) = \left(\frac{\sqrt{1-D^2}}{\tan\alpha_0} - D\right)(x_0 - P\sin(\beta+\gamma))\,. \tag{3.137}$$

From Eq. (3.137), it becomes evident that the paths where τ_S is constant are rays (due to the atan2 function) beginning at the point $(P\sin(\beta+\gamma), P\omega\cos(\beta+\gamma))$. Based on Eq. (3.134), the ray where $\tau_S = 0$ has the gradient

$$\frac{\Delta u_0}{\Delta x_0} = \frac{\sqrt{1-D^2}}{\tan(\beta+\gamma)} - D, \tag{3.138}$$

and its orientation is such that if $\beta + \gamma \in [-\frac{\pi}{2}, \frac{\pi}{2}]$, the line resides in the half-plane satisfying

$$C_2 > -DC_1, \tag{3.139}$$

$$u_0 > -Dx_0 + P(\sin(\beta+\gamma) + \omega\cos(\beta+\gamma)), \tag{3.140}$$

alternatively, if $\beta+\gamma \notin [-\frac{\pi}{2}, \frac{\pi}{2}]$, the line is situated in the opposite half-plane:

$$C_2 < -DC_1. \tag{3.141}$$

Beginning along the ray corresponding to $\tau_S = 0$ and rotating clockwise for $\varepsilon > 0$ or anticlockwise for $\varepsilon < 0$, the increase in τ_S is proportional to the angle of rotation. A full rotation brings the maximal level-crossing time to

$$\tau_{S,\max} = \frac{2\pi}{|\varepsilon|}. \tag{3.142}$$

Plotting the value of $e^{2D\tau_S}$ (as in Eq. (3.133)) as a function of the angle of rotation around $(P\sin(\beta+\gamma), P\omega\cos(\beta+\gamma))$ reveals an increasing logarithmic spiral (see the red curve in Figs. 3.15b, 3.17 and 3.18, and the blue curve in Fig. 3.16). Taking into account Eq. (3.130), this suggests that the anticipated non-escaping set resides within an ellipse, rotated by 45°, with a major axis

$$a = \sqrt{1+D}(1-P) \tag{3.143}$$

and minor axis

$$b = \sqrt{1-D}(1-P), \tag{3.144}$$

expanding exponentially along the spiral's angle.

3.2.4 The safe basin's area

Analytical estimation of the safe basin area is feasible. Specifically, this is done by replacing the boundary of the 'fast' escaping set ∂S_F with the unit circle, representing the safe basin of a truncated quadratic potential without damping and excitation. This approach underestimates the safe region's area when considering damping since part of the safe region is excluded by disregarding the damping effect. Due to damping, the particle is decelerated sufficiently not to reach the boundary (as shown in Fig. 3.15a). However, concerning the excitation effect, replacing S_F with the unit disk is not significantly limiting, as the difference between the two sets remains minor for sufficiently small excitation amplitudes, keeping the analytic estimate reasonably accurate (as indicated in Fig. 3.15b).

The 'slow' safe region S_S is similarly simplified. Rather than considering the interior of the rotated ellipse from Eq. (3.133), we disregard D in the inequality's left-hand side, leading to a circle centered at

$$\tilde{C} := (P\sin(\beta+\gamma), P\omega\cos(\beta+\gamma)). \tag{3.145}$$

Further simplification involves neglecting ω in the circle's position, defining the point

$$C := (P\sin(\beta+\gamma), P\cos(\beta+\gamma)) \tag{3.146}$$

as the origin of a new polar coordinate system (r, φ), rotated by

$$\measuredangle(\overrightarrow{OC}, \vec{e}_{x_0}) = \frac{\pi}{2} - \beta - \gamma \tag{3.147}$$

relative to the original (x_0, u_0) system. From Eqs. (3.146) and (3.147), it is evident that the center and orientation of the logarithmic spiral depend on β. However, in the new coordinate system (r, φ), the excitation phase β is irrelevant (see Fig. 3.18). The slope of the line where $\tau_S = 0$, as given in Eq. (3.138), corresponds to the same angle $\frac{\pi}{2} - \beta - \gamma$ when D is neglected. Thus, $\varphi = 0$ marks the starting angle of the spiral (see Fig. 3.16). The ensuing calculations are for $\varepsilon < 0$, which is analogous but mirrored for $\varepsilon > 0$.
The unit circle shifted to $(-P, 0)$ is described by

$$R_C(\varphi) = -P\cos\varphi + \sqrt{1 - P^2\sin^2\varphi}. \tag{3.148}$$

The logarithmic spiral's equation is

$$R_S(\varphi) = (1-P)e^{\frac{D}{|\varepsilon|}\varphi}. \tag{3.149}$$

The influence of independent parameters D and ε can be represented using their ratio, $D^* = D/|\varepsilon|$. Two scenarios arise concerning solutions to

$$\begin{aligned} R_C(\varphi) &= R_S(\varphi) \\ (1-P)e^{D^*\varphi} &= -P\cos\varphi + \sqrt{1 - P^2\sin^2\varphi}. \end{aligned} \tag{3.150}$$

In the simpler case with large D^*, the only real solution is in $\varphi_0 = 0$. For a smaller critical value D^*_{crit}, there are two distinct solutions of Eq. (3.150), $\varphi = 0$ and $\varphi_1 = \varphi_2 = \varphi_{\text{crit}}$. With even smaller D^*, three distinct real roots of Eq. (3.150) are found, $0 = \varphi_0 < \varphi_1 < \varphi_2 < 2\pi$. Unfortunately, Eq. (3.150) cannot be explicitly solved for φ, but a graphical solution is

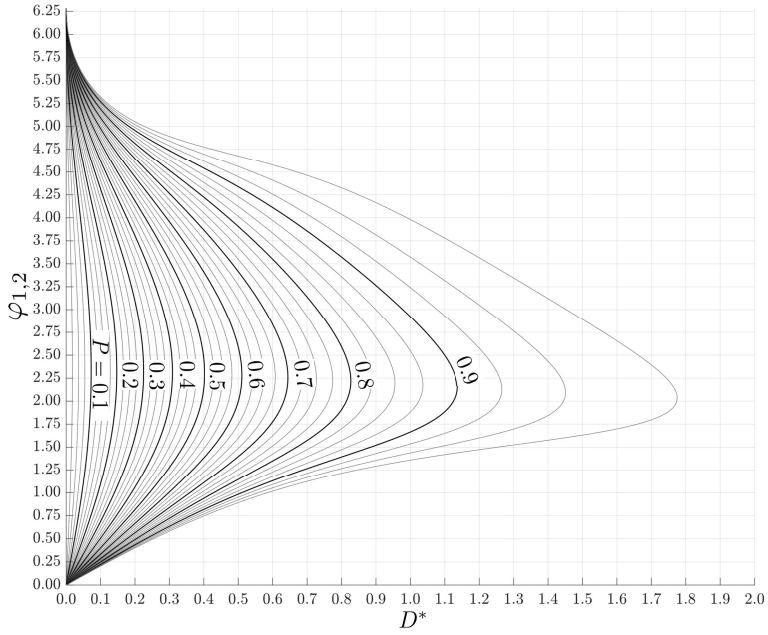

Figure 3.19: The solutions of $(1-P)e^{D^*\varphi} = -P\cos\varphi + \sqrt{1-P^2\sin^2\varphi}$ depend on the parameters D^* and P. For $D^* > D_{\text{crit}}$, the only real solution is $\varphi_0 = 0$. Figure adapted from [225]

provided in Fig. 3.19. An reasonably accurate heuristic estimate (see Fig. 3.21) for D^*_{crit} is

$$D^*_{\text{crit}} \approx \frac{3}{4}\text{atanh}(P). \tag{3.151}$$

To ascertain the safe basin's size, we compute

$$GIM = \frac{1}{2}\int_0^{2\pi} (\min\{R_C(\varphi), R_S(\varphi)\})^2 \mathrm{d}\varphi. \tag{3.152}$$

If $D^* > D_{\text{crit}}$, then $R_S(\varphi) > R_C(\varphi) \quad \forall\varphi \in [0, 2\pi)$, and the integral equals the area of the unit circle π. Otherwise, the integral becomes

$$GIM = \frac{1}{2}\left(\int_0^{\varphi_1} R_C^2(\varphi)\mathrm{d}\varphi + \int_{\varphi_1}^{\varphi_2} R_S^2(\varphi)\mathrm{d}\varphi + \int_{\varphi_2}^{2\pi} R_C^2(\varphi)\mathrm{d}\varphi\right). \tag{3.153}$$

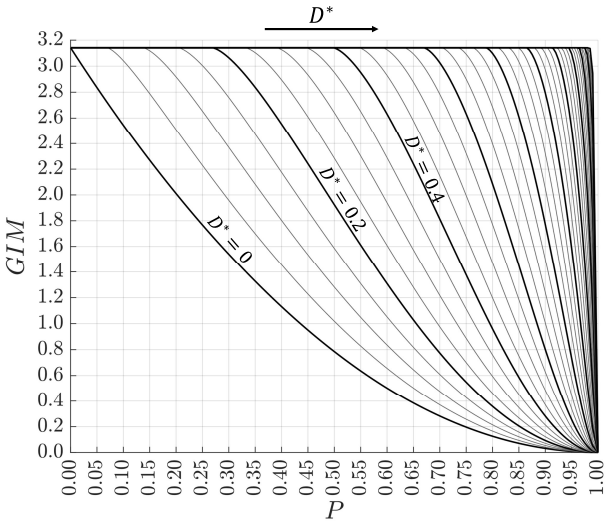

Figure 3.20: Illustration of the safe basin's size (GIM) in relation to parameters P (amplitude of forced response) and D^* (damping-frequency perturbance ratio). The thick curves denote the values $D^* = 0, 0.2, 0.4, \ldots, 2$. The erosion profiles (starting at P_{crit}) for a fixed $D^* > 0$ are often referred to as the 'Dover cliff' profiles. There are no safe basins for $P > 1$. Figure adapted from [225]

The indefinite integral of $R_C^2(\varphi)$ is

$$I_C(\varphi) := \int R_C^2(\varphi)\mathrm{d}\varphi = \frac{P^2}{2}\sin(2\varphi) + \varphi - P\sin\varphi\sqrt{1-(P\sin\varphi)^2} - \arcsin(P\sin\varphi). \tag{3.154}$$

The indefinite integral of $R_S^2(\varphi)$ is expressed as

$$I_S(\varphi) := \int R_S^2(\varphi)\mathrm{d}\varphi = \frac{(1-P)^2}{2D^*}e^{2D^*\varphi}. \tag{3.155}$$

Therefore, the safe basin's size is given by

$$GIM = \frac{I_C(\varphi_1) + I_S(\varphi_2) - I_S(\varphi_1) + 2\pi - I_C(\varphi_2)}{2}. \tag{3.156}$$

These computations also allow for a graphical representation of the safe basin area (GIM) versus D^* and P (see Fig. 3.20 and the right side of Fig. 3.21a). In particular, for nonzero damping, the safe basin size does not immediately decrease as the excitation amplitude, and hence P, increases.

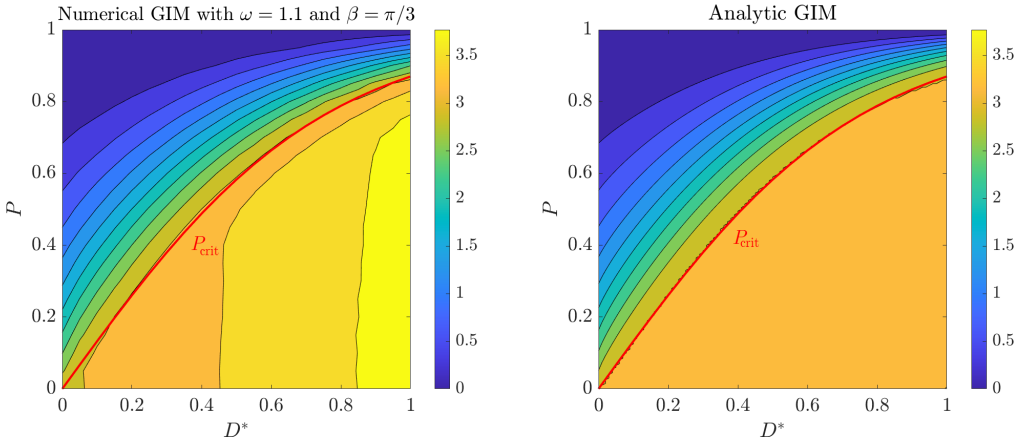

(a) Left: Numerically computed *GIM* values for $\omega = 1.1$ and $\beta = \pi/3$. Right: Analytically computed *GIM* values

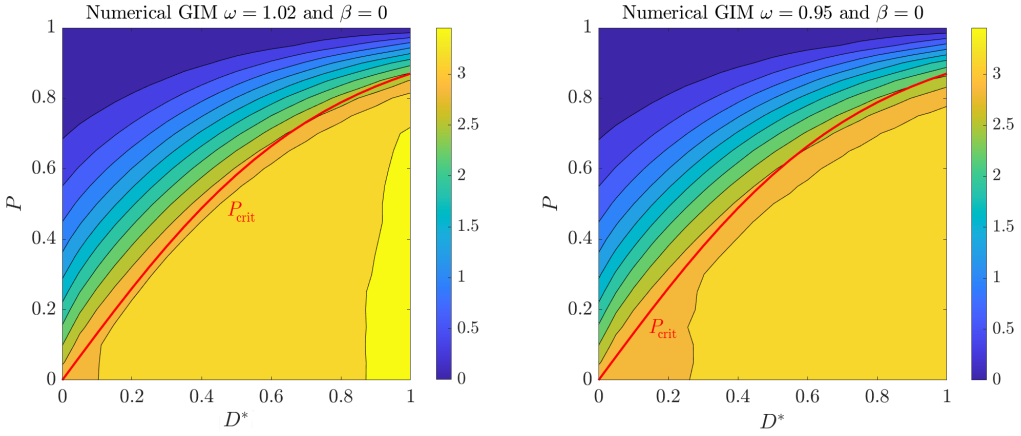

(b) Left: Numerically computed values of *GIM* for $\omega = 1.02$ and $\beta = 0$. Right: Numerically computed values for $\omega = 0.95$ and $\beta = 0$

Figure 3.21: The size of the safe region (*GIM*) is shown against the parameters D^* and P. The boundary indicating the critical level of forced vibration amplitude, represented as a red line (P_{crit}), is determined according to Eq. (3.157). It is apparent that for P values less than P_{crit}, the extent of the safe region expands in the numerically derived diagrams, a result attributed to the addition of damping (refer to Fig. 3.15a). When P is below P_{crit}, that is, below the red line, the impact of excitation on the magnitude of the safe region appears to be minimal upon direct numerical calculation, being predominantly affected by D^*. The growth of the stability region with respect to D^* is disregarded in the approximation of ∂S_F using the unit circle. Figures adapted from [225]

Below a critical amplitude for forced excitation P_{crit}, the safe basin is solely determined by the 'fast' mechanism as defined by Eq. (3.109). This critical P_{crit} aligns with the 'cliff' and can be approximated using Eq. (3.151) as

$$P < P_{\text{crit}} \approx \tanh\left(\frac{4}{3}D^*\right). \tag{3.157}$$

However, once the critical amplitude P_{crit} is exceeded, both mechanisms become essential for the level-crossing process. As P increases, the 'slow' level-crossing process increasingly dominates, and a larger portion of the safe basin boundary arc length is defined by ∂S_S.
In Fig. 3.20, we can observe the 'Dover cliff' erosion profiles (P increases at constant D^*) of safe basins. Such profiles were first documented in nonlinear damped escape problems with external harmonic excitation [200, 202]. In this scenario, since P is a linear function of the excitation amplitude f, the graph can classically be interpreted to show the size of safe basins against f, keeping D, ω, and β constant. There are two critical values of P: one in P_{crit}, where the 'fast' erosion of the safe basin begins, and another in $P = 1$, where the safe basin vanishes. The abrupt erosion at P_{crit} is often associated with the homoclinic tangency of the particle's orbit [199]; however, this study shows that sudden erosion of the safe region can also occur in linear systems. This erosion profile is not an inherent characteristic of nonlinearity but rather a consequence of the decay of the transient motion.
The study presented in this chapter provides reasonably accurate estimates of the safe basins' size and location in the classic example of a harmonically forced damped linear oscillator, serving as a benchmark for investigating nonlinear system effects.

3.2.5 Numerical Results and Model Validation

This section focuses on validating the analytical model against direct numerical results. In Fig. 3.21, the total area of the safe basin (GIM) is illustrated depending on the values of D^* and P. On the left of Fig. 3.21a, the numerically generated contour plot is shown for $\omega = 1.1$ and $\beta = \frac{\pi}{3}$. The red line represents the estimated parameter combination where the logarithmic spiral tangentially meets the unit circle. Despite a not-so-small value of $\varepsilon = 0.1 - 0.1056$, the analytic model shows a commendable accuracy. However, it should be noted that ε is not constant as it depends on D, thus affecting D^*. In Fig. 3.21b, the numerically calculated GIM is depicted for $\omega = 0.95$ and $\omega = 1.02$, both with $\beta = 0$. The correlation with the analytic prediction is slightly less precise here than for $\omega = 1.1$, but it is still fairly accurate. As D^* increases, the difference between the numerical and analytical results increases, mainly due to errors in positioning ∂S_S based on the maximum estimate of Eq. (3.124) by Eq. (3.127). An error magnitude

of 5-6% may occur and can significantly influence the spiral's growth rate. Applying Poincaré's small-parameter method might yield more accurate results for the maximum of Eq. (3.124). However, it would considerably complicate the equations, making further analytic continuation unfeasible.
Direct numerical simulations involve extensive calculations. The grids in Fig. 3.21a and Fig. 3.21b have only 21×21 nodes due to the computational intensity - each grid point's GIM requires 101×101 simulations on the initial condition plane, totaling 4 498 641 individual simulations.
To assess the reduction in computational cost in computing ∂S_S and ∂S_F versus the direct numerical integration of Eq. (3.98), simulations were performed using $F = \{0.05, 0.1, 0.15\}$, $\Omega = 1.1$, $D = 0.02$, and $\beta = \pi/2$. These utilized a 401×601 grid across initial conditions on $[-1, 1] \times [-1.5, 1.5]$. The results indicated a 200-350-fold decrease in computational cost using ∂S_S and ∂S_F compared to direct integration of Eq. (3.98).

3.2.6 Conclusions and scope for future research

This chapter described the stabilizing effect of viscous damping on the safe basins from a symmetrically truncated quadratic potential well under harmonic excitation, focusing on excitation frequencies near the system's natural frequency.
Two competing mechanisms, 'fast' and 'slow' level crossing, are identified as defining the safe basins. The 'fast' mechanism relates to the particle's initial energy and its sufficiency in driving the particle out of the potential well, which is particularly significant when the damping is considerable compared to the frequency difference between excitation and the potential well.
The 'slow' mechanism is akin to a beat phenomenon, becoming prominent when the decay of transient motion is slow, allowing for the accumulation of a large amplitude resonant oscillation.
A complicated interaction between these mechanisms affects the size of the safe basin. Up to a specific forced amplitude (P_{crit}), the 'fast' mechanism predominates, keeping the safe basin size nearly constant. Beyond P_{crit}, as the excitation increases, the 'slow' mechanism gains importance, leading to rapid safe basin erosion. At a force amplitude of 1, level crossing inevitably occurs for any initial condition, resulting in the disappearance of the safe basin.
Although the model studied is linear, the identification of these competing mechanisms also has implications for nonlinear systems. The typical 'Dover cliff' erosion profile, observed in many damped, nonlinear escape scenarios, is not inherently due to system nonlinearity, but rather, it results from the transient motion's decay and the interplay of the system's forced response.

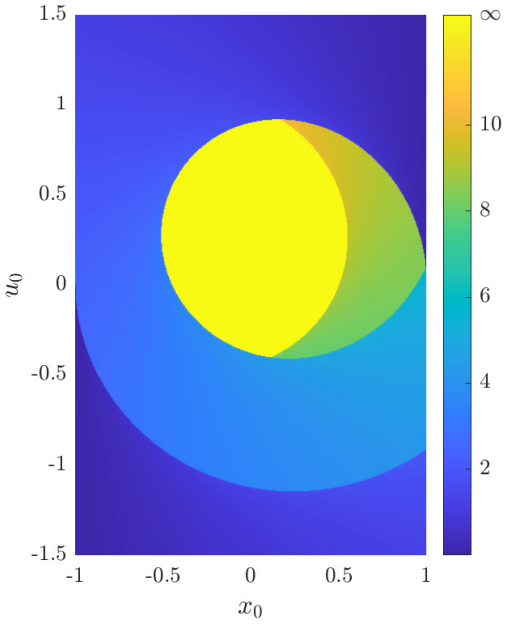

Figure 3.22: Numerically derived level-crossing time (color scale, ∞ indicating no crossing) and safe basin (yellow region) on the $x_0 - u_0$ initial condition plane for $D = 0.02$, $f = 0.4$, $\omega = 0.5$, and $\beta = 0$. Figure adapted from [225]

In strongly damped cases, the transient motion rapidly decays, preventing the beat-like vibration that causes the 'slow' mechanism. Therefore, the shape of the safe basin is mainly determined by the 'fast' mechanism, especially when the oscillation amplitude of the particular solution P is below one. For $P > 1$, the forced oscillation is strong enough to swing into the critical region, eliminating the safe basin.

When the frequency of excitation differs from the resonant frequency of the well, the 'slow' mechanism gradually becomes less important. As a result, the envelope's peaks become less prominent, leaving the 'fast' mechanism as the primary cause for level crossing. As shown in Fig. 3.22, with an excitation frequency ($\omega = 0.5$) significantly lower than the natural frequency, the 'slow' beat-based mechanism loses its prominence. The superposition of transient and steady-state motion does not yield apparent peaks in the envelope, rendering the 'fast' mechanism the primary cause for level crossing. Indeed, no level crossing occurs after the first excitation period, suggesting a limit set by the excitation time period.

For large differences between excitation and natural frequencies, the boundaries ∂S_F and ∂S_S, defined by Eqs. (3.109) and (3.128), are less accurate due to the assumption of small perturbance in the excitation frequency. However, the characteristics of the safe

basin resemble those identified by *Genda et al.* [224] (see Sect. 3.1) for the conservative case, for which analytical estimates exist.
Numerical results also indicate that the excitation's initial phase has a negligible effect on the safe basin's size but significantly influences its location (cf. Figs. 3.16 and 3.18). Consequently, the analytic model in Sect. 3.2.4 disregards the dependence on the initial phase β.
This study provides a semianalytic formula to calculate the safe basin area based on the system's parameters, as shown in Fig. 3.20. These insights are valuable for designing physical systems with dynamics similar to those studied here. For example, in applications where extended safe basins are desired to mitigate oscillations under noisy excitation, it is beneficial to maintain $P < P_{\text{crit}}$. Additionally, in preventing the failure of brittle materials under harmonic load, it is crucial to ensure that initial conditions do not significantly compromise the system's integrity.
This chapter has explored the stabilizing effect of viscous damping on safe basins from a symmetrically truncated quadratic potential well under harmonic excitation near the system's natural frequency. The identified 'fast' and 'slow' level-crossing mechanisms have significant implications for linear systems and potentially for nonlinear ones. The observed 'Dover cliff' erosion profile in safe basins, often attributed to nonlinearities, results from the interplay between decaying motion due to initial conditions and the system's forced response.
Future research could investigate whether safe basins can be accurately estimated analytically in systems with small, polynomial-type nonlinearities or non-standard features like Coulomb friction or constant restoring force [229]. Another interesting question is whether damping always stabilizes escape and level-crossing, including in scenarios with nonlinear damping.
Finally, understanding the safe basins' shapes and escape probabilities in noisy dynamics holds practical significance. Although noise might lead to a nonzero escape probability for any initial condition, there is a possibility of defining proper safe basins with zero escape probability, especially when the noise amplitude is bounded.
This work aims to improve the understanding of escape or level-crossing mechanisms, contributing to the safer design of devices and systems.

4 Critical forcing of escape

As reported in Chapter 1, investigating the critical forcing amplitude necessary to cause particle escape has significant literature. As the distinction between escape and level crossing is not sharp, most results apply equally to the latter case.
In this section, we focus solely on systems initially at rest, that is, with homogeneous initial conditions. At time $t = 0$, the harmonic excitation of the form $F\sin(\Omega t + \beta)$ is activated, and the particle begins to move. Throughout this chapter, the primary focus is on analyzing the main resonance.
First, in Sect. 4.1, we review the undamped and linearly damped driven harmonic oscillator. In Sect. 4.2, a general analytic scheme is presented to analyze systems with weak nonlinearities, and an example is given for the level crossing problem with quadratic-quartic nonlinearity. In Sect. 4.3, a Melnikov analysis proves that in sufficiently smooth, undamped systems, oscillations approaching the potential well boundary become chaotic, and it provides an explanation of why parts of the critical force boundary become so uneven in such systems. In Sect. 4.4, an experimental validation of the different escape mechanisms is presented.

4.1 Linear oscillators

4.1.1 Harmonically driven, undamped harmonic oscillator

We investigate the level-crossing problem of the following system

$$\ddot{x} + x = F\sin(\Omega t + \beta), \tag{4.1}$$
$$x(0) = 0, \tag{4.2}$$
$$\dot{x}(0) = 0. \tag{4.3}$$

The motion fulfilling Eq. (4.1) is given by

$$x(t) = R\sin(t + \alpha) + P\sin(\Omega t + \beta), \tag{4.4}$$

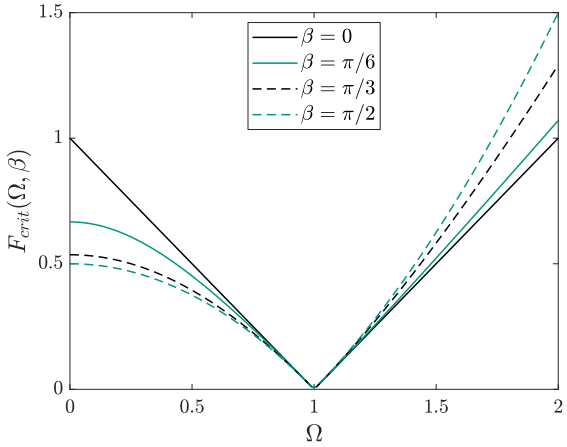

Figure 4.1: Excitation and initial phase dependent critical forcing amplitude of the undamped, harmonic oscillator

with

$$P = \frac{F}{1-\Omega^2}, \tag{4.5}$$

$$R = |P|\sqrt{1+(\omega^2-1)\cos^2\beta}, \tag{4.6}$$

$$\alpha = \operatorname{atan2}(-P\sin\beta, -P\Omega\cos\beta) = \begin{cases} \arctan\left(\frac{\tan\beta}{\Omega}\right) & \text{for } \Omega < 1, \\ \arctan\left(\frac{\tan\beta}{\Omega}\right) + \pi & \text{for } \Omega > 1. \end{cases} \tag{4.7}$$

The critical level is at $x_{\text{crit}} = \pm 1$, thus the force necessary to reach it is given by

$$F_{\text{crit}} = \frac{|1-\Omega^2|}{\max_{t\in[0,\infty)} \sqrt{1+(\Omega^2-1)\cos^2\beta}\sin(t+\alpha)+\sin(\Omega t+\beta)}, \tag{4.8}$$

where the optimization problem has to be solved to obtain the exact value, which is a challenging task for general Ω. However, for $\Omega \in \mathbb{I}$, similar arguments as in Sect. 2.4 guarantee that the supremum of the function in the denominator is given by

$$\sup_{t\in[0,\infty)} \sqrt{1+(\Omega^2-1)\cos^2\beta}\sin(t+\alpha)+\sin(\Omega t+\beta) = \sqrt{1+(\Omega^2-1)\cos^2\beta}+1, \tag{4.9}$$

yielding the critical force amplitude

$$F_{\text{crit}}(\Omega, \beta) = \frac{|1 - \Omega^2|}{\sqrt{1 + (\Omega^2 - 1)\cos^2 \beta} + 1}, \tag{4.10}$$

which formula was also found by *Karmi* in [89]. Eq. (4.10) is visualized in Fig. 4.1.

4.1.2 Damped-driven harmonic oscillator

An extension of the previous model is achieved by adding linear damping to the system. The equation of motion becomes

$$\ddot{x} + 2D\dot{x} + x = F \sin(\Omega t + \beta), \tag{4.11}$$
$$x(0) = 0, \tag{4.12}$$
$$\dot{x}(0) = 0. \tag{4.13}$$

The solution is

$$x(t) = Re^{-Dt} \sin(\Omega_0 t + \alpha) + P \sin(\Omega t + \beta + \gamma), \tag{4.14}$$

with

$$\Omega_0 = \sqrt{1 - D^2}, \tag{4.15}$$
$$\varepsilon = \Omega - \Omega_0, \tag{4.16}$$
$$P = \frac{F}{\sqrt{(1 - \Omega^2)^2 + 4D^2\Omega^2}}, \tag{4.17}$$
$$\gamma = \operatorname{atan2}(-2D\Omega, 1 - \Omega^2) = \begin{cases} \arctan \frac{2D\Omega}{\Omega^2 - 1} & \text{for } \Omega < 1, \\ \arctan \frac{2D\Omega}{\Omega^2 - 1} + \pi & \text{for } \Omega > 1, \end{cases} \tag{4.18}$$
$$R = PK, \tag{4.19}$$
$$K = \sqrt{\frac{1 + (\Omega^2 - 1)\cos^2(\beta + \gamma) + D\Omega \sin(2\beta + 2\gamma)}{1 - D^2}}, \tag{4.20}$$
$$\alpha = \operatorname{atan2}(-\Omega_0 \sin(\beta + \gamma), -D \sin(\beta + \gamma) - \Omega \cos(\beta + \gamma)). \tag{4.21}$$

The critical level is at $x_{\text{crit}} = \pm 1$, thus the critical force is defined by

$$F_{\text{crit}} = \frac{\sqrt{(1 - \Omega^2)^2 + 4D^2\Omega^2}}{\max_{t \in [0,\infty)] } Ke^{-Dt} \sin(\Omega_0 t + \alpha) + \sin(\Omega t + \beta + \gamma)}. \tag{4.22}$$

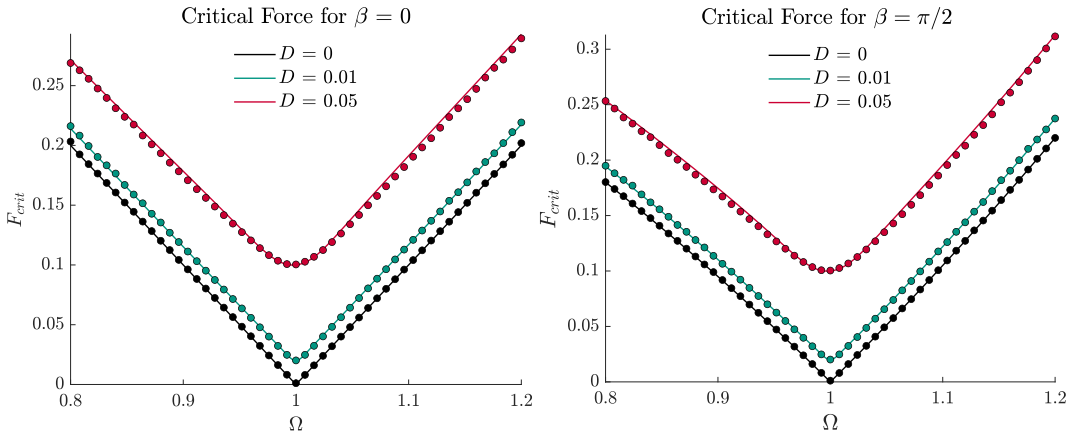

(a) $\beta = 0$ **(b)** $\beta = \frac{\pi}{2}$

Figure 4.2: Frequency-dependent critical forcing amplitude for various damping and initial phase values. The solid lines represent the analytic estimates, while the markers represent the critical force values obtained from the direct numerical simulations of Eq. (4.11)

Eq. (4.22) contains an optimization problem that is impossible to solve analytically. We must make some assumptions and simplify the equations to gain further analytic insight into the process. In the following, we assume that the frequency shift ε is small. In this case, the solution is a beat-like motion (cf. Fig. 3.14). We focus on the envelope of the solution, which we can estimate using the total energy. After neglecting the terms of $O(\varepsilon)$, we have the squared amplitude

$$A^2(t) = 2E = P^2\left(K^2 e^{-2Dt} + 1 + 2Ke^{-2Dt}\cos(\varepsilon t - \alpha + \beta + \gamma)\right). \tag{4.23}$$

The criterion of level crossing becomes $A^2_{\text{crit}} = 1$. Due to homogeneous initial conditions $A^2(0) = 0$. For $t \to \infty$ we have $A^2(t \to \infty) = P^2$. The cosine term causes oscillations such that $A^2(t)$ has infinitely many local maxima. However, the global maximum is the first local maximum, closest to time 0. We cannot find its location exactly, but we can approximate it by replacing the cosine term with 1. Thus, we have

$$A^2_{\max} = P^2\left(Ke^{-Dt_{\max}} + 1\right)^2, \tag{4.24}$$

$$t_{\max} = \mod\left(\frac{\alpha - \beta - \gamma}{\varepsilon}, \frac{2\pi}{|\varepsilon|}\right). \tag{4.25}$$

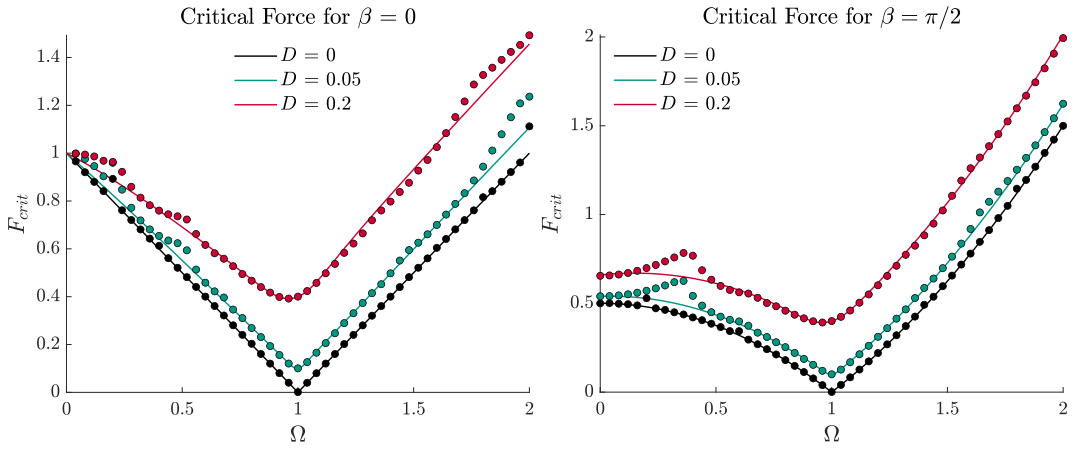

(a) $\beta = 0$ **(b)** $\beta = \frac{\pi}{2}$

Figure 4.3: Frequency-dependent critical forcing amplitude for various damping and initial phase values with $(\Omega - \Omega_0) \notin O(\varepsilon)$ and nonsmall damping values. The solid lines represent the analytic estimates, while the markers represent the critical force values obtained from the direct numerical simulations of Eq. (4.11)

The estimate of the critical force is given as

$$F_{\text{crit}} = \frac{\sqrt{(1-\Omega^2)^2 + 4D^2\Omega^2}}{Ke^{-Dt_{\max}} + 1} \tag{4.26}$$

Fig. 4.2 shows the comparison of Eq. (4.26) to direct numerical simulations of Eq. (4.11) for various initial phase and damping values. The analytic estimate agrees well with the numerically obtained results. We can observe that additional damping shifts the minimum of the critical force upwards and makes its sharp minimum smooth.
We can also observe that the effect of the initial phase vanishes around $\Omega = 1$, but it is not negligible for greater and lower values of Ω.
In Fig. 4.3, the analytic estimate is compared to numerical simulations where the assumption of small frequency deviation and small damping is no longer met. Surprisingly, Eq. (4.26) still works well for the right-hand side of the curve. However, on the left-hand side, an interesting phenomenon around $\Omega = 1/3$ can be observed in the case $\beta = \pi/2$, resulting in a bulk on the critical force curve. In the case of $D = 0$, we can observe interesting patterns for both investigated values of β. The excitation frequency values used for the numerical simulations are rational numbers. Sometimes they are the ratio of small integers (e.g., 0.2, 0.4, 2), which results in significantly higher critical force values than they would for any irrational number from their infinitesimal vicinity. To describe these values, the methods presented in Sect. 2.4 could yield more exact estimates.

Furthermore, we can observe that for large frequency deviations, the role of the initial phase becomes significant.

4.2 Critical forcing of harmonically driven conservative systems with small nonlinearity

In the previous sections, we have seen the influence of excitation frequency on the critical force amplitude necessary to drive the particle to a critical level.
Interest may arise in analyzing the level-crossing behavior of nonlinear systems when the excitation frequency approximates the natural frequency set by the potential well.
The following chapter is based on [221, 68].
We assume a weakly nonlinear system of the form

$$\ddot{x} + \underbrace{x + \varepsilon N(x)}_{=:U_0'(x)} = \underbrace{\varepsilon F \sin(\Omega\tau + \beta)}_{=:F(\tau)}, \tag{4.27}$$

where $\Omega - 1 \in O(\varepsilon)$ and $N(x)$ is an odd function. Without loss of generality, the potential energy at the bottom of the potential well $U_0(0) = 0$ can be chosen; thus,

$$U_0(x) = \frac{1}{2}x^2 + \varepsilon \underbrace{\int_0^x N(\tilde{x})\mathrm{d}\tilde{x}}_{=:U_N(x)}. \tag{4.28}$$

The critical energy level in which we are interested, E_{crit}, can be set to $1/2$, corresponding to an amplitude close to one.

$$A_{\mathrm{crit}} = \left(U_0'\right)^{-1}\left(E_{\mathrm{crit}} = \frac{1}{2}\right). \tag{4.29}$$

The system in Eq. (4.27) is close to a conservative one. The unperturbed form of this equation allows for the transition to variables that represent the total energy and phase of the system.

$$E = \frac{1}{2}\dot{x}^2 + U_0(x), \tag{4.30}$$

$$\theta = \int_0^x \frac{\mathrm{d}\gamma}{\pm\sqrt{2E - 2U_0(\gamma)}} - \tau. \tag{4.31}$$

The selection of the sign in the preceding equation depends on the sign of $\dot{x}$.

The differential equations governing the new variables in the perturbed framework evolve slowly:

$$\dot{E} = \pm\varepsilon\sqrt{2E - 2U_0(x)}F(\tau), \tag{4.32}$$

$$\dot{\theta} = -\varepsilon F(\tau)\int_0^x \frac{\mathrm{d}\gamma}{2E - 2U_0(\gamma)}. \tag{4.33}$$

Averaging of these equations over a period of the excitation is possible. The corresponding first-order approximate equations can be expressed as:

$$\dot{E} = \pm\varepsilon\left\langle\sqrt{2E - 2U_0F(\tau)}\right\rangle, \tag{4.34}$$

$$\dot{\theta} = -\varepsilon\left\langle F(\tau)\int_0^x \frac{\mathrm{d}\gamma}{2E - 2U_0(\gamma)}\right\rangle, \tag{4.35}$$

with $\langle\cdot\rangle$ indicating averaging over explicit time. However, to utilize these equations, $U_0(x)$ needs explicit representation in terms of the new variables (E, θ). Typically, this cannot be achieved directly, so an approximate heuristic method is used for analytic predictions.
Assume that the solution to Eq. (4.27) may be approximated by nearly harmonic oscillations:

$$x = A(t)\sin(\Omega\tau + \beta + \Psi(t)), \tag{4.36}$$

$$\dot{x} = v(A(t))\cos(\Omega\tau + \beta + \Psi(t)). \tag{4.37}$$

Here, $A(t)$ represents the amplitude of oscillation and $\Psi(t)$ the phase shift. These variables are linked to the system's energy, which changes gradually according to Eqs. (4.32)-(4.33). Utilizing the transformation (4.30)-(4.31), we can equate the total energy with the potential energy at maximum displacement, i.e., at $x = A$:

$$E = U_0(A). \tag{4.38}$$

Thus, the time derivative of the energy can be estimated to the first order by the derivative of the amplitude:

$$\dot{E} = U_0'(A)\dot{A}. \tag{4.39}$$

However, the maximum velocity occurs as the system reaches the energy minimum of the potential. Therefore, the amplitude of the velocity can be estimated as:

$$v(A) = \sqrt{2U_0(A)} = \sqrt{A^2 + 2\varepsilon U_N(x)} \approx A + \varepsilon\frac{U_N(A)}{A}. \tag{4.40}$$

Integrating Eqs. (4.39) and (4.40) into (4.34), we obtain the governing equation for the averaged amplitude $\xi = \langle A \rangle$ as:

$$\dot{\xi} = \varepsilon \frac{\sqrt{2U_0(\xi)}}{U_0'(\xi)} \langle F(\tau)\cos(\Omega\tau + \beta + \Psi(t))\rangle \,. \tag{4.41}$$

For consistency with the transformations (4.36) and (4.37), we derive the equation for the phase shift:

$$\begin{aligned} A(\Omega + \dot{\Psi}) = A\cos^2(\Omega\tau + \beta + \Psi(t)) \\ + U_0'(A\sin(\Omega\tau + \beta + \Psi(t)))\sin(\Omega\tau + \beta + \Psi(t)) \\ - \varepsilon F(\tau)\sin(\Omega\tau + \beta\Psi(t)). \end{aligned} \tag{4.42}$$

Introducing the small discrepancy between the excitation frequency and the system's eigenfrequency at the potential well's bottom:

$$\delta = \Omega - 1 = O(\varepsilon), \tag{4.43}$$

Eq. (4.42) simplifies to:

$$\begin{aligned} A\dot{\Psi} = -\delta A - A\sin^2(\Omega\tau + \beta + \Psi(t)) \\ + U_0'(A\sin(\Omega\tau + \beta + \Psi(t)))\sin(\Omega\tau + \beta\Psi(t)) \\ - \varepsilon F(\tau)\sin(\Omega\tau + \beta + \Psi(t)). \end{aligned} \tag{4.44}$$

Moreover, due to $U_0'(y)|_{y\to 0} = y$, combining the second and third terms of the right-hand side is possible:

$$\begin{aligned} A\dot{\Psi} = -\delta A + \varepsilon N(A\sin(\Omega\tau + \beta + \Psi(t)))\sin(\Omega\tau + \beta + \Psi(t)) \\ - \varepsilon F(\tau)\sin(\Omega\tau + \beta\Psi(t)), \\ \varepsilon N(x) = U_0'(x) - x. \end{aligned} \tag{4.45}$$

Division by A yields

$$\begin{aligned} \dot{\Psi} = -\delta + \frac{1}{A}\varepsilon N(A\sin(\Omega\tau + \beta + \Psi(t)))\sin(\Omega\tau + \beta + \Psi(t)) \\ - \frac{1}{A}\varepsilon F(\tau)\sin(\Omega\tau + \beta + \Psi(t)). \end{aligned} \tag{4.46}$$

Now, we can average Eq. (4.46). The second term on the right-hand side might be difficult to evaluate. However, a simple meaning to this expression can be given: it is

the deviation of the amplitude-dependent angular eigenfrequency of the nonlinear free oscillations from the linearized system's eigenfrequency, one. We can define:

$$\omega^*(A) := \omega(A) - 1, \tag{4.47}$$

and write the averaged phase shift $\psi = \langle \Psi \rangle$ as

$$\dot{\psi} = -\delta + \omega^*(\xi) - \frac{\varepsilon}{A} \langle F(\tau) \sin(\Omega\tau + \beta + \psi(t)) \rangle . \tag{4.48}$$

According to [103], the oscillation period of a particle of mass m with a specific total energy E in a potential well $U(x)$ in the absence of excitation, representing a conservative system can be determined by the following.

$$T(E) = \sqrt{2m} \int_{x_1(E)}^{x_2(E)} \frac{\mathrm{d}x}{\sqrt{E - U(x)}}. \tag{4.49}$$

Here, x_1 and x_2 denote the positions corresponding to the maximal displacements in the potential for the specified total energy E. Then,

$$\omega(\xi) = \frac{2\pi}{T(E(\xi))}. \tag{4.50}$$

The term $\omega^*(\xi)$ describes how nonlinearity influences the oscillation frequency within the potential well. With small nonlinearity, $\omega^*(\xi) \in O(\varepsilon)$ holds.
The effects of the averaged external excitation are quantified as follows:

$$\langle F(\tau) \cos(\Omega\tau + \beta + \Psi(t)) \rangle = -\frac{\varepsilon}{2} F \sin(\psi), \tag{4.51}$$

$$\langle F(\tau) \sin(\Omega\tau + \beta + \Psi(t)) \rangle = \frac{\varepsilon}{2} F \cos(\psi). \tag{4.52}$$

By incorporating (4.51) into Eqs. (4.41) and (4.48), we derive the final expressions for the first-order approximations:

$$\dot{\xi} = -\frac{\varepsilon}{2} \frac{\sqrt{2U_0(\xi)}}{U_0'(\xi)} F \sin(\psi), \tag{4.53}$$

$$\dot{\psi} = -\delta + \omega^*(\xi) - \frac{\varepsilon}{2} \frac{F}{\xi} \cos(\psi), \tag{4.54}$$

with the initial conditions

$$\xi(0) = \xi_0, \quad \psi(0) = \psi_0. \tag{4.55}$$

The initial values of x_0 and $\dot{x}_0$ can be used to determine ψ_0 and ξ_0. From Eqs. (4.36)-(4.37) we have

$$x_0 = \xi_0 \sin(\beta + \psi_0), \tag{4.56}$$
$$v_0 = v(\xi_0) \cos(\beta + \psi_0). \tag{4.57}$$

By Eq. (4.40), we can approximate $v(\xi) \approx \xi$ and obtain estimates for the initial values of the 'slow' variables as

$$\xi_0 = \sqrt{x_0^2 + v_0^2}, \tag{4.58}$$
$$\psi_0 = \arctan\left(\frac{x_0}{v_0}\right) - \beta. \tag{4.59}$$

Although the transformation is exact only under purely quadratic potential conditions, it remains a close approximation for minor nonlinearities, and if necessary, it can be improved with a perturbation method of the form

$$\xi_0 = \xi_{0,0} + \varepsilon\xi_{0,1} + \dots \tag{4.60}$$
$$\psi_0 = \psi_{0,0} + \varepsilon\psi_{0,1} + \dots \tag{4.61}$$

However, we do not go into detail about this calculation.

4.2.1 Solution by integrating factors

A solution to Eqs. (4.53)-(4.54) can be constructed using integrating factors. First, we define:

$$g(\xi) := \frac{v(\xi)}{U'(\xi)} = \frac{\sqrt{2U(\xi)}}{U'(\xi)} \approx 1 + \varepsilon\left(\frac{U_N(\xi)}{\xi^2} - \frac{N(\xi)}{\xi}\right). \tag{4.62}$$

After dividing Eq. (4.54) by Eq. (4.53) and reordering the terms, the equation becomes:

$$\underbrace{\delta - \omega^*(\xi) + \varepsilon\frac{F}{2\xi}\cos\psi}_{=:p(\xi,\psi)} - \underbrace{\varepsilon\frac{F}{2}\sin\psi g(\xi)}_{=:q(\xi,\psi)}\frac{\mathrm{d}\psi}{\mathrm{d}\xi} = 0. \tag{4.63}$$

An appropriate integrating factor $\mu(\xi)$ is defined as $\mu(\xi) := e^{\int f(\xi)\mathrm{d}\xi}$ with:

$$f(\xi) := \frac{1}{q}\left(\frac{\partial p}{\partial\psi} - \frac{\partial q}{\partial\xi}\right) = \frac{1}{g(\xi)}\left(\frac{1}{\xi} - g'(\xi)\right). \tag{4.64}$$

Thus,

$$\mu(\xi) = \frac{e^{\int \frac{1}{g(\xi)\xi} \mathrm{d}\xi}}{g(\xi)}. \tag{4.65}$$

Multiplying (4.63) by $\mu(\xi)$, we determine the partial derivatives for the first integral $C(\xi, \psi)$:

$$\begin{aligned} \frac{\partial C(\xi,\psi)}{\partial \xi} &= \left(\delta - \omega^*(\xi) + \varepsilon \frac{F}{2\xi} \cos\psi\right) \mu(\xi), \\ \frac{\partial C(\xi,\psi)}{\partial \psi} &= -\varepsilon \frac{F}{2} g(\xi)\mu(\xi) \sin\psi. \end{aligned} \tag{4.66}$$

The first integral is then expressed as:

$$C(\xi,\psi) = \varepsilon \frac{F}{2} e^{\int \frac{1}{g(\xi)\xi} \mathrm{d}\xi} \cos\psi + \int \left(\delta - \omega^*(\xi)\right) \frac{e^{\int \frac{1}{g(\xi)\xi} \mathrm{d}\xi}}{g(\xi)} \mathrm{d}\xi. \tag{4.67}$$

Eq. (4.67) is a conservation law of the system. The value of C remains constant along the solution trajectories. For the critical energy level $E_{\text{crit}} = 1/2$ the corresponding critical amplitude ξ_{crit} reached at the maximum of the critical trajectory can be calculated, allowing the definition of C_{crit}. The values of ψ for which ξ is maximal can be found by dividing Eq. (4.53) by Eq. (4.54) and equating it to zero since ξ being continuous can have a maximum when its derivative vanishes, resulting in $\psi_{\text{crit}} = \{0, \pi\}$ as possible values where an extremum may occur. As we shall see later, it is essential at which value of ψ, the maximum of ξ, is taken.
When the integrals are evaluated, their values are known up to an arbitrary constant. This problem can be solved by fixing the scale, for example, setting $C(0, \psi) = 0$. When $\xi = 0$, the value ψ is indifferent.
After inserting ξ_{crit} and ψ_{crit} into Eq. (4.67), the critical value C_{crit} can be calculated and compared to those obtained by $C_0(\xi_0, \psi_0)$.
In the following, an example with nonlinearity

$$N(x) = -x^3 \tag{4.68}$$

shall be given to demonstrate the application of the method described above.

4.2.2 Example with quadratic-quartic potential

The equation of motion is given as

$$\ddot{x} + x - \varepsilon x^3 = \varepsilon F \sin(\Omega\tau + \beta). \tag{4.69}$$

Therefore, we have

$$U_0(x) = \frac{1}{2}x^2 - \varepsilon \underbrace{\frac{x^4}{4}}_{=:U_N(x)} \tag{4.70}$$

and

$$v(A) = \sqrt{A^2 + \varepsilon\frac{A^4}{2}} \approx A + \varepsilon\frac{A^3}{4}. \tag{4.71}$$

The critical displacement is given by

$$U_0(\xi_{\text{crit}}) = \frac{1}{2} \tag{4.72}$$

$$\xi_{\text{crit},1,2} = \pm\sqrt{\frac{1-\sqrt{1-2\varepsilon}}{\varepsilon}} = \pm\left(1 + \frac{1}{4}\varepsilon + O(\varepsilon^2)\right) \tag{4.73}$$

The deviation of the eigenfrequency from one, caused by the nonlinearity, is given as

$$\omega^*(\xi) = -\frac{\varepsilon}{A}\left\langle A^3 \sin^3(\Omega\tau + \beta + \Psi(t)) \sin(\Omega\tau + \beta + \Psi(t))\right\rangle + O(\varepsilon^2) \tag{4.74}$$

$$= -\varepsilon\frac{3}{8}\xi^2 + O(\varepsilon^2). \tag{4.75}$$

Thus, the first-order differential equations of the slow variables are

$$\dot{\xi} = -\frac{\varepsilon}{2}\frac{A + \varepsilon\frac{A^3}{4}}{A - \varepsilon A^3}F\sin(\psi) = -\frac{\varepsilon}{2}F\sin(\psi) + O(\varepsilon^2) \tag{4.76}$$

$$\dot{\psi} = -\delta - \varepsilon\frac{3}{8}\xi^2 - \frac{\varepsilon}{2}\frac{F}{\xi}\cos(\psi), \tag{4.77}$$

Division of Eq. (4.76) by Eq. (4.77) eliminates the time and yields

$$\frac{\mathrm{d}\xi}{\mathrm{d}\psi} = \frac{F\sin(\psi)}{2\Delta + \frac{3}{4}\xi^2 + \frac{F}{\xi}\cos(\psi)}, \tag{4.78}$$

with $\Delta := \delta/\varepsilon$. We can reorganize Eq. (4.78) as

$$\left(2\Delta + \frac{3}{4}\xi^2 + \frac{F}{\xi}\cos(\psi)\right)\mathrm{d}\xi - F\sin(\psi)\mathrm{d}\psi = 0 \tag{4.79}$$

Eq. (4.79) is not exact since

$$\frac{\partial p}{\partial \psi} - \frac{\partial q}{\partial \xi} \neq 0, \tag{4.80}$$

however, by Eq. (4.65) an appropriate Euler multiplicator is given leading to

$$\left(2\Delta\xi + \frac{3}{4}\xi^3 + F\cos(\psi)\right)\mathrm{d}\xi - \xi F\sin(\psi)\mathrm{d}\psi = 0. \tag{4.81}$$

The first integral becomes

$$C(\psi,\xi) = \xi F\cos(\psi) + \Delta\xi^2 + \frac{3}{16}\xi^4. \tag{4.82}$$

Stationary solutions of Eqs. (4.76)-(4.77) can be found by setting the left-hand side equal to zero and solving the resulting nonlinear algebraic equations. This yields

$$\tilde{\psi}_1 = 0, \tag{4.83}$$
$$\tilde{\psi}_2 = \pi, \tag{4.84}$$

for the stationary value of the phase shift. Then, from Eq. (4.77), we have

$$p(\xi) := \frac{3}{4}\xi^3 + 2\Delta\xi \pm F = 0, \tag{4.85}$$

with three solutions, respectively

$$\tilde{\xi}_{1/2,1} = \frac{\left(2^{\frac{1}{3}}\left(\sqrt{128\Delta^3 + 81F^2} \mp 9F\right)^{\frac{2}{3}} - 4\cdot 2^{\frac{2}{3}}\Delta\right)}{3\left(\sqrt{128\Delta^3 + 81F^2} \mp 9F\right)^{\frac{1}{3}}}, \tag{4.86}$$

$$\tilde{\xi}_{1/2,2} = \frac{4\cdot 2^{\frac{2}{3}}(1+\sqrt{3}\jmath)\Delta + 2^{\frac{1}{3}}\jmath(\sqrt{3}+\jmath)\left(\sqrt{128\Delta^3 + 81F^2} \mp 9F\right)^{\frac{2}{3}}}{6\left(\sqrt{128\Delta^3 + 81F^2} \mp 9F\right)^{\frac{1}{3}}}, \tag{4.87}$$

$$\tilde{\xi}_{1/2,3} = \frac{4 \cdot 2^{\frac{2}{3}}(1 - \sqrt{3}\jmath)\Delta + 2^{\frac{1}{3}}(-1 - \sqrt{3}\jmath)\left(\sqrt{128\Delta^3 + 81F^2} \mp 9F\right)^{\frac{2}{3}}}{6\left(\sqrt{128\Delta^3 + 81F^2} \mp 9F\right)^{\frac{1}{3}}}. \tag{4.88}$$

Whether there are one real and two imaginary roots or three real roots depends on the sign of the discriminant of the polynomial in Eq. (4.85), which independently of the signs of F is given by

$$\mathrm{Discr}(p) = -24\Delta^3 - \frac{243}{16}F^2. \tag{4.89}$$

Three real roots exist if the discriminant is positive. It is the case for

$$F < -\frac{8\sqrt{2}}{9}|\Delta|^{3/2}\,\mathrm{sign}(\Delta). \tag{4.90}$$

Eq. (4.90) implies that three real roots are possible only for $\Delta < 0$. Furthermore, for $\tilde{\psi}_1 = 0$, one of the roots, while for $\tilde{\psi}_2 = \pi$, two are always negative and thus unphysical. Furthermore, for $\tilde{\psi}_1 = 0$, there is always a negative root, while for $\tilde{\psi}_2 = \pi$, there is always a positive root.
In summary, if the discriminant in Eq. (4.90) is positive, there are two stationary solutions $\tilde{\xi}_{1,1}$ (saddle) and $\tilde{\xi}_{1,3}$ (center) in $\tilde{\psi}_1 = 0$ and one stationary solution $\tilde{\xi}_{2,1}$ (center) in $\tilde{\psi}_2 = \pi$.
If the discriminant is negative, there is only one stationary solution in $(\pi, \tilde{\xi}_{2,1})$.
The critical forcing amplitude is calculated for homogeneous initial conditions, which case does not distinguish itself by any qualitative difference but by its technical relevance. The resulting trajectory is called the limiting phase trajectory (LPT, [132, 133]).
As we shall see, at the critical force value, three different mechanisms can be distinguished based on the phase shift's value ψ at the moment of escape:

- the Type 1 Maximum Mechanism if escape occurs at $\psi = \pi$,
- the Type 2 Maximum Mechanism if escape occurs at $\psi = 0$,
- the Saddle Mechanism for values $\psi \in (0, \pi)$.

In [68], describing the same example as above, the Type 1 Maximum Mechanism and the Saddle Mechanism are described correctly, although the Type 2 Maximum Mechanism is not mentioned. Later, in [57], the Type 2 Maximum Mechanism was correctly identified for another dynamical system.
The Type 1 and 2 Maximum Mechanisms are explained simply: the smallest F value is sought, such that the largest value of ξ in Eq. (4.82) reaches ξ_{crit}, the critical level.

Since at the maximum of the amplitude, ξ is continuous in ψ, for the critical forcing value, the curve defined by $C(\psi, \xi)$ is tangential to the line $\xi = \xi_{\text{crit}}$. It is only possible at $\psi = \pi$ (MM Type 1) or at $\psi = 0$ (MM Type 2), yielding the two equations for the critical force

$$C(\pi, \xi_{\text{crit}}) = \xi_{\text{crit}} F_{\text{crit,MM1}} \cos(\pi) + \Delta \xi_{\text{crit}}^2 + \frac{3}{16} \xi_{\text{crit}}^4 = 0, \tag{4.91}$$

$$F_{\text{crit,MM1}}(\Delta) = \Delta \xi_{\text{crit}} + \frac{3}{16} \xi_{\text{crit}}^3, \tag{4.92}$$

and

$$C(0, \xi_{\text{crit}}) = \xi_{\text{crit}} F_{\text{crit,MM2}} \cos(0) + \Delta \xi_{\text{crit}}^2 + \frac{3}{16} \xi_{\text{crit}}^4 = 0, \tag{4.93}$$

$$F_{\text{crit,MM2}}(\Delta) = -\Delta \xi_{\text{crit}} - \frac{3}{16} \xi_{\text{crit}}^3. \tag{4.94}$$

The two curves meet at $F = 0$ and $\Delta_{\text{MM}} := -\frac{3}{16} \xi_{\text{crit}}^2$. Although both Eqs. (4.92) and (4.94) are defined for all real Δ values, we expect the force to be positive, thus

$$F_{\text{crit,MM}}(\Delta) = \begin{cases} \Delta \xi_{\text{crit}} + \frac{3}{16} \xi_{\text{crit}}^3 & \text{for } \Delta < \Delta_{\text{MM}} \\ -\Delta \xi_{\text{crit}} - \frac{3}{16} \xi_{\text{crit}}^3 & \text{for } \Delta_{\text{MM}} < \Delta. \end{cases} \tag{4.95}$$

However, Eq. (4.95) does not describe the entire critical forcing amplitude curve correctly since the planar curve defined by the implicit function $C(\psi, \xi) = 0$ is not connected for some Δ values. If $C_{\text{saddle}} < 0$, the level set $C(\psi, \xi)$ below the saddle and above the saddle is disjoint. Along the critical values defined by Eq. (4.95), the trajectories are still tangential, but the LPT corresponds only to the level set below the saddle. The saddle energy must fulfill $C_{\text{saddle}} \geq 0$ for an escape. In the critical case, equality holds.
The location of the saddle is defined by Eq. (4.85). Thus, the following two nonlinear equations have to be fulfilled

$$\frac{3}{4} \xi_{\text{saddle}}^3 + 2\Delta \xi_{\text{saddle}} + F_{\text{crit,SM}} = 0 \tag{4.96}$$

$$\frac{3}{16} \xi_{\text{saddle}}^4 + \Delta \xi_{\text{saddle}}^2 + \xi_{\text{saddle}} F_{\text{crit,SM}} = 0. \tag{4.97}$$

Eqs. (4.96)-(4.97) have the solution

$$\xi_{\text{saddle}}(\Delta) = \frac{4}{3} \sqrt{-\Delta}, \tag{4.98}$$

$$F_{\text{crit,SM}}(\Delta) = \frac{8}{9} (-\Delta)^{3/2} \quad \text{for } \Delta < 0. \tag{4.99}$$

However, this criterion is only valid if the location of the saddle is below the value of the critical level, i.e., $\xi_{\text{saddle}} \leq \xi_{\text{crit}}$, yielding a further constraint on the values of Δ. Equality holds if

$$\xi_{\text{saddle}} = \frac{4}{3}\sqrt{-\Delta_{\text{SM}}} = \xi_{\text{crit}}, \tag{4.100}$$

$$\Delta_{\text{SM},2} = -\frac{9}{16}\xi_{\text{crit}}^2. \tag{4.101}$$

At this point, $F_{\text{crit,SM}}(\Delta)$ is tangential to $F_{\text{crit,MM2}}(\Delta)$.
On the other hand, the fulfillment of Eqs. (4.96)-(4.97) alone is not sufficient for escape since the trajectory, after passing the saddle, must also reach the critical level. The corresponding critical force is defined by the Type 1 Maximum Mechanism in Eq. (4.92). Both criteria are fulfilled at the same time for $F_{\text{crit,SM}}(\Delta_{\text{SM},1}) = F_{\text{crit,MM1}}(\Delta_{\text{SM},1})$, i.e,

$$\frac{8}{9}(-\Delta_{\text{SM},1})^{3/2} = \Delta_{\text{SM},1}\xi_{\text{crit}} + \frac{3}{16}\xi_{\text{crit}}^3, \tag{4.102}$$

yielding

$$\Delta_{\text{SM},1} = -\frac{9}{64}\xi_{\text{crit}}^2, \tag{4.103}$$

$$F_{\text{SM},1} = \frac{3}{64}\xi_{\text{crit}}^3, \tag{4.104}$$

which is the location of the sharp minimum. For $\Delta_{\text{SM},1} < \Delta$, the criterion for the saddle mechanism becomes stronger. Thus, the critical force curve is defined as follows.

$$F_{\text{crit}}(\Delta) = \begin{cases} \Delta\xi_{\text{crit}} + \frac{3}{16}\xi_{\text{crit}}^3 & \text{for } \Delta < \Delta_{\text{SM},2}, \\ \frac{8}{9}(-\Delta)^{3/2} & \text{for } \Delta_{\text{SM},2} \leq \Delta \leq \Delta_{\text{SM},1}, \\ -\Delta\xi_{\text{crit}} - \frac{3}{16}\xi_{\text{crit}}^3 & \text{for } \Delta_{\text{SM},1} < \Delta. \end{cases} \tag{4.105}$$

In the analytic approximation, the initial excitation phase does not influence the critical forcing curve in any way. However, in the original problem setting, as we shall see in Fig. 4.9, the initial excitation phase does influence the V-curve.
Eq. (4.105) is represented graphically in Fig. 4.4 for $\varepsilon = 0.05$.
The Type I and II Maximum Mechanisms and the Saddle Mechanisms are depicted in Figs. 4.5)-(4.7.
In Fig. 4.8, time series data of direct numerical simulations is shown representing the three distinct escape mechanisms.

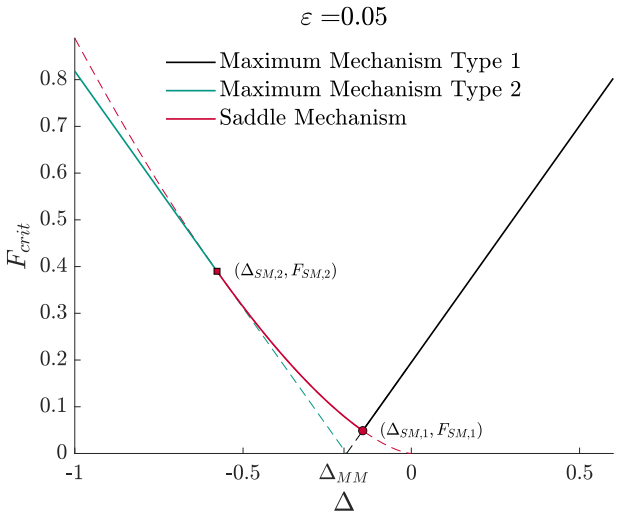

Figure 4.4: Critical forcing amplitude depicted against the discrepancy between excitation frequency and the linearized natural frequency of the potential well for homogeneous initial conditions. Three concurring escape mechanisms can be observed

In Fig. 4.9, the analytical, critical force curve is shown for various values of ε. $\varepsilon = 0.5$ corresponds to escape from a quadratic-quartic well without truncation, while ε values below 0.5 correspond to truncated potentials/level crossing.
For small values of ε, the analytical estimate is in excellent agreement with the numerical simulations, and the initial phase of the excitation is, in fact, insignificant. As the nonlinearity becomes more important, the deviation between simulation and analytical results for excitation frequencies further away from the V-curve's minimum gains significance ($\varepsilon = 0.05 - 0.2$). The analytical and numerical results deviate everywhere for the fully nonlinear case with $\varepsilon = 0.5$. Not even the location of the sharp minimum is approximated well. It is also important to note that with strong nonlinearity, as we shall see in Sect. 4.3, chaos emerges, making the right-hand side of the V-curve very uneven (cf. Fig. 4.10).

4.2.3 Conclusions and scope for future research

This section has revised the 1:1 resonance analysis of the level-crossing problem of undamped harmonically driven one-degree-of-freedom systems with small nonlinearity. The results shown here are based on [68] and [221], with an important correction made to the above articles by identifying the omitted Type 2 Maximum Mechanism, responsible for the far left side of the V-shaped critical forcing curve. This mechanism was correctly identified in [57] for a purely quartic potential, and it is indeed a universal mechanism

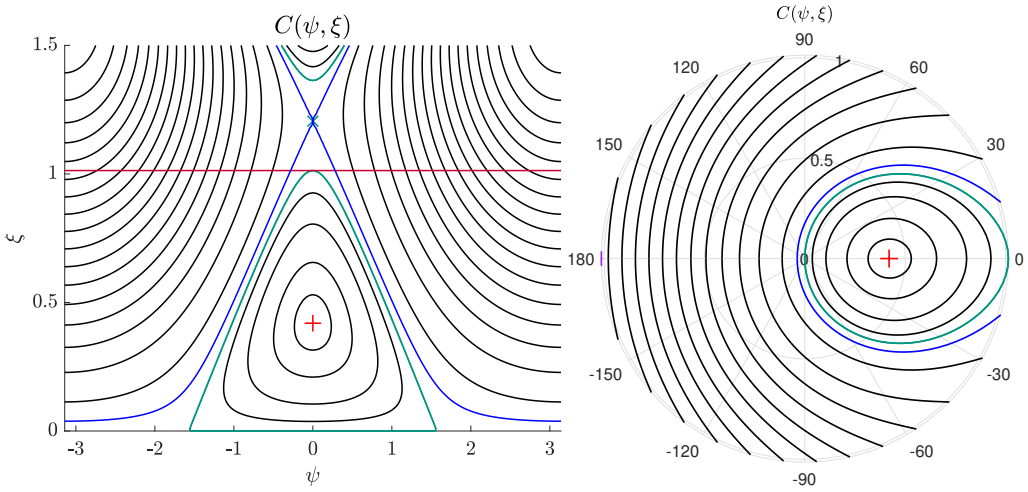

(a) Cartesian plot **(b)** Polar plot

Figure 4.5: Type 2 Maximum Mechanism with critical forcing for $\Delta = -0.8$ and $\varepsilon = 0.05$. The level sets of $C(\psi, \xi)$ are represented in black, the LPT is shown in green and the critical level is shown in red, the saddle level set is shown in blue

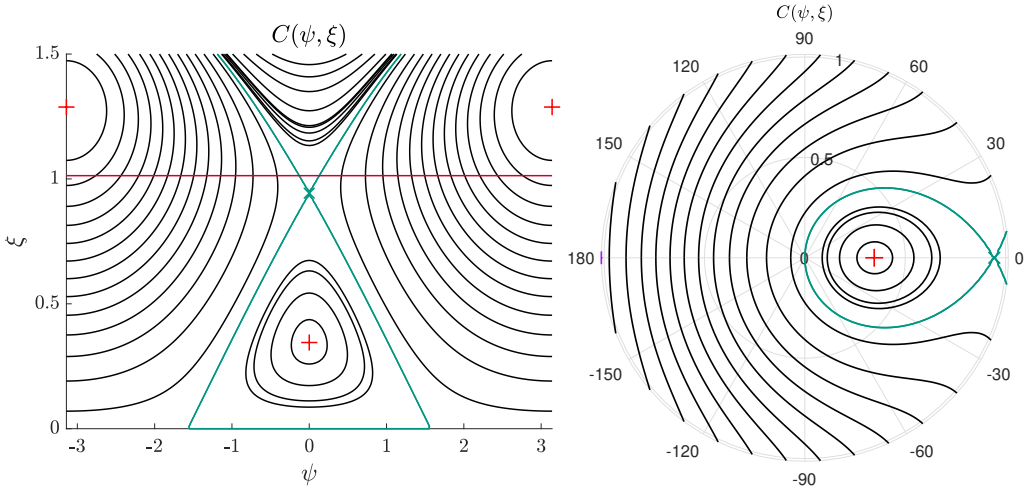

(a) Cartesian plot **(b)** Polar plot

Figure 4.6: Saddle Mechanism with critical forcing for $\Delta = -0.5$ and $\varepsilon = 0.05$. The level sets of $C(\psi, \xi)$ are represented in black, the LPT is shown in green, and the critical level is shown in red

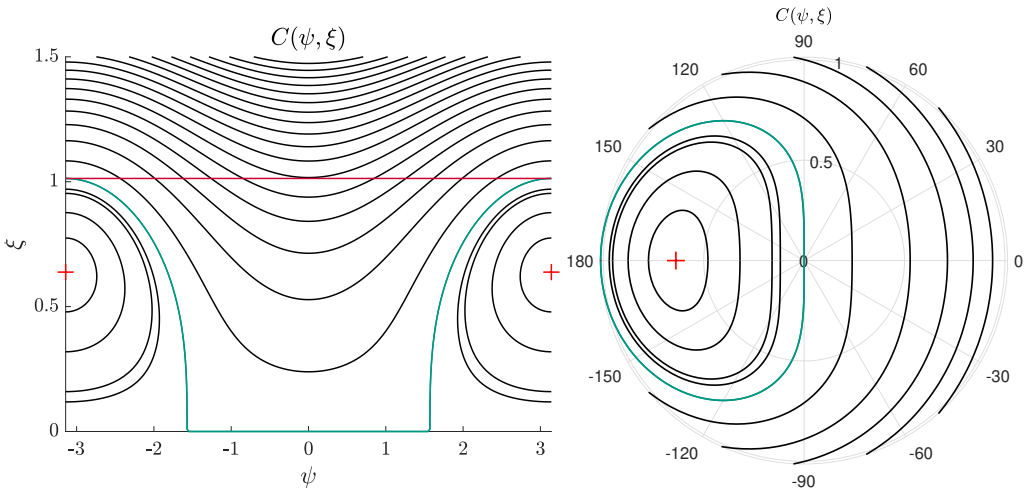

(a) Cartesian plot **(b)** Polar plot

Figure 4.7: Type 1 Maximum Mechanism with critical forcing for $\Delta = 0$ and $\varepsilon = 0.05$. The level sets of $C(\psi, \xi)$ are represented in black, the LPT in green, and the critical level in red. The saddle does not exist

in any escape problem, also to be found even in the linear case, in which it gives the whole left-hand side of the V-curve.

The approach applied in this chapter is valid for small nonlinearities; it is convenient due to the polynomial expressions arising in the calculations; however, for large nonlinearities, the results deviate significantly from the simulation results. In [57, 67, 68], action-angle variables offer more accurate results for large nonlinearities using elliptic functions.

As we have observed, there is always a steady-state solution. Additional fixed points arise for some excitation frequency ranges, such as an unstable saddle point and a stable (but not asymptotically stable) center point, which is well known from previous studies on the Duffing oscillator focusing on steady-state solutions. With a softening characteristic, the backbone curve is tilted to the left, which is why only one steady-state solution exists for $\Delta > 0$. Since the system is not damped, transients never decay, but periodic patterns can be observed in the solution's envelope around the amplitude of the stable fixed points.

Only one saddle can exist with the simple nonlinearity $N(x) = -x^3$. However, it is possible to construct a more complicated restoring force function (including further polynomial terms) such that further fixed points arise, giving rise to more complex dynamics with additional escape mechanisms.

Damping further complicates the picture since the first integral, given in Eq. (4.82), does not exist (or, at least until now, has not been found); therefore, the simple escape criteria

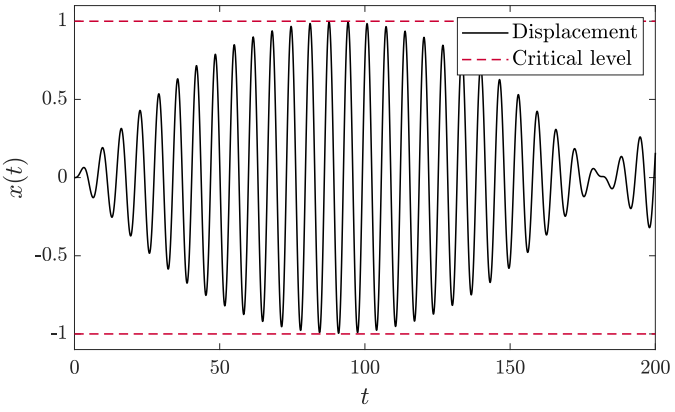

(a) Type 2 Maximum Mechanism with $\Delta = -1$ and $F = 0.8$

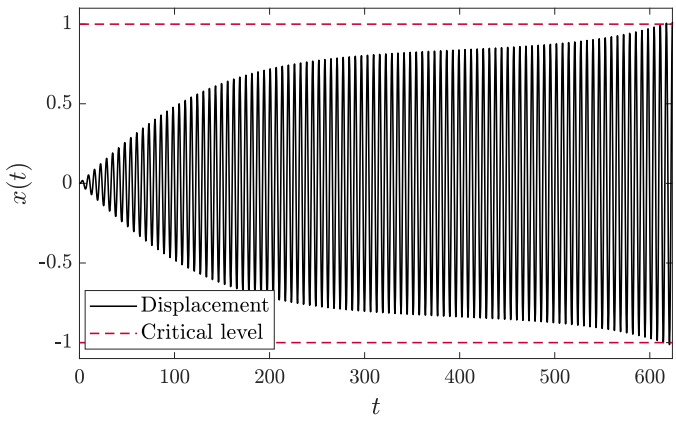

(b) Saddle Mechanism with $\Delta = -0.4$ and $F = 0.223$

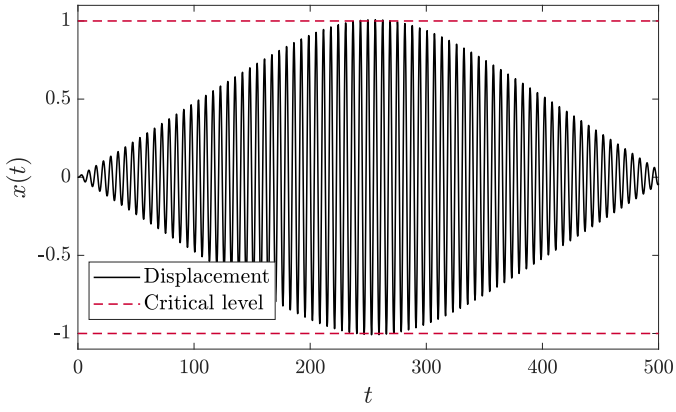

(c) Type 1 Maximum Mechanism with $\Delta = 0$ and $F = 0.19$

Figure 4.8: Simulation time series data showing the three distinct escape mechanisms for $\varepsilon = 0.05$ and homogeneous initial conditions

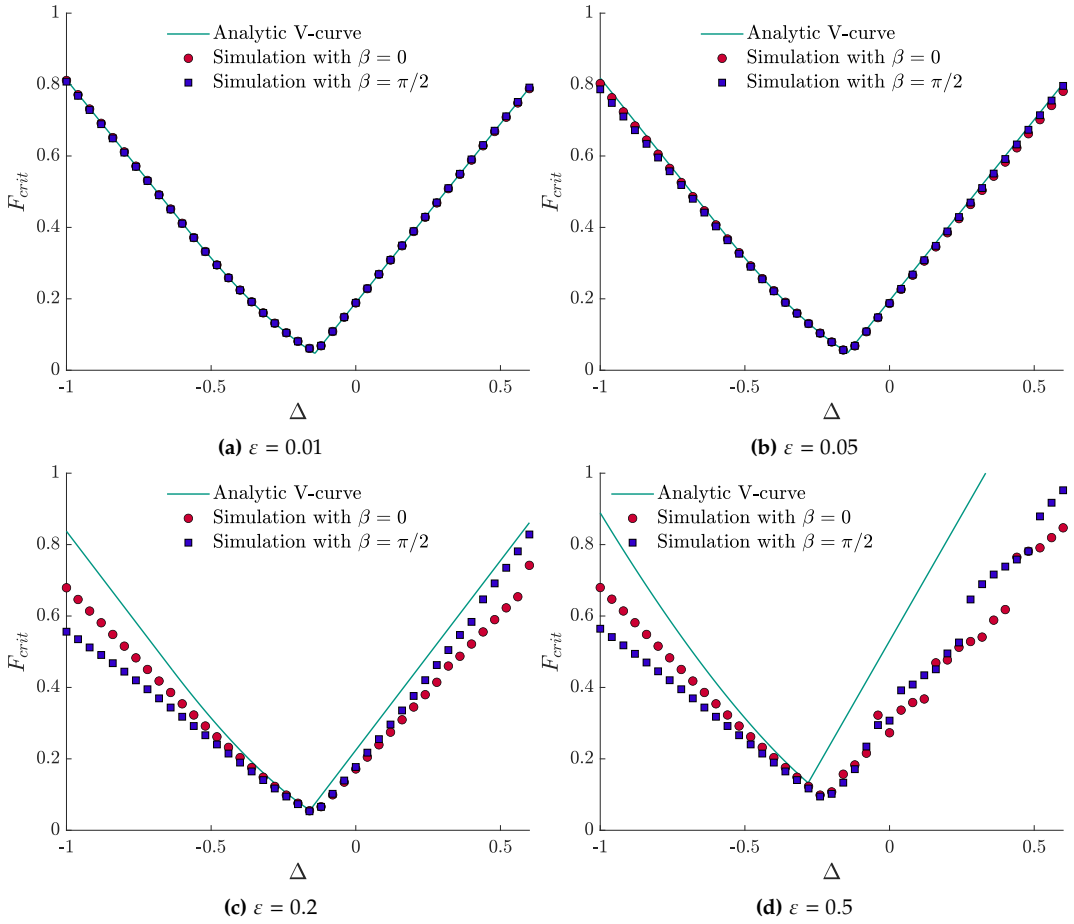

Figure 4.9: Analytically determined critical force amplitude compared to numerical simulation data for initial excitation phase $\beta = 0$ and $\beta = \pi/2$, respectively

presented in this chapter cannot be exploited. However, it is likely that the 'fast' and 'slow' as well as the Type 1 and Type 2 Maximum and Saddle Mechanisms all play a role in such a scenario.

4.3 Melnikov analysis of an undamped particle's escape from an arbitrary one-dimensional potential well under harmonic excitation

In the following section, the Melnikov analysis of the escape problem of an undamped particle from an arbitrary, one-dimensional potential well under weak harmonic excitation is performed. The analysis shows that escape through the maximum mechanism is triggered by chaotic motion. The topic was investigated almost 40 years ago by [197] for the canonical cubic oscillator with small linear damping. Through Melnikov analysis, *Thompson et al.* showed that chaotic phenomena occur before escape. In [175], *Sanjuan* used Melnikov analysis to investigate escape in a quadratic-cubic potential in the presence of nonlinear damping.
Such chaotic phenomena seem universal in escape problems, indifferent to the potential shape. In the following analysis, we assume twice continuously differentiable potential functions and show through Melnikov analysis that chaos is indeed present in all sufficiently smooth undamped one-dimensional escape problems where weak harmonic excitation is considered.
The system equation is given by

$$\ddot{x} + V'(x) = \varepsilon F \sin \Omega t . \tag{4.106}$$

To meaningfully consider escape, the potential $V(x)$ must fulfill some other properties other than the two-fold continuous differentiability. It has to have at least a (local) minimum and a (local) maximum. If a local minimum is adjacent to two local maxima of the same potential energy, they are connected by two (symmetric) heteroclinic orbits in the phase space. However, if there is only one adjacent local maximum, or two, but with different potential energy, the lower one is connected to itself with a homoclinic orbit in the phase space. Thus, the safe basin of the unperturbed system is bounded by the separatrix.
Our purpose is to show that the perturbed system becomes chaotic in the vicinity of the separatrix. Let us focus on the homoclinic case. We rewrite Eq. (4.106) as a system of first-order differential equations

$$\dot{x} = \underbrace{y}_{=:f_1(x,y)} \tag{4.107}$$

$$\dot{y} = \underbrace{-V'(x)}_{=:f_2(x,y)} + \underbrace{\varepsilon F \sin \Omega t}_{=:g_2(x,y,t)} . \tag{4.108}$$

In addition, we define $g_1(x, y, t) := 0$ for later use (cf. Eq. (4.115)). Let us denote the unstable hyperbolic fixed point (local maximum) of the unperturbed system by $\mathbf{x}_H = (x_H, 0)$ and define x_T to be the other turning point of the particle, that is, $V(x_T) = V(x_H) := E_H$.
The equation of the separatrix is given by the level set of the total energy at the hyperbolic fixed point, i.e.,

$$V(x_{sx}) + \frac{y_{sx}^2}{2} = E_H. \tag{4.109}$$

Thus, we have

$$y_{sx}(x) = \pm\sqrt{2(E_H - V(x))}. \tag{4.110}$$

Insertion of Eq. (4.110) in Eq. (4.107) yields

$$\frac{\mathrm{d}x}{\mathrm{d}t} = \pm\sqrt{2(E_H - V(x))}. \tag{4.111}$$

Applying zero velocity initial conditions ($x(0) = x_T$, $\dot{x}(0) = 0$) and separating the variables results in

$$F(x) := \int_{x_T}^{x} \frac{\mathrm{d}\tilde{x}}{\sqrt{2(E_H - V(\tilde{x}))}} = \pm t. \tag{4.112}$$

Note, that in the region bounded by the separatrix $V(x) < E_H$, thus, the term under the square root is positive and t is monotonous in x, hence,

$$x_{sx}(t) = F^{-1}(t), \tag{4.113}$$

$$y_{sx}(t) = \dot{x}_{sx}(t) = \pm\sqrt{2(E_H - V(F^{-1}(t)))}. \tag{4.114}$$

The Melnikov function is given by

$$M(t_0) = \int_{-\infty}^{\infty} \mathbf{f}((\mathbf{q}^0(t - t_0))) \wedge \mathbf{g}(\mathbf{q}^0(t - t_0), t)\mathrm{d}t, \tag{4.115}$$

with $\mathbf{f} \wedge \mathbf{g} = f_1 g_2 - f_2 g_1$ and

$$\mathbf{f}(\mathbf{x}) = \begin{pmatrix} f_1(x, y) \\ f_2(x, y) \end{pmatrix}, \qquad \mathbf{g}(\mathbf{x}, t) = \begin{pmatrix} g_1(x, y, t) \\ g_2(x, y, t) \end{pmatrix}, \qquad \mathbf{q}^0 = \begin{pmatrix} x_{sx}(t) \\ y_{sx}(t) \end{pmatrix}, \tag{4.116}$$

which, in our case, simplifies to

$$\mathbf{f}(\mathbf{x}) = \begin{pmatrix} y \\ -V'(x) \end{pmatrix}, \qquad \mathbf{g}(\mathbf{x}, t) = \begin{pmatrix} 0 \\ \varepsilon F \sin \Omega t \end{pmatrix}, \tag{4.117}$$

hence,

$$M(t_0) = \varepsilon F \int_{-\infty}^{\infty} y_{sx}(t - t_0) \sin \Omega t \mathrm{d}t \tag{4.118}$$

$$= \varepsilon F \int_{-\infty}^{\infty} y_{sx}(t) \sin \Omega (t + t_0) \mathrm{d}t \tag{4.119}$$

$$= \varepsilon F \cos \Omega t_0 \underbrace{\int_{-\infty}^{\infty} y_{sx}(t) \sin \Omega t \mathrm{d}t}_{=:I} + \varepsilon F \sin \Omega t_0 \underbrace{\int_{-\infty}^{\infty} y_{sx}(t) \cos \Omega t \mathrm{d}t}_{=0}, \tag{4.120}$$

where the last term is always zero, since $y_{sx}(t)$ is odd in t. Thus, the negative and positive sides of the integral (Cauchy principal value) are canceled out. Integral I exists since

$$\int_{-\infty}^{\infty} y_{sx}(t) \sin \Omega t \mathrm{d}t \leq \int_{-\infty}^{\infty} |y_{sx}(t) \sin \Omega t| \mathrm{d}t \tag{4.121}$$

$$\leq \int_{-\infty}^{\infty} |y_{sx}(t)| \mathrm{d}t = 2 \int_{0}^{\infty} |y_{sx}(t)| \mathrm{d}t = 2|x_H - x_T|. \tag{4.122}$$

Hence, the Melnikov function has infinitely many zeros in t_0, implying that the stable and unstable manifolds intersect, which leads to chaotic behavior due to its well-known relation to the Smale horseshoe map.
Similar arguments can be applied in the case of a homoclinic separatrix.
This result is important because it shows that chaotic phenomena occur prior to the escape of a harmonically excited, undamped particle from a wide class of potential wells. In [96], chaos appears in the maximum mechanism when the forcing value falls in a critical region, sufficient to induce oscillations reaching the vicinity of the unperturbed system's separatrix. Escape through the saddle mechanism does not show chaotic behavior since, in this case, the critical energy level is far below the separatrix's. In this case, a critical forcing value exists, above which a sudden transient jump from the vicinity of the small-amplitude stationary solution takes place, and the particle escapes. Fig. 4.10 illustrates this well.

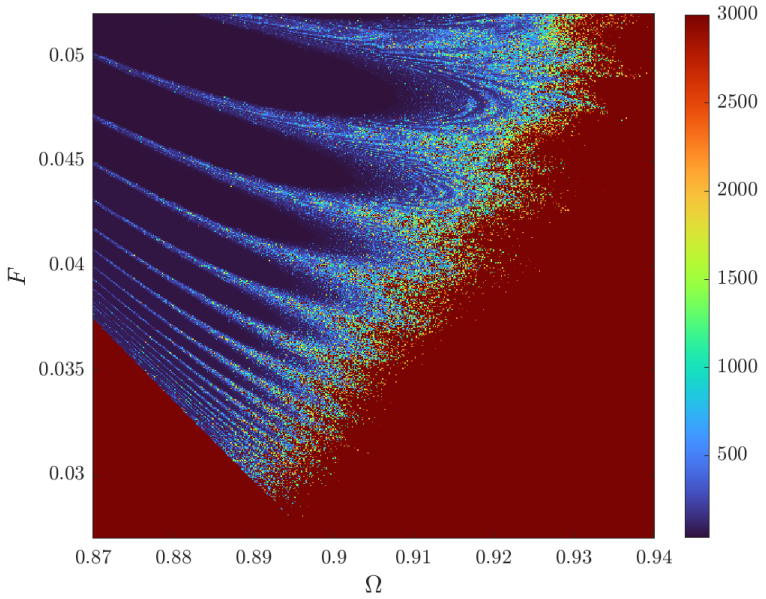

Figure 4.10: Escape time from the potential $V(x) = x^2/2 - x^4/4$ of an undamped particle depicted against the excitation frequency and the forcing amplitude using homogeneous initial conditions

4.4 Experimental validation of escape mechanisms

Through this dissertation, escape is analyzed analytically and numerically. In this chapter, however, we focus on the experimental validation of the distinct escape mechanisms described in Sect. 4.2, the Saddle, and the Type I and II Maximum Mechanisms.

The experiment is carried out on the modified Duffing oscillator test rig of the Institute of Engineering Mechanics at KIT (see Fig. 4.11).

The mechanical part of the experiment consists of a vertically placed shaft supported by two air bearings. The pressure of the air bearings can be regulated between 0 and 6 bars. When the air pressure is turned off, additional ball bearings support the shaft, but they become 'deactivated' once the air supply is on. This setup, although energy-intensive, provides very low friction values.

A copper disk is mounted on the shaft for dual purposes. First, it provides an additional moment of inertia. Second, it allows the creation of eddy currents when the electromagnet around the plate is turned on, generating additional viscous damping. With a direct current generator, it is also possible to precisely regulate the viscous damping strength by setting the voltage value U_D.

Figure 4.11: Experimental setup of a double-well oscillator created by the geometrical nonlinearities of coil springs

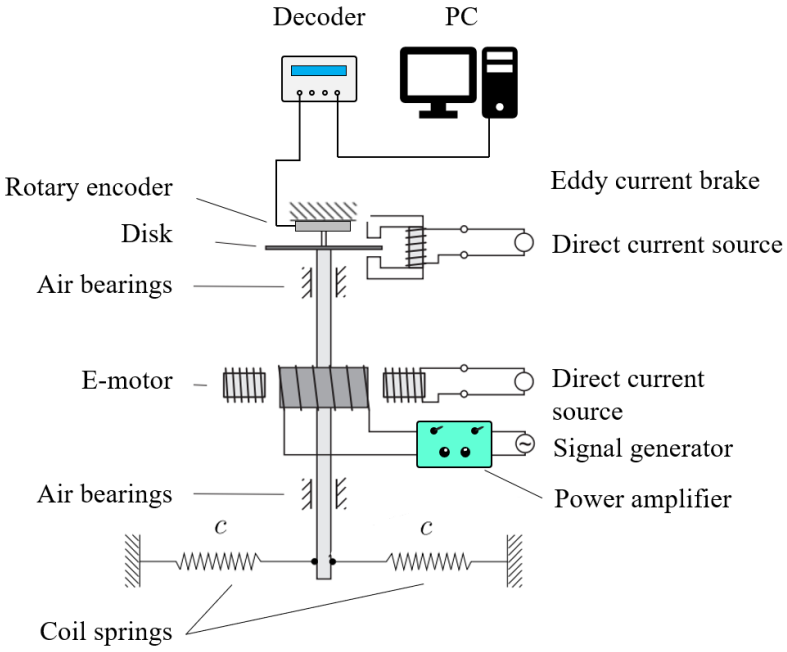

Figure 4.12: Sketch of the experimental setup

Two coil springs attach the shaft to the test rig's frame. Their placement is such that the distance between their fixation point on the frame and the fixation points on the shaft is less than the springs' relaxed length, resulting in compressed springs when the springs' longitudinal axis passes through the shaft. Since the springs are placed facing each other, the resulting restoring moment created by them is symmetrical. It has two stable equilibria on both sides of the unstable, symmetrical equilibrium.
A schematic model is given in Fig. 4.13. The system has a rotatory degree of freedom with dependent coordinate φ. A disk comprising the total moment of inertia of the rotatory system J is attached to a spring of stiffness c. In the symmetrical state, the spring length is d, greater than the spring's relaxed length $l_0 = l(0)$. The spring is fixed to the disk at a distance R from the center point of the disk. Some dry friction acts with coefficient μ in bearings and joints. Furthermore, variable viscous damping with coefficient $k \in [k_{\min}, k_{\max}]$ is also present. If the eddy current brake is deactivated, the viscous damping coefficient takes the value $k = k_{\min}$. In addition, an electric motor provides the external momentum $M(t)$ to excite the system. The stator is an electromagnet whose current can be controlled from a variable DC source. The rotor

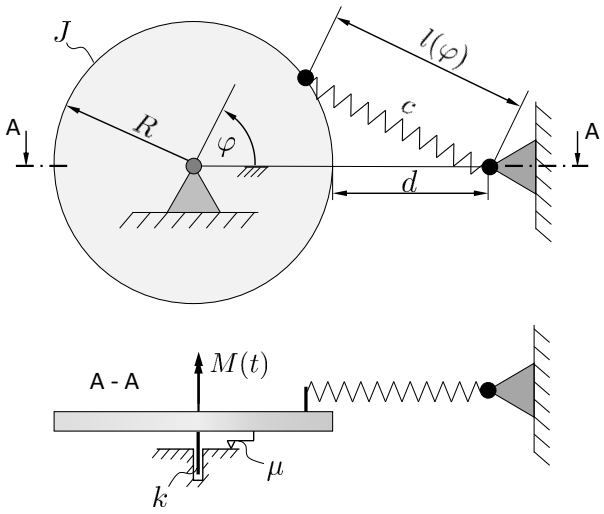

Figure 4.13: Schematic representation of the underlying mechanical system

is supplied with an electric current from a function generator, the signal of which is passed through a power amplifier to reach the necessary strength.
All parameter values and the function $M(t)$ are to be identified.
Using the notations of Fig. 4.11, the equation of motion is given by

$$J\ddot{\varphi} + k\dot{\varphi} + \mu \operatorname{sign}\dot{\varphi} + cR(R+d)\left(1 - \frac{l_0}{\sqrt{2R^2 + d^2 + 2Rd - 2R(R+d)\cos\varphi}}\right)\sin\varphi = M(t). \tag{4.123}$$

The equilibria of the system are at

$$\varphi_{1,2} = \{0, \pi, \}, \tag{4.124}$$

$$\varphi_{3,4} = \pm \arccos\left(\frac{2R^2 + d^2 + 2Rd - l_0^2}{2R(R+d)}\right). \tag{4.125}$$

With the parameter values used in the experimental setup, $\varphi_2 = \pi$ cannot exist since the spring does not permit such expansion. Also, it is evident that for $d < l_0$, the equilibrium $\varphi_1 = 0$ is unstable, and the equilibria $\varphi_{3,4}$ are stable.

Since Eq. (4.123) is quite complicated due to the square-root and trigonometric functions, a double-well Duffing model was chosen to simplify the model without sacrificing significant accuracy.
The simplified equation of motion is thus given by

$$\ddot{\varphi}(t) + \frac{k}{J}\dot{\varphi}(t) + \frac{\mu}{J}\operatorname{sign}\dot{\varphi}(t)) + \frac{cR\,(R+d)}{J}\left(1 - \frac{l_0}{d}\right)\varphi + \frac{1}{J}\left(-\frac{cR\,(R+d)\left(1-\frac{l_0}{d}\right)}{6} + \frac{cR\,(R+d)^2\,l_0 R}{2d^3}\right)\varphi^3 + = \frac{M(t)}{J}. \tag{4.126}$$

The equation is strongly nonlinear in the parameters; thus, estimating them based on time series data is difficult. Even in the case of success, it is only possible up to a constant multiplier, as the excitation moment is not known due to missing information on the motor's torque constant: the motor's torque divided by the armature current. However, this information is not needed to model the system's dynamics. We introduce the new parameters

- A – the coefficient of the linear part of the restoring moment: $A = \frac{cR(R+d)}{J}\left(1 - \frac{l_0}{d}\right)$,
- B – the coefficient of the cubic part of the restoring moment: $B = -\frac{cR(R+d)\left(1-\frac{l_0}{d}\right)}{6J} + \frac{cR(R+d)^2 l_0 R}{2d^3 J}$,
- C – a bias term to match the coordinate system with the zero position of the encoder,
- D– the viscous damping coefficient per unit moment of inertia, $D = k/J$,
- E– the dry friction coefficient per unit moment of inertia, $E = \mu/J$,
- F– voltage–torque proportionality factor of the motor per unit moment of inertia, $F = M(t)/Ju_M(t)$.

It is assumed that motor voltage $u_M(t)$ is related to the motor current by Ohm's law: we neglect the back electromotive force (for justification, see Fig. 4.14) and the inductance of the rotor as we work with very low frequencies. Since we measure voltage and not electric current, F is not equivalent to the torque constant but related to it.
The equation of motion is thus given by:

$$\ddot{\varphi}(t) + D\dot{\varphi}(t) + E\operatorname{sign}\dot{\varphi}(t)) - A(\varphi(t) - C) + B(\varphi(t) - C)^3 = Fu_M(t). \tag{4.127}$$

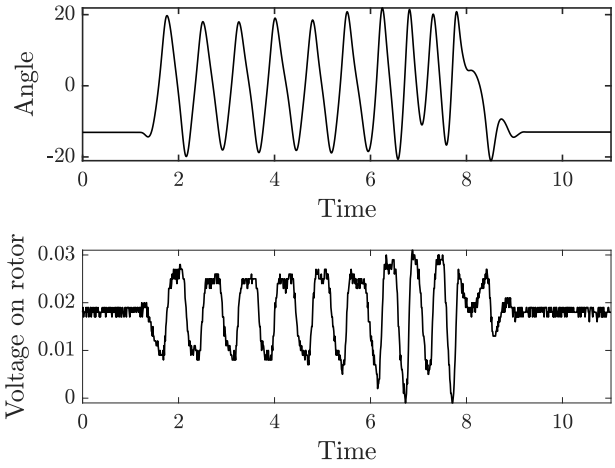

Figure 4.14: Back electromotive force under manual rotations of the shaft. The values are 2-3 orders of magnitude smaller than the voltage values used in the experiments

The system described by Eq. (4.127) has an unstable equilibrium at $\varphi_1 = C$ and stable equilibria at $\varphi_2 = C + \sqrt{A/B}$ and $\varphi_3 = C - \sqrt{A/B}$. Around both stable equilibria, $\sqrt{2A}$ gives the linearized angular eigenfrequency. Eq. (4.127) is valid for $\dot{\varphi} \neq 0$.
Parameter values A, B, C, D, E and F must be estimated to compare the system with numerical simulations. Furthermore, since we do not measure it directly, the estimation of $u_M(t)$, based on the recorded signal of the signal generator $u_S(t)$, is necessary.
To make the parameter identification possible, we measure the value of the rotation angle and the signal generator's output voltage. The former is performed with a 21-bit digital rotational encoder from Netzer Precision, based on the SSI protocol. Sensor values are read using an Arduino™ Mega 2560 Rev 3 and transferred directly via serial communication to MATLAB™.
The signal generator's output voltage is also measured using the Arduino board utilizing a digital ADS1115 16-bit ADC module. With this setup, achieving a maximum sampling frequency of up to 200 Hz is possible. This frequency is enough to accurately describe the mechanical system's underlying dynamics. During the measurements, a sampling frequency of 100 Hz was used. The setup is shown in Fig. 4.15.

4.4.1 Estimation of the motor voltage

When running a measurement, we can observe that a constant voltage set on the function generator does not result in any torque on the motor (cf. Fig. 4.17). However, this is only possible if no current flows through the armature, equivalent to no voltage on the rotor. This happens because the power amplifier acts as a high-pass filter, cutting down signal

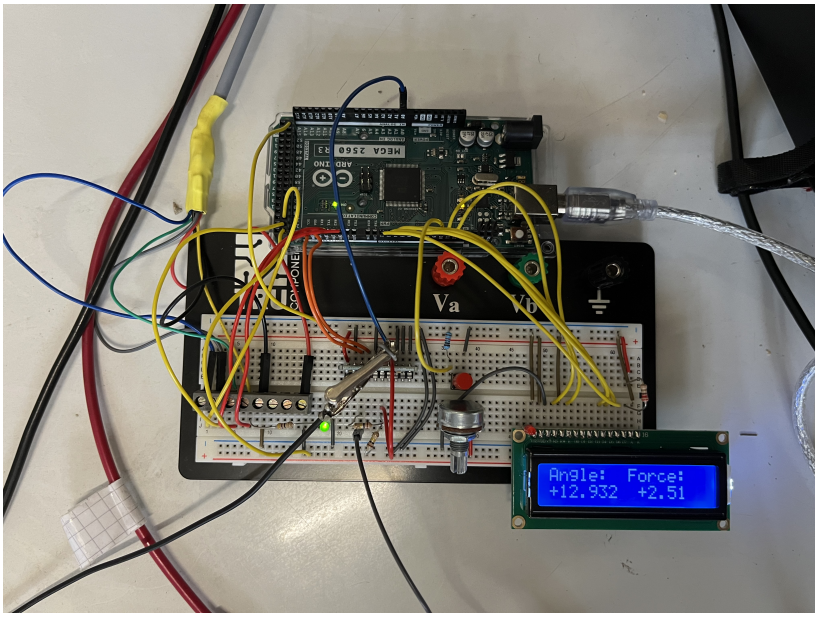

Figure 4.15: Data acquisition with Arduino

components below 10 Hz. Indeed, the datasheet of the power amplifier type 2706 from Brüel & Kjaer confirms this observation, describing the frequency domain with a flat response between 10-20 000 Hz. However, our system lies significantly below this range since we investigate harmonic excitation with frequencies between 1.4-2.5 Hz. In this range, the amplifier still amplifies the signal components, however, the amplification is significantly smaller than the set value and it is frequency-dependent.
The data sheet of the power amplifier does not provide a Bode diagram, so a measurement was performed to determine the amplification in this domain. A harmonic voltage with a constant amplitude of 50 mV and stepwise varying frequency was generated and amplified. The power amplifier's output was measured, and the signal amplitude was calculated for all different frequencies. The measurement data is depicted in Fig. 4.17, and the resulting amplification function is plotted in Fig. 4.18.
For numerical purposes, the power amplifier was modeled with a DT_1 element, whose transfer function is given by

$$G(s) = \frac{K_D s}{1 + T_1 s}, \tag{4.128}$$

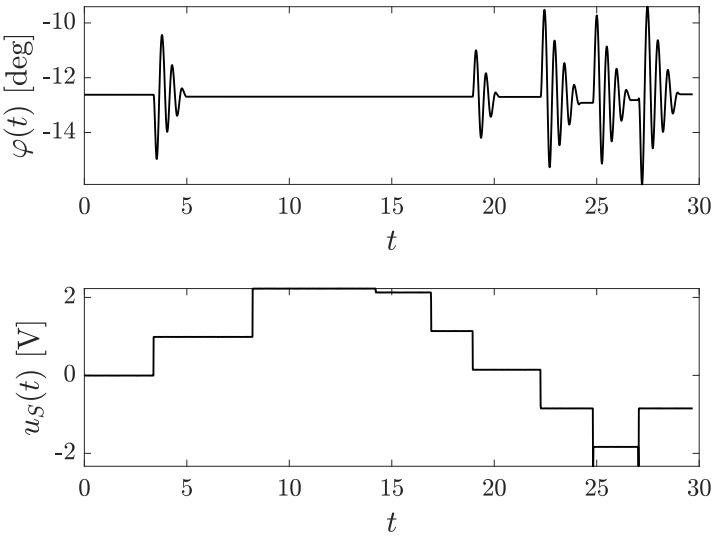

Figure 4.16: Effects of the power amplifier: a) the function generator's voltage signal is high-pass filtered, b) only voltage values from a certain range have an effect; out of this range, no excitation appears at all

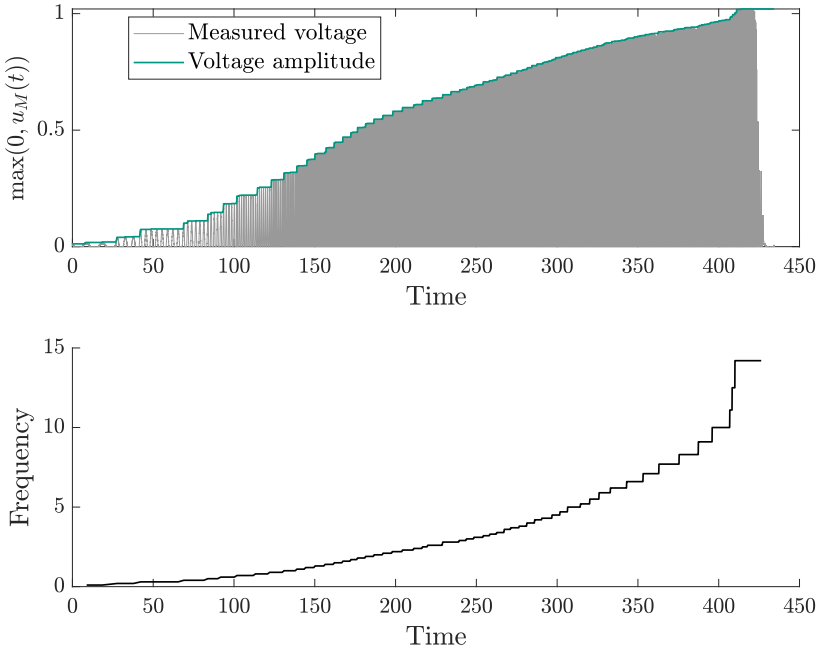

Figure 4.17: Measurement of $u_M(t)$ under varying frequency values of $u_S(t)$ with constant amplitude voltage of 50 mV.

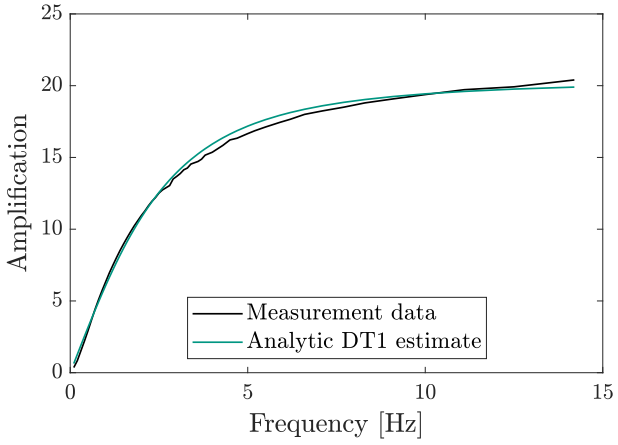

Figure 4.18: Frequency-dependent amplification function of the power amplifier

with $K_D = 1.02$ and $T_1 = 0.05$ fitted to the measurements (see Fig. 4.18). The impulse response is given by

$$g(t) = \frac{K_D \delta(t)}{T_1} - \frac{K_D e^{-\frac{t}{T_1}}}{T_1^2}. \tag{4.129}$$

The amplification and phase shift can be determined by inserting $s = \jmath\omega$:

$$G(\jmath\omega) = \frac{K_D \omega}{\sqrt{1 + T_1^2 \omega^2}} e^{\jmath \arctan \frac{1}{T_1 \omega}}, \tag{4.130}$$

resulting in

$$A(\omega) = \frac{K_D \omega}{\sqrt{1 + T_1^2 \omega^2}}, \qquad \theta(\omega) = \arctan \frac{1}{T_1 \omega}. \tag{4.131}$$

The power amplifier's estimated step response and Bode plot are shown in Fig. 4.19. Assuming homogeneous initial conditions the calculation of any excitation signal $u_M(t)$ based on $u_S(t)$ and the transfer function also becomes possible by calculating

$$U_M(s) = G(s) U_S(s) = \frac{K_D s}{1 + T_1 s} U_S(s) \tag{4.132}$$

$$u_M(t) = \mathcal{L}^{-1}\left\{ \frac{K_D s}{1 + T_1 s} U_S(s) \right\} \tag{4.133}$$

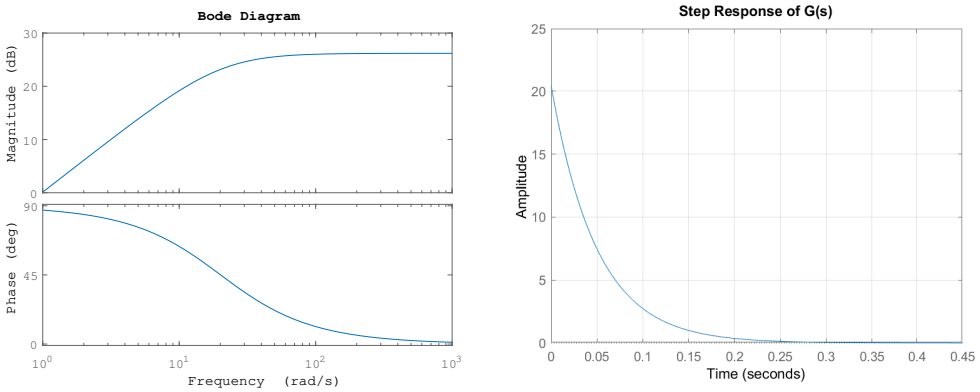

(a) Bode plot

(b) Step response

Figure 4.19: Estimated characteristics of the power amplifier

$$u_M(t) = \int_0^t g(t-\tau) u_S(\tau) d\tau \tag{4.134}$$

$$u_M(t) = \frac{K_D}{T_1} \left(u_S(t) - \frac{1}{T_1} \int_0^t e^{-\frac{t-\tau}{T_1}} u_S(\tau) d\tau \right). \tag{4.135}$$

From Eq. (4.135), we see that the power amplifier's output is not simply a scalar multiple of its input but is to be corrected by an additional term resulting from the integral.
To identify parameters, we will evaluate the convolution integral numerically. However, with the signal generator, we can precisely control the input of the power amplifier. Thus, we refer to $u_S(t)$ as the input, and the resulting plots should be interpreted accordingly.

4.4.2 Parameter identification

The process of identifying the parameters of the model involves a two-step approach. Firstly, the parameters are identified using the measured acceleration. Secondly, the parameters are fine-tuned using a comparison between the measured angle values and the values given by the numerical solution of Eq. (4.127).

First step

Since the angle measurement is very accurate, its numerical differentiation generates little noise, and it is possible to obtain the acceleration numerically. Then, the parameter values in Eq. (4.127) are sought for which the sum of squares of differences between acceleration data and the corresponding predictions is minimized. Eq. (4.127) is nonlinear in the parameters, so an exact formula as in linear Gaussian least squares

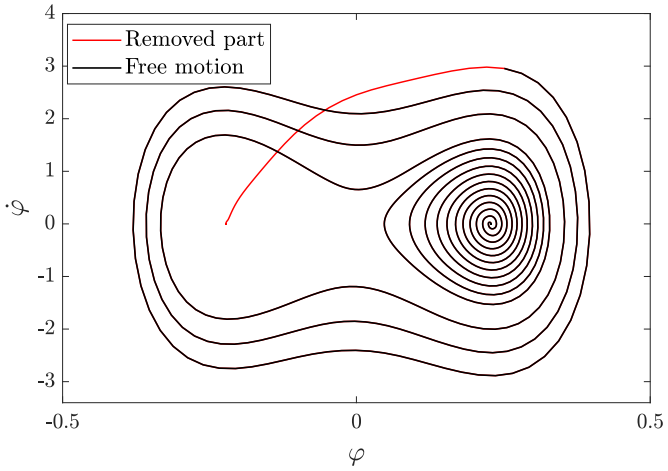

Figure 4.20: Phase portrait of the shaft's rotation after initially pushing it by hand

cannot be given. However, numerically, the determination of the parameters is simple. MATLAB's inbuilt function `fitnlm` yields the parameter values with the corresponding statistics.

For more precise results, parameter values without external excitation are first identified. The system is initially pushed, and the decaying motion is registered. The data is cleaned by removing the pushing part to focus only on free motion. A graphical representation of the data and its removed values is shown in Fig. 4.20.

The experiment is carried out several times, and the data are combined into a common vector, which is provided as input to `fitnlm`. In mathematical terms, the optimization problem is given by

$$\min_{\mathbf{p}_\mathrm{a}} J_\mathrm{a}(\mathbf{t};\mathbf{p}_\mathrm{a}) = \frac{1}{N}\sum_{t_i\in\mathbf{t}}\left(\ddot{\varphi}(t_i) - \hat{\ddot{\varphi}}(t_i,\mathbf{p}_\mathrm{a})\right)^2 \tag{4.136}$$

where N is the number of data points, $\mathbf{p}_\mathrm{a} = [A,B,C,D,E,F]^\mathrm{T}$ and $\mathbf{t}$ is the vector containing all the time instances of the measurements. Based on Eq. (4.127), the acceleration estimate is given by

$$\hat{\ddot{\varphi}}(t_i) = -D\dot{\varphi}(t_i) - E\,\mathrm{sign}\,\dot{\varphi}(t_i) + A(\varphi(t_i)-C) - B(\varphi(t_i)-C)^3 - Fu_M(t_i). \tag{4.137}$$

Parameter estimates were made for two damping values: no added viscous damping and $U_D = 30\,V$. In tables 4.1)-(4.2, the coefficient estimates with their most important statistics are given.

Table 4.1: Estimated model coefficients without added viscous damping, $U_D = 0\,V$.

Coefficient	Estimate	Standard error	t-statistic	p-value
A	78.131	0.111 91	698.17	0
B	1530.6	1.4136	1082.8	0
C	0.002 696 9	$5.3394 \cdot 10^{-5}$	50.51	0
D	0.234 54	0.012 704	18.463	$1.5043 \cdot 10^{-73}$
E	0.262 14	0.015 059	17.407	$7.9516 \cdot 10^{-66}$

Table 4.2: Estimated model coefficients with added viscous damping $U_D = 30\,V$.

Coefficient	Estimate	Standard error	t-statistic	p-value
A	76.722	0.131 04	585.5	0
B	1511.3	1.8776	804.89	0
C	0.003 392 9	$7.198 \cdot 10^{-5}$	47.137	0
D	1.3582	0.016 086	84.435	0
E	0.1345	0.015 311	8.7843	$2.5647 \cdot 10^{-18}$

The p-values are very small, and thus, all parameters contribute significantly to the improvement of the model. The models demonstrate a very good fit to the data. The high R-squared values of 0.997 and 0.996, respectively, indicate that the models explain almost all the variability in the response variable.
The underlying model given by Eq. (4.127) is only a simplification of the more exact model given by Eq. (4.126), which is also just a simplification of reality. However, the exceptionally high value of the coefficient of determination (R^2) signifies that even the simplified model is very close to reality.
The two-dimensional surface for the case with $U_D = 30\,V$ is given by $\hat{\dot{\varphi}}(\varphi, \dot{\varphi})$ as well as the measured data are plotted in Fig. 4.22.
In Tables 4.1)-(4.2, there are slight differences between the two estimates. However, they should have the same values for the parameters A, B, C, and E, which could suggest that there may be interactions between the parameters that have not been considered or that the optimization problem has multiple solutions. Furthermore, temperature changes could have influenced the experiment results because the two sets of measurements were not taken simultaneously. In particular, the value of E shows a significant difference. The assumption of Coulomb friction might be an oversimplification. For example, for a better model, the friction force should be assumed to be proportional to the spring force in the pivots of the springs' sockets. In Fig. 4.21, we can see a scenario in which the shaft is rotated by hand in both directions of the two equilibria and then released to return to its resting position. We can observe that the values to which the shaft returns when released from the left differ from the values of the right, defining an angle interval,

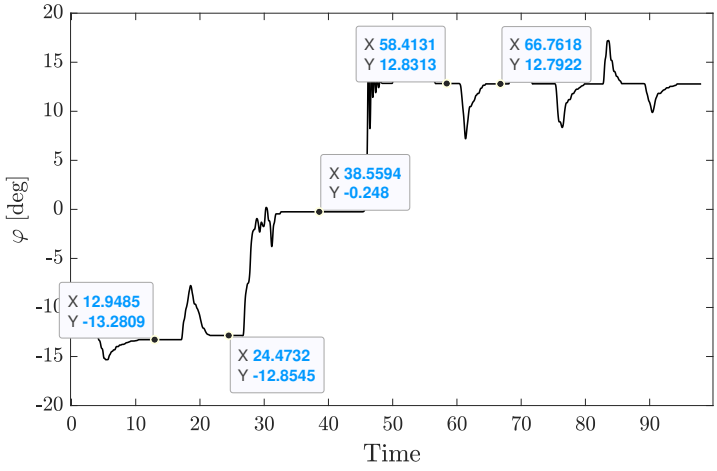

Figure 4.21: Test on the assumption with Coulomb friction by manually rotating the shaft away from its equilibria, respectively, and letting it return to them

respectively, where the stiction is greater than the springs' restoring force. However, this interval is significantly different for φ_2 ($\Delta\varphi_2 = 0.0391° = 0.000682$ rad) than for φ_3 ($\Delta\varphi_3 = 0.4264° = 0.007442$ rad), reaching an order of magnitude.
It is possible to estimate the value of E with these data directly. The linearization of Eq. (4.127) around $\varphi_{2,3}$ without external excitation is given by

$$\ddot{\varphi} + D\dot{\varphi} + E\text{sign}(\dot{\varphi}) + 2A(\varphi - \varphi_{2,3}) = 0. \tag{4.138}$$

At the angle value equivalent to the half-width of the stiction region, the restoring torque is equal to the maximal friction value when in equilibrium, that is,

$$E_{2,3} = \frac{2A\Delta\varphi_{2,3}}{2} = A\Delta\varphi_{2,3}, \tag{4.139}$$

$$E_2 = 0.053, \tag{4.140}$$

$$E_3 = 0.58. \tag{4.141}$$

Since the difference between E_2 and E_3 in the friction coefficient value is greater than an order of magnitude, we will use the value $E = 0.5$ in the further numerical validation.
Similarly, it is also possible to identify the value of the parameter F. Exciting the system with a harmonic voltage generates the data depicted in Fig. 4.23.
Eq. (4.137) is then fitted on the acceleration data yielding fit with $R^2 = 0.999$ with the following parameter values listen in Table 4.3. The values are close to the previous estimates based on the free decaying motion of the system; however, the proportionality factor of F became known.

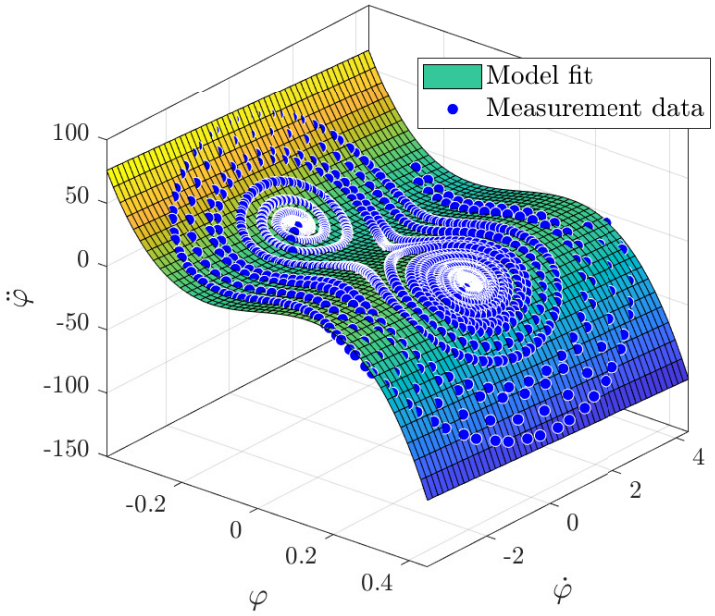

Figure 4.22: Measured vs. predicted values of the angular acceleration with added viscous damping $U_D = 30\,V$

Table 4.3: Estimated coefficients of the model with added viscous damping, $U_D = 30\,V$.

Coefficient	Estimate	Standard error	t-statistic	p-value
A	83.424	0.112 96	738.54	0
B	1574	4.9257	319.54	0
C	0.001 538 6	0.000 337 13	4.5637	$5.3327 \cdot 10^{-6}$
D	1.1757	0.018 587	63.256	0
E	0.453 21	0.014 872	30.473	$8.6553 \cdot 10^{-168}$
F	−0.968 23	0.005 994 8	−161.51	0

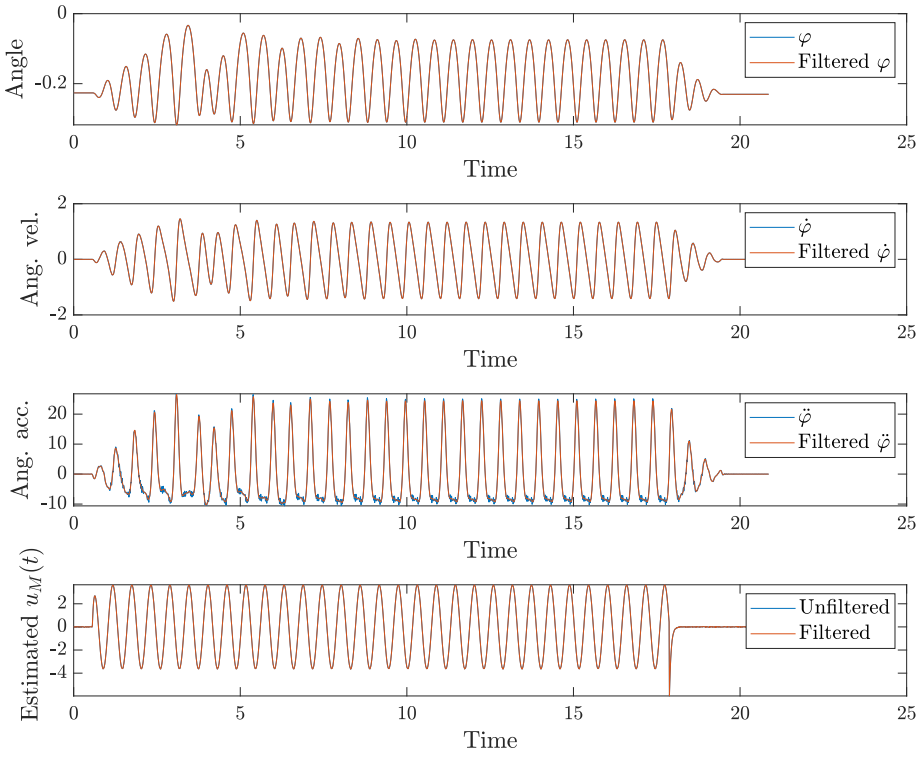

Figure 4.23: Measurement data with excitation frequency $f = 1.75$ Hz, voltage range $\Delta u_S = 750$ mV and starting phase $\beta = 0$ with additional damping $U_D = 30\,V$

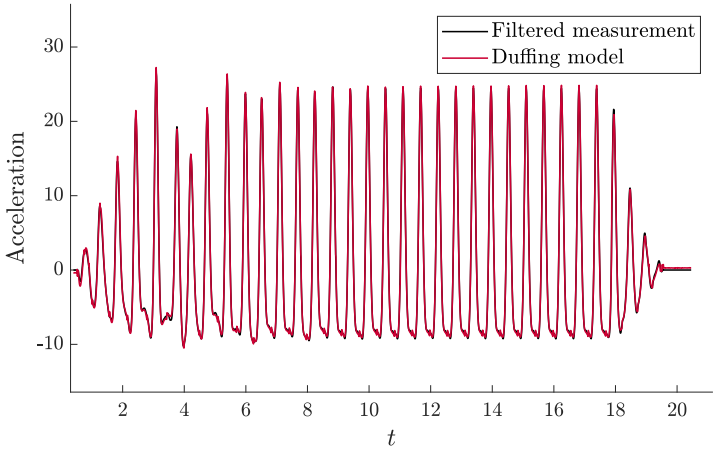

Figure 4.24: Measurement vs. fitted data with excitation frequency $f = 1.75$ Hz, voltage range $\Delta u_S = 750$ mV and starting phase $\beta = 0$ with additional damping $U_D = 30\,V$. $R^2 = 0.999$

Second step

In the second step of the parameter identification, the measured position data is used to find the optimal model parameters. The parameter estimates from the first step, described in Sect. 4.4.2, are used as initial values. Furthermore, the initial conditions also have to be estimated, which is done by using the measured initial angle value and the initial velocity calculated numerically based on the measurement data.

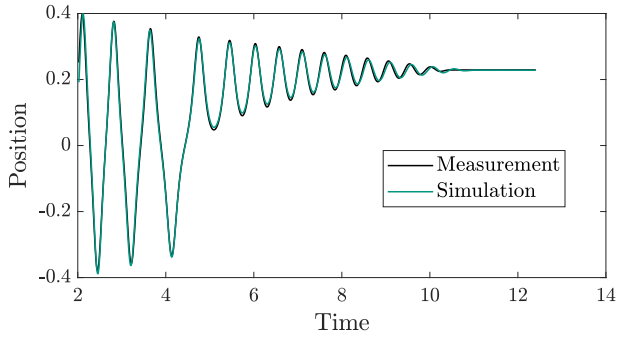

Figure 4.25: Comparison of the measurement data and numerical simulation with optimized parameters without added damping

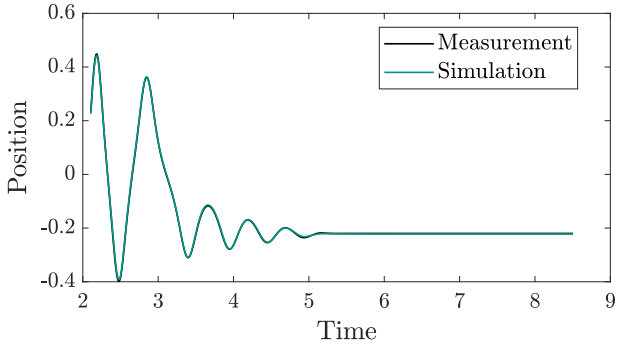

Figure 4.26: Comparison of the measurement data and numerical simulation with optimized parameters with $U_D = 30\,V$

Then, the numerical solution of Eq. (4.127) is calculated and evaluated at the same time instances where the measurements were recorded. The Euclidian norm of the difference of the two vectors is finally calculated and used as the cost function in the optimization. The non-gradient-based `fmincon` function of MATLAB is used for optimization since the objective function is nonsmooth due to the possibility of escape. In Figs. 4.25)-(4.26 the numerical solutions are compared to the measurement data with and without added viscous damping. The identified parameters are listed in Table 4.4.

Parameters	$U_D = 0\,V$	$U_D = 30\,V$
A	84.7163	84.70781
B	1618.60	1628.687
C	-0.00067	0.005982
D	0.28932	1.009082
E	0.255610	0.751432
x_0	0.191728	0.226265
u_0	3.09931	4.198380

Table 4.4: Optimal parameter values found based on measurements depicted in Figs. 4.25 and 4.26

The parameter values A and B corresponding to the conservative part of the dynamics differ from those found in the first step in Sect. 4.4.2. However, they are close to each other, as should be, since the difference in the two simulations is only the additional damping. However, the value of E is significantly different in both cases, indicating that the assumption of Coulomb friction might be an oversimplification. Another reason may be that it is difficult to differentiate the roles of Coulomb and viscous damping based on measurement data since the identified parameter values show an increase in E in Table 4.4 compared to Tables 4.1)-(4.2, however, the estimated value of D decreases from 1.3582 to 1.0091 in the case of $U_D = 30\,V$.
Later on, in the numerical simulations for model validation, damping coefficient values of $D = 0.25$ and $D = 1$ will be used, respectively. They correspond to Leer damping ratios of approximately 0.01 and 0.04.
Finally, the second step of the parameter identification of the excited system is also performed by fitting on the measured angle data (see Fig. 4.27). The optimal parameter values corresponding to the second step are listed in Table 4.5. The change in the value of the parameter F is not very significant, around 10%. In the subsequent numerical simulation, we will use a value of $F = -0.9$ to account for the proportionality factor between the electromotor torque and the voltage.

Parameter	Value
A	84.0838
B	1582.89
C	0.00156
D	0.76176
E	0.72437
F	-0.8885
x_0	-0.2531
u_0	0

Table 4.5: Estimated parameter values corresponding to the second step of the optimization including excitation with $u_S(t) = 2.5 + 0.375\,\sin(1.75 \cdot 2\pi t)$ and added damping $U_D = 30\,V$

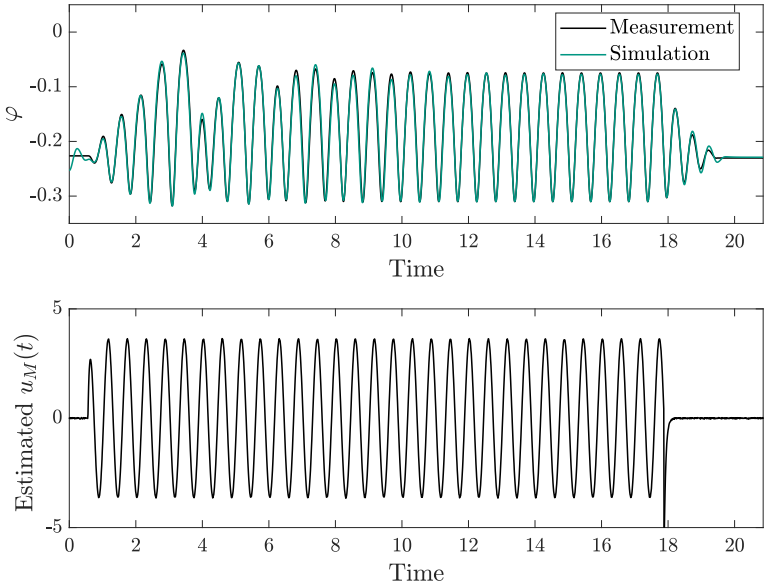

Figure 4.27: Comparison of the measurement data and numerical simulation with optimized parameters under external excitation $u_S(t) = 2.5 + 0.375 \sin(1.75 \cdot 2\pi t)$ and added damping $U_D = 30\,V$. The initial motion in the estimate before the excitation is turned in is observable due to the implementation of the Coulomb friction in Eq. (4.127), which is valid only for $\dot{\varphi} \neq 0$

Table 4.6 summarizes the parameter identification results, showing the values for the subsequent section's simulations.

Parameters	$U_D = 0\,V$	$U_D = 30\,V$
A	84	84
B	1600	1600
C	0	0
D	0.25	1
E	0.5	0.5
F	-0.9	-0.9

Table 4.6: Optimal parameter values used in simulations for validation of the V-curve

4.4.3 Measurement of the critical $\Omega - F_S$ curve with homogeneous initial conditions

In this section, measurement results corresponding to critical forcing values are presented. At the beginning of all measurements, the shaft rested at φ_3. The signal generator was set to

$$u_S(t) = \frac{F_S}{2} \sin\left(2\pi\Omega t + \beta\right), \tag{4.142}$$

with two different values for $\beta = \{0, \pi\}$. Two different voltage values were applied to the eddy current brake $U_D = \{0\,V, 30\,V\}$. If the shaft leaves the well corresponding to φ_3, escape is reported; otherwise, after 50 seconds, no escape is reported. This observation time interval is sufficient since the motion is damped and all transient processes decay during this time. The results are shown in Fig. 4.28. Deep blue color corresponds to escape, yellow color to no escape, and turquoise dots to cases when both scenarios could be observed with the same parameter values in consecutive experiments, which is only possible in the vicinity of the escape boundary and highlights the sensitivity of the measurement outcome for small, uncontrollable parameter fluctuations. Fig. 4.29 shows the $\Omega - F_S$ curves generated by numerical integration of the model identified in the previous section. Parameter values listed in Table 4.6 were used for the simulation. It is important to note that the power amplifier's frequency-dependent amplification factor is not included in the scale; in the numerical simulations, the amplifier's effect was taken into account to approximate the physical system's dynamics as accurately as possible.
Comparing Fig. 4.28 with Fig. 4.29, we can observe the following similarities in both the numerical and experimental results related to the critical excitation amplitudes:

- A sharp minimum exists, and the overall shape of the critical forcing boundary on the $\Omega - F_S$ plane is V-shaped, although uneven on its right-hand side due to the maximum mechanism.
- The curve's minimum is not at the linearized eigenfrequency of the well but is shifted to the left. In φ_3 the linearized eigenfrequency is $\sqrt{2A} = 12.96$ rad/s $= 2.06$ Hz. However, the measured minimum is around 1.7-1.8 Hz, depending on the damping value.
- The right-hand side of each plot contains escape 'bays' and no escape 'peninsulas.' An increasing excitation amplitude value does not automatically result in an escape; it might also return an already escaping scenario to a non-escaping one.
- The initial phase β plays a minor role in the escape process, mainly on the right-hand side of the V-curve.

- The excitation amplitude necessary to achieve escape increases significantly when damping is added to the system dynamics. While in the case without added damping, the minimum is at $F_S = 0.4$, in the case of added damping, it shifts to $F_S = 0.7$.
- Damping increases the value of the critical force amplitudes and shifts the curve's minimum to the left from 1.8 Hz to 1.7 Hz.
- On the left-hand side of the minimal critical force, the saddle mechanism dominates, while on the right-hand side, the maximum mechanism (see Figs. 4.32, 4.30a)
- The escape 'bays' and no-escape 'peninsulas' do not disappear when the viscous damping increases.

The agreement between the numerical simulations and the measurements mutually validates the accuracy of the results. Furthermore, the above observations agree with those described in earlier literature based on numerical simulations [67, 68].
In the following, some additional figures demonstrate the variety of nonlinear effects in the system. Fig. 4.30 shows that a larger excitation amplitude does not always result in escape if, with a lower amplitude, an escape has already occurred. However, this effect could only be observed on the right-hand side of the V-shaped critical force curve.
Fig. 4.31 shows chaotic escape. During more than 30 excitation periods, the particle remains in the well where its motion has started, yet all of a sudden, it escapes.
Fig. 4.32 shows how the saddle mechanism works. The amplitude increases slowly, approaching a critical distance from the saddle. At a point when it almost seems that it has reached a stationary state, the amplitude starts to increase rapidly, and within a few excitation periods, the system escapes from its original potential well.
In Fig. 4.33, a similar scenario is plotted; however, the jump after the gradual increase of the amplitude is not sufficient to directly reach the well's boundary; however, it comes close to it, spending enough time there to end up with a significantly different phase from the previous one. Now, the excitation pumps more energy into the system, causing escape.
Fig. 4.34 shows a scenario where the opposite of what we observed in Fig. 4.33 occurs. The amplitude first increases slowly, then rapidly, almost reaching the saddle, but finally falls back into the same well. Compared to the excitation, its phase is changed so that it has a smaller local maximum amplitude value in the next growth period than the previous one. After repeating this growth-decay period a couple more times, finally, transients are damped out, and the motion reaches a periodic, stationary motion.
Finally, Fig. 4.35 shows a parameter setting where the system sometimes remains in the original potential well and sometimes escapes. This observation indicates chaotic behavior.

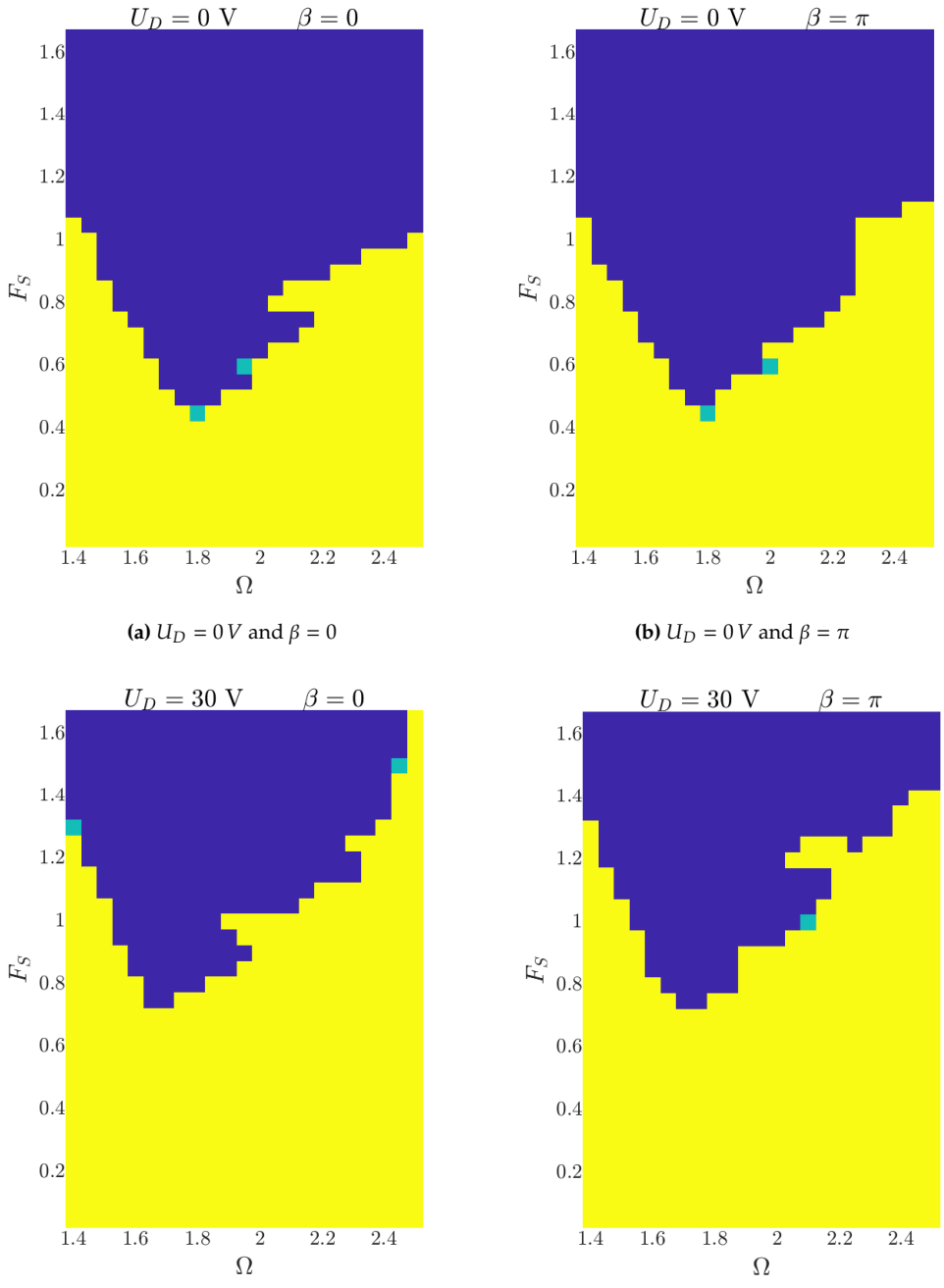

(a) $U_D = 0\,V$ and $\beta = 0$

(b) $U_D = 0\,V$ and $\beta = \pi$

(c) $U_D = 30\,V$ and $\beta = 0$

(d) $U_D = 30\,V$ and $\beta = \pi$

Figure 4.28: Measured $\Omega - F_S$ map with homogeneous initial conditions. $u_S(t) = \frac{F_S}{2}\sin(2\pi\Omega t + \beta)$. The yellow color represents no escape; the deep blue represents escape, and the turquoise when both were observed in consecutive measurements with the same parameters

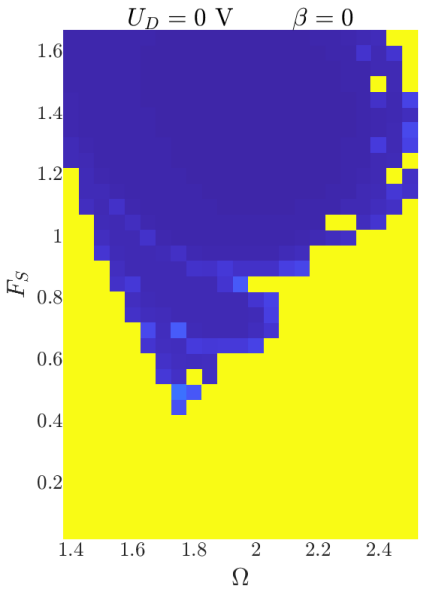

(a) $U_D = 0\,V$ and $\beta = 0$

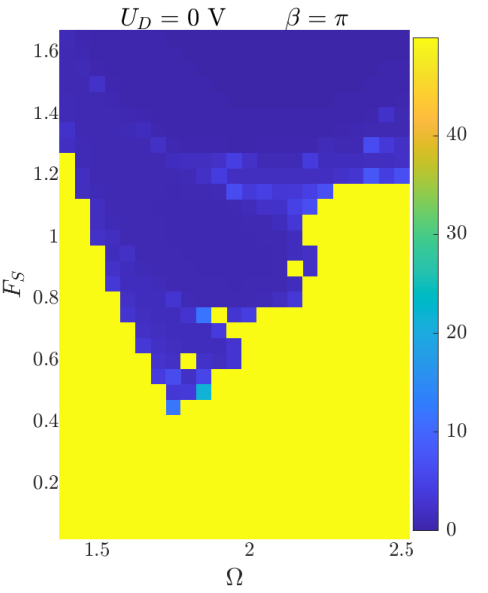

(b) $U_D = 0\,V$ and $\beta = \pi$

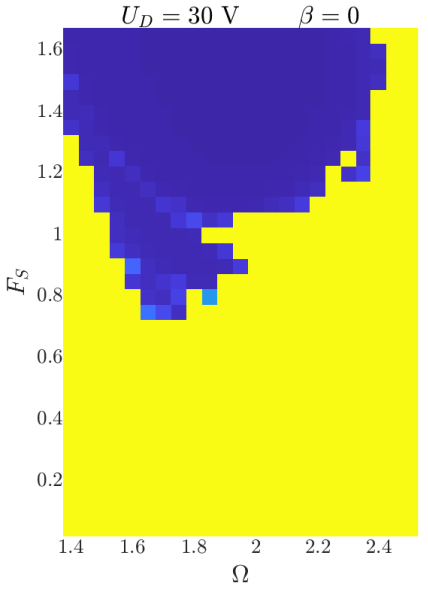

(c) $U_D = 30\,V$ and $\beta = 0$

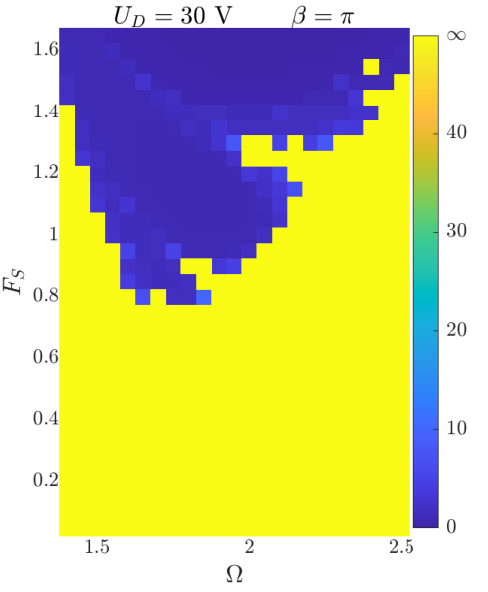

(d) $U_D = 30\,V$ and $\beta = \pi$

Figure 4.29: Simulated $\Omega - F_S$ map with homogeneous initial conditions. $u_S(t) = \frac{F_S}{2}\sin(2\pi\Omega t + \beta)$. The color scale represents the time necessary to escape. If no escape is observed after 50 seconds, the yellow color is used, and no escape is associated with the given parameter values

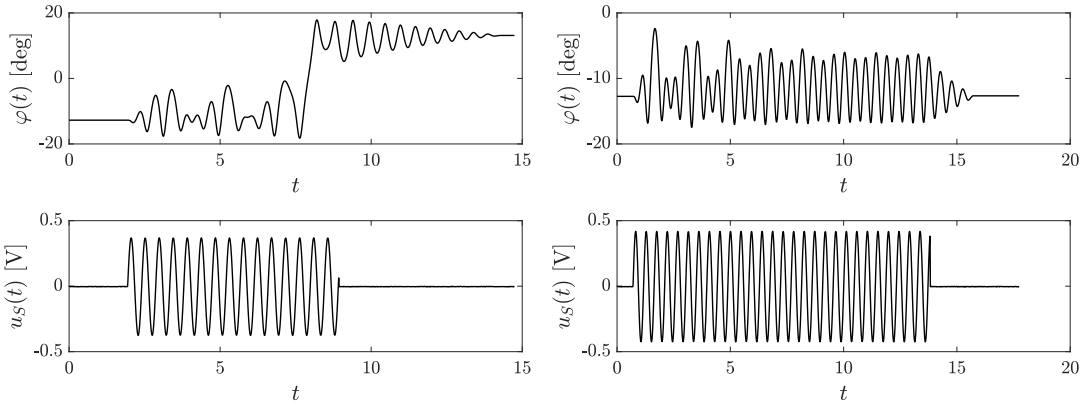

(a) Escape 'bay' with F_S = 375 mV

(b) No-escape 'peninsula' with F_S = 425 mV

Figure 4.30: Time series comparison of measurements with parameters from an escape 'bay' and a no-escape 'peninsula.' Ω = 2.15 Hz, U_D = 0 V, β = 0

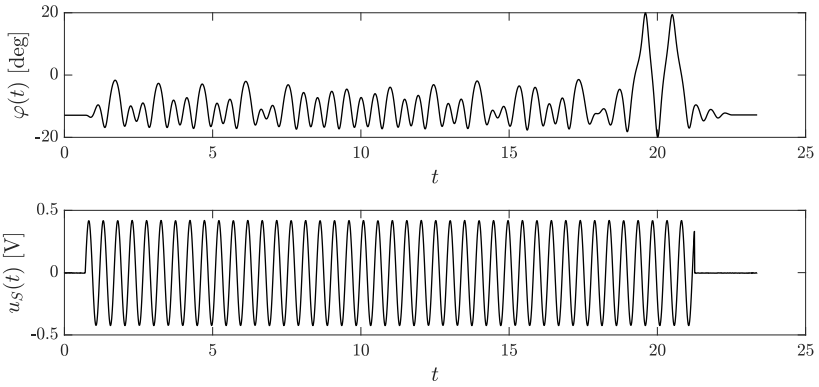

Figure 4.31: Chaotic escape with Type 1 MM, experimental data. F_S = 425 mV, Ω = 2.05 Hz, U_D = 0 V, β = 0

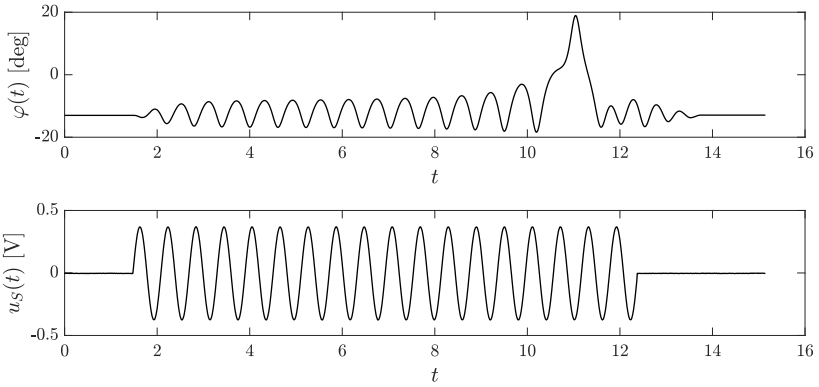

Figure 4.32: Escape through the SM, experimental data. F_S = 375 mV, Ω = 1.65 Hz, U_D = 30 V, β = 0

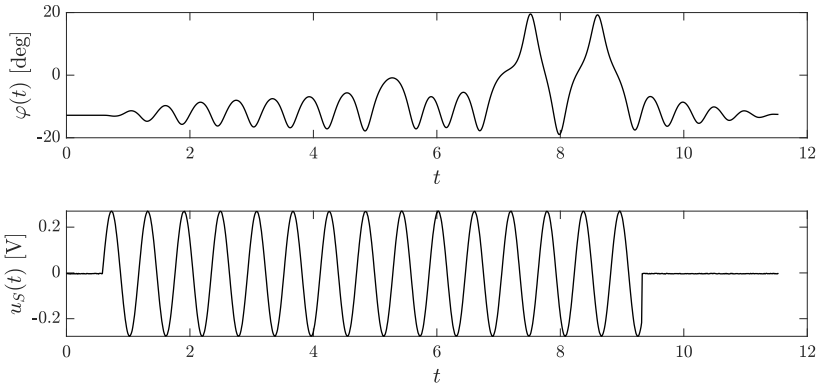

Figure 4.33: SM and Type 1 MM combined, experimental data. F_S = 275 mV, Ω = 1.7 Hz, U_D = 0 V, β = 0

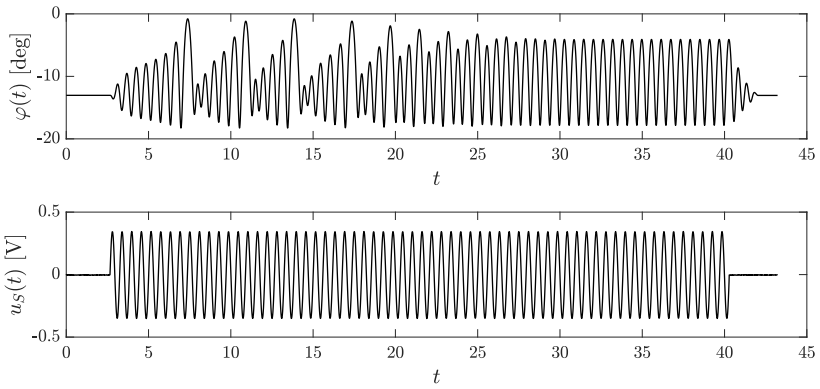

Figure 4.34: Non-escaping scenario with combined SM and Type 1 MM, experimental data. F_S = 350 mV, Ω = 1.7 Hz, U_D = 30 V, β = 0

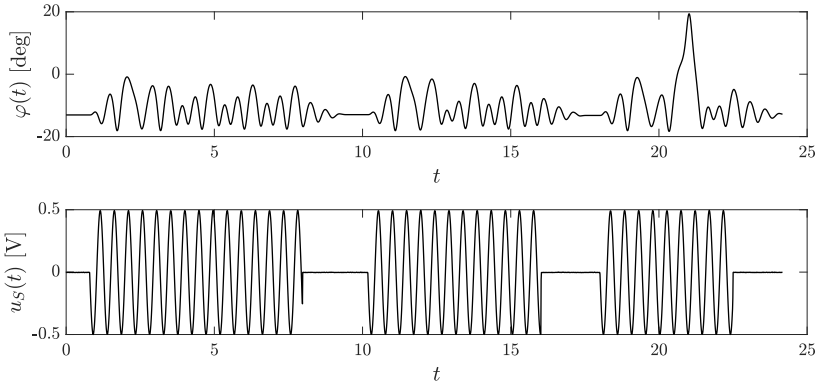

Figure 4.35: A chaotic scenario where for the same parameters and initial conditions, the system first remains within the well, but in a consecutive measurement escapes from the well, experimental data. F_S = 500 mV, Ω = 2.1 Hz, U_D = 30 V, $\beta = \pi$

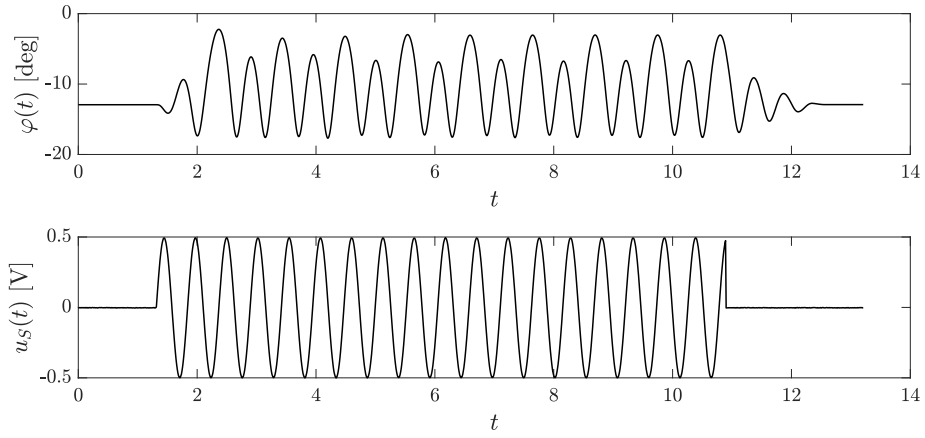

Figure 4.36: Jump into a solution with a double period, experimental data. $F_S = 1000$ mV, $\Omega = 1.9$ Hz, $U_D = 30$ V, $\beta = 0$

Although the escape time in the experiment was not directly measured, in most cases, we can observe that the fate of a trajectory, whether it escapes or not, is determined in the first few periods of the excitation. In the numerical simulations, we can explicitly observe this on the color scale where escape times larger than 20 seconds are rare, which means that few parameter combinations result in trajectories that 'survive' more than 30-50 excitation periods in the well. If they do so, their trajectory is chaotic (see Fig. 4.31). More commonly, if a trajectory does not escape in its first few 'attempts,' as in Figs. 4.34 and 4.30b, it reaches a steady-state vibration due to the damping, which we can also interpret as the 'slow' escape mechanism, described in Chapter 3, although the situation is more complicated here due to the significant nonlinearities. It is no longer valid that the first escape 'attempt' must succeed. For example, in Fig. 4.30a and 4.33, only the third and second 'attempts,' respectively, were successful.
Interestingly, non-escaping, steady-state solutions do not always have the same period as the excitation; a jump into a solution with a double period was, for example, observed in a measurement (see Fig. 4.36).

4.4.4 Measurement of the critical $\Omega - F_S$ curve for slowly increasing excitation amplitude

This section investigates the critical excitation amplitude necessary for escape without transients. We achieve this by slowly increasing the amplitude to a harmonic excitation, allowing enough time for the transients to decay. At a certain excitation amplitude, the steady-state solution always loses its stability, and depending on the excitation frequency,

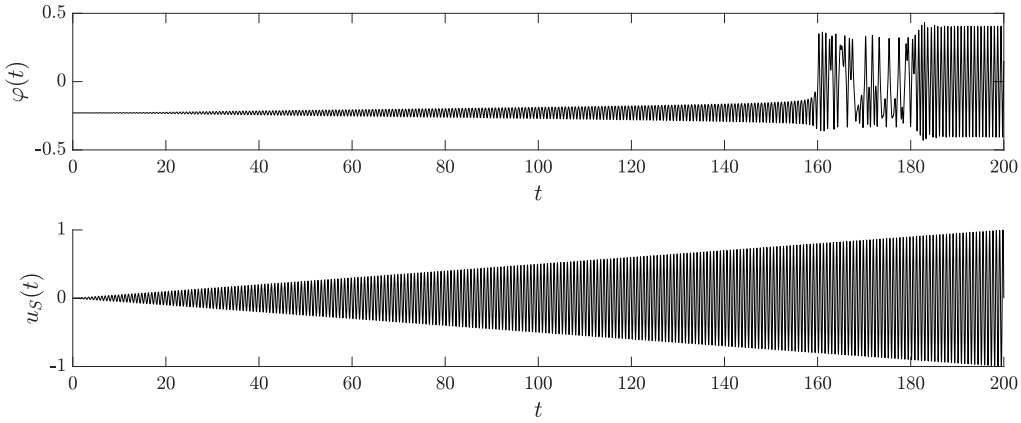

Figure 4.37: Numerical simulation time series data with amplitude sweep at $\Omega = 1.4$ Hz, $D = 1$. The starting phase is irrelevant in this case. Escape occurs at $F_{S,crit} = 1.601$ V. The saddle mechanism is observable; a sudden increase in the oscillation amplitude starts already far from the well's boundary. After the transient process following the escape, the solution finally stabilizes around a periodic, full-well oscillation

escape occurs rapidly (saddle mechanism), or a period-doubling cascade starts, finally leading to chaos and escape (maximum mechanism).
In the numerical simulations, the function generator's output is given by

$$u_S(t) = \frac{F_{\max}}{2} \frac{t}{t_{\max}} \sin(2\pi\Omega t), \tag{4.143}$$

with $F_{\max}$ V and $t_{\max}$ being large enough to surely drive out the particle from its original well with a quasi-statically increasing amplitude.
In this scenario, the excitation's initial phase is irrelevant since the system vibration will adjust to it rapidly.
This adjustment can be observed in the experiments and the numerical simulations with and without added viscous damping. Figs. 4.37)-(4.40 demonstrate the above observations graphically.
Fig. 4.41 shows the critical forcing amplitude values for the numerical and experimental results. We can observe that the sharp minimum also exists here. Furthermore, the numerical simulations predict this minimum with reasonable accuracy—an added viscous damping results in a shift of the minimum. The minimally necessary excitation amplitude increases from $F_S = 0.5$ V to $F_S = 0.8$ V. As before, the corresponding frequency also shifts towards the left, from around $\Omega_{\min} = 1.75$ Hz to $\Omega_{\min} = 1.65$ Hz. Considering that the linearized eigenfrequency of the system is around $\Omega_{\text{lin}} = 2.05$ Hz, this change is quite significant.

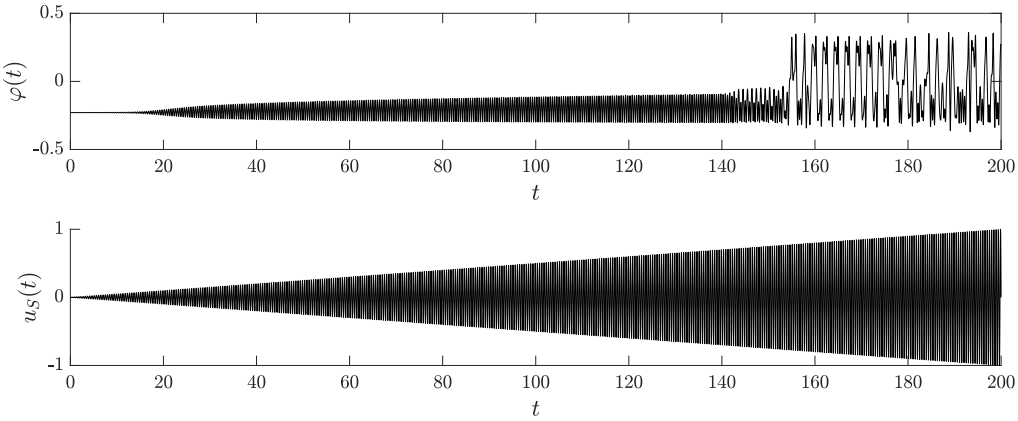

Figure 4.38: Numerical simulation time series data with amplitude sweep at $\Omega = 2.1$ Hz, $D = 1$. The starting phase is irrelevant in this case. Escape occurs at $F_{\mathrm{S,crit}} = 1.549$ V. Here, the maximum mechanism dominates. Escape is predictable due to the period-doubling bifurcations taking place just before reaching the critical excitation amplitde

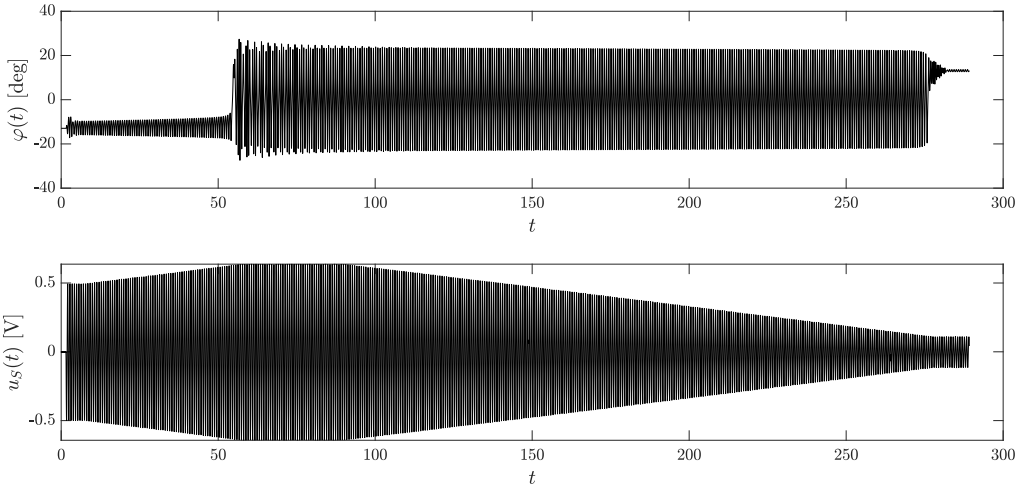

Figure 4.39: Experimental time series data with amplitude sweep at $\Omega = 1.4$ Hz, $U_D = 0$ V. The starting phase is irrelevant in this case. Escape occurs at $F_{\mathrm{S,crit}} = 1.244$ V. The saddle mechanism is observable; a sudden increase in the oscillation amplitude starts already far from the well's boundary. After the transients' decay, the solution's stabilization to a periodic full-well oscillation can be observed. This solution remains stable even when the excitation amplitude is decreased to a fraction of its previous value, causing escape. When the full-swing oscillation loses stability, the vibrations continue in a single well and reduce significantly in amplitude

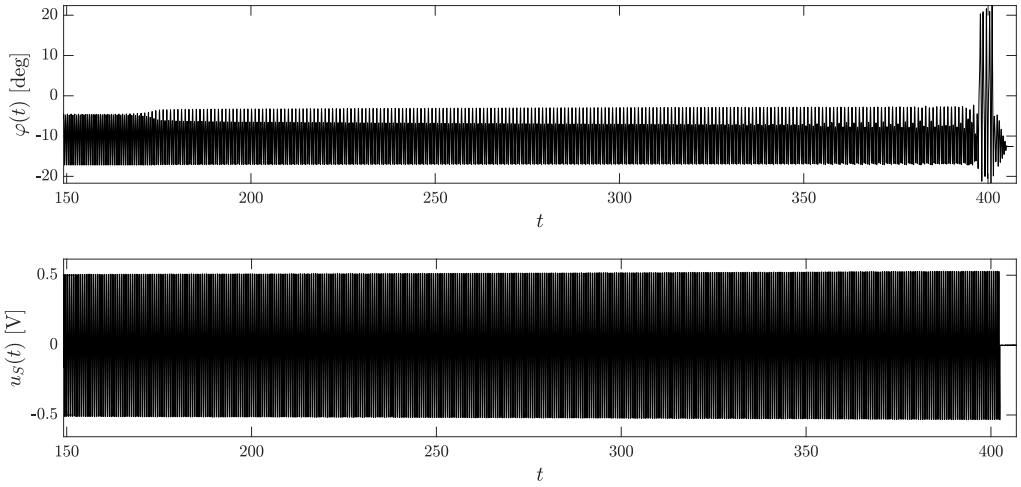

Figure 4.40: Experimental time series data with amplitude sweep at $\Omega = 2.0$ Hz, $U_D = 0$ V. The starting phase is irrelevant in this case. Escape occurs at $F_{S,crit} = 1.070$ V. Before escape occurs, a cascade of period-doubling bifurcation can be observed

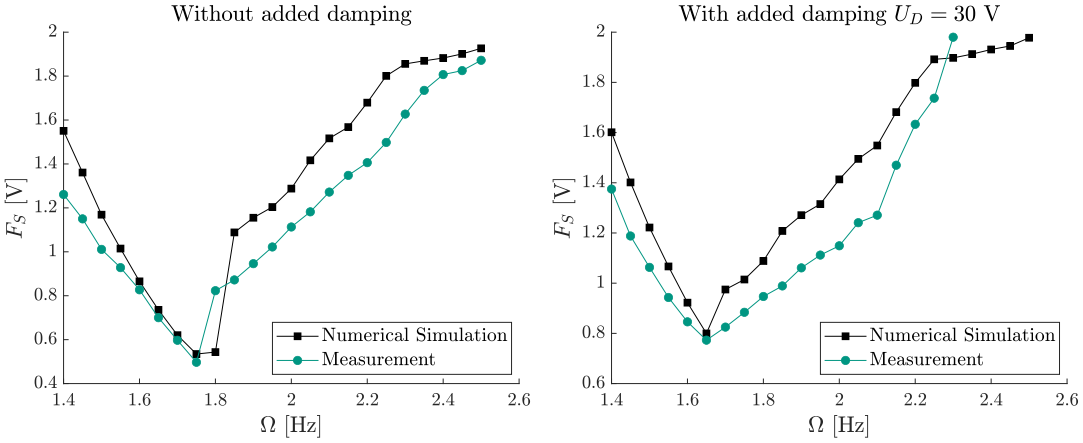

(a) Without additional damping

(b) With additional damping $U_D = 30$ V

Figure 4.41: Comparison of numerical results with the experimental ones by slowly increasing the excitation amplitude and noting its value at the moment of escape. Despite some quantitative differences, the prediction of the sharp minimum's location and value shows good agreement

4.4.5 Conclusions and scope for further research

The purpose of this section was to experimentally validate the escape mechanisms described previously in the literature [67, 68, 198] and in Chapters 3)-(4.
A test rig in ITM's laboratory has been modified and equipped with a high-precision, capacitive angle encoder. With the test rig, the precise setting of the viscous damping through eddy currents is possible, and an electromotor can apply arbitrarily shaped exciting torque.
The underlying model is estimated using a double-well Duffing oscillator, identifying model parameters encompassing viscous damping, dry friction, and excitation proportionality factors.
Compared to the simulation results of the identified model, the experimental results show a good agreement when comparing the critical forcing values of escape under harmonic excitation. Indeed, starting with homogeneous initial conditions, even such details as nonescaping 'peninsulas' and escape 'bays' are correctly identified. The appearance of these irregularities of the V-shaped critical force boundary may be related to the 'slow' escape mechanism. As Fig. 4.41 compared to Figs. 4.28)-(4.29 shows the amplitude values at which the escape 'bays' appear are lower than those necessary to cause escape from a quasi-steady-state solution. It indicates that escape in this amplitude regime is only possible because of transients. The envelope covering the vibrations, as in Fig. 3.13b in Sect. 3, has various peaks before reaching a steady-state solution. In the nonlinear case, although not always, the escape occurs at the first of these envelope peaks.
Even though a larger excitation amplitude can cause the vibration amplitude to increase more quickly, the highest point of the envelope encompassing the vibration is not always larger than the highest point of an envelope related to a smaller excitation, since the peak in the latter case occurs earlier than in the former, allowing the transients to decrease in the meantime.
An alternate interpretation suggests the coexistence of several attractors in the phase space, which possess intricately intertwined catchment areas in initial conditions and system and excitation parameters. As demonstrated in Fig. 4.39, there is a coexistence of periodic solutions and possibly even chaotic attractors, a determination that is challenging to make based on experiments due to the lengthy transients before a periodic solution is reached. For example, Fig. 4.42 presents a measurement in which the motion does not exhibit discernible patterns, leaving it uncertain whether continued observation would reveal a periodic solution.
Numerous potential avenues for future studies are raised. This research examined the proximity of 1:1 resonance. The possibility of sub- or superharmonic resonance occurring and its influence on the shape of the critical $\Omega - F$ curve is a fascinating inquiry.

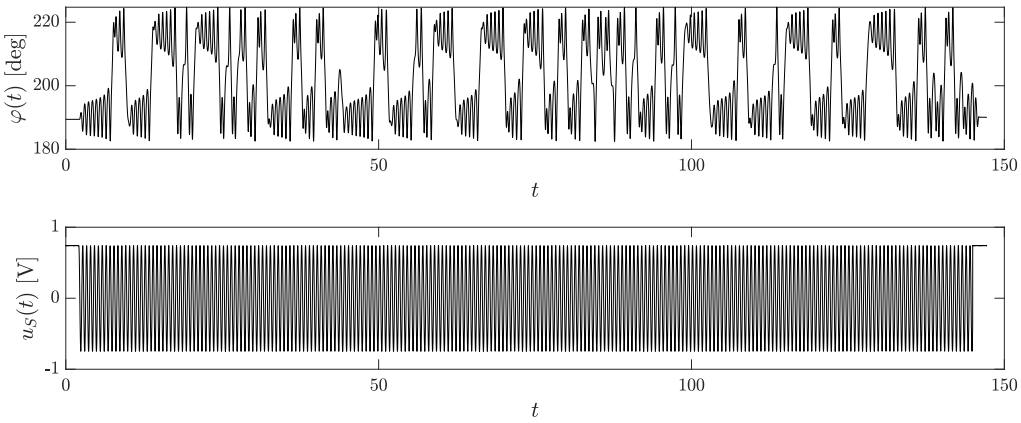

Figure 4.42: Measured time series data with harmonic excitation. $\Omega = 1.6$ Hz, $F_S = 1.5$ V, $U_D = 30$ V, $\beta = \pi/2$ and added dry friction (non-quantified). The motion seems to be chaotic and does not settle to a recognizable pattern

Investigating escape under frequency-modulated signals, particularly sweep signals, is another area of study with significant technical importance since, for a machine operating at a certain speed, it is essential to pass through resonance to reach its operational point. Similarly, when the machine is deactivated, it experiences a passage through resonance in the opposite direction. Understanding the working mechanisms of the saddle and maximum can allow us to anticipate varying system responses in both directions.

5 Escape of multibody systems with different time-scales

In the previous chapters, we investigated the escape of a single particle from a potential well. This chapter will focus on the escape of coupled particle systems. The common property of the analyzed systems is the presence of different time scales. The particles are strongly coupled, resulting in the chain's internal vibrations having frequencies much higher than the 'slow' vibrations of the chain's center of mass.
The text and figures of this chapter are based on the studies by *Genda et al.* [221, 222, 228].

5.1 Escape of an n-particle chain from a potential under polyharmonic excitation

In [221], *Genda et al.* investigated the escape dynamics of a pair of strongly coupled particles from a truncated quadratic potential under biharmonic excitation. The analysis was extended to strongly coupled n-particle chains under polyharmonic excitation in [228]. Since the latter case includes the former, we will provide only the more general version and an example with a three-particle chain.

5.1.1 Problem setting

We investigate the system shown in Figure 5.1. The scenario is constrained to one-dimensional movement along the x axis. The system consists of n particles, each with masses m_1, m_2, ..., m_n. Linear viscous damping acts between the neighboring particles, represented by $n-1$ dashpot dampers, each with a damping coefficient k_1, k_2, ..., k_{n-1}, and the elastic restoring force within the particles is provided by $n-1$ linear springs, each with a stiffness coefficient c_1, c_2, ..., c_{n-1}. A polyharmonic force of $F_1(t)$, $F_2(t)$, ..., $F_n(t)$ can act on each particle. Initially, the particles are placed within a potential well, and each particle experiences a unique restoring force given by $V_1(x_1)$, $V_2(x_2)$, ..., $V_n(x_n)$, where $V_i(x_i) = m_i V(x_i)$. The base potential $V(\cdot)$ is determined later.

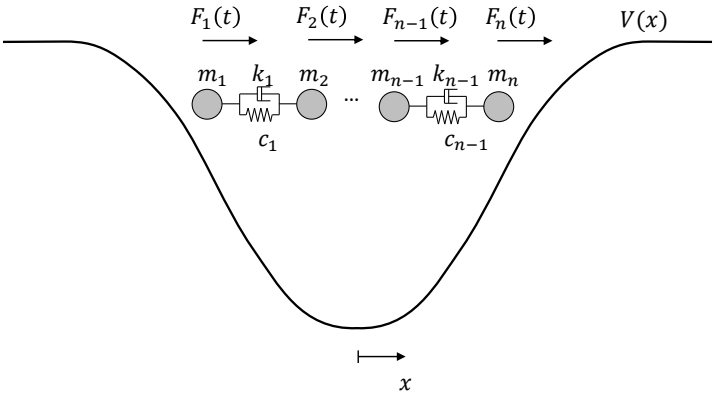

Figure 5.1: A potential well containing an internally damped, coupled n-particle system is considered. The particles in the system have an equilibrium distance of zero, which implies the possibility of mutual penetration without physical constraints. Figure adapted from [228]

It is important to note that particles can pass through each other in this model because of the zero equilibrium distance between them. For a model including particle collisions, refer to Sect. 5.2.

Derivation of the equations of motion

We formulate the equations of motion for the system described by applying the Euler-Lagrange equations.

$$\frac{\mathrm{d}}{\mathrm{d}t}\frac{\partial T}{\partial \dot{q}_i}(t,\dot{\mathbf{q}}(t)) = -\frac{\partial U}{\partial q_i}(t,\mathbf{q}(t)) - \frac{\partial D}{\partial \dot{q}_i}(t,\dot{\mathbf{q}}(t)) + Q_i^*(t) \qquad \text{for } i = 1,\ldots,n, \tag{5.1}$$

where $q_i = x_i$ represent the generalized coordinates, and

$$T = \sum_{i=1}^{n} \frac{1}{2} m_i \dot{x}_i^2, \tag{5.2}$$

$$U = \sum_{i=1}^{n-1} \frac{1}{2} c_i (x_{i+1} - x_i)^2 + V_i(x_i), \tag{5.3}$$

$$D = \sum_{i=1}^{n-1} \frac{1}{2} k_i (\dot{x}_{i+1} - \dot{x}_i)^2, \tag{5.4}$$

$$Q_i^*(t) = F_i(t) = F_{i,0}\sin(\Omega_0 t + \beta_{i,0}) + \sum_{p=1}^{P} F_{i,p}\sin\left(\Omega_{i,p} t + \beta_{i,p}\right), \tag{5.5}$$

with P belonging to the positive natural numbers $\mathbb{N}^+$. The continuous potential $V(x)$ is required to be bounded above, meaning

$$\lim_{|x|\to\infty} V(x) \leq C, \text{ for some } C \in \mathbb{R}. \tag{5.6}$$

Additionally, the system is scaled such that the potential well has a stable equilibrium point at $x = 0$, with its linearized angular eigenfrequency 1, that is:

$$V'(x = 0) = 0, \tag{5.7}$$
$$V''(x = 0) = 1. \tag{5.8}$$

In the following, the term frequency will signify the angular frequency measured in radians per second.
Moreover, we assert that $V(x)$ has a single well W and exhibits a softening behavior as delineated by:

$$V''(x) \leq \frac{V'(x)}{x} \leq 1. \tag{5.9}$$

This inequality is derived from the notion of a 'softening characteristic,' where the stiffness of the potential, defined as $c(x) := V'(x)/x$, diminishes as one moves away from the well's bottom, denoted by an increasing $|x|$. Conversely, the maximal stiffness at $x = 0$ is expressed as:

$$\lim_{x\to 0} \frac{V'(x)}{x} = \lim_{x\to 0} \frac{V'(x) - V'(0)}{x - 0} = V''(x)|_{x=0} = 1. \tag{5.10}$$

Considering that $V(x)$ is bounded above, the maximum on the left-hand side of $V(x)$ is marked as x_l, with x_l belonging to $\mathbb{R}^- \cup \{-\infty\}$, and the maximum on the right-hand side is denoted as x_r, with x_r in $\mathbb{R}^+ \cup \{\infty\}$. Thus, the well is given by $W = (x_l, x_r)$.
Escape is defined as before in Def. 3.0.3, but now, all particles must satisfy the definition. Given the strong coupling between the particles, separation of the particle chain is unfeasible, i.e., the case is not possible when some particles escape to the right while others escape to the left side of the well. Fig. 5.2 provides a visual illustration of a potential that meets these criteria.
It is assumed that the masses m_i are of order $O(1)$, and the forces exerted by the coupling springs substantially surpass those attributed to the potential, i.e., $c_i \gg 1 \geq \max_{x\in(x_l,x_r)} V_i''(x)$, which implies $c_i \in O(\varepsilon^{-1})$. Further, non-small damping is assumed, with k_i being of order $O(1)$. Given these assumptions regarding c_i and k_i, the internal modes of the chain exhibit underdamped characteristics, leading to the receptance frequency response function displaying $n - 1$ local maxima (cf. Fig. 5.3). These

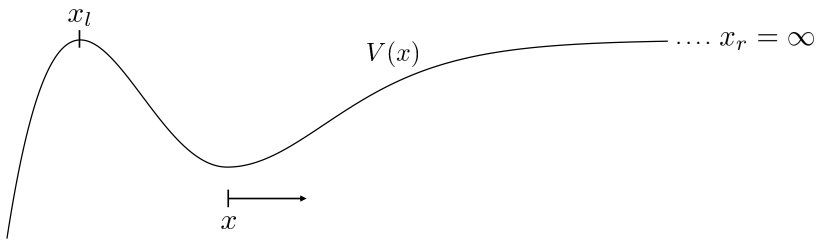

Figure 5.2: Illustration of a potential that is considered feasible. The potential's interior extends from x_l to x_r. Figure adapted from [228]

peaks are identified as *resonant frequencies*. It is hypothesized that the lowest resonant frequency for relative movements within the particle chain markedly surpasses the linearized eigenfrequency of the potential well.
Each particle is excited by up to $P + 1$ harmonic forces, of which one component is assumed to have the same low frequency $\Omega_0 \in O(1)$, but can vary in the excitation amplitude $F_{i,0}$ and initial phase $\beta_{i,0}$.
Subsequent excitation frequencies are considered significantly higher than the base frequency, that is, $\Omega_{i,p} \gg \Omega_0$, and are not necessarily uniform across all particles, meaning that $\Omega_{i,p}$ may vary independently from $\Omega_{j,p}$.
These excitation patterns are particularly relevant in the context of cantilever beams employed as sensors within microelectromechanical systems. A notable application is observed in atomic force microscopy, where a transcendental equation determines the cantilever beam's eigenfrequencies and are linearly independent over the rational numbers (cf. Def. 2.3.7).
Incorporating Eqs. (5.2-5.5) into Eq. (5.1) leads to the nonlinear differential equation system:

$$\mathbf{M}\ddot{\mathbf{x}} + \mathbf{K}\dot{\mathbf{x}} + \mathbf{C}\mathbf{x} + \mathbf{v}'(\mathbf{x}) = \mathbf{f}(t), \tag{5.11}$$

where the matrices and vectors are defined as follows:

$$\mathbf{M} = \operatorname{diag}(m_1, m_2, \ldots, m_n) \in \mathbf{R}^{n\times n}, \tag{5.12}$$

$$\begin{aligned}\mathbf{K} = {} & \operatorname{diag}(k_1, k_1 + k_2, \ldots, k_{n-2} + k_{n-1}, k_{n-1}) - \operatorname{subdiag}(k_1, k_2, \ldots, k_{n-1}) \\ & - \operatorname{superdiag}(k_1, k_2, \ldots, k_{n-1}) \in \mathbf{R}^{n\times n},\end{aligned} \tag{5.13}$$

$$\begin{aligned}\mathbf{C} = {} & \operatorname{diag}(c_1, c_1 + c_2, \ldots, c_{n-2} + c_{n-1}, c_{n-1}) - \operatorname{subdiag}(c_1, c_2, \ldots, c_{n-1}) \\ & - \operatorname{superdiag}(c_1, c_2, \ldots, c_{n-1}) \in \mathbf{R}^{n\times n},\end{aligned} \tag{5.14}$$

$$\mathbf{x} = \left[x_1, x_2, \ldots, x_n\right]^\top \in \mathbf{R}^n, \tag{5.15}$$

$$\mathbf{v}'(\mathbf{x}) = \left[V_1'(x_1), V_2'(x_2), \ldots, V_n'(x_n)\right]^\top \in \mathbf{R}^n, \tag{5.16}$$

$$\mathbf{f}(t) = \left[F_1(t), F_2(t), \ldots, F_n(t)\right]^\top \in \mathbf{R}^n, \tag{5.17}$$

with diag(·), subdiag(·), and superdiag(·) indicating diagonal, subdiagonal, and superdiagonal matrices, respectively. Moreover, bold lowercase symbols indicate vectors in the time domain, whereas bold uppercase symbols represent matrices. In line with the standard literature notation, the vectors denoting Laplace transforms are also represented by bold uppercase characters.

Coordinate decoupling

Currently, the differential equation manifests strong coupling among the coordinates in a nonlinear manner. Moreover, the significant stiffness of the springs, in contrast to the potential's moderate restoring force, leads to a slow-fast dynamic within the system. By implementing a suitable coordinate transformation, we can achieve a formulation where the nonlinear terms only weakly couple the system, leaving the linear terms to dominate the coupling. This simplification allows for the analytical treatment of the resulting 'fast' linear system of ordinary differential equations, facilitating the derivation of analytical solutions for the 'fast' variables and permitting the focus to shift exclusively to the analysis of the 'slow' variable. The approach is as follows.
New coordinates, η and y_i for $i \in \{2, \ldots, n\}$, are introduced as:

$$\eta = \frac{\sum_{i=1}^n m_i x_i}{\sum_{i=1}^n m_i} \quad \text{and} \quad y_i = x_i - x_{i-1}, \quad \text{for } i \geq 2. \tag{5.18}$$

Here, the first coordinate, η, signifies the center of mass for the chain, while the subsequent coordinates, y_i, denote the relative displacements between adjacent particles. Defining $M = \sum_{i=1}^n m_i$, the transformation is expressed as:

$$\mathbf{y} = \begin{bmatrix} \eta \\ y_2 \\ y_3 \\ \vdots \\ y_n \end{bmatrix} = \underbrace{\begin{bmatrix} \frac{m_1}{M} & \frac{m_2}{M} & \frac{m_3}{M} & \cdots & \frac{m_n}{M} \\ -1 & 1 & 0 & \ldots & 0 \\ 0 & -1 & 1 & \ddots & \vdots \\ \vdots & \ddots & \ddots & \ddots & 0 \\ 0 & \ldots & 0 & -1 & 1 \end{bmatrix}}_{=:\mathbf{S}^{-1}} \begin{bmatrix} x_1 \\ x_2 \\ x_3 \\ \vdots \\ x_n \end{bmatrix}. \tag{5.19}$$

Introducing the notation $M_{kl} = \sum_{i=k}^{l} m_i$, where $l > c \in \mathbb{N}^+$, enables us to determine $\mathbf{S}$, the transformation matrix for converting coordinates from $\mathbf{y}$ to $\mathbf{x}$ as follows:

$$\mathbf{S} = \frac{1}{M}\begin{bmatrix} M & -M_{2n} & -M_{3n} & \dots & \dots & \dots & -M_{nn} \\ M & M_{11} & -M_{3n} & \dots & \dots & \dots & -M_{nn} \\ M & M_{11} & M_{12} & -M_{4n} & \dots & \dots & -M_{nn} \\ \vdots & & & & \ddots & & \vdots \\ M & M_{11} & \dots & M_{1(k-1)} & -M_{(k+1)n} & \dots & -M_{nn} \\ M & M_{11} & \dots & \dots & \dots & M_{1(n-2)} & M_{1(n-1)} \end{bmatrix}. \tag{5.20}$$

For the new coordinate system $\mathbf{y}$, the matrices representing damping and stiffness are expressed as

$$\tilde{\mathbf{K}} = \begin{bmatrix} 0 & 0 & 0 & \dots & \dots & 0 \\ 0 & \frac{k_1}{m_1} + \frac{k_1}{m_2} & -\frac{k_2}{m_2} & 0 & \dots & 0 \\ \vdots & -\frac{k_1}{m_2} & \frac{k_2}{m_2} + \frac{k_2}{m_3} & -\frac{k_3}{m_3} & \ddots & \vdots \\ & \ddots & & \ddots & & 0 \\ \vdots & & 0 & -\frac{k_{n-3}}{m_{n-2}} & \frac{k_{n-2}}{m_{n-2}} + \frac{k_{n-2}}{m_{n-1}} & -\frac{k_{n-1}}{m_{n-1}} \\ 0 & \dots & & 0 & -\frac{k_{n-2}}{m_{n-1}} & \frac{k_{n-1}}{m_{n-1}} + \frac{k_{n-1}}{m_n} \end{bmatrix}, \tag{5.21}$$

$$\tilde{\mathbf{C}} = \begin{bmatrix} 0 & 0 & 0 & \dots & \dots & 0 \\ 0 & \frac{c_1}{m_1} + \frac{c_1}{m_2} & -\frac{c_2}{m_2} & 0 & \dots & 0 \\ \vdots & -\frac{c_1}{m_2} & \frac{c_2}{m_2} + \frac{c_2}{m_3} & -\frac{c_3}{m_3} & \ddots & \vdots \\ & \ddots & & \ddots & & 0 \\ \vdots & & 0 & -\frac{c_{n-3}}{m_{n-2}} & \frac{c_{n-2}}{m_{n-2}} + \frac{c_{n-2}}{m_{n-1}} & -\frac{c_{n-1}}{m_{n-1}} \\ 0 & \dots & 0 & 0 & -\frac{c_{n-2}}{m_{n-1}} & \frac{c_{n-1}}{m_{n-1}} + \frac{c_{n-1}}{m_n} \end{bmatrix}. \tag{5.22}$$

In the transformed coordinate system, it becomes evident that the internal viscous damping no longer influences the center of mass η.
Substituting $\mathbf{x} = \mathbf{S}\mathbf{y}$ into Eq. (5.11), the motion equations in new coordinates can be written as:

$$\mathbf{M}\mathbf{S}\ddot{\mathbf{y}} + \mathbf{K}\mathbf{S}\dot{\mathbf{y}} + \mathbf{C}\mathbf{S}\mathbf{y} + \mathbf{v}'(\mathbf{S}\mathbf{y}) = \mathbf{f}(t), \tag{5.23}$$

$$\ddot{\mathbf{y}} + \underbrace{\mathbf{S}^{-1}\mathbf{M}^{-1}\mathbf{K}\mathbf{S}}_{=:\tilde{\mathbf{K}}}\dot{\mathbf{y}} + \underbrace{\mathbf{S}^{-1}\mathbf{M}^{-1}\mathbf{C}\mathbf{S}}_{=:\tilde{\mathbf{C}}}\mathbf{y} + \underbrace{\mathbf{S}^{-1}\mathbf{M}^{-1}\mathbf{v}'(\mathbf{S}\mathbf{y})}_{=:\tilde{\mathbf{v}}'} = \underbrace{\mathbf{S}^{-1}\mathbf{M}^{-1}\mathbf{f}(t)}_{=:\tilde{\mathbf{f}}(t)}. \tag{5.24}$$

This transformation simplifies the analysis of the dynamics by decoupling the 'slow' and 'fast' variables.
The matrices $\tilde{\mathbf{K}}$ and $\tilde{\mathbf{C}}$, given in Eqs. (5.21)-(5.22), illustrate the system's transformed stiffness and damping characteristics, respectively. In further analysis, we compute the modified potential force vector $\tilde{\mathbf{v}}'$ as follows:

$$\tilde{\mathbf{v}}' = \mathbf{S}^{-1}\mathbf{M}^{-1}\begin{bmatrix} m_1 V'(\mathbf{s}_1\mathbf{y}) \\ m_2 V'(\mathbf{s}_2\mathbf{y}) \\ \vdots \\ m_n V'(\mathbf{s}_n\mathbf{y}) \end{bmatrix} = \begin{bmatrix} \frac{\sum_{i=1}^{n} m_i V'(\mathbf{s}_i\mathbf{y})}{M} \\ V'(\mathbf{s}_2\mathbf{y}) - V'(\mathbf{s}_1\mathbf{y}) \\ \vdots \\ V'(\mathbf{s}_n\mathbf{y}) - V'(\mathbf{s}_{n-1}\mathbf{y}) \end{bmatrix}, \tag{5.25}$$

utilizing the notation $\mathbf{S} = (\mathbf{s}_1, \mathbf{s}_2, \ldots, \mathbf{s}_n)e^{\mathrm{T}}$, where each $\mathbf{s}_i \in \mathbb{R}^n$.
According to [61] and [62], the particular solutions for $y_2 \ldots y_n$ are minimally affected by their coupling to η, attributable to the non-small damping between the particles and the weak coupling to the 'outer' potential field, given that $c_i/m_i \in O(\varepsilon^{-1})$. In contrast, the maximum stiffness of the potential, $\max_{x\in(x_l,x_r)} V'(x)/x$, is of order $O(1)$.
Assuming small relative displacements, that is, $|y_i| < 1$ for $i = 2 \ldots n$, and considering that the particles predominantly reside within the potential well, i.e., $x_i \in W = (x_l, x_r)$, the potential force can be linearized around x_{i-1} as:

$$V'(x) \approx V'(x_{i-1}) + V''(x_{i-1})(x - x_{i-1}), \tag{5.26}$$

and given $\mathbf{s}_i\mathbf{y}_i = x_i$, we deduce:

$$V'(\mathbf{s}_i\mathbf{y}) - V'(\mathbf{s}_{i-1}\mathbf{y}) \approx V''(x_{i-1})y_i, \tag{5.27}$$

which can be disregarded since $V''(x) \leq 1 \ll c_i$ according to our assumptions. Therefore, the vector simplifies to:

$$\tilde{\mathbf{v}}' \approx \left[\frac{\sum_{i=1}^{n} m_i V'(\mathbf{s}_i\mathbf{y})}{M}, 0, \ldots, 0\right]^{\top}. \tag{5.28}$$

Analogously, the transformed force vector $\tilde{\mathbf{f}}(t)$ is calculated as:

$$\tilde{\mathbf{f}}(t) = \left[\frac{\sum_{i=1}^{n} F_i(t)}{M}, \frac{F_2(t)}{m_2} - \frac{F_1(t)}{m_1}, \ldots, \frac{F_n(t)}{m_n} - \frac{F_{n-1}(t)}{m_{n-1}}\right]^{\top}. \tag{5.29}$$

It is important to note that while a linear model can effectively approximate the 'fast' subsystem by neglecting nonlinear terms, such a simplification is unattainable for the 'slow' subsystem. The omission of nonlinearities in the equation of η would significantly alter its dynamics, primarily because the 'fast' dynamics is influenced by the linear

springs and dampers, whose effects are neutralized in the 'slow' system, leaving the potential's force as the primary dynamic driver for the center of mass.

Steady-state solutions for the fast subsystem

Analytically deriving the eigenmodes, eigenfrequencies, and specific solutions for $y_2(t)...y_n(t)$ in a closed form with arbitrary parameter values is often unfeasible. Therefore, the focus shifts to a particular scenario where all masses, dampers, and springs are uniform, i.e., $m_i = m$, $k_i = k$, and $c_i = c$ for all $i \in \{1, \dots, n\}$ and $i \in \{1, \dots, n-1\}$, respectively. The center of mass's equation of motion simplifies to:

$$\ddot{\eta} + \frac{\sum_{i=1}^{n} V'(\mathbf{s}_i \mathbf{y})}{n} = \frac{\sum_{i=1}^{n} F_i(t)}{nm}. \tag{5.30}$$

Addressing Eq. (5.30) necessitates initial resolution for $y_2, \dots, y_n$, achieved by considering the matrix sub-section that excludes the first row and column, thus yielding:

$$\overline{\mathbf{y}} = [y_2 \quad y_3 \quad \dots \quad y_n]^\top \in \mathbb{R}^{n-1}, \tag{5.31}$$

$$\overline{\mathbf{K}} = \tilde{\mathbf{K}}_{2:n,2:n} \in \mathbb{R}^{(n-1)\times(n-1)}, \tag{5.32}$$

$$\overline{\mathbf{C}} = \tilde{\mathbf{C}}_{2:n,2:n} \in \mathbb{R}^{(n-1)\times(n-1)}, \tag{5.33}$$

$$\bar{\mathbf{f}} = \tilde{\mathbf{f}}_{2:n} \in \mathbb{R}^{n-1}, \tag{5.34}$$

where the subscript notation $p : q$ and $p : q, r : s$ refers to vector and matrix segments, respectively. The reduced system's motion equations are encapsulated as:

$$\ddot{\overline{\mathbf{y}}} + \overline{\mathbf{K}}\dot{\overline{\mathbf{y}}} + \overline{\mathbf{C}}\overline{\mathbf{y}} = \bar{\mathbf{f}}(t), \tag{5.35}$$

where $\overline{\mathbf{K}}$ and $\overline{\mathbf{C}}$ represent tridiagonal Toeplitz matrices.
Given the non-negligible damping values, the homogeneous solution of the differential equation decays rapidly, leading our interest toward the particular solution in response to polyharmonic excitation. Using the linear nature of the simplified problem, we can determine this solution by applying the Laplace transform. Assuming that initial conditions are null, the Laplace transform of Eq. (5.35) is represented as:

$$s^2\overline{\mathbf{Y}}(s) + s\overline{\mathbf{K}\mathbf{Y}}(s) + \overline{\mathbf{C}\mathbf{Y}}(s) = \bar{\mathbf{F}}(s), \tag{5.36}$$

where $\overline{\mathbf{Y}}(s) = \mathcal{L}\{\overline{\mathbf{y}}(t)\}$ and $\bar{\mathbf{F}}(s) = \mathcal{L}\{\bar{\mathbf{f}}(t)\}$, leading to:

$$\underbrace{\begin{bmatrix} s^2+2\frac{k}{m}s+2\frac{c}{m} & -\frac{k}{m}s-\frac{c}{m} & 0 & \dots & 0 \\ -\frac{k}{m}s-\frac{c}{m} & \ddots & \ddots & \ddots & \vdots \\ 0 & \ddots & \ddots & \ddots & 0 \\ \vdots & \ddots & \ddots & \ddots & -\frac{k}{m}s-\frac{c}{m} \\ 0 & \dots & 0 & -\frac{k}{m}s-\frac{c}{m} & s^2+2\frac{k}{m}s+2\frac{c}{m} \end{bmatrix}}_{=:\mathbf{A}(s)} \begin{bmatrix} Y_2 \\ Y_3 \\ \vdots \\ Y_{n-1} \\ Y_n \end{bmatrix} = \begin{bmatrix} \overline{F}_2 \\ \overline{F}_3 \\ \vdots \\ \overline{F}_{n-1} \\ \overline{F}_n \end{bmatrix}. \tag{5.37}$$

Introducing $a = s^2 + 2\frac{k}{m}s + 2\frac{c}{m}$ to denote the main diagonal values and $b = -\frac{k}{m}s - \frac{c}{m}$ for the values of the sub and superdiagonals, the eigenvalues λ_K, for $K = 1...n-1$, of the matrix are determined as:

$$\lambda_K = a - 2b\cos\left(\frac{K\pi}{n}\right), \tag{5.38}$$

with the corresponding eigenvectors being:

$$\mathbf{v}^K = \left[\sin\left(\frac{\pi K}{n}\right), \dots, \sin\left(\frac{(n-1)\pi K}{n}\right)\right]^\top, \quad K \in \{1, \dots, n-1\}. \tag{5.39}$$

The eigenvectors in this representation are not of unit length, so they need to be normalized. The K^{th} eigenvector has length

$$\left|\mathbf{v}^K\right| = \sqrt{\sum_{l=1}^{n-1} \sin^2\left(\frac{l\pi K}{n}\right)} = \sqrt{\frac{n-1}{2} - \frac{1}{2}\underbrace{\sum_{l=1}^{n-1}\cos\left(\frac{2\pi l K}{n}\right)}_{=-1}} = \sqrt{\frac{n}{2}}, \tag{5.40}$$

which is derived using the trigonometric identity $\sin^2 x = \frac{1-\cos 2x}{2}$ and the summation property of roots of unity. We can observe that all eigenvectors share the same magnitude. The orthogonal and symmetric matrix $\mathbf{Q}$ is formed as:

$$\mathbf{Q} = \sqrt{\frac{2}{n}}\left[\mathbf{v}^1, \quad \mathbf{v}^2, \quad \dots, \quad \mathbf{v}^{n-1}\right], \tag{5.41}$$

implying $\mathbf{Q} = \mathbf{Q}^{-1} = \mathbf{Q}^\top$. Thus, $\mathbf{A} \in \mathbb{C}^{(n-1)\times(n-1)}$ can be decomposed as:

$$\mathbf{A} = \mathbf{Q}\mathbf{\Lambda}\mathbf{Q}^\top = \mathbf{Q}\mathbf{\Lambda}\mathbf{Q}, \tag{5.42}$$

facilitating the expression of $\mathbf{A}^{-1}$ as:

$$\mathbf{A}^{-1} = \mathbf{Q}\mathbf{\Lambda}^{-1}\mathbf{Q}. \tag{5.43}$$

The entries of $\mathbf{A}^{-1}$ are then:

$$A_{ij}^{-1}(s) = \frac{2}{n}\sum_{K=1}^{n-1} \frac{\sin\left(\frac{i\pi K}{n}\right)\sin\left(\frac{j\pi K}{n}\right)}{s^2 + 2\frac{k}{m}s + 2\frac{c}{m} - 2\left(\frac{k}{m}s + \frac{c}{m}\right)\cos\left(\frac{\pi K}{n}\right)}. \tag{5.44}$$

By the system's linearity, the particular solution for the polyharmonic excitation is deduced by assessing the impact of a single harmonic excitation and then applying superposition for all harmonic forces affecting the particle chain.
To begin, we analyze the response to a harmonic function $F_i \sin(\omega_i t + \beta_i)$, applied to the i^{th} reduced coordinate (not the i^{th} particle), where $i \in \{1, \ldots, n-1\}$. The response is given by

$$\overline{\mathbf{Y}}(s = \jmath\omega_i) = \mathbf{A}^{-1}(\jmath\omega_i)\left[0, \ldots, F_i e^{\jmath\beta_i}, \ldots, 0\right]^\top = F_i e^{\jmath\beta_i}\mathbf{a}_i^{-1}(\jmath\omega_i), \tag{5.45}$$

where $\mathbf{a}_i^{-1}$ signifies the i^{th} column within the inverse of matrix $\mathbf{A}$, and $\jmath$ represents the imaginary unit. Consequently, the expression for the K^{th} row of vector $\overline{\mathbf{y}}(t)$ is expressed as

$$\overline{y}_K(t) = \left|\overline{Y}_K(\omega_i)\right| \sin\Big(\omega_i t + \overline{\Psi}_K(\omega_i)\Big), \tag{5.46}$$

where the phase angle $\overline{\Psi}_K(\omega_i)$ equates to the argument $\angle\overline{Y}_K(\omega_i)$.
When the i^{th} particle is excited according to Eq. (5.5), in the y coordinates, such excitation appears twice, as outlined by Eq. (5.29), except at the end of the chain, where it occurs only once. Therefore, we have $2(P+1)(n-1)$ distinct harmonic components combined. The complex amplitudes of the simple harmonic excitation on the i^{th} particle, due to the p^{th} harmonic excitation, $p \in \{0, \ldots, P\}$, manifesting with either a positive or negative sign as depicted in Eq. (5.29), are denoted by $\overline{\mathbf{Y}}_{i,p,+}$ and $\overline{\mathbf{Y}}_{i,p,-}$, respectively, for $i \in \{1, 2, \ldots, n\}$. We obtain the following:

$$\overline{\mathbf{Y}}_{i-1,p,+}(\jmath\Omega_{i,p}) = F_{i,p}e^{\jmath\beta_{i,p}}\mathbf{a}_i^{-1}(\jmath\Omega_{i,p}), \quad i \in \{2, \ldots, n\}, \quad p \in \{0, 1, \ldots, P\}, \tag{5.47}$$

$$\overline{\mathbf{Y}}_{i,p,-}(\jmath\Omega_{i,p}) = -F_{i,p}e^{\jmath\beta_{i,p}}\mathbf{a}_i^{-1}(\jmath\Omega_{i,p}), i \in \{1, 2, \ldots, n-1\}, \quad p \in \{0, 1, \ldots, P\}. \tag{5.48}$$

The particular solution for the relative displacements is thus described by

$$y_K(t) = \sum_{i=1}^{n-1}\sum_{p=0}^{P}\sum_{q\in\{-,+\}} \left|\overline{Y}_{i,p,q,K-1}(\jmath\Omega_{i,p})\right| \sin\Big(\Omega_{i,p}t + \overline{\Psi}_{i,p,q,K-1}(\jmath\Omega_{i,p})\Big), \tag{5.49}$$

with K ranging from 2 to n, and $\overline{Y}_{i,p,q,K-1}$ signifying the $(K-1)^{\text{th}}$ row of the vector $\overline{\mathbf{Y}}_{i,p,q}$. In this way, we obtain reasonably good estimates for $y_2(t), \ldots, y_n(t)$.

Resonant frequencies

Our interest predominantly lies in understanding the system's dynamics around its resonant frequencies. To determine the resonance peaks and their corresponding amplifications, it suffices to analyze the system under a single harmonic excitation, as illustrated in Eq. (5.45), targeting the i^{th} reduced coordinate (and not the i^{th} particle). The detailed formulation for the K^{th} row of the vector $\overline{\mathbf{Y}}$ is thus:

$$\overline{Y}_K(\jmath\omega_i) = \frac{2}{n}\sum_{l=1}^{n-1} \left.\frac{\sin\left(\frac{i\pi l}{n}\right)\sin\left(\frac{K\pi l}{n}\right)}{s^2 + 2\frac{k}{m}s + 2\frac{c}{m} - 2\left(\frac{k}{m}s + \frac{c}{m}\right)\cos\left(\frac{\pi l}{n}\right)}\right|_{s=\jmath\omega_i} F_i e^{\beta_i} \tag{5.50}$$

$$= \frac{2}{n}\sum_{l=1}^{n-1} \frac{\sin\left(\frac{i\pi l}{n}\right)\sin\left(\frac{K\pi l}{n}\right)}{\left[2\frac{c}{m}\left(1-\cos\left(\frac{\pi l}{n}\right)\right) - \omega_i^2\right] - \jmath\left[2\omega_i\frac{k}{m}\left(1-\cos\left(\frac{\pi l}{n}\right)\right)\right]} F_i e^{\beta_i}. \tag{5.51}$$

Significant oscillations occur when the magnitude of Y_i is large, which can happen when the absolute value of at least one denominator in the sum gets close to zero. The magnitude of the denominator is given as:

$$\left|\left[2\frac{c}{m}\left(1-\cos\left(\frac{\pi l}{n}\right)\right) - \omega_i^2\right] - \jmath\left[2\omega_i\frac{k}{m}\left(1-\cos\left(\frac{\pi l}{n}\right)\right)\right]\right| = \tag{5.52}$$

$$\sqrt{\left[2\frac{c}{m}\left(1-\cos\left(\frac{\pi l}{n}\right)\right) - \omega_i^2\right]^2 + 4\omega_i^2\frac{k^2}{m^2}\left(1-\cos\left(\frac{\pi l}{n}\right)\right)^2} = \tag{5.53}$$

$$\sqrt{\omega_i^4 + 4\left(1-\cos\left(\frac{l\pi}{n}\right)\right)\left[\frac{k^2}{m^2}\left(1-\cos\left(\frac{l\pi}{n}\right)\right) - \frac{c}{m}\right]\omega_i^2 + \left(\frac{2c}{m}\left(1-\cos\frac{\pi l}{n}\right)\right)^2}. \tag{5.54}$$

Since $k > 0$, the absolute value of the denominator is a continuously differentiable function for any $\omega_i \in \mathbb{R}$. We can find its minimum value by setting its derivative equal to zero.

The square-root function's monotonicity implies that the expression's minimum value is attained where the inner fourth-order polynomial is minimized. This polynomial, being symmetric with a positive coefficient for ω_i^4, suggests two potential outcomes: a local maximum at $\omega_i = 0$ with symmetric local minima around this point, or a singular minimum at $\omega_i = 0$. The function's value increases as it diverges from zero, with the latter scenario indicating a highly overdamped aperiodic system, which lies beyond the

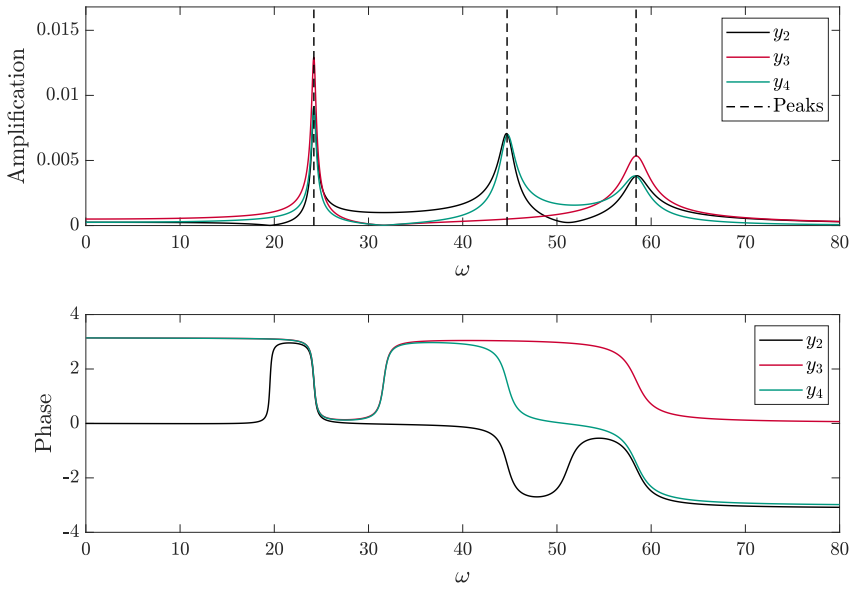

Figure 5.3: Illustration of amplification and phase relative to the excitation frequency for a system comprising $n = 4$ particles, with parameters set at $m = 1$, $k = 0.8$, $c = 1000$. The excitation is applied to the second particle in the chain. Analytically determined peak frequencies as per Eq. (5.56) are indicated by dashed black lines. Figure adapted from [228]

scope of this study (see Eq. (5.60)). Differentiating the expression within the square root yields:

$$4\omega_i^3 + 8\left(1 - \cos\left(\frac{l\pi}{n}\right)\right)\left(\frac{k^2}{m^2}\left(1 - \cos\left(\frac{l\pi}{n}\right)\right) - \frac{c}{m}\right)\omega_i = 0, \tag{5.55}$$

solving which we obtain:

$$\omega_{i,12} = \pm\sqrt{2\left(1 - \cos\left(\frac{l\pi}{n}\right)\right)\left(\frac{c}{m} - \frac{k^2}{m^2}\left(1 - \cos\left(\frac{l\pi}{n}\right)\right)\right)}, \tag{5.56}$$

$$\omega_{i,3} = 0. \tag{5.57}$$

By substituting values for $l = 1...n - 1$, we derive analytical approximations for the resonant frequencies of the chain. A visual representation of a system with particles $n = 4$ is presented in Fig. 5.3.

The frequencies deduced from Eq. (5.56) represent the spectrum at which resonant responses may be triggered. Nonetheless, excitation at specific nodes does not guarantee resonant motion for all frequencies, as resonant activity also demands that the numerator

$\sin\left(\frac{i\pi l}{n}\right)\sin\left(\frac{K\pi l}{n}\right)$ in Eq. (5.51) remains non-zero. For instance, in Fig. 5.3, showing a system with $n = 4$ and $l = 2$, $\overline{y}_2 \equiv y_3$ (therefore, $K = 2$) is not excitable by the second resonant frequency $i = 2$, due to the numerator becoming null.
Building on Eq. (5.56), we can also approximate the maximum value of the damping coefficient k_{crit}, which allows all internal modes of the chain to remain oscillatory. For all resonant peaks to exist, the condition under the square root for all $l \in \{1, \dots, n-1\}$ must yield a real number, satisfied when:

$$\frac{c}{m} > \frac{k^2}{m^2}\left(1 - \cos\left(\frac{l\pi}{n}\right)\right), \quad \forall l \in \{1, \dots, n-1\}, \tag{5.58}$$

$$cm > k^2\left(1 - \cos\left(\frac{(n-1)\pi}{n}\right)\right) = k^2\left(1 + \cos\left(\frac{\pi}{n}\right)\right), \tag{5.59}$$

$$\sqrt{\frac{cm}{2}} > \sqrt{\frac{cm}{1 + \cos\frac{\pi}{n}}} =: k_{\text{crit}} > k. \tag{5.60}$$

The possible values for n range from 2 to infinity, placing the critical damping coefficient within the interval

$$k_{\text{crit}} \in \left(\sqrt{\frac{cm}{2}}, \sqrt{cm}\right]. \tag{5.61}$$

Special case: harmonic excitation

Owing to the superposition principle, the simplified linear system in Eq. (5.35), our primary interest is directed towards the behavior of the i^{th} body when it undergoes simple harmonic excitation.
Analytical solutions for $y_2(t), \dots, y_n(t)$ are sought in the context of excitation exclusively by the high-frequency force $F_{i,p}\sin(\Omega_{i,p}t + \beta_{i,p})$. The governing equation for η emerges as an undamped second-order nonlinear differential equation, indicating the absence of damping and, consequently, never decaying transients. In contrast, the system of equations that describe $y_2(t), \dots, y_n(t)$ approximates a damped linear second-order differential equation system, where significant damping ensures rapid convergence to a steady-state solution, as depicted in Eq. (5.49). Under a singular harmonic excitation, the steady-state solutions $y_2(t), \dots, y_n(t)$ resonate as pure harmonics around the common center of mass $\eta(t)$:

$$\mathbf{z}(t) := \mathbf{x}(t) - \eta(t)\mathbf{e} = \mathbf{S}\mathbf{y}(t) - \eta(t)\mathbf{e}, \tag{5.62}$$

$$\mathbf{z}(t) = \frac{1}{n} \underbrace{\begin{bmatrix} -(n-1) & -(n-2) & \dots & -1 \\ 1 & -(n-2) & \dots & -1 \\ 1 & 2 & \dots & -1 \\ \vdots & \vdots & \ddots & \vdots \\ 1 & 2 & \dots & n-1 \end{bmatrix}}_{\in \mathbb{R}^{n \times (n-1)}} \begin{bmatrix} y_2 \\ y_3 \\ \vdots \\ y_n \end{bmatrix}, \tag{5.63}$$

where $\mathbf{e} = [1 \quad 1 \quad \dots \quad 1]^\top$. Through Eq. (5.63), it becomes evident that the components of $\mathbf{z}$ are linear combinations of $y_2, \dots, y_n$, each constituting a sum of $n-1$ sine functions with varying amplitudes and phases but sharing the same frequency $\Omega_{i,p}$. To simplify such sums, the trigonometric identity below is useful:

$$\sum_{i=1}^{n} A_i \sin(\omega t + \varphi_i) = A \sin(\omega t + \varphi), \tag{5.64}$$

where

$$A = \sqrt{\left(\sum_{i=1}^{n} A_i \cos\varphi_i\right)^2 + \left(\sum_{i=1}^{n} A_i \sin\varphi_i\right)^2}, \tag{5.65}$$

$$\varphi = \operatorname{atan2}\left(\sum_{i=1}^{n} A_i \sin\varphi_i, \sum_{i=1}^{n} A_i \cos\varphi_i\right), \tag{5.66}$$

with $\operatorname{atan2}(y, x)$ denoting the two-argument arctangent function, offering precise phase determination over $(-\pi, \pi)$, in contrast to the range of $\arctan(y/x)$ limited to $(-\pi/2, \pi/2)$. The amplitude and phase of the harmonic oscillation for the j^{th} body are efficiently derived using complex numbers, as established in Eq. (5.45) for $\overline{\mathbf{Y}}(\jmath\Omega_{j2})$:

$$\mathbf{Z}(\jmath\Omega_{j2}) = \overline{\mathbf{SY}}(\jmath\Omega_{j2}), \tag{5.67}$$

$$A_K = |Z_K(\jmath\Omega_{j2})|, \tag{5.68}$$

$$\Psi_K = \angle Z_K(\jmath\Omega_{j2}), \tag{5.69}$$

$$z_K(t) = A_K \sin\big(\Omega_{j2} t + \Psi_K\big). \tag{5.70}$$

The relative movements of the particles around the center of mass are harmonic functions that exhibit distinct amplitudes and phase angles despite sharing a common frequency. When the system is subject to multiple harmonics simultaneously, due to the linearity of Eq. (5.35), the relative motions $\mathbf{z}(t)$ of the particles around the chain's center of mass can be described by the sum of harmonics with frequency components corresponding to the excitation.

Given the strong coupling between the particles, it becomes evident that frequencies exciting the center of mass of the particle chain within the potential well are considerably lower than those of the internal chain vibrations. This distinction allows for the omission of low-frequency excitation terms in the calculation of $\mathbf{z}$, as visually represented in Fig. 5.4 within Sect. 5.1.3.
This insight leads to a revisitation of Eq. (5.30), which, for model reduction, employs the methodology suggested in Sect. 2.3. This approach models high-frequency oscillations through the classical probability density of the particle positions, offering a simplified way to capture the system dynamics.

5.1.2 Averaging-based model reduction

The preceding section provided analytic descriptions for the motion of particles around their common center of mass, which are now incorporated into Eq. (5.30) using Eq. (5.63), leading to:

$$\ddot{\eta} + \frac{\sum_{i=1}^{n} V'(\eta + z_i(t))}{n} = \frac{\sum_{i=1}^{n} F_i(t)}{nm}. \tag{5.71}$$

Because $z_i(t)$ and $F_{i,p}\sin\left(\Omega_{i,p}t + \beta_{i,p}\right)$ are 'fast' variables, the equation is averaged to isolate the 'slow' dynamics, introducing $\xi := \langle\eta\rangle$ to signify the averaged position of the center of mass. The 'fast' harmonic forces average out, yielding:

$$\ddot{\xi} + \left\langle \frac{\sum_{i=1}^{n} V'(\xi + z_i(t))}{n} \right\rangle = \frac{\sum_{i=1}^{n} F_{i,0}\sin(\Omega_0 t + \beta_{i,0})}{nm}. \tag{5.72}$$

Application of Eq. (5.64) further reduces Eq. (5.72) to:

$$\ddot{\xi} + \left\langle \frac{\sum_{i=1}^{n} V'(\xi + z_i(t))}{n} \right\rangle = F_0\sin(\Omega_0 t + \beta_0), \tag{5.73}$$

where

$$F_0 := \frac{\sqrt{\left(\sum_{i=1}^{n} F_{i,0}\cos\beta_{i,0}\right)^2 + \left(\sum_{i=1}^{n} F_{i,0}\sin\beta_{i,0}\right)^2}}{nm}, \tag{5.74}$$

$$\beta_0 := \operatorname{atan2}\left(\sum_{i=1}^{n} F_{i,0}\sin\beta_{i,0}, \sum_{i=1}^{n} F_{i,0}\cos\beta_{i,0}\right). \tag{5.75}$$

Averaging the left side of Eq. (5.72) demands a more nuanced approach. Sect. 2.3 elucidates that the time average of the function $f(x + g(t))$, with $g(t)$ as the 'fast' variable, is obtainable not only through time integration but also through a cross-

correlation integral with $f(x)$ and the classical probability density (CPD) $\rho(x)$ of $g(t)$, as demonstrated in Theorem 2.3.3:

$$\langle f(x+g(t))\rangle = \frac{1}{T}\int_0^T f(x+g(t))\mathrm{d}t = \int_{-\infty}^{\infty} f(y)\rho(y-x)\mathrm{d}y. \tag{5.76}$$

Moreover, based on Theorem 2.3.6, the averaged function can be represented through the moments of $\rho(x)$ for analytic functions, via:

$$\langle f(x+g(t))\rangle = \int_{-\infty}^{\infty} f(y)\rho(y-x)\mathrm{d}y = \sum_{K=0}^{\infty} m_K \frac{f^{(K)}(x)}{K!}. \tag{5.77}$$

Here, m_K denotes the K^{th} moment of $\rho(x)$. This formula is applicable, provided the support of $\rho(x)$ is within the convergence radius of the Taylor series expansion for $f(x)$. Consequently, once the moments of the 'fast' variables $z_i(t)$ are determined, averaging Eq. (5.73) becomes more straightforward, particularly when $f(x)$ is a polynomial, necessitating only the computation of a finite number of moments.
For a rigorous understanding of the CPD and the derivation of CPDs of various functions, one can consult the works of [227] and [166].
The zeroth moment of any CPD is always one. In the specific context of our study, where $z_i(t)$ represents a polyharmonic function, the superposition of multiple harmonics, it is possible under certain conditions to determine the moments of this polyharmonic summation. The probability density function (PDF) for a composite of independent variables is obtained by convolution of their respective PDFs [43]. CPDs, akin to PDFs, are nonnegative and integrate to one, yet they conceptually differ fundamentally. CPDs abstract away from the precise timing of particle positions, instead focusing on the spatial distribution by considering the duration a particle occupies a specific position. PDFs, on the other hand, are used to describe random variables. Theorem 2.3.8 elucidates an analytical approach to determine the CPD for polyharmonic functions.
Integrating Eq. (5.77) with Theorem 2.3.11 facilitates the derivation of the effective restoring force in Eq. (5.73). While solving Eq. (5.77) can generally pose challenges or require numerical approaches; the scenario simplifies for polynomial potentials $V(x)$, allowing straightforward, even analytic solutions.
This methodology completes the reduction of the initially n degree-of-freedom (DoF) system to a single DoF system, under the condition that the 'fast' excitation frequencies $\Omega_{i,p}$ are linearly independent over $\mathbb{Q}$. Fig. 5.5 illustrates the difference in CPDs for commensurable versus incommensurable frequencies ω_1 and ω_2, showcasing the effects of commensurability on the CPD.
Subsequent sections will highlight examples that underscore the applicability of the discussed analytic results. After reducing the system to a single DoF, the literature offers

various methodologies for further analyzing the escape behavior of the system [221, 67, 68, 88, 95]. The emphasis here will thus be on the reduction process rather than delving into the specific analytical methods applicable to 1 DoF escape problems in conservative systems.

5.1.3 Example

We examine an illustrative case where the number of particles is $n = 3$, and the potential is a quadratic-quartic polynomial given by

$$V(x) = \frac{1}{2}x^2 - \frac{1}{4}x^4. \tag{5.78}$$

We assume that the masses, damping, and stiffness coefficients are identical. Further, we assume that the stiffness is large and the damping is non-negligible. Thus, we can assume without loss of generality that $m = 1$. The equations of motion are expressed as

$$\begin{bmatrix} \ddot{x}_1 \\ \ddot{x}_2 \\ \ddot{x}_3 \end{bmatrix} + \begin{bmatrix} k & -k & 0 \\ -k & 2k & -k \\ 0 & -k & k \end{bmatrix} \begin{bmatrix} \dot{x}_1 \\ \dot{x}_2 \\ \dot{x}_3 \end{bmatrix} + \begin{bmatrix} c & -c & 0 \\ -c & 2c & -c \\ 0 & -c & c \end{bmatrix} \begin{bmatrix} x_1 \\ x_2 \\ x_3 \end{bmatrix} + \begin{bmatrix} V'(x_1) \\ V'(x_2) \\ V'(x_3) \end{bmatrix} = \underbrace{\begin{bmatrix} F_{1,0}\sin(\Omega_0 t + \beta_0) \\ F_{2,1}\sin(\Omega_2 t + \beta_2) \\ F_{3,1}\sin(\Omega_3 t + \beta_3) \end{bmatrix}}_{=:\begin{bmatrix} F_1(t) \\ F_2(t) \\ F_3(t) \end{bmatrix}}. \tag{5.79}$$

Here, $\Omega_0 \approx 1$ represents a low frequency, whereas Ω_2 and Ω_3 signify high frequencies, exciting the chain's internal vibrational modes. The transformation to new coordinates, specifically the center of mass and relative displacements, is given as

$$\begin{bmatrix} \eta \\ y_2 \\ y_3 \end{bmatrix} = \begin{bmatrix} \frac{1}{3} & \frac{1}{3} & \frac{1}{3} \\ -1 & 1 & 0 \\ 0 & -1 & 1 \end{bmatrix} \begin{bmatrix} x_1 \\ x_2 \\ x_3 \end{bmatrix}. \tag{5.80}$$

Accordingly, the differential equations in these new coordinates are reformulated as

$$\ddot{\eta} + \frac{V'(\eta - \frac{2}{3}y_2 - \frac{1}{3}y_3) + V'(\eta + \frac{1}{3}y_2 - \frac{1}{3}y_3) + V'(\eta + \frac{1}{3}y_2 + \frac{2}{3}y_3)}{3} = \frac{\sum_{i=1}^{3} F_i(t)}{3}, \tag{5.81}$$

and in a more succinct form

$$\ddot{\eta} + \frac{\sum_{i=1}^{3} V'(\eta + z_i(t))}{3} = \frac{\sum_{i=1}^{3} F_i(t)}{3}, \tag{5.82}$$

where $z_i := x_i - \eta$. The equations that describe the relative motions are

$$\begin{bmatrix} \ddot{y}_2 \\ \ddot{y}_3 \end{bmatrix} + \begin{bmatrix} 2k & -k \\ -k & 2k \end{bmatrix} \begin{bmatrix} \dot{y}_2 \\ \dot{y}_3 \end{bmatrix} + \begin{bmatrix} 2c & -c \\ -c & 2c \end{bmatrix} \begin{bmatrix} y_2 \\ y_3 \end{bmatrix} + \underbrace{\begin{bmatrix} V'(x_2) - V'(x_1) \\ V'(x_3) - V'(x_2) \end{bmatrix}}_{\text{negligible}} = \begin{bmatrix} F_2(t) - \underbrace{F_1(t)}_{\text{negligible}} \\ F_3(t) - F_2(t) \end{bmatrix}, \tag{5.83}$$

indicating that in Eq. (5.83), the forces due to potential and low-frequency excitation are minimal compared to the spring forces, making them negligible. The linearized equation system's Laplace transform is given by

$$\underbrace{\begin{bmatrix} s^2 + 2ks + 2c & -ks - c \\ -ks - c & s^2 + 2ks + 2c \end{bmatrix}}_{=:\mathbf{A}(s)} \begin{bmatrix} Y_2(s) \\ Y_3(s) \end{bmatrix} = \mathbf{F}(s), \tag{5.84}$$

where $\mathbf{F}(\mathbf{s})$ denotes the Fourier transform of the excitations. The inverse of matrix $\mathbf{A}(s)$ is computed as

$$\mathbf{A}^{-1}(s) = \frac{1}{(s^2 + ks + c)(s^2 + 3ks + 3c)} \begin{bmatrix} s^2 + 2ks + 2c & ks + c \\ ks + c & s^2 + 2ks + 2c \end{bmatrix}. \tag{5.85}$$

For ease of calculation, the functions are defined by

$$G_l(s) := s^2 + lks + lc \quad \text{for } l \in \{1, 2, 3\}, \tag{5.86}$$

$$G_0(s) := ks + c. \tag{5.87}$$

The transfer function is derived by setting $s = \jmath\omega$, which allows us to reformulate Eqs. (5.86)-(5.87) as follows:

$$G_l(\jmath\omega) = -\omega^2 + lc + \jmath\omega lk = \sqrt{(-\omega^2 + lc)^2 + \omega^2 l^2 k^2} \exp\left(\jmath \arctan \frac{\omega lk}{-\omega^2 + lc}\right), \tag{5.88}$$

$$G_0(\jmath\omega) = c - \jmath\omega k = \sqrt{c^2 + \omega^2 k^2} \exp\left(\jmath \arctan \frac{-\omega k}{c}\right), \tag{5.89}$$

leading to

$$\mathbf{G}(\jmath\omega) = \frac{1}{G_1(\jmath\omega) G_3(\jmath\omega)} \begin{bmatrix} G_2(\jmath\omega) & G_0(\jmath\omega) \\ G_0(\jmath\omega) & G_2(\jmath\omega) \end{bmatrix}. \tag{5.90}$$

Resonance frequencies are anticipated around the values

$$\omega_{1,\text{peak}} = \sqrt{c - \frac{k^2}{2}} \quad \text{and} \quad \omega_{2,\text{peak}} = \sqrt{3\left(c - \frac{3k^2}{2}\right)}. \tag{5.91}$$

We define the high-frequency excitation values as

$$\Omega_2 = \omega_{2,\text{peak}}, \tag{5.92}$$

$$\Omega_3 = \omega_{1,\text{peak}}. \tag{5.93}$$

The amplitude and phase of the stationary solutions for $F_2(t)$ are determined by

$$\begin{bmatrix} Y_{2,2} \\ Y_{3,2} \end{bmatrix} = \frac{1}{G_1(\jmath\Omega_2)G_3(\jmath\Omega_2)} \begin{bmatrix} G_2(\jmath\Omega_2) & G_0(\jmath\Omega_2) \\ G_0(\jmath\Omega_2) & G_2(\jmath\Omega_2) \end{bmatrix} \begin{bmatrix} F_2 e^{\jmath\beta_2} \\ -F_2 e^{\jmath\beta_2} \end{bmatrix}. \tag{5.94}$$

Using the identity $G_2(\jmath\omega) - G_0(\jmath\omega) = G_1(\jmath\omega)$, Eq. (5.94) simplifies to

$$\begin{bmatrix} Y_{2,2} \\ Y_{3,2} \end{bmatrix} = \frac{1}{G_3(\jmath\Omega_2)} \begin{bmatrix} 1 \\ -1 \end{bmatrix} F_2 e^{\jmath\beta_2}, \tag{5.95}$$

$$\begin{bmatrix} Y_{2,2} \\ Y_{3,2} \end{bmatrix} = \frac{2\sqrt{3}F_2}{9k\sqrt{4c - 3k^2}} e^{\jmath\left(\beta_2 - \arctan\left(\frac{\sqrt{12c-18k^2}}{3k}\right)\right)} \begin{bmatrix} 1 \\ -1 \end{bmatrix}, \tag{5.96}$$

with Eq. (5.96) derived by substituting Eq. (5.92).
Likewise, the stationary solution for $F_3(t)$ is derived as

$$\begin{bmatrix} Y_{2,3} \\ Y_{3,3} \end{bmatrix} = \frac{1}{G_1(\jmath\Omega_3)G_3(\jmath\Omega_3)} \begin{bmatrix} G_0(\jmath\Omega_3) \\ G_2(\jmath\Omega_3) \end{bmatrix} F_3 e^{\jmath\beta_3}. \tag{5.97}$$

Substituting Eq. (5.93) in Eq. (5.97) gives

$$\begin{bmatrix} Y_{2,3} \\ Y_{3,3} \end{bmatrix} = \frac{2F_3 e^{\jmath(\beta_3 - \gamma_1 - \gamma_3)}}{k\sqrt{4c - k^2}\sqrt{16c^2 + 44ck^2 - 17k^4}} \begin{bmatrix} \sqrt{4c^2 + 4ck^2 - 2k^4} e^{\jmath\gamma_0} \\ \sqrt{4c^2 + 20ck^2 - 7k^4} e^{\jmath\gamma_2} \end{bmatrix}, \tag{5.98}$$

where

$$\gamma_0 := \arctan \angle G_0(\jmath\omega_{1,\text{peak}}) = \arctan\left(\frac{k\sqrt{4c - 2k^2}}{2c}\right), \tag{5.99}$$

$$\gamma_l := \arctan \angle G_l(\jmath\omega_{1,\text{peak}}) = \arctan\left(\frac{lk\sqrt{4c - 2k^2}}{(2l-2)c + k^2}\right) \quad \text{for } l \in \{1, 2, 3\}. \tag{5.100}$$

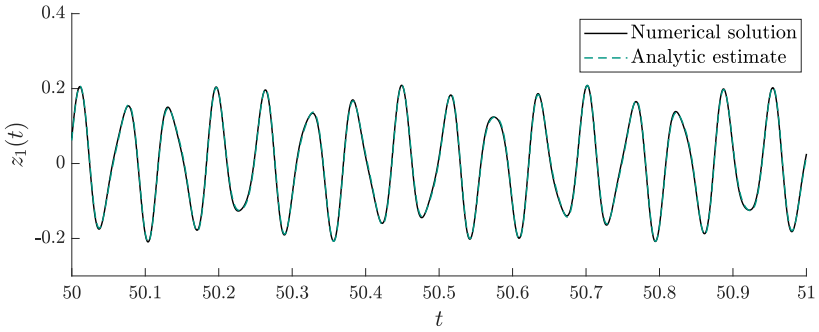

Figure 5.4: Comparison of the numerical solution of $z_1(t)$ with the analytic one for $n = 3$, $m = 1$, $k = 3$, $c = 10000$, $F_0 = 0.33$, $F_2 = 200$, $F_3 = 100$, Ω_0=1, $\Omega_2 = \sqrt{3(c - \frac{3k^2}{2})}$, $\Omega_3 = \sqrt{c - \frac{k^2}{2}}$, $\beta_0 = \beta_2 = \beta_3 = \frac{\pi}{2}$. Figure adapted from [228]

Utilizing the complex amplitudes $Y_{2,2} \dots Y_{3,3}$, the steady-state solutions can be expressed as

$$y_2(t) = |Y_{2,2}| \sin(\omega_{2,\text{Peak}} t + \angle Y_{2,2}) + |Y_{2,3}| \sin(\omega_{1,\text{Peak}} t + \angle Y_{2,3}), \tag{5.101}$$

$$y_3(t) = |Y_{3,2}| \sin(\omega_{2,\text{Peak}} t + \angle Y_{3,2}) + |Y_{3,3}| \sin(\omega_{1,\text{Peak}} t + \angle Y_{3,3}). \tag{5.102}$$

The oscillatory motion of the particles around their center of mass is represented by

$$z_1(t) = -\frac{2}{3} y_2(t) - \frac{1}{3} y_3(t) = Z_{1,1} \sin(\omega_{1,\text{Peak}} t + \zeta_{1,1}) + Z_{1,2} \sin(\omega_{2,\text{Peak}} t + \zeta_{1,2}), \tag{5.103}$$

$$z_2(t) = \frac{1}{3} y_2(t) - \frac{1}{3} y_3(t) = Z_{2,1} \sin(\omega_{1,\text{Peak}} t + \zeta_{2,1}) + Z_{2,2} \sin(\omega_{2,\text{Peak}} t + \zeta_{2,2}), \tag{5.104}$$

$$z_3(t) = \frac{1}{3} y_2(t) + \frac{2}{3} y_3(t) = Z_{3,1} \sin(\omega_{1,\text{Peak}} t + \zeta_{3,1}) + Z_{3,2} \sin(\omega_{2,\text{Peak}} t + \zeta_{3,2}), \tag{5.105}$$

where $Z_{1,1} \dots Z_{3,2}$ and $\zeta_{1,1} \dots \zeta_{3,2}$ are determined via Eqs. (5.64-5.66). Consequently, the particles' movements relative to their center of mass are characterized by biharmonic functions. Given that $\omega_{1,\text{Peak}}$ and $\omega_{2,\text{Peak}}$ are irrationally related, implying their linear independence over $\mathbb{Q}$, Theorem 2.3.8 is applicable for calculating the moments of the fast variable's CPD.

The motion described by z_l with $l \in \{1, 2, 3\}$ is biharmonic. According to [227], for a function $f(t) = A_1 \sin(\omega_1 t + \beta_1) + A_2 \sin(\omega_2 t + \beta_2)$ with ω_1 and ω_2 being incommensurable and $A_1 \geq A_2$ (without loss of generality), the CPD can be derived analytically. In

our polynomial case, only the first moments are required. By employing Theorem 2.3.11 with $P = 2$, we derive

$$m_K = \left(\sum_{\left(\sum_{j=1}^{2} j_i\right)=K} \prod_{j=1}^{2} \frac{m_{j,j_i}}{j_i!} \right) K!, \tag{5.106}$$

with $m_{j,1}$ and $m_{j,2}$ elucidated by Eq. (2.66). The first few moments are as follows:

$$m_0 = 1, \tag{5.107}$$

$$m_1 = m_3 = m_5 = 0, \tag{5.108}$$

$$m_2 = \frac{A_1^2 + A_2^2}{2}, \tag{5.109}$$

$$m_4 = \frac{3}{8}A_1^4 + \frac{3}{2}A_1^2A_2^2 + \frac{3}{8}A_2^4. \tag{5.110}$$

Therefore, the corresponding moments for z_l are computed by substituting A_1 and A_2 with $Z_{l,1}$ and $Z_{l,2}$, respectively.
Let the average center of mass be denoted by $\xi = \langle \eta \rangle$. In Eq. (5.82), the terms necessitating averaging are $V'(\eta + z_l(t))$ for $l \in \{1, 2, 3\}$. Using Eq. (5.77), the average calculations for analytic functions $f(x)$, such as in Eq. (5.78), can be simplified through a series expansion. Thus, we obtain

$$\langle V'(\eta + z_l(t)) \rangle = m_0 V'(\eta) + \underbrace{m_1}_{=0} V''(\eta) + \frac{m_2 V'''(\eta)}{2} + \underbrace{\dots}_{=0} \tag{5.111}$$

$$= (1 - 3m_2)\eta - \eta^3 = \left(1 - 3\frac{Z_{1,l}^2 + Z_{2,l}^2}{2}\right)\eta - \eta^3, \tag{5.112}$$

where terms beyond m_4 are null due to $V^{(k)}(x) = 0$ for $k \geq 4$. Incorporating this result into Eq. (5.82), we deduce

$$\ddot{\xi} + \left(1 - \underbrace{\frac{\sum_{l=1}^{3} Z_{1,l}^2 + Z_{2,l}^2}{2}}_{=:d}\right)\xi - \xi^3 = \frac{F_{1,0}\sin(\Omega_0 t + \beta_0)}{3}, \tag{5.113}$$

$$\ddot{\xi} + \omega_d^2 \xi - \xi^3 = \frac{F_{1,0}\sin(\Omega_0 t + \beta_0)}{3}. \tag{5.114}$$

In this context, d is defined as a detuning parameter, which is affected by various underlying elements that lead to steady-state oscillations around the center of mass, indicated by $z_1(t), z_2(t)$, and $z_3(t)$. The equation reflects the dynamics of an individual particle subjected to harmonic forcing, although the system's linear eigenfrequency is adjusted to $\omega_d = \sqrt{1-d}$.
By introducing suitable dimensionless time and space variables

$$\tau := \omega_d t, \quad \chi := \frac{\xi}{\omega_d}, \tag{5.115}$$

we derive

$$\chi'' + \chi - \chi^3 = F \sin(\Omega\tau + \beta_0), \tag{5.116}$$

accompanied by

$$F := \frac{F_{1,0}}{3\omega_d^3}, \quad \Omega := \frac{\Omega_0}{\omega_d}, \tag{5.117}$$

where $\square'$ symbolizes differentiation in terms of τ.
The equation given by (5.118) has received considerable attention in scholarly discussions [68, 88, 89, 95, 96], and as such, it will not be elaborated upon further in this work.
In the following section, we perform numerical analysis to compare the 'slow' dynamics of the direct integration of Eq. (5.79) with the reduced system dynamics given by Eq. (5.118).

5.1.4 Numerical Evaluation

The subsequent sections detail a numerical comparison between the original 3 DoF system and its simplified 1 DoF counterpart. This comparison involves computing the escape time within a defined parameter space for Ω_0 and $F_{1,0}$. The simulation employs nondimensional parameters as follows: $n = 3$, $m = 1$, $k = 3$, $c = 10000$, $F_2 = 200$, $F_3 = 100$, $\Omega_2 = \sqrt{3(c - \frac{3k^2}{2})}$, $\Omega_3 = \sqrt{c - \frac{k^2}{2}}$, and $\beta_0 = \beta_2 = \beta_3 = \frac{\pi}{2}$.
Utilizing these parameters, the simplified model is expressed by

$$\ddot{\xi}_1 + 0.9668\,\xi - \xi^3 = \frac{F_0}{3}. \tag{5.118}$$

This equation is derived by incorporating the influence of internal chain vibrations on its center of mass. A simplistic approach might ignore the effects of internal vibrations, but such an oversimplification results in inaccuracies, as evidenced in Fig. 5.5b. This figure contrasts the time evolution of both the original 3 DoF model (given by Eq. (5.79))

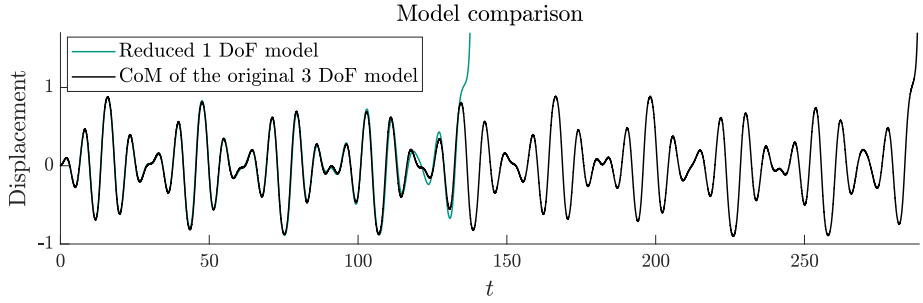

(a) Reduced model considers the effect of internal 'fast' vibrations, resulting in the detuning parameter $d = 0.0332$. The reduced model follows the original dynamics reasonably well

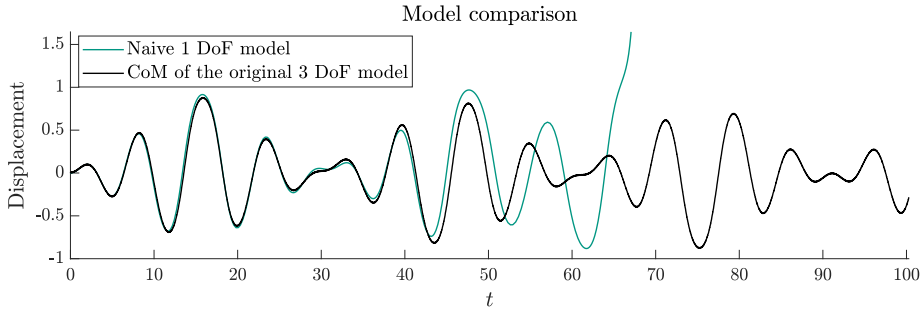

(b) Naive model with $d = 0$. The inaccuracy of the naively reduced model is evident

Figure 5.5: Comparative time evolution between the full 3 DoF model (cf. Eq. (5.79)) and the reduced 1 DoF models (naive and averaging-based ones) under $F_0 = 0.33$, $\Omega_0 = 1$, and $\beta_0 = 0$ with homogeneous initial conditions. The parameters of the full model are as described in the main text. Figures adapted from [228]

and the overly simplified model (given by Eq. (5.118) with setting $d = 0$), with excitation $F_0 = 0.33$, $\Omega_0 = 1$, $\beta_0 = 0$, and homogeneous initial conditions. On the contrary, Fig. 5.5a shows the time evolution of both the original and the model reduced by averaging, revealing a more accurate match.

Through Melnikov analysis, it has previously been established that before escape in a quadratic-cubic potential, chaotic motion may occur [175, 200]. It is plausible to extend this understanding to a quadratic-quartic potential. Such dynamics hint at a fractal boundary delineating the escaping and nonescaping regions. Within this chaotic domain, slight changes in initial conditions or model inaccuracies significantly affect the system. Therefore, predicting exact escape times using a simplified model becomes practically impossible within the chaotic boundary region. However, the reduced model can provide precise results outside this chaotic zone. A parameter study explored this theory, setting the Ω_0 range between 0.6 and 1.2 and F_0 between 0 and 1. This examination also compares the performance of the averaging method against a naive approach that ignores internal chain vibrations. Fig. 5.6 presents the escape times

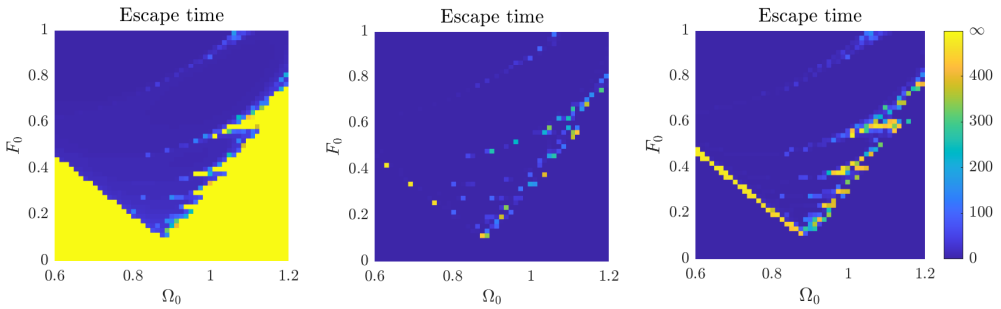

(a) Original model escape times **(b)** Absolute error in escape times, reduced vs. original **(c)** Absolute error in escape times, naive vs. original

Figure 5.6: Validation of models: (a) shows escape times for the original system by varying F_0 and Ω_0 under uniform initial conditions. (b) shows the absolute error in the escape time between the original and reduced models, which incorporates a detuning factor of $d = 0.0332$. (c) illustrates the discrepancy from a naive model reduction that omits internal vibration effects, meaning $d = 0$. This oversimplification reveals a marked shift in the escape boundary's frequency and force amplitude, as deduced from Eq. (5.117), while the model reduced by averaging shows a better alignment with the original model. Parameters not explicitly mentioned here are as specified in the main text. Figures adapted from [228]

for the original model (cf. Fig. 5.6a), along with the absolute errors from both the averaging-based method (cf. Fig. 5.6b) and the naive approach (cf. Fig. 5.6c). The naive approach notably shifts the V-shaped escape boundary, underscoring that disregarding internal vibrations yields an imprecise reduced model. This boundary shift is aligned with the predictions of Eq. (5.117).

The stiffness of the reduced differential equation is significantly smaller than that of the original equations, leading to a drastic enhancement in computational efficiency and a significant reduction in simulation duration for the provided example. Specifically, the computational cost was reduced by 99.75%, highlighting the efficiency of the model reduction process.

5.1.5 Discussion

This study has introduced a method to reduce the complexity of the dynamics of strongly coupled chains of n particles under external excitation in a potential well. By exploiting the discrepancy in frequency scales between the chain's rapid internal oscillations and the 'slow' movement of the center of mass within the potential well, the introduced method achieves a significant model simplification from n DoF to 1 DoF.

The original model accommodates polyharmonic excitation that excites all particles, provided that it also comprises a singular low frequency. Thus, it ensures that not only high-frequency internal vibrations are excited but also the chain's center of mass in the potential well.

The model includes non-negligible damping forces between the particles, facilitating the quick dissipation of transient, high-frequency movements. This setup allows for direct analytical determination of the fast vibratory states, assuming that the potential-induced forces are negligible compared to those of linear springs. As a result, the fast relative movements are identified as time-dependent functions within the nonlinear differential equation that models the motion of the chain's center of mass. The cumulative effect of these rapid oscillations on the motion of the center of mass is estimated by averaging with reasonable accuracy.
An example involving a triharmonic force exciting a three-particle chain within a quadratic-quartic potential well illustrates the reduction process. Analytical reduction is complemented by numerical validation through escape time calculations across various excitation forces and frequencies. For the selected quadratic-quartic potential, the high-frequency excitation's effect is primarily observed as a detuning of the potential's linearized natural frequency, facilitating the application of several preexisting analytical techniques.

5.1.6 Conclusions and future research directions

The approach to model reduction presented here shows two primary benefits. First, it elucidates the 'slow' dynamics and the underlying 'slow' force fields governing the system. Second, it yields a significant reduction in computational costs. In the presented case of a three-particle system, we observed a 99.75% decrease in the simulation time. This advantage is expected to grow as the system expands to include more particles with intensified interactions, which complicates the differential equation system and increases its stiffness, thereby emphasizing the importance of model reduction.
Looking ahead, there are multiple avenues to expand this research. One potential direction involves applying the reduction techniques to more complicated potential wells that deviate from polynomial expressions to evaluate the versatility of the current methodologies. Another exciting area is the exploration of different excitation models, including stochastic or dynamically varying forces, to assess their impact on the system's slow dynamics and computational load.
Further investigations could also focus on the model's scalability with an increased particle count and more complex interaction dynamics. Specifically, determining the computational benefits in more rigid systems would be enlightening. Given the significant time savings demonstrated in the example of three particles, developing a scaling principle to predict computational savings in larger configurations might be feasible.
Expanding the model to include two- and three-dimensional potential wells represents another promising research domain.

An alternative research path may explore scenarios without damping among particles. This condition is vital for its potential implications on the model's precision and efficacy, especially considering how the absence of transient decay might affect the results.
Lastly, investigating the dynamics of particle chains with nonlinear interparticle couplings could provide valuable insights. This exploration would aim to understand how increasing system complexity impacts the slow and rapid dynamics, offering a more nuanced view of the model's applicability and potential limitations.

5.2 Escape of a chain of two colliding particles from a potential under biharmonic excitation

The following section will extend the particle chain model with collision. We will investigate the escape dynamics of a pair of strongly coupled particles in a potential well under bi-harmonic excitation. The text and figures of this section have been adapted from [222].

5.2.1 Description of the model

We analyze the scenario presented in Fig. 5.7. This analysis involves a system where two particles with masses m_1 and m_2 undergo bi-harmonic excitation within a one-dimensional quadratic potential well. The particles are connected by a stiff linear spring, characterized by a large stiffness coefficient c, and are damped by a viscous damper with a damping coefficient k of the order $O(1)$. For each particle, the potential wells are distinct and expressed as $V_1(x) = m_1 V(x)$ for the first particle and $V_2(x) = m_2 V(x)$ for the second, with masses m_1 and m_2 being of order $O(1)$. $V(x)$ is not specified explicitly but shall fulfill all requirements of a potential described in Sect. 5.1. The system is subjected to driving forces $F_1(t)$ and $F_2(t)$. The design ensures that the particles do not pass through each other and interact once they reach a separation of $\Delta := r_1 + r_2$. The collision at this point is nearly perfectly elastic, denoted by $R \approx 1$.
The equations governing the particles' movement are:

$$\begin{aligned}
&\begin{bmatrix} m_1 & 0 \\ 0 & m_2 \end{bmatrix} \begin{bmatrix} \ddot{x}_1 \\ \ddot{x}_2 \end{bmatrix} + \begin{bmatrix} k & -k \\ -k & k \end{bmatrix} \begin{bmatrix} \dot{x}_1 \\ \dot{x}_2 \end{bmatrix} + \begin{bmatrix} c & -c \\ -c & c \end{bmatrix} \begin{bmatrix} x_1 \\ x_2 \end{bmatrix} + \begin{bmatrix} m_1 V'(x_1) \\ m_2 V'(x_2) \end{bmatrix} = \begin{bmatrix} F_1(\tau) \\ F_2(\tau) \end{bmatrix}, \quad \text{if } x_1 + \Delta < x_2, \\
&x_{1+} = x_{1-}, \quad \text{if } x_1 + \Delta = x_2, \\
&x_{2+} = x_{2-}, \\
&\dot{x}_{1+} = \frac{R m_2 (\dot{x}_{2-} - \dot{x}_{1-}) + m_1 \dot{x}_{1-} + m_2 \dot{x}_{2-}}{m_1 + m_2}, \\
&\dot{x}_{2+} = \frac{R m_1 (\dot{x}_{1-} - \dot{x}_{2-}) + m_1 \dot{x}_{1-} + m_2 \dot{x}_{2-}}{m_1 + m_2}.
\end{aligned} \tag{5.119}$$

The excitation in this study is configured as follows to stimulate both the center of mass motion in the well (Ω_{11}) and the relative motion between particles (Ω_{12}):

$$F_1(\tau) = F_{11} \sin(\Omega_{11}\tau + \beta_{11}) + F_{12} \sin(\Omega_{12}\tau + \beta_{12}), \tag{5.120}$$

$$F_2(\tau) = 0. \tag{5.121}$$

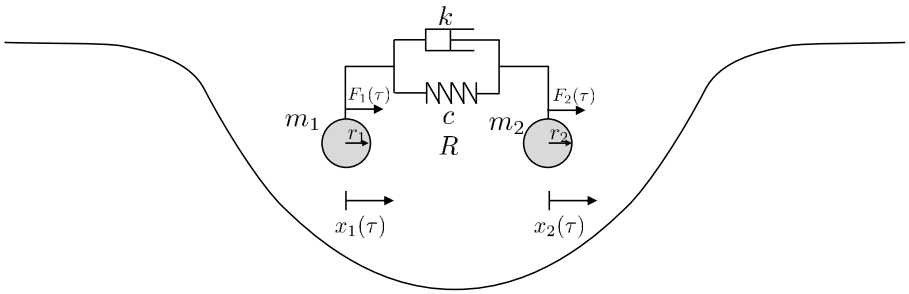

Figure 5.7: Illustration of the collision problem in a potential well influenced by harmonic excitation

The physical coordinates x_1 and x_2 undergo a linear transformation to new variables

$$y_1 := \frac{m_1 x_1 + m_2 x_2}{m_1 + m_2}, \qquad y_2 := x_2 - x_1, \tag{5.122}$$

where y_1 signifies the center of mass motion and y_2 represents the relative particle distance greater than or equal to Δ during the oscillations. Incorporating the inverse transformation into Eq. (5.119) yields

$$\begin{aligned}
&\ddot{y}_1 + \mu V'(y_1 - (1-\mu)y_2) + (1-\mu)V'(y_1 + \mu y_2) \\
&\quad = \frac{1}{m_1 + m_2}\left(F_{11}\sin(\Omega_{11}\tau + \beta_{11}) + F_{12}\sin(\Omega_{12}\tau + \beta_{12})\right) && \text{if } y_2 > \Delta, \\
&y_{1+} = y_{1-}, && \text{if } y_2 = \Delta, \\
&\dot{y}_{1+} = \dot{y}_{1-}, \\
&\ddot{y}_2 + \frac{k}{m}\dot{y}_2 + \frac{c}{m}y_2 + \underbrace{V'(y_1 + \mu y_2) - V'(y_1 - (1-\mu)y_2)}_{\text{minor coupling term of } O(1) \text{ as } \frac{c}{m} \gg V'(x)} \\
&\quad = -\frac{F_{11}}{m_1}\sin(\Omega_{11}\tau + \beta_{11}) - \frac{F_{12}}{m_1}\sin(\Omega_{12}\tau + \beta_{12}) && \text{if } y_2 > \Delta, \\
&y_{2+} = y_{2-}, && \text{if } y_2 = \Delta, \\
&\dot{y}_{2+} = -R\dot{y}_{2-},
\end{aligned} \tag{5.123, 5.124}$$

with

$$\frac{1}{m} := \frac{1}{m_1} + \frac{1}{m_2}, \qquad \mu := \frac{m_1}{m_1 + m_2}. \tag{5.125}$$

This reformulation demonstrates that Eq. (5.124) is coupled to Eq. (5.123) via a small and negligible term (cf. Sect. 5.1). However, the coupling in the other direction is non-negligible. Thus, Eq. (5.124) can be simplified to a linear equation, facilitating straightforward solutions.

$$\begin{aligned} \ddot{y}_2 + \frac{k}{m}\dot{y}_2 + \frac{c}{m}y_2 = &-\frac{F_{11}}{m_1}\sin(\Omega_{11}\tau + \beta_{11}) \\ &- \frac{F_{12}}{m_1}\sin(\Omega_{12}\tau + \beta_{12}) \qquad \text{if } y_2 > \Delta, \\ y_{2+} = y_{2-}, &\qquad \text{if } y_2 = \Delta \\ \dot{y}_{2+} = R\dot{y}_{2-}, & \end{aligned} \tag{5.126}$$

The resonant frequency of y_2 without taking into account the collisions is

$$\Omega_{02} = \sqrt{\frac{c}{m} - \frac{k^2}{2m^2}}. \tag{5.127}$$

Assuming that the excitation frequency Ω_{12} is at least as large as Ω_{02} and $\Omega_{11} \ll \Omega_{02}$, Eq. (5.124) describes primarily 'fast' motions, while Eq. (5.123) describes the 'slow' motion. Given that the damping ratio k/m is nonsmall, the homogeneous part of the solution decays rapidly from the 'slow' motion's perspective, rendering the particular solution the significant one, as in [61, 62].
Due to collisions, Ω_{02} is not a resonant frequency of the 'fast' subsystem.
To obtain the 'fast' motion and the resonant frequencies of the 'fast' subsystem, a preliminary analysis based on [60] must be performed.

5.2.2 Resonance of the colliding particles under high-frequency excitation

Fidlin already analyzed the resonance frequencies of Eq. (5.126) in Chapter 3.5 of [60]. Although this section reiterates much of the book's discussion, a slight deviation in the outcome is noted here because of a typographical error within the source material.
Before taking advantage of the results of [60], a necessary initial step involves transforming the coordinates to standardize the coefficient of y_2 in Eq. (5.126) to unity.
Defining a new, dimensionless time scale $t = \omega_0\tau$, where $\omega_0 = \sqrt{c/m}$, enables the expression of dimensionless time derivatives as

$$\dot{y}_2 = \frac{\mathrm{d}y_2}{\mathrm{d}\tau} = \omega_0\frac{\mathrm{d}y_2}{\mathrm{d}t} = \omega_0 y_2', \tag{5.128}$$

$$\ddot{y}_2 = \frac{\mathrm{d}^2y_2}{\mathrm{d}\tau^2} = \omega_0^2\frac{\mathrm{d}^2y_2}{\mathrm{d}t^2} = \omega_0^2 y_2'', \tag{5.129}$$

with the prime (′) indicating derivatives with respect to the dimensionless time. Thus, Eq. (5.126) rewritten in dimensionless time appears as

$$y_2'' + \frac{k}{\omega_0 m} y_2' + y_2 = \underbrace{-\frac{F_{11}}{m_1 \omega_0^2} \sin\left(\frac{\Omega_{11}}{\omega_0} t + \beta_{11}\right)}_{\text{negligible}} - \frac{F_{12}}{m_1 \omega_0^2} \sin\left(\frac{\Omega_{12}}{\omega_0} t + \beta_{12}\right). \tag{5.130}$$

Setting Ω_{11} near $\Omega_{01} = 1$ minimizes the first term's impact on y_2. By establishing the parameters

$$\beta := \frac{k}{\omega_0 m}, \quad \varepsilon := \frac{F_{12}}{m_1 \omega_0^2}, \quad \omega := \frac{\Omega_{12}}{\omega_0}, \tag{5.131}$$

Eq. (5.130) simplifies to

$$y_2'' + \beta y_2' + y_2 = -\varepsilon \sin(\omega t + \beta_{12}), \qquad \text{if } y_2 > \Delta, \tag{5.132}$$

$$y_{2+} = y_{2-}, \qquad \text{if } y_2 = \Delta \tag{5.133}$$

$$y_{2+}' = -R y_{2-}'. \tag{5.134}$$

Applying the 'unfolding transformation'

$$y_2 = |z| + \Delta, \tag{5.135}$$

lets us transcribe Eq. (5.132) into

$$z'' + \beta z' + z = (-\Delta - \varepsilon \sin(\omega t + \beta_{12})) \operatorname{sgn}(z) \quad \text{if } z \neq 0, \tag{5.136}$$

$$z_+' - z_-' = -(1 - R) z_- \quad \text{if } z = 0. \tag{5.137}$$

Employing the Van der Pol transformation

$$z = A \sin \varphi, \quad z' = A \cos \varphi, \tag{5.138}$$

and defining the uniformly rotating phase

$$\psi = \omega t + \beta_{12}, \tag{5.139}$$

allows for rewriting Eq. (5.136) as

$$\begin{aligned} A' &= -\beta A \cos^2 \varphi + (-\Delta - \varepsilon \sin \psi) \cos \varphi \operatorname{sgn}(\sin \varphi) && \text{if } \varphi \neq n\pi, \\ A_+ - A_- &= -(1 - R) A_- && \text{if } \varphi = n\pi, \end{aligned} \tag{5.140}$$

$$\varphi' = 1 + \beta \sin\varphi \cos\varphi + \frac{\Delta + \varepsilon \sin\psi}{A} |\sin\varphi|, \tag{5.141}$$

$$\psi' = \omega. \tag{5.142}$$

With the usual definitions of the *resonant surface* and *resonant solutions* from [60], we concentrate on those ω values at which the averaged right-hand side of the equation exhibits discontinuities. Such points are interesting since they are likely to correspond to large amplitude responses. The terms considered 'dangerous' for their potential to cause significant responses are defined as follows:

$$< \sin\psi \cos\varphi \ \mathrm{sgn} \sin\varphi > = \frac{1}{2\pi} \int_0^{2\pi} \sin(\omega t + \gamma) \cos t \ \mathrm{sgn} \sin t \, \mathrm{d}t, \tag{5.143}$$

$$< \sin\psi |\sin\varphi| > = \frac{1}{2\pi} \int_0^{2\pi} \sin(\omega t + \gamma) |\sin t| \mathrm{d}t, \tag{5.144}$$

$$\gamma = \psi_0 - \varphi_0, \tag{5.145}$$

which are non-zero for specific frequencies $\omega_l = 2l$, $l = 1, 2, 3, \ldots$. We introduce the small parameter

$$\delta = \frac{\omega}{2l} - 1, \tag{5.146}$$

and the 'slow' phase difference

$$\theta = \varphi - \frac{\psi}{2l}, \tag{5.147}$$

which enables us to transform Eq. (5.140) as

$$\begin{aligned} A' = &-\beta A \cos^2\varphi - \Delta \cos\varphi \mathrm{sgn}(\sin\varphi) \\ &- \varepsilon \sin\big(2l(\varphi - \theta)\big) \cos\varphi \ \mathrm{sgn}(\sin\varphi) \qquad \text{if } \varphi \neq n\pi, \end{aligned} \tag{5.148}$$

$$A_+ - A_- = -(1 - R)A_- \qquad \text{if } \varphi = n\pi, \tag{5.149}$$

$$\theta' = -\delta + \beta \sin\varphi \cos\varphi + \frac{\Delta + \varepsilon \sin\big(2l(\varphi - \theta)\big)}{A} |\sin\varphi|, \tag{5.150}$$

$$\varphi' = 1 + \beta \sin\varphi \cos\varphi + \frac{\Delta + \varepsilon \sin\big(2l(\varphi - \theta)\big)}{A} |\sin\varphi|. \tag{5.151}$$

To execute discontinuous averaging effectively for small δ values, one considers the integrals

$$J_1 = \frac{1}{2\pi} \int_0^{2\pi} \sin(2l\varphi) |\sin\varphi| \mathrm{d}\varphi = \frac{1}{\pi} \int_0^{\pi} \sin(2l\varphi) \sin\varphi \mathrm{d}\varphi = 0, \tag{5.152}$$

$$J_2 = \frac{1}{2\pi}\int_0^{2\pi} \cos(2l\varphi)|\sin\varphi|\mathrm{d}\varphi = -\frac{2}{\pi(4l^2-1)}, \tag{5.153}$$

$$J_3 = \frac{1}{2\pi}\int_0^{2\pi} \sin(2l\varphi)\cos\varphi\ \mathrm{sgn}\sin\varphi\mathrm{d}\varphi = \frac{4l}{\pi(4l^2-1)}, \tag{5.154}$$

$$J_4 = \frac{1}{2\pi}\int_0^{2\pi} \cos(2l\varphi)\cos\varphi\ \mathrm{sgn}\sin\varphi\mathrm{d}\varphi = 0. \tag{5.155}$$

These results facilitate the deduction of averaged differential equations:

$$A' = -\left(\frac{1}{2}\beta + \frac{1-R}{\pi}\right)A - \frac{4l\varepsilon}{\pi(4l^2-1)}\cos 2l\theta, \tag{5.156}$$

$$\theta' = -\delta + \frac{2\Delta}{\pi A} + \frac{2\varepsilon}{\pi(4l^2-1)}\frac{\sin(2l\theta)}{A}. \tag{5.157}$$

Notably, Eq. (5.156) corrects an error from Eq. (3.95) in [60], addressing a misprinted factor.
To find the steady-state solutions A_* and θ_*, one sets the derivatives to zero, leading to

$$\beta_l A_* = -\frac{2\varepsilon}{\pi(4l^2-1)}\cos 2l\theta_*, \tag{5.158}$$

$$\delta A_* - \frac{2\Delta}{\pi} = \frac{2\varepsilon}{\pi(4l^2-1)}\sin 2l\theta_*. \tag{5.159}$$

With further manipulations involving definitions

$$\beta_l = \frac{\frac{1}{2}\beta + \frac{1-R}{\pi}}{2l}, \qquad \varepsilon_l = \frac{\varepsilon}{4l^2-1}, \tag{5.160}$$

the equation for A_* simplifies to a relation where only the stable solution is relevant:

$$A_* = \frac{2}{\pi}\frac{\delta\Delta + \sqrt{\varepsilon_l^2(\beta_l^2+\delta^2) - \Delta^2\beta_l^2}}{\beta_l^2+\delta^2}. \tag{5.161}$$

Determining the maximal amplitude $A_{*,\max}$ involves optimizing in δ, leading to

$$A_{*,\max} = \frac{\varepsilon_l}{\beta_l}, \tag{5.162}$$

which interestingly reveals that the peak amplitude is invariant under different choices of Δ.

Now, the solution for the displacement $z(t)$ can be expressed as

$$z(t) = A_* \sin\left(\frac{\omega t}{2l} + \varphi_0\right), \tag{5.163}$$

where φ_0 is the initial phase, irrelevant for further calculations. Consequently, $y_2(t)$ becomes

$$y_2(t) = A_* \left|\sin\left(\frac{\omega t}{2l} + \varphi_0\right)\right| + \Delta. \tag{5.164}$$

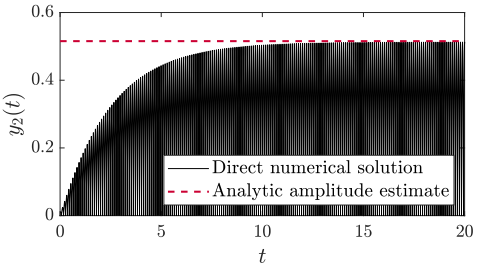

(a) $m_1 = 1$, $m_2 = 5$, $\Omega_{12} = 61.9677$ ($l = 1$) and $\Delta = 0$

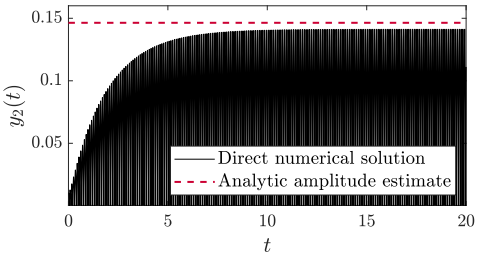

(b) $m_1 = 2$, $m_2 = 1$, $\Omega_{12} = 138.61$ ($l = 2$) and $\Delta = 0.0003$.

Figure 5.8: Comparison of the numerical solution for y_2 with the theoretically estimated stationary amplitude for $c = 800$, $k = 0.5$, $R = 0.99$, and $F_{12} = 15$. The analytical model can predict the stationary amplitude with good accuracy for $l = 1$, but the accuracy decreases for $l > 1$

5.2.3 Derivation of the effective slow potential using the CPD of high-frequency oscillations

Knowing the amplitude y_2, one can derive the CPD for the high-frequency oscillations around the center of mass y_1. The new position variables z_1 and z_2 are determined by:

$$\begin{bmatrix} z_1 \\ z_2 \end{bmatrix} = \begin{bmatrix} -\frac{m_2}{m_1+m_2} y_2 \\ \frac{m_1}{m_1+m_2} y_2 \end{bmatrix}, \tag{5.165}$$

indicating asymmetrical movement around y_1 unless $m_1 = m_2$. The movement distribution for each particle is characterized by a modified arcsine distribution, highlighted in the following figure, demonstrating an asymmetrical CPD.
To establish the probability density functions for z_1 and z_2, we set:

$$A_{1*} = (1-\mu)A_*, \quad A_{2*} = \mu A_*, \quad \Delta_1 = (1-\mu)\Delta, \quad \Delta_2 = \mu\Delta, \tag{5.166}$$

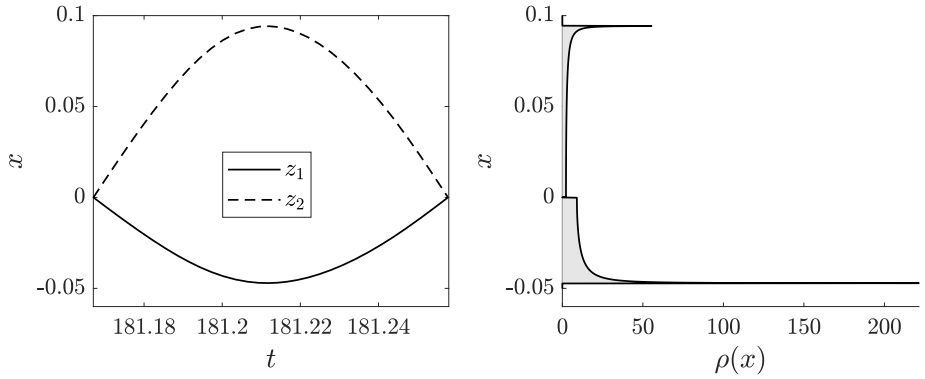

Figure 5.9: One period of the high-frequency oscillation and the corresponding CPD with $m_1 = 2$, $m_2 = 1$, $\Delta = 0.003$, $c = 800$, $k = 0.5$, $R = 0.99$, and $F_{12} = 15$ and $\Omega_{12} = 138.61$ ($l = 2$)

leading to

$$z_1 = -A_{1*}\left|\sin\left(\frac{\omega t}{2l} + \varphi_0\right)\right| - \Delta_1, \quad z_2 = A_{2*}\left|\sin\left(\frac{\omega t}{2l} + \varphi_0\right)\right| + \Delta_2. \tag{5.167}$$

The CPDs of $z_1(t)$ and $z_2(t)$ can be determined by formulas (2.51) and (2.55). Since z_1 and z_2 are half sines, we can also adapt the CPD of a sine function, which yields

$$\rho_1(x) = \begin{cases} \frac{2}{\pi\sqrt{A_{1*}^2 - (x+\Delta_1)^2}} & \text{for } -A_{1*} - \Delta_1 < x < -\Delta_1, \\ 0 & \text{otherwise,} \end{cases} \tag{5.168}$$

$$\rho_2(x) = \begin{cases} \frac{2}{\pi\sqrt{A_{2*}^2 - (x-\Delta_2)^2}} & \text{for } \Delta_2 < x < A_{2*} + \Delta_2, \\ 0 & \text{otherwise.} \end{cases} \tag{5.169}$$

Since the cross-correlation integral is a linear operator, we can obtain the integral at once by calculating the combined CPD of the motion as a weighted sum:

$$\rho(x) = \mu\rho_1(x) + (1-\mu)\rho_2(x). \tag{5.170}$$

Fig. 5.9 gives a graphical example of such a CPD.
Now that the stationary 'fast' motion has been described with sufficient accuracy, we turn back to the problem of escape and the related problem of deriving an effective potential for the center of mass.
The resonance of the center of mass within the potential well remains unaltered by collisions.

Eq. (5.123) describing the motion of the center of mass can now be reformulated to incorporate the averaged effects over the high-frequency oscillations z_1 and z_2, as follows:

$$\ddot{y}_1 + \mu V'(y_1 + z_1) + (1-\mu)V'(y_1 + z_2) = \frac{1}{m_1 + m_2}\big(F_{11}\sin(\Omega_{11}\tau + \beta_{11}) + F_{12}\sin(\Omega_{12}\tau + \beta_{12})\big). \quad (5.171)$$

Since $z_1(t)$ and $z_2(t)$ are very fast compared to y_1, which has linearized eigenfrequency one at the origin, we calculate the average of Eq. (5.171).
Instead of computing the averaging integral in time, we use Theorem 2.3.3 to obtain the average of $\tilde{V}'(y_1 + z_{1/2})$ over a period of the 'fast' vibration as a cross-correlation of V' and ρ.

$$\tilde{V}'(y_1) = \int_{-\infty}^{\infty} V'(x)\rho(x - y_1)\,\mathrm{d}x. \quad (5.172)$$

The average of the right-hand side becomes

$$\underbrace{\frac{F_{11}}{m_1 + m_2}}_{=:F}\sin(\Omega_{11}\tau + \beta_{11}) \quad (5.173)$$

Without further specification of V', we cannot proceed, however. To demonstrate the method, we choose an appropriate potential function

$$V(x) = \begin{cases} \frac{1}{2}x^2 - \frac{1}{2} & |x| \le 1, \\ 0 & |x| > 1. \end{cases} \quad (5.174)$$

Since both V' and ρ are piecewise functions, their cross-correlation is also piecewise. The following piece boundaries are needed:

$$\begin{aligned} d_1 &= -1 - \Delta_2 - A_{2*}, & d_2 &= -1 - \Delta_2, \\ d_3 &= -1 + \Delta_1, & d_4 &= -1 + \Delta_1 + A_{1*}, \\ d_5 &= 1 - \Delta_2 - A_{2*}, & d_6 &= 1 - \Delta_2, \\ d_7 &= 1 + \Delta_1, & d_8 &= 1 + \Delta_1 + A_{1*}. \end{aligned} \quad (5.175)$$

Assuming $\Delta + A_* < 2$, we can guarantee $d_1 < d_2 \ldots < d_8$. Then, we define the domains

$$D_1 = \{x \in \mathbb{R} | x \le d_1\}, \quad (5.176)$$

$$D_i = \{x \in \mathbb{R} | d_{i-1} \leq x < d_i\} \qquad \text{for } i = 2 \dots 8, \tag{5.177}$$

$$D_9 = \{x \in \mathbb{R} | d_8 \leq x\}. \tag{5.178}$$

The result of Eq. (5.172) becomes:

$$\tilde{V}'(y_1) = \begin{cases} 0 & x \in D_1, \\ (1-\mu)\left(y_1 + \Delta_2 + \frac{2}{\pi}\left(\sqrt{A_{2*}^2 - (1+\Delta_2+y_1)^2} - (y_1+\Delta_2)\arcsin\left(-\frac{1+\Delta_2+y_1}{A_{2*}}\right)\right)\right) & x \in D_2, \\ (1-\mu)\left(y_1 + \Delta_2 + \frac{2}{\pi}A_{2*}\right) & x \in D_3, \\ \mu\left(\frac{2}{\pi}\left(\sqrt{A_{1*}^2 - (\Delta_1 - 1 - y_1)^2} + (\Delta_1 - y_1)\arcsin\left(\frac{\Delta_1 - 1 - y_1}{A_1}\right) - A_{1*}\right)\right) + (1-\mu)\left(y_1 + \Delta_2 + \frac{2}{\pi}A_{2*}\right) & x \in D_4, \\ y_1 & x \in D_5, \\ \mu\left(y_1 - \Delta_1 - \frac{2}{\pi}A_{1*}\right) + (1-\mu)\left(\frac{2}{\pi}\left(A_{2*} - \sqrt{A_{2*}^2 - (1-\Delta_2-y_1)^2} + (\Delta_2+y_1)\arcsin\left(\frac{1-\Delta_2-y_1}{A_{2*}}\right)\right)\right) & x \in D_6, \\ \mu\left(y_1 - \Delta_1 - \frac{2}{\pi}A_{1*}\right) & x \in D_7, \\ \mu\left(-\frac{2}{\pi}\left(\sqrt{A_1^2 - (1+\Delta_1-y_1)^2} + (\Delta_1 - y_1)\arcsin\left(\frac{1+\Delta_1-y_1}{A_{1*}}\right)\right) - \Delta_1 + y_1\right) & x \in D_8, \\ 0 & x \in D_9. \end{cases} \tag{5.179}$$

Note that D_3 and D_7 are typically small due to the assumption of the particles' small physical size.
Thus, the differential equation describing the 'slow' motion is given by

$$\ddot{y}_1 + \tilde{V}'(y_1) = F \sin(\Omega_{11}\tau + \beta_{11}). \tag{5.180}$$

Although $\tilde{V}'(y_1)$ describes the effective force field, integrating it once more offers the effective potential $\tilde{V}(y_1)$. Due to the complexity of $\tilde{V}'(y_1)$, the exact form is intricate, and we do not express it in closed form.
In Fig. 5.10, a graphical example depicts the analytically calculated effective restoring force and its (numerically) obtained integral, the effective potential for selected parameter values.
One critical consequence of the asymmetric integration kernel is the asymmetry of the effective force field. Consequently, the potential energy at the right boundary of the potential diverges from that on the left side, potentially causing uneven escape dynamics. The likelihood of escape towards the right may vary compared to that towards the left. As the ratio m_1/m_2 diverges from unity, the asymmetry intensifies, resulting in vibrations centered around a point other than 0.

5.2.4 Numerical results and discussion

It is possible to assess the accuracy of the order reduction method by displaying the escape time on a low excitation frequency–force diagram. Fig. 5.11 shows such a comparison between the reduced and original models. It should be noted that the sharp

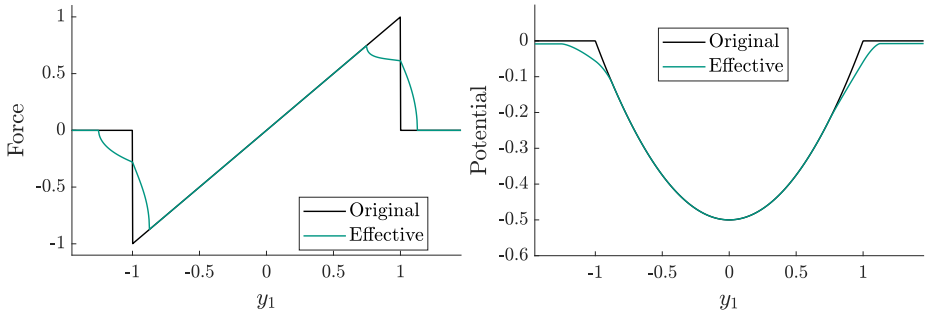

(a) Force–$\tilde{V}'(y_1)$ **(b)** Potential–$\tilde{V}(y_1)$

Figure 5.10: Non-linear original and effective restoring force and potential for $m_1 = 2$, $m_2 = 1$, $c = 800$, $k = 0.5$, $R = 0.99$, $F_{12} = 15$, $\Omega_{12} = 69.306$ ($l = 1$), $\Delta = 0.0003$

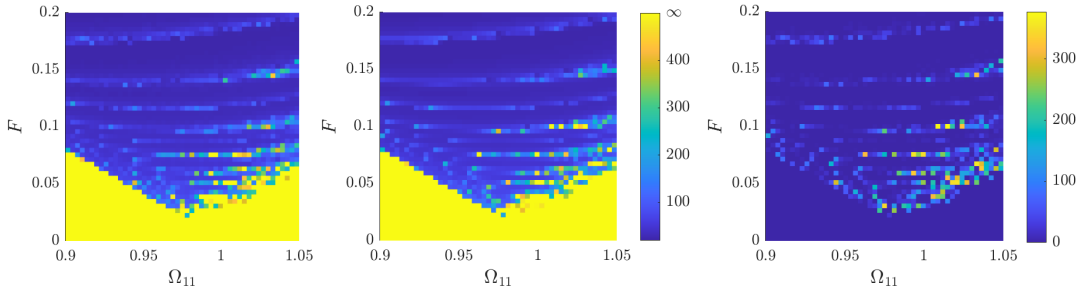

(a) Original model **(b)** Reduced model **(c)** Absolute error in the escape time

Figure 5.11: Contrasting the original and reduced models with excitation at the first resonant frequency, $\Omega_{12} = 69.34$ ($l = 1$) and parameter values $m_1 = 2$, $m_2 = 1$, $c = 800$, $k = 0.5$, $F_{12} = 15$, $R = 0.99$, $\Delta = 0.0003$, $\beta_{11} = -\pi/2$ and homogeneous initial conditions. The color scale represents the escape time. $F := \frac{F_{11}}{m_1+m_2}$. In the one-degree-of-freedom system, a simulation time reduction from 5 hours to 4 minutes has been observed

minimum (Ω_C, F_C) observed in many studies can be determined with relative accuracy. However, there is no frequency-dependent critical forcing value above which escape occurs for any forcing amplitude. Instead, the transition from no escape to escape occurs along a fractal-like boundary, and there are even separate nonescaping 'islands' in the sea of escaping $\Omega_{11} - F_{11}$ parameter combinations.

5.2.5 Conclusions

This section explored the escape dynamics of a strongly coupled, colliding pair of particles from a potential well under bi-harmonic excitation. By transforming the physical coordinates to those representing the center of mass and the inter-particle distance, we could segregate the motion into slower and faster components. The fast

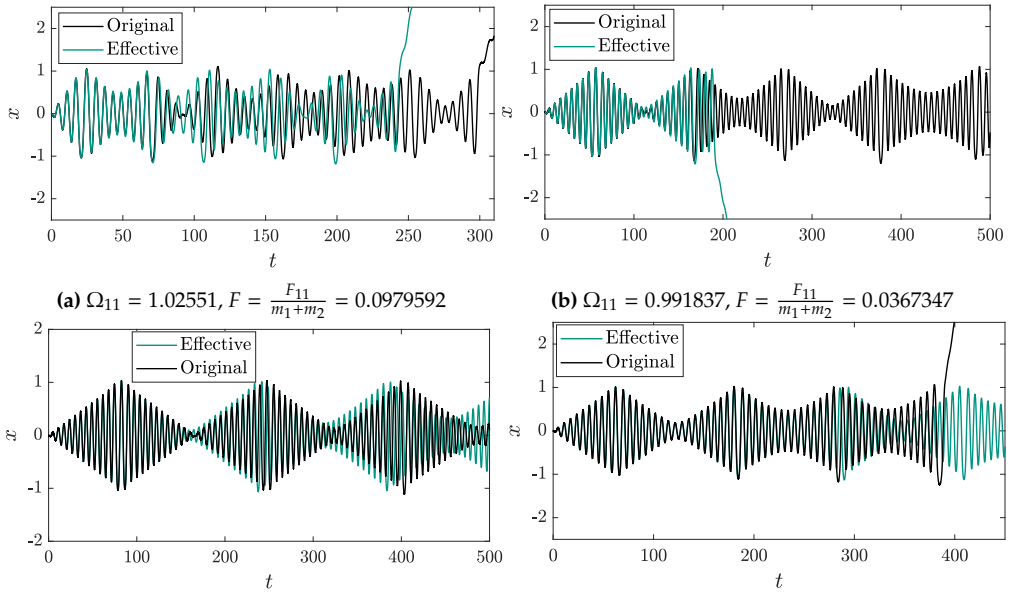

(a) $\Omega_{11} = 1.02551$, $F = \frac{F_{11}}{m_1+m_2} = 0.0979592$

(b) $\Omega_{11} = 0.991837$, $F = \frac{F_{11}}{m_1+m_2} = 0.0367347$

(c) $\Omega_{11} = 0.99$, $F = \frac{F_{11}}{m_1+m_2} = 0.025$

(d) $\Omega_{11} = 1.0071429$, $F = \frac{F_{11}}{m_1+m_2} = 0.032653061$

Figure 5.12: Time series comparison of the original and the reduced model with parameters $m_1 = 2$, $m_2 = 1$, $c = 800$, $k = 0.5$, $F_{12} = 15$, $\Omega_{12} = 69.306$ ($l = 1$), $\Delta = 0.0003$ and homogeneous initial conditions. All four combinations of escape/no escape are possible

motion's oscillation amplitudes were determined using the 'unfolding transformation.' Then, the averaging method based on the fast motion's probability density function was utilized to obtain the effective restoring force acting on the particles' center of mass. The derived expressions for the effective force field are entirely analytical, enabling significant reductions in simulation time (from 5 hours to 4 minutes, as demonstrated). Critical system characteristics, such as the positioning of non-escaping islands within the $\Omega_{11} - F_{11}$ domain, are effectively preserved. Although this investigation focused on escape within a truncated quadratic potential, the outlined PDF-centric averaging approach readily adapts to various potential forms.

6 Positioning of an overdamped particle

In the preceding chapters, we explored the concept of escape from a passive standpoint. In this chapter, we switch to an active perspective and discuss the positioning of a particle in a potential well using harmonic excitation. The variable that will be altered is only the excitation amplitude. The following text and the included figures are adapted from the study by *Genda et al.* [223].
This chapter is organized as follows: Sect. 6.1 introduces the problem setting. In Sect. 6.2 the steady-state solutions are determined using the harmonic balance method, followed by Sect. 6.3, where the stability analysis of these solutions is performed. Sect. 6.4 validates our theoretical findings through numerical simulations. The implications and limitations of our study are discussed in Sect. 6.5. We conclude with Sect. 6.6, which summarizes this chapter and suggests avenues for future investigation.

6.1 Problem setting

The following study focuses on the dynamic behavior of a strongly damped particle within a cosine potential when subjected to harmonic excitation. The system's differential equation is represented in Eq. (6.1). This scenario is mechanically similar to a pendulum experiencing damping in a gravitational setting, additionally influenced by periodic external forces. The primary equation governing the motion is formulated as follows:

$$m\ddot{x} + k\dot{x} + c\sin x = f\sin(\omega\tau + \beta), \tag{6.1}$$

where τ [s] represents the time, x [m] is the displacement, and

- m [kg] represents the mass of the particle,
- k [kg/s] denotes the damping coefficient, significant enough to cause overdamped dynamics; i.e., $k = O(1)$.
- $c\sin x$ [kg $\cdot$ m/s^2] is the restoring force due to the potential.

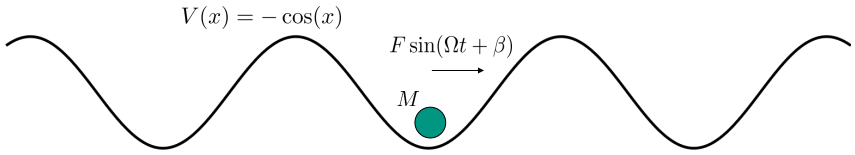

Figure 6.1: Problem setting. Figure adapted from [223]

- f [kg·m/s^2] indicates the magnitude of the external force, which is also considered to be of the order $O(1)$.

The excitation frequency ω [rad/s] and the initial phase β [rad] are given without specific constraints.
We reduce the number of parameters through the transformation of coordinates $\tau = \omega_0 t$ (where prime denotes differentiation with respect to τ), with ω_0 defined as c/k and introducing the dimensionless frequency $\Omega := k\omega/c$, along with dimensionless mass and force parameters

$$M := \frac{cm}{k^2}, \qquad F := \frac{f}{k\omega_0}. \tag{6.2}$$

Subsequently, the equation of motion is reformulated as

$$Mx'' + x' + \sin x = F\sin(\Omega t + \beta). \tag{6.3}$$

Numerical analysis indicates that the steady-state solutions of the system extend beyond simple oscillations at the potential's minimum, as presented in Fig. 6.2a. They may also stabilize around the potential's peak for certain values of F, as demonstrated in Fig. 6.2c. Moreover, it is possible to achieve solutions that exist in states intermediate to these extremes, as emphasized in Fig. 6.2b. This introduces the potential for symmetry breaking in the stationary states, a phenomenon that will be explored analytically in the subsequent section.

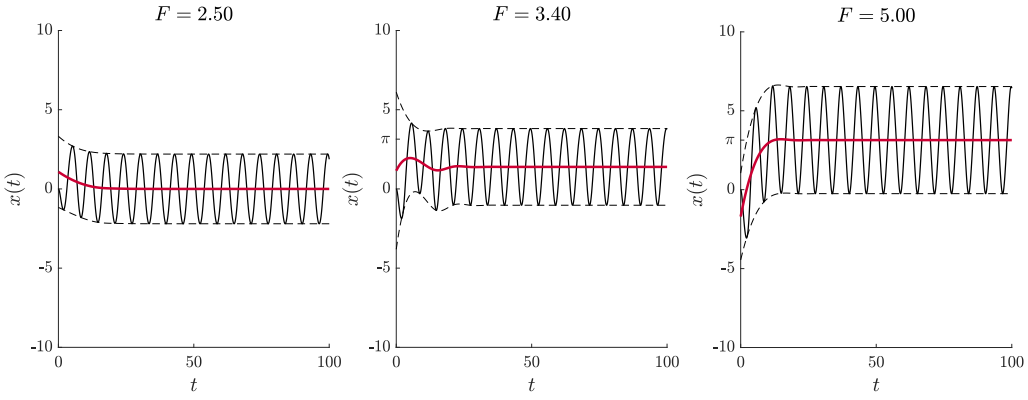

(a) Bottom **(b)** Intermediate **(c)** Top

Figure 6.2: Different solution types (illustrated with black solid lines) for parameter values $M = 1$, $\Omega = 1$, $\beta = \pi/2$ under homogeneous initial conditions $(x(0) = 0, \dot{x} = 0)$. Depending on the selected value of F, the center of the vibration (indicated by the red line) can maintain stability at either the bottom, top, or any position along the cosine potential. This center of oscillation is approximated by the average of the upper and lower boundary lines of the numerical simulation (shown as dashed black lines). Figure adapted from [223]

6.2 Analytical approach

When significant damping is present, numerical simulations of Eq. (6.3) only reveal periodic solutions, without chaotic phenomena or irregularities such as period doubling. Thus, for further examination, we assume that the system, after undergoing a transient phase, achieves a stationary stage where the fundamental frequency aligns with the driving frequency. Our goal is to identify these steady-state solutions and evaluate their stability.

Given that the system settles into periodic solutions in its steady state, the harmonic balance method is appropriate for analyzing the system's long-term dynamics. To accommodate asymmetric solutions, a constant (bias) term is introduced alongside the primary harmonic term:

$$x_0(t) = A_0 + A_1 \sin(\Omega t + \beta - \Psi). \tag{6.4}$$

Incorporating this expression into the differential equation, as specified by Eq. (6.3), yields:

$$\begin{aligned} M(-\Omega^2 A_1 \sin(\Omega t + \beta - \Psi)) + A_1 \Omega \cos(\Omega t + \beta - \Psi) \\ + \sin(A_0 + A_1 \sin(\Omega t + \beta - \Psi)) = F \sin(\Omega t + \beta). \end{aligned} \tag{6.5}$$

The complexity of the inclusion of a sine function within another sine function in Eq. (6.5) is handled using the Jacobi-Anger expansion, represented by Eqs. (6.6)-(6.7):

$$\sin(z\sin(\theta)) = 2\sum_{n=1}^{\infty} J_{2n-1}(z)\sin\left[(2n-1)\theta\right], \tag{6.6}$$

$$\cos(z\sin(\theta)) = J_0(z) + 2\sum_{n=1}^{\infty} J_{2n}(z)\cos(2n\theta), \tag{6.7}$$

where $J_n(z)$ denotes the Bessel function of the first kind of order n.
By applying Eqs. (6.6)-(6.7) to Eq. (6.5) and matching terms up to the first harmonic of Ωt, we arrive at three nonlinear algebraic equations by isolating the constant, the $\sin(\Omega t + \beta)$, and the $\cos(\Omega t + \beta)$ terms:

$$J_0(A_1)\sin A_0 = 0, \tag{6.8}$$

$$-A_1\Omega^2 M\cos\Psi + A_1\Omega\sin\Psi + 2\cos A_0 J_1(A_1)\cos\Psi = F, \tag{6.9}$$

$$A_1\Omega^2 M\sin\Psi + A_1\Omega\cos\Psi - 2\cos A_0 J_1(A_1)\sin\Psi = 0. \tag{6.10}$$

Eq. (6.8) indicates three distinct solution categories, or, as referred to in the following, solution families: either A_0 is located at the cosine potential's minimum (bottom solution family) or maximum (top solution family), or A_1 matches a zero of the Bessel function J_0 (intermediate solution family), i.e.,

$$A_{0,1} = 2k\pi, \qquad k \in \mathbf{Z}, \tag{6.11}$$

$$A_{0,2} = (2k+1)\pi, \qquad k \in \mathbf{Z}, \tag{6.12}$$

$$A_{1,3} = J_0^{-1}(0), \qquad A_{1,3} > 0, \tag{6.13}$$

where $J_0^{-1}(0)$ signifies all positive zeroes of the zeroth-order Bessel function of the first kind. For the scenarios depicted by Eqs. (6.11)-(6.12), the determination of A_1 and Ψ requires further calculations from Eqs. (6.9)-(6.10), whereas in the case of Eq. (6.13), the values of A_0 and Ψ are deduced from the remaining equations.
For an illustrative representation of the solution families, refer to Fig. 6.7b. The three identified solution families are detailed as follows:

6.2.1 Bottom solution family

By substituting Eq. (6.11) in Eqs. (6.9)-(6.10) and performing algebraic manipulations, we can isolate Ψ and A_1 in two separate equations:

$$\sin\Psi_1 = \frac{A_{1,1}\Omega}{F},$$

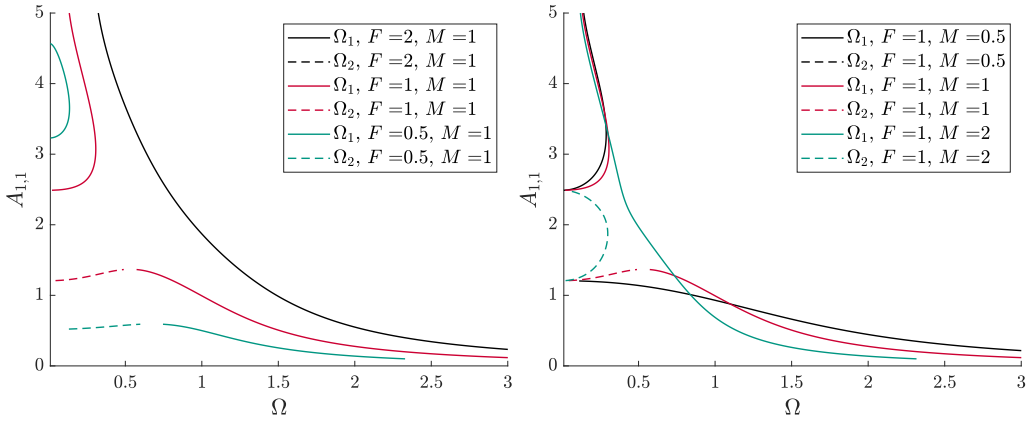

(a) F varies **(b)** M varies

Figure 6.3: Graphical representation of the solutions of Eq. (6.15). Solutions within a certain amplitude range might only exists, if Ω_2 is real

$$\left(A_{1,1}\Omega^2 M - 2J_1(A_{1,1})\right)^2 + A_{1,1}^2\Omega^2 = F^2. \tag{6.14}$$

Although an explicit solution for $A_{1,1}$ from Eq. (6.14) is not available, it is possible to express $\Omega(A_{1,1})$ as

$$\Omega_{1,2} = \sqrt{\frac{1}{M}\left(\frac{2J_1(A_{1,1})}{A_{1,1}} - \frac{1}{2M} \pm \sqrt{\frac{1}{4M^2} - \frac{2J_1(A_{1,1})}{A_{1,1}M} + \frac{F^2}{A_{1,1}^2}}\right)}. \tag{6.15}$$

A graphical representation of the solutions for various values of F and M are shown in Fig. 6.4

For $A_{1,1}$ we can propose an asymptotic solution for high F values where the influence of the cosine potential's force is minor in comparison to damping and inertial forces:

$$A_{1,1} \approx \frac{F}{\Omega}\frac{1}{\sqrt{\Omega^2 M^2 + 1}}, \quad \text{for } F \gg 1. \tag{6.16}$$

6.2.2 Top solution family

In a similar manner, by inserting Eq. (6.12) in Eqs. (6.9)-(6.10) and executing analogous algebraic steps, equations containing only Ψ and A_1 can be derived:

$$\sin\Psi_2 = \frac{A_{1,2}\Omega}{F},$$

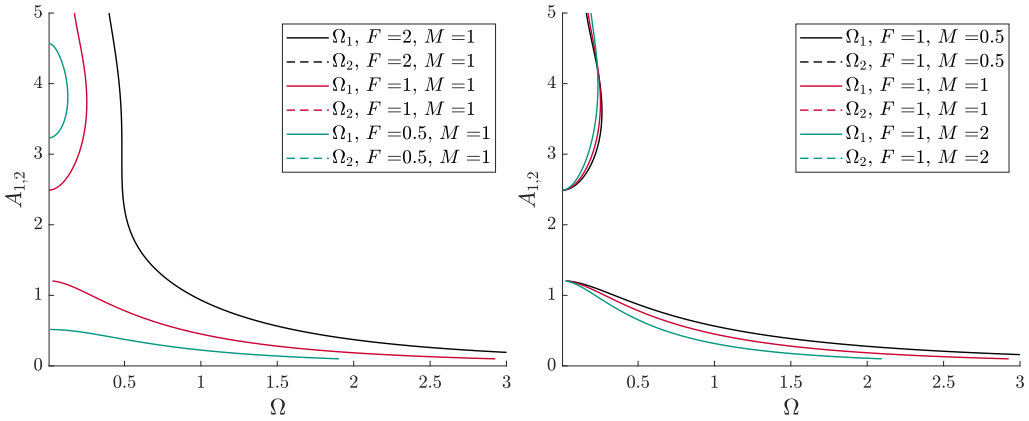

(a) F varies **(b)** M varies

Figure 6.4: Graphical representation of the solutions of Eq. (6.18). Solutions within a certain amplitude range might not exist at all

$$\left(A_{1,2}\Omega^2 M + 2J_1(A_{1,2})\right)^2 + A_{1,2}^2\Omega^2 = F^2, \tag{6.17}$$

highlighting that the equations for the bottom solution family and the top solution family diverge solely in the sign preceding $2J_1(A_{1,2})$. The frequency obtained as a function of the amplitude is given by

$$\Omega_{1,2} = \sqrt{\frac{1}{M}\left(-\frac{2J_1(A_{1,1})}{A_{1,1}} - \frac{1}{2M} \pm \sqrt{\frac{1}{4M^2} + \frac{2J_1(A_{1,1})}{A_{1,1}M} + \frac{F^2}{A_{1,1}^2}}\right)}, \tag{6.18}$$

where Ω_2 (with a negative sign preceding the inner square root) is physically infeasible since always complex-valued. The solution exhibits a complex pattern for small Ω values, characterized by several roots. Consequently, subsequent discussions will focus on $\Omega \geq 1$, where root multiplicity ceases to be a concern.

6.2.3 Intermediate solution family

The approach to identifying this set of solutions is different from the previous cases because the feasible values for A_1 are predetermined and the focus turns to determining A_0. Denoting the k^{th} root of $J_0(A_1)$ as α_k, we rewrite Eqs. (6.9)-(6.10) as:

$$\left(2\cos A_0 J_1(\alpha_k) - \alpha_k\Omega^2 M\right)\cos\Psi + \alpha_k\Omega\sin\Psi = F, \tag{6.19}$$

$$-\left(2\cos A_0 J_1(\alpha_k) - \alpha_k\Omega^2 M\right)\sin\Psi + \alpha_k\Omega\cos\Psi = 0, \tag{6.20}$$

leading to the following formulas:

$$\sin \Psi_3 = \frac{\alpha_k \Omega}{F},$$
$$\left(2 \cos A_0 J_1(\alpha_k) - \alpha_k \Omega^2 M\right)^2 + \alpha_k^2 \Omega^2 = F^2. \tag{6.21}$$

From Eq. (6.21), A_0 can be calculated as

$$A_0 = 2\pi l \pm \arccos\left(\frac{\alpha_k \Omega^2 M \pm \sqrt{F^2 - \alpha_k^2 \Omega^2}}{2 J_1(\alpha_k)}\right), \quad l \in \mathbf{Z}. \tag{6.22}$$

Eq. (6.22) yields two different types of solutions, as the square root can have a positive or negative sign. However, these solutions might be complex-valued and thus unphysical for certain parameter values.
Real intermediate solutions exist depending on whether the argument of the arccos function is within the range $[-1, 1]$. For such a solution to exist,

$$\alpha_k \Omega < F \tag{6.23}$$

must hold. Additionally, the argument of the arccos function remains real if the following condition is satisfied:

$$-1 \leq \frac{\alpha_k \Omega^2 M \pm \sqrt{F^2 - \alpha_k^2 \Omega^2}}{2 J_1(\alpha_k)} \leq 1. \tag{6.24}$$

For $J_1(\alpha_k) > 0$, the existence condition becomes

$$-2J_1(\alpha_k) - \alpha_k \Omega^2 M \leq \pm\sqrt{F^2 - \alpha_k^2 \Omega^2} \leq 2J_1(\alpha_k) - \alpha_k \Omega^2 M, \tag{6.25}$$

whereas for $J_1(\alpha_k) < 0$, the condition is

$$-2J_1(\alpha_k) - \alpha_k \Omega^2 M \geq \pm\sqrt{F^2 - \alpha_k^2 \Omega^2} \geq 2J_1(\alpha_k) - \alpha_k \Omega^2 M. \tag{6.26}$$

Whether a real solution with plus or minus sign in front of the square root exists can be answered by case analysis. Here, we focus on the scenario where $J_1(\alpha_k) > 0$, as outlined in Eq. (6.25), with the understanding that the procedure and the results of Eq. (6.26) are analogous.

The left-hand term of Eq. (6.25) is invariably negative, and its right-hand term becomes negative when

$$\frac{2J_1(\alpha_k)}{\alpha_k\Omega^2} < M, \tag{6.27}$$

under which circumstances only the negative square root, $-\sqrt{F^2-\alpha_k^2\Omega^2}$, is applicable. Consequently, we find that

$$\sqrt{(\alpha_k\Omega^2M-2J_1(\alpha_k))^2+\alpha_k^2\Omega^2} \le F \le \sqrt{(\alpha_k\Omega^2M+2J_1(\alpha_k))^2+\alpha_k^2\Omega^2}, \tag{6.28}$$

which also satisfies the condition outlined in Eq. (6.23).
However, if the condition

$$\frac{2J_1(\alpha_k)}{\alpha_k\Omega^2} > M, \tag{6.29}$$

is fulfilled, $-\sqrt{F^2-\alpha_k^2\Omega^2}$ satisfies the right side of Eq. (6.25), but the positive square root, $+\sqrt{F^2-\alpha_k^2\Omega^2}$, also becomes feasible under the condition that

$$\alpha_k\Omega \le F \le \sqrt{(2J_1(\alpha_k)-\alpha_k\Omega^2M)^2+\alpha_k^2\Omega^2}, \tag{6.30}$$

thereby allowing for two potential solution forms:

$$A_0 = 2\pi l \pm \arccos\left(\frac{\alpha_k\Omega^2M \pm \sqrt{F^2-\alpha_k^2\Omega^2}}{2J_1(\alpha_k)}\right), \quad l \in \mathbf{Z}, \tag{6.31}$$

to exist. For the range

$$\sqrt{(\alpha_k\Omega^2M-2J_1(\alpha_k))^2+\alpha_k^2\Omega^2} \le F \le \sqrt{(\alpha_k\Omega^2M+2J_1(\alpha_k))^2+\alpha_k^2\Omega^2}, \tag{6.32}$$

only the solution

$$A_0 = 2\pi l \pm \arccos\left(\frac{\alpha_k\Omega^2M - \sqrt{F^2-\alpha_k^2\Omega^2}}{2J_1(\alpha_k)}\right), \quad l \in \mathbf{Z}, \tag{6.33}$$

remains feasible.

The observation of two distinct solutions within the intermediate solution family under the parameter conditions of Eq. (6.29) results from the limitations of the applied harmonic balance ansatz, as it incorporates only a constant term along with the first harmonic to approximate the periodic steady-state response of Eq. (6.3). The limitation of this approach is evident in the parameter region specified, leading to the emergence of a physically invalid solution. Incorporating additional terms into the harmonic balance ansatz could eliminate this discrepancy. In fact, such dual solutions could not be detected in numerical simulations: as the force amplitude increases, the vibration center A_0 transitions smoothly and continuously between the bottom and top of the potential (see Figs. 6.6a and 6.7a).
The analysis for cases where $J_1(\alpha_k) < 0$ follows a similar logic, revealing an analogous artificial dual-solution parameter space.

6.3 Stability analysis of steady-state solutions

After identifying the periodic steady-state solutions of Eq. (6.3), the next step involves determining their stability. To this end, we introduce a small perturbation δ to the steady-state solution x_0, such that:

$$x(t) = x_0(t) + \delta(t), \tag{6.34}$$

and incorporate it into Eq. (6.3) to obtain:

$$Mx_0'' + M\delta'' + x_0' + \delta' + \sin(x_0 + \delta) = F\sin(\Omega t + \beta), \tag{6.35}$$

By linearizing the sine term around x_0, the equation simplifies to:

$$Mx_0'' + M\delta'' + x_0' + \delta' + \sin(x_0) + \cos(x_0)\delta = F\sin(\Omega t + \beta). \tag{6.36}$$

Given x_0 satisfies Eq. (6.3) under the first harmonic approximation, simplifying Eq. (6.35) by canceling terms leads to:

$$M\delta'' + \delta' + \cos(x_0)\delta = 0. \tag{6.37}$$

Eq. (6.37) represents a linear differential equation with parametric excitation, as x_0 varies over time. To analyze stability, one approach involves calculating Hill's determinant. By transforming time with $\tau := \Omega t/2$, we arrive at the following:

$$\frac{M\Omega^2}{4}\ddot{\delta} + \frac{\Omega}{2}\dot{\delta} + \cos\left(A_0 + A_1\sin(2\tau - \Psi)\right)\delta = 0, \tag{6.38}$$

where $\dot{\square} := \frac{d\square}{d\tau}$.
At the boundary between stable and unstable parameters, the solution oscillates with a period of π or 2π, as stated by Hill's theory [130]. For a solution with period length π, it can be expressed as a Fourier series:

$$\delta(t) = \sum_{n=0}^{\infty} a_n \cos(2n\tau) + \sum_{n=1}^{\infty} b_n \sin(2n\tau), \tag{6.39}$$

with undetermined coefficients a_n and b_n. The time-dependent parameter in δ can similarly be expressed as a series:

$$\cos\left(A_0 + A_1 \sin(2\tau - \Psi)\right) = \sum_{n=0}^{\infty} c_n \cos(2n\tau) + \sum_{n=1}^{\infty} d_n \sin(2n\tau), \tag{6.40}$$

with coefficients c_n and d_n defined by:

$$c_0 = \frac{1}{\pi} \int_0^{\pi} \cos\left(A_0 + A_1 \sin(2\tau - \Psi)\right) d\tau, \tag{6.41}$$

$$c_n = \frac{2}{\pi} \int_0^{\pi} \cos\left(A_0 + A_1 \sin(2\tau - \Psi)\right) \cos(2n\tau) d\tau \quad \text{for } n \in \mathbb{N}^+, \tag{6.42}$$

$$d_n = \frac{2}{\pi} \int_0^{\pi} \cos\left(A_0 + A_1 \sin(2\tau - \Psi)\right) \sin(2n\tau) d\tau \quad \text{for } n \in \mathbb{N}^+. \tag{6.43}$$

To evaluate Eqs. (6.41)-(6.43), leveraging the Jacobi-Anger expansion simplifies the integrand as follows:

$$\begin{aligned}
&\cos(A_0 + A_1 \sin(2\tau - \Psi)) = \cos(A_0)\cos(A_1 \sin(2\tau - \Psi)) - \sin(A_0)\sin(A_1 \sin(2\tau - \Psi)) \\
&\quad = \cos(A_0)\left(J_0(A_1) + 2\sum_{n=1}^{\infty} J_{2n}(A_1)\cos(4n\tau - 2n\Psi)\right) \\
&\qquad - \sin(A_0)\left(2\sum_{n=1}^{\infty} J_{2n-1}(A_1)\sin((2n-1)(2\tau - \Psi))\right) \\
&\quad = \cos(A_0)\left(J_0(A_1) + 2\sum_{n=1}^{\infty} J_{2n}(A_1)(\cos(4n\tau)\cos(2n\Psi) + \sin(4n\tau)\sin(2n\Psi))\right) \\
&\qquad - \sin(A_0)\Bigg(2\sum_{n=1}^{\infty} J_{2n-1}(A_1)(\sin(2(2n-1)\tau)\cos((2n-1)\Psi) \\
&\qquad\qquad - \cos(2(2n-1)\tau)\sin((2n-1)\Psi))\Bigg).
\end{aligned} \tag{6.44}$$

This expansion allows for the calculation of the coefficients c_n and d_n by decomposing the cosine term into its harmonic components. This enables a systematic analysis of the stability of periodic steady-state solutions.
Given the orthogonality of sines and cosines, the Fourier coefficients are derived as follows:

$$c_0 = \cos(A_0)J_0(A_1), \tag{6.45}$$

$$c_n = \begin{cases} 2\sin(A_0)J_n(A_1)\sin(n\Psi) & \text{for } n \text{ odd in } \mathbb{N}^+, \\ 2\cos(A_0)J_n(A_1)\cos(n\Psi) & \text{for } n \text{ even in } \mathbb{N}^+, \end{cases} \tag{6.46}$$

$$d_n = \begin{cases} -2\sin(A_0)J_n(A_1)\cos(n\Psi) & \text{for } n \text{ odd in } \mathbb{N}^+, \\ 2\cos(A_0)J_n(A_1)\sin(n\Psi) & \text{for } n \text{ even in } \mathbb{N}^+. \end{cases} \tag{6.47}$$

Substituting Eq. (6.39) in Eq. (6.38) and equating the coefficients for $\cos(2n\tau)$ and $\sin(2n\tau)$ results in an infinite linear system for a_n and b_n as follows:

$$\begin{bmatrix} 0 \\ 0 \\ 0 \\ 0 \\ 0 \\ \vdots \end{bmatrix} = \begin{bmatrix} c_0 & \frac{c_1}{2} & \frac{d_1}{2} & \frac{c_2}{2} & \frac{d_2}{2} & \dots \\ c_1 & c_0 + \frac{c_2}{2} - M\Omega^2 & \frac{d_2}{2} + \Omega & \frac{c_1}{2} + \frac{c_3}{2} & \frac{d_1}{2} + \frac{d_3}{2} & \dots \\ d_1 & \frac{d_2}{2} - \Omega & c_0 - \frac{c_2}{2} - M\Omega^2 & -\frac{d_1}{2} + \frac{d_3}{2} & \frac{c_1}{2} - \frac{c_3}{2} & \dots \\ c_2 & \frac{c_1}{2} + \frac{c_3}{2} & -\frac{d_1}{2} + \frac{d_3}{2} & c_0 + \frac{c_4}{2} - 4M\Omega^2 & \frac{d_4}{2} + 2\Omega & \dots \\ d_2 & \frac{d_1}{2} + \frac{d_3}{2} & \frac{c_1}{2} - \frac{c_3}{2} & \frac{d_4}{2} - 2\Omega & c_0 - \frac{c_4}{2} - 4M\Omega^2 & \dots \\ \vdots & \vdots & \vdots & \vdots & \vdots & \ddots \end{bmatrix} \begin{bmatrix} a_0 \\ a_1 \\ b_1 \\ a_2 \\ b_2 \\ \vdots \end{bmatrix}. \tag{6.48}$$

For a non-trivial solution to exist, the determinant of the Hill matrix in Eq. (6.48) must vanish. Calculating directly the determinant of an infinite matrix is impossible; therefore, an approximation is employed by truncating the first $(2n + 1)$ rows and columns. In particular, for $n = 0$, we obtain a single value c_0, which leads to the stability boundary approximation:

$$\Delta_0 := c_0 = \cos(A_0)J_0(A_1) \stackrel{!}{=} 0. \tag{6.49}$$

We can also calculate the determinant for $n = 1$ and $n = 2$, to obtain a better estimate. However, the calculations are much more intricate in these cases. Therefore, before proceeding, we limit the investigation to the bottom solution family by inserting $A_0 = 0$, resulting in the determinants

$$\Delta_1 := J_0(A_1)\left(M^2\Omega^4 - 2J_0(A_1)M\Omega^2 + J_0(A_1)^2 - J_2(A_1)^2 + \Omega^2\right) \tag{6.50}$$

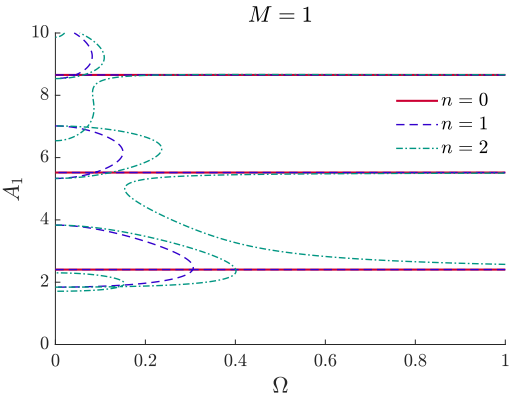

(a) For non-small M, the solutions of $\Delta_1 = 0$ and $\Delta_2 = 0$ remain distinct

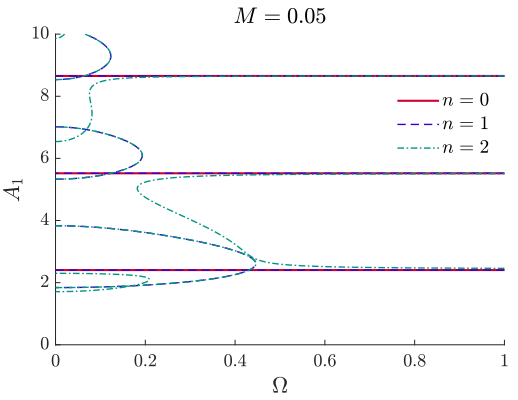

(b) For small M, the solutions of $\Delta_1 = 0$ converges to solutions of $\Delta_2 = 0$. Although Δ_2 has further solutions

Figure 6.5: Numerically evaluated solutions of $\Delta_n = 0$ for $n = \{0, 1, 2\}$ with $M = \{0.05, 1\}$ and A_0. For $n = 0$ and $n = 1$, $c_0 = 0$ is a solution; however, for $n = 2$ it is only an approximation, to which the solution for large Ω values converges

and

$$\begin{aligned}\Delta_2 := &\left(M^2\Omega^4 - 2J_0(A_1)M\Omega^2 + J_0(A_1)^2 - J_2(A_1)^2 + \Omega^2)\right) \times \\ &\Big(16J_0(A_1)M^2\Omega^4 - 8J_0(A_1)^2M\Omega^2 + 8J_2(A_1)^2M\Omega^2 + J_0(A_1)^3 - 2J_0(A_1)J_2(A_1)^2 \\ &- J_0(A_1)J_4(A_1)^2 + 4J_0(A_1)\Omega^2 + 2J_2(A_1)^2J_4(A_1)\Big),\end{aligned} \tag{6.51}$$

respectively. We can observe that $\Delta_1 = 0$ admits the solution $J_0(A_1) = 0$, but other solutions, at least for a certain parameter region, become feasible. In contrast to that, $\Delta_2 = 0$ does not admit $J_0(A_1) = 0$ as a solution anymore, yet by showing the numerically obtained solutions depending on the value of Ω, we can observe that for reasonably large values of Ω this solution converges to the previously established one, $J_0(A_1) = 0$ (see Fig. 6.5).

For even higher values of n, we offer the following argument to make plausible why the truncation at $n = 0$ should not result in large errors compared. The explanation for this approximation is supported by three observations:

1. Bessel functions of the first kind are bounded between -1 and 1 for nonnegative arguments;
2. $J_n(A_1)$ approaches zero for large n and moderate A_1 values;

3. the Hill matrix's diagonal elements become increasingly negative with $n^2M\Omega^2$, suggesting that the determinant's dominant term is the product of its diagonal elements, which can be represented as

$$D = c_0 \prod_{n=1}^{\infty} \left(c_0 + \frac{c_{2n}}{2} - n^2 M\Omega^2\right)\left(c_0 - \frac{c_{2n}}{2} - n^2 M\Omega^2\right). \tag{6.52}$$

Thus, apart from c_0, no other term in the determinant can approach zero, confirming the stability boundary approximation made with $n = 0$. This approach remains valid for non-negligible frequency values, where numerical simulations corroborate the stability boundary's proximity to that predicted by $c_0 = 0$ (see Fig. 6.5). The complexity increases for smaller Ω values due to slower growth of the matrix's diagonal terms, potentially introducing additional stability boundaries. However, exploring these scenarios exceeds the scope of this analysis.
The stability boundary for periodic solutions with a period of 2π, when analyzed under truncation at $n = 0$, yields an identical condition to that found in Eq. (6.49). This outcome also aligns with a straightforward averaging of the time-dependent parameter in Eq. (6.38):

$$\langle \cos(A_0 + A_1 \sin(2\tau - \Psi)) \rangle = \cos A_0 J_0(A_1). \tag{6.53}$$

Considering the averaged disturbance $\tilde{\delta} = \langle \delta \rangle$, the averaged form of Eq. (6.38) simplifies to:

$$\frac{M\Omega^2}{4}\ddot{\tilde{\delta}} + \frac{\Omega}{2}\dot{\tilde{\delta}} + \cos A_0 J_0(A_1)\tilde{\delta} = 0. \tag{6.54}$$

By examining A_0 and A_1 for different solution families, a straightforward linear stability analysis can be used to assess the stability of steady-state solutions identified in Sects. 6.2.1-6.2.3. For a solution to be asymptotically stable, the condition $\cos A_0 J_0(A_1) > 0$ must hold.

6.3.1 Stability of the bottom solution family

For the bottom solution family, where the vibration center A_0 is at the bottom of the potential well, $\cos A_0 = 1$. The solution is considered stable if $J_0(A_1)$ is positive. Since A_1 changes continuously with F, the stability boundaries are defined between two

consecutive roots of $J_0(A_1) = 0$. Applying this to Eq. (6.14), we obtain the critical forcing values at which the stability of the steady-state solution changes:

$$F_{\text{crit,1,k}} = \sqrt{(2J_1(\alpha_k) - \alpha_k \Omega^2 M)^2 + \alpha_k^2 \Omega^2}, \tag{6.55}$$

where α_k denotes the k^{th} root of $J_0(A_1)$. Consequently, the stable regions for the steady-state solution at the bottom of the potential well can be described as follows:

$$\sqrt{(2J_1(\alpha_{2k}) - \alpha_{2k} \Omega^2 M)^2 + \alpha_{2k}^2 \Omega^2} < F < \sqrt{(2J_1(\alpha_{2k+1}) - \alpha_{2k+1} \Omega^2 M)^2 + \alpha_{2k+1}^2 \Omega^2}, \tag{6.56}$$

with $k \in \mathbf{N}$ and defining $\alpha_0 := 0$.

6.3.2 Stability of the top solution family

In the case where the vibration center is at the top of the potential, the scenario mirrors that of the bottom solution family but with $\cos A_0 = -1$. Therefore, the solutions at the top of the potential are stable when $J_0(A_1)$ takes negative values. Critical forcing values, marking transitions in the stability of the steady-state solutions, are given by

$$F_{\text{crit,2,k}} = \sqrt{(2J_1(\alpha_k) + \alpha_k \Omega^2 M)^2 + \alpha_k^2 \Omega^2}, \tag{6.57}$$

where α_k denotes the k^{th} root of $J_0(A_1)$. Consequently, the stability criteria for steady-state solutions are defined as

$$\sqrt{(2J_1(\alpha_{2k+1}) + \alpha_{2k+1} \Omega^2 M)^2 + \alpha_{2k+1}^2 \Omega^2} < F < \sqrt{(2J_1(\alpha_{2k+2}) + \alpha_{2k+2} \Omega^2 M)^2 + \alpha_{2k+2}^2 \Omega^2}, \tag{6.58}$$

with $k \in \mathbf{N}$.
Critical forcing values calculated in Eq. (6.14) and Eq. (6.17) diverge due to the alteration of the sign within the square root. As such, the stable regions for the top and bottom solution families are distinct and do not include all feasible values of F. This discrepancy implies that for certain ranges of F, neither the bottom nor the top solution families are stable, suggesting the existence of an intermediate stable solution situated between these two.

6.3.3 Stability of the intermediate solution family

The linear stability analysis does not offer direct insight into the stability of the intermediate solution family because the values of A_1 are derived from the zeros of

$J_0(A_1)$. As a result, the expression $\cos A_0 J_0(A_1)$ invariably equals zero, which produces an eigenvalue in Eq. (6.38) with a zero real part. The linear approximation employed here does not allow for a definitive conclusion on stability. Nevertheless, both topological reasoning and extensive numerical simulations indicate that the intermediate solution family, as described by Eq. (6.22), is stable for

$$\sqrt{\left(2J_1(\alpha_{2k+1}) - \alpha_{2k+1}\Omega^2 M\right)^2 + (\alpha_{2k+1}\Omega)^2} < F < \sqrt{\left(2J_1(\alpha_{2k+1}) + \alpha_{2k+1}\Omega^2 M\right)^2 + (\alpha_{2k+1}\Omega)^2} \tag{6.59}$$

and

$$\sqrt{\left(2J_1(\alpha_{2k+2}) + \alpha_{2k+2}\Omega^2 M\right)^2 + (\alpha_{2k+2}\Omega)^2} < F < \sqrt{\left(2J_1(\alpha_{2k+2}) - \alpha_{2k+2}\Omega^2 M\right)^2 + (\alpha_{2k+2}\Omega)^2}, \tag{6.60}$$

where k belongs to $\mathbb{N}$ and we define α_0 as zero. It is noted that the sign of $J_1(\alpha_k)$ changes with each successive k, which aligns Eqs. (6.59)-(6.60) with the stability regions described by Eqs. (6.56) and (6.58).

6.4 Verification

Fig. 6.6a illustrates the numerically determined equilibrium of the center of vibration against the values of F and M. A focused analysis of the parameter space for $F = 2.65 \ldots 2.71$ and $M = 0.001 \ldots 0.05$ is presented in Fig. 6.7a. The estimated analytical center of steady-state oscillations is shown in Fig. 6.6b. Although there is qualitative agreement between the analytical and numerical findings, certain discrepancies are observed; for example, the numerically derived critical value for the stability change in $M = 0$ is found at $F_{\text{crit,num}}(M = 0) = 2.677$, in contrast to the analytical forecast of $F_{\text{crit,anal}}(M = 0) = 2.619$. Consequently, the transition range from $A_0 = 0$ to $A_0 = \pi$ also shifts slightly for $M \neq 0$.

The precision of the harmonic balance method could be further enhanced by adding an additional term as follows:

$$x_0(t) = A_0 + A_1 \sin(\Omega t - \Psi_1) + A_2 \sin(2\Omega t - \Psi_2). \tag{6.61}$$

However, this would increase the complexity of the resulting algebraic equations to an analytically unmanageable level.

However, through numerical analysis, it is apparent that the intermediate solution breaks the symmetry, characterized not only by the offset of its center of vibration but also by the appearance of nonzero even Fourier components. To illustrate this, Fig. 6.8

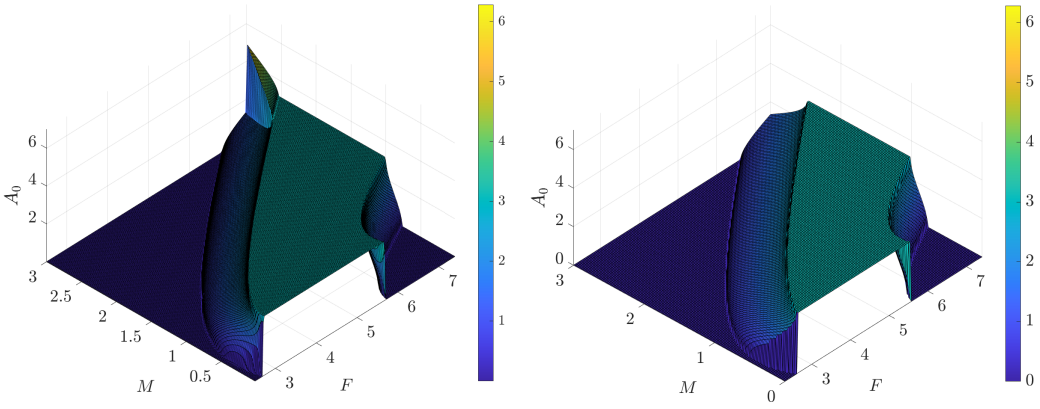

(a) Numerically determined equilibrium position of the center of vibration A_0. The bifurcation in the upper corner is attributed to Eq. (6.33) that allows multiple solutions within a family of solutions. The actual position reached in the steady state depends on the excitation phase and the initial conditions

(b) Analytically determined equilibrium position of the center of vibrations A_0. The lower corner is inaccurately portrayed due to a spurious dual solution resulting from the truncated harmonic balance ansatz. Simulations reveal a smooth transition of A_0 from 0 to π

Figure 6.6: Representation of the steady-state center of vibration A_0 against the values of F and M with $\Omega = 1$, $\beta = \pi/2$ fixed under homogeneous initial conditions ($x(0) = 0$ and $\dot{x}(0) = 0$). The color scale indicates the magnitude of A_0. The abrupt change in the upper corner of Fig. 6.6a results from a shift in the center of the steady-state solution within the same solution family. Such changes are feasible as Eqs. (6.11)-(6.13) only identify stable solution families without specifying the exact solution family member to which the steady-state solution converges. Figures adapted from [223]

provides two instances in which the Fourier coefficients of the periodic steady-state oscillation are calculated through numerical integration of Eq. (6.62)

$$C_k = \frac{1}{T}\int_{t_\infty}^{t_\infty+T} x(t)e^{-i\Omega kt}\,\mathrm{d}t, \tag{6.62}$$

with T representing the period $2\pi/\Omega$, and t_∞ signifying a sufficiently advanced time to disregard the transient dynamics. These coefficients allow for the representation of the steady-state oscillation as:

$$x(t) = \sum_{k=-\infty}^{\infty} C_k e^{i\Omega kt}. \tag{6.63}$$

As F increases, the stability of the solution at the bottom of the potential is lost according to Eq. (6.56), yet solutions near the top of the potential do not immediately become stable as per Eq. (6.58). A solution with an offset center becomes symmetric only there

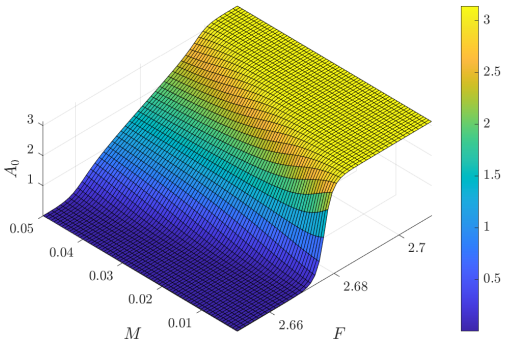

(a) High-resolution view of the bottom part of Fig. 6.6a. The color scale represents the value of A_0. For $M \to 0$, the function converges to a step function at $F_{\text{crit}} = 2.677$, changing its value from $A_0 = 0$ to $A_0 = \pi$

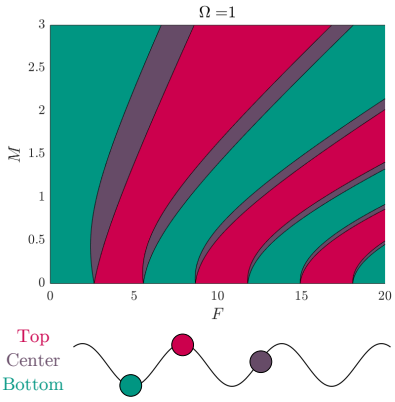

(b) Classification of the stable steady-state solution families

Figure 6.7: Comparison of numerical findings and analytical predictions regarding parameters F and M. The illustration on the left presents numerical findings for small values of M, while the right represents the stable steady-state solution families derived analytically: lower (green), upper (red), and intermediate (purple). Figures adapted from [223]

where the underlying potential exhibits symmetry, occurring only at integer multiples of π. A symmetric solution around these discrete values has an identical shape on both sides of its center, incorporating solely odd harmonics in its Fourier expansion (refer to Fig. 6.8a). In contrast, solutions with a different offset center, reflecting asymmetry in the restoring force, are expected to be asymmetric, leading to a Fourier expansion that includes both odd and even harmonics (see Fig. 6.8b).

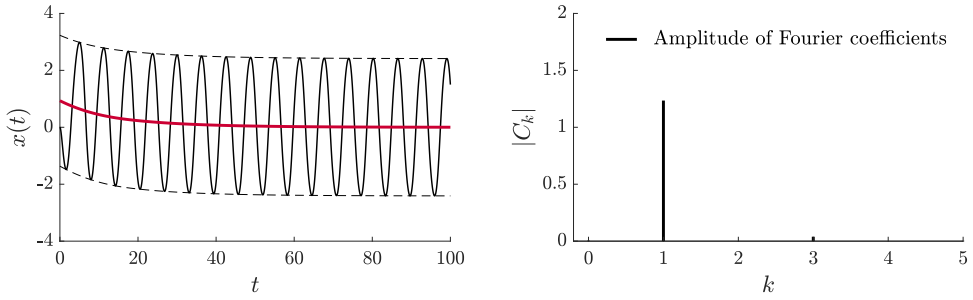

(a) Symmetric steady-state solution for $F = 2.5$

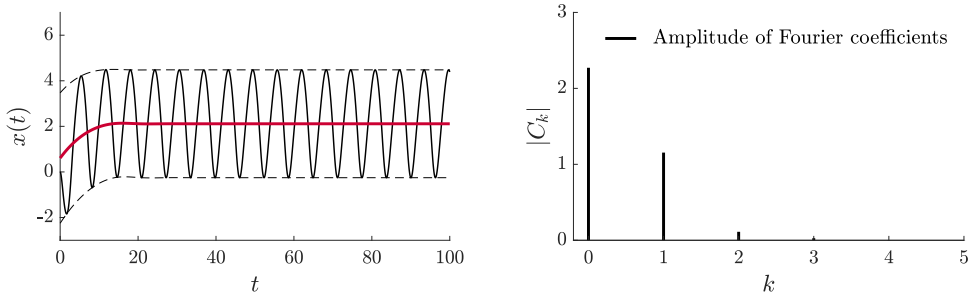

(b) Asymmetric steady-state solution for $F = 3$

Figure 6.8: Decomposition of the solution $x(t)$ as it approaches steady state (on the left) and the spectral amplitudes $|C_k|$ (on the right) for the parameters $M = 0.5$, $F = \{2.5, 3\}$, $\Omega = 1$ and $\beta = -\pi/2$ with initial conditions $x(0) = 0$ and $\dot{x}(0) = 0$. The red line represents the center of the oscillation and the dashed line indicates the slowly evolving envelope of the oscillation. Figures adapted from [223]

6.5 Discussion

This chapter has investigated the dynamic behavior of an overdamped particle in a cosine potential subjected to harmonic excitation. The study reveals that the particle's mass, along with the force's amplitude and frequency, influences the steady-state oscillation's center. We can observe that increasing values of F cause a gradual shift in the oscillation's center from a bottom equilibrium position $2k\pi$ towards an upper equilibrium $(2k \pm 1)\pi$, until a specific force threshold is crossed, stabilizing the oscillation's center at the top of the potential. Upon further increasing F, the oscillation center reverses toward the lower equilibrium, a cycle that repeats with increasing values of F, although the transition between the lower and the upper equilibrium occurs faster and faster with increasing values of F. This phenomenon of continuous transition is attributed to the particle's mass, as a massless particle exhibits an abrupt jump in the steady-state oscillation's center, contrasting with the gradual shift seen in massive particles.
The initial conditions of the system and the excitation phase can also have an effect on the steady-state vibrations, determining the center of vibration within the respective stable

solution family, as shown in Fig. 6.6a, where the upper corner shows the bifurcation of the steady-state center of vibration. However, the solution family itself remains unchanged.
Upon closer inspection, the asymmetry in the system's dynamics, initially attributed to the particle's mass, is inherent to the system itself. Excluding the particle's mass simplifies the system to symmetric dynamics, an oversimplification that overlooks the intrinsic asymmetry captured by Eqs. (6.9)-(6.10).
The amplitude of the steady-state oscillation is predominantly shaped by the damping effect and the mass of the particle; however, the potential's force also plays a role, influencing the oscillation amplitude through its average impact over one oscillation period. Depending on the intensity of the excitation force, this average force can either amplify or diminish the oscillation amplitude relative to the same damped, driven particle when disregarding the effect of the potential. The latter, degenerate case, would always result in stabilization of the center of vibration either at a lower or an upper extremum of the potential. However, due to $M \neq 0$, when stability is lost in a bottom or top equilibrium, stability at the opposite extremum of the potential has not yet been gained, necessitating an intermediate equilibrium for any stable periodic solution.
In contrast, in the massless particle scenario, the system simplifies to first-order dynamics, diverging from traditional mechanical systems and challenging our expectations. The absence of mass equates the vibration amplitudes at both equilibrium points, facilitating immediate stability transfer upon destabilization at one. To explore the transition towards zero mass, the singular perturbation method might offer insights, albeit beyond this study's scope.

6.6 Conclusions and scope for future research

The appearance of stable and biased steady-state solutions within a seemingly symmetric setup underscores the pivotal role of an ansatz in research. An ansatz, essentially an educated guess, significantly simplifies complex problems by focusing on essential variables and dynamics. Its apt selection allows for critical insights, though, in the present case, the challenge lies in identifying an ansatz that, while seemingly redundant, allows for the uncovering of asymmetry in symmetric problems. Examples such as the Kármán vortex street and turbulent flows in pipes illustrate the utility of a well-chosen ansatz in revealing underlying physical phenomena.
The results described in this chapter offer scope for practical applications, such as in electromagnetic or acoustic field-driven molecular systems, where excitation amplitude adjustments alone can modulate position control, bypassing the need for phase manipulation.

A further question arising is the nature of potentials that facilitate continuous vibration center adjustments through mere excitation amplitude enhancements. Exploring the conditions that such potentials have to fulfill is a promising area for future investigation.

7 Summary and Outlook

The main goal of this thesis was to investigate **why escape processes often show nonsmooth characteristics in systems with smooth dynamics.**
The answer to this question is **the contemporaneous existence of different, concurring escape mechanisms.**
In an analysis focusing on 1:1 resonance, we explored how these escape mechanisms produce unique patterns resulting in abrupt, nonsmooth changes in the system dynamics. In undamped systems, the critical forcing curve depicted against the excitation frequency forms a distinctive V-shaped sharp minimum. In the truncated quadratic potential, the Type 1 and 2 maximum mechanisms form the V-curve. In contrast, in the case of nonlinear restoring force, the concurring maximum and saddle mechanisms are responsible for this pattern.
In moderately damped systems, the slow and fast escape mechanisms concur, resulting in sharp, safe basin boundaries and the typical 'Dover cliff' erosion profile, where the safe basin size initially following a plateau drops drastically when the excitation amplitude is further increased.
In strongly damped systems, the initial conditions are of little importance in the escape dynamics since transient processes decay rapidly. However, even so, as demonstrated in Chapter 6, the dynamics of such systems can show significant complexity and result in unexpected, symmetry-breaking solutions.

The following summary provides an overview of each chapter's key findings and discusses possibilities for further research.
Chapter 3 investigated the safe basins of a harmonically driven particle in a quadratic truncated potential, simplifying the analysis to a linear problem. It examined the peculiar structures of safe basins, which occur when the excitation frequency and the potential's natural frequency are integer ratios, resulting in stable, circular portions and illusory parts that disappear with slight perturbations of the frequency ratio.
In the second part of the chapter, the focus was on the effect of viscous damping under harmonic excitation. Similarly to the undamped case, the transient motion cannot be neglected, and it is responsible for two essential escape mechanisms: the 'fast' and the

'slow.' The initial energy of the particle drives the 'fast' mechanism and is significant when the damping is high relative to the frequency difference between excitation and the natural frequency. The 'slow' mechanism resembles a beat phenomenon and becomes prominent when transient motion decays slowly, allowing large amplitude oscillations to develop.

The interplay between these mechanisms determines the size and stability of safe basins, which have significant implications for system safety. The chapter showed that viscous damping increases the size of safe basins but also shows that damping is responsible for the frequently observed erosion profiles of the safe basin area, the Dover cliff profile, where a rush decrease in the safe basin area starts at a critical forcing amplitude. These insights are essential for designing safer systems in industrial applications, where extended safe basins are desired to mitigate oscillations under noisy excitation. Future research could explore the effects of different types of damping on safe basins, such as nonlinear damping or friction. In addition, the impact of noise on safe basins could be investigated to understand how external disturbances affect stability.

Chapter 4 approached escape problems from another perspective, focusing on the critical forcing values depending on the excitation frequency and initial excitation phase and extending the examination of escape dynamics to driven undamped systems with small nonlinearities. It describes the two escape mechanisms (Type 1 Maximum and Saddle) found by *Gendelman* [68] and introduces a third Type 2 Maximum Mechanism, so far not documented in the case of perturbed quadratic potential. The chapter validates these mechanisms through an experiment using a modified test rig with a high-precision capacitive rotational encoder. The measurements revealed that the complex dynamics found in nonlinear, driven-undamped systems persist in the slightly damped case. The measurement confirmed the existence of multiple attractors in the phase space, including chaotic ones. It used a driven, damped double-well Duffing oscillator to model the test rig's dynamics, with the primary objective of identifying the model parameters. Simulations performed on the model showed good agreement with measurement data in the escape dynamics. Future research should focus on exploring sub- and superharmonic resonances, examining escape under frequency-modulated signals, and further exploring complex dynamics in nonlinear systems to enhance system performance, reliability, and safety in engineering applications.

Chapter 5 investigated the escape of multibody systems with different time scales, focusing on n-particle chains under polyharmonic excitation and a colliding, driven pair of particles. The proposed reduction techniques simplify dynamics into slower and faster components by transforming the system into center-of-mass and interparticle distance coordinates, leading to significant computational cost savings. These techniques offer a scalable approach for examining complex systems while preserving fundamental dynamics, with applications to various systems and substantial implications for engineering

and scientific research. Future research can explore applying these techniques to more complicated potential wells, including non-polynomial forms, incorporating different types of excitation like stochastic or time-dependent forces, examining model scalability with increasing particle counts and intricate interactions, and applying model reduction to 2D and 3D potentials. Additionally, investigating scenarios without damping and examining particle chains with nonlinear couplings could enhance the understanding of system dynamics.

Chapter 6 examines control strategies for escape dynamics in overdamped systems, highlighting the discovery of stable and biased steady-state solutions in seemingly symmetric setups, underscoring the importance of an appropriate ansatz in research. These findings suggest practical applications in systems driven by electromagnetic or acoustic fields, where excitation amplitude adjustments can modulate position control without complex phase manipulation. Further research could explore potentials that allow continuous vibration center adjustments through changes in excitation amplitude and other control strategies to manage escape dynamics in complex environments effectively.

List of Figures

Bibliography

[1] Abdi, J., A. Koochi, A. Kazemi, and M. Abadyan (2011): Modeling the effects of size dependence and dispersion forces on the pull-in instability of electrostatic cantilever NEMS using modified couple stress theory. *Smart Materials and Structures* **20**, p. 055011.

[2] Abdoli, I., H. Löwen, J.-U. Sommer, and A. Sharma (2023): Tailoring the escape rate of a Brownian particle by combining a vortex flow with a magnetic field. *Journal of Chemical Physics* **158**(1), p. 014902.

[3] Alsaleem, F., M. Younis, and M. Ibrahim (2009): A study for the effect of the PCB motion and electrostatic force on the dynamics of MEMS devices under mechanical shock. *Journal of Microelectromechanical Systems* **18**, pp. 597–609.

[4] Ansari, R., R. Gholami, M. Shojaei, V. Mohammadi, and M. Darabi (2012): Surface stress effect on the pull-in instability of hydrostatically and electrostatically actuated rectangular nanoplates with various edge supports. *ASME Journal of Engineering Materials and Technology* **134**(4), p. 041013.

[5] Arecchi, F., R. Badii, and A. Politi (1984): Scaling of first passage times for noise induced crises. *Phys. Lett. A* **103A**(1), pp. 3–7.

[6] Asghari, M., M. Kahrobaiyan, and M. Ahmadian (2010): A nonlinear Timoshenko beam formulation based on the modified couple stress theory. *International Journal of Engineering Science* **48**, pp. 1749–1761.

[7] Bai, Z. and P.-X. Wang (2016): Escape rate of Brownian particles from a metastable potential well under time derivative Ornstein-Uhlenbeck noise. *European Physical Journal B* **89**(4), p. 85.

[8] Bao, M. and H. Yang (2007): Squeeze film air damping in MEMS. *Sensors and Actuators A: Physical*, pp. 3–27.

[9] Barone, A. and G. Paterno (1982): *Physics and Applications of the Josephson Effect*. New York: Wiley.

[10] Batra, R., M. Porfiri, and D. Spinello (2007): Review of modeling electrostatically actuated microelectromechanical systems. *Smart Materials and Structures* **16**(3), R23–R31.

[11] Belenky, V. and N. Sevastianov (2007): *Stability and Safety of Ships—Risk of Capsizing*. Jersey City: The Society of Naval Architects and Marine Engineers.

[12] Beni, Y., A. Koochi, A. Kazemi, and M. Abadyan (2012): Modeling the influence of surface effect and molecular force on pull-in voltage of rotational nano–micro mirror using 2-DOF model. *Canadian Journal of Physics* **90**, pp. 963–974.

[13] Benzi, R., A. Sutera, and A. Vulpiani (1981): The mechanism of stochastic resonance. *Journal of Physics A: Mathematical and General* **14**, pp. L453–L457.

[14] Benzi, R. and A. Sutera (2004): Stochastic resonance in two-dimensional Landau Ginzburg equation. *Journal of Physics A: Mathematical and General* **37**(32), p. L391.

[15] Benzi, R. (2010): Stochastic resonance: from climate to biology. *Nonlinear Processes in Geophysics* **17**(5), pp. 431–441.

[16] Bethe, H., G. Brown, J. Applegate, and J. Lattimer (1979): *Equation of state in the gravitational collapse of stars*. Vol. 324, pp. 487–533.

[17] Bochobza-Degani, O. and Y. Nemirovsky (2004): Experimental verification of a design methodology for torsion actuators based on a rapid pull-in solver. *Journal of Microelectromechanical Systems* **13**, pp. 121–130.

[18] Bolotin, V. (1999): Dynamic instabilities in mechanics of structures. *ASME Applied Mechanics Reviews* **52**, R1–R9.

[19] Borovic, B., A. Liu, D. Popa, H. Cai, and F. Lewis (2005): Open-loop versus closed-loop control of MEMS devices: choices and issues. *Journal of Micromechanics and Microengineering* **15**, pp. 1917–1924.

[20] Boscaggin, A., R. Ortega, and F. Zanolin (2014): Subharmonic solutions of the forced pendulum equation: a symplectic approach. *Archiv der Mathematik* **102**, pp. 459–468.

[21] Budiansky, B. and J. W. Hutchinson (1964): Dynamic buckling of imperfection-sensitive structures. In: *Proc. XI Internat. Cong. Appl. Mech.* Munich.

[22] Budiansky, B. (1967): Dynamic buckling of elastic structures: criteria and estimates. In: *Dynamic stability of structures*. Elsevier, pp. 83–106.

[23] Budiansky, B. (1974): Theory of buckling and post-buckling behavior of elastic structures. *Advances in applied mechanics*. Cited by 723.

[24] Buratti, N. and M. Tavano (2014): Dynamic buckling and seismic fragility of anchored steel tanks by the added mass method. *Earthquake Engineering and Structural Dynamics* **43**(1), pp. 1–21.

[25] Burns, D. and V. Bright (1997): Nonlinear flexures for stable deflection of an electrostatically actuated micromirror. *Proceedings of SPIE: Microelectronic Structures and MEMS III* **3226**, pp. 125–135.

[26] Bushnell, D. (2012): *Computerized buckling analysis of shells*. Vol. 9. Springer Science & Business Media.

[27] Bustillo, J., R. Howe, and R. Muller (1998): Surface micromachining for microelectromechanical systems. *Proceedings of the IEEE* **86**(8), pp. 1552–1574.

[28] Caprini, L., F. Cecconi, and U. M. B. Marconi (2021): Correlated escape of active particles across a potential barrier. *Journal of Chemical Physics* **155**(16), p. 164902.

[29] Castagnino, M. and R. Ferraro (1984): The radiation from moving mirrors: The creation and absorption of particles. *Annals of Physics* **154** (1), pp. 1–23.

[30] Castaner, L., J. Pons, R. Nadal-Guardia, and A. Rodriguez (2001): Analysis of extended actuation range of electrostatic actuators by current pulse drive. *Sensors and Actuators A: Physical* **90**, pp. 181–190.

[31] Champneys, A. et al. (2019): Happy catastrophe: recent progress in analysis and exploitation of elastic instability. *Front. Appl. Math. Stat.* **5**.

[32] Chandrasekhar, S. (1943): Stochastic problems in physics and astronomy. *Reviews of Modern Physics*.

[33] Chaterjee, S. and G. Pohit (2009): A large deflection model for the pull-in analysis of electrostatically actuated microcantilever beams. *Journal of Sound and Vibration* **322**, pp. 969–986.

[34] Cheng, C., G. Salina, N. Grønbech-Jensen, J. Blackburn, M. Lucci, and M. Cirillo (2019): Modeling escape from a one-dimensional potential well at zero or very low temperatures. *Journal of Applied Physics* **126**(24), p. 244302.

[35] Chuang, W., H. Lee, P. Chang, and Y. Hu (2010): Review on the modeling of electrostatic MEMS. *Sensors* **10**(6), pp. 6149–6171.

[36] Cornfeld, I., S. Fomin, and Y. Sinai (1982): *Ergodic Theory*. Vol. 245. New York: Springer.

[37] De Boer, M. and T. Michalske (1999): Accurate method for determining adhesion of cantilever beams. *Journal of Applied Physics* **86**, pp. 817–827.

[38] De Coster, J., H. Tilmans, J. van Beek, T. Rijks, and R. Puers (2004): The influence of mechanical shock on the operation of electrostatically driven RF-MEMS switches. *Journal of Micromechanics and Microengineering* **14**, S49.

[39] De Tommasi, D., G. Puglisi, G. Saccomandi, and G. Zurlo (2010): Pull-in and wrinkling instabilities of electroactive dielectric actuators. *Journal of Physics D: Applied Physics* **43**, p. 325501.

[40] De, S. and N. Aluru (2004): Full-Lagrangian schemes for dynamic analysis of electrostatic MEMS. *Journal of Microelectromechanical Systems* **13**, pp. 737–758.

[41] De, S. and N. Aluru (2006): A hybrid full-Lagrangian technique for the static and dynamic analysis of magnetostatic MEMS. *Journal of Micromechanics and Microengineering* **16**, pp. 2646–2658.

[42] Dean Jr., R. and A. Luque (2009): Applications of microelectromechanical systems in industrial processes and services. *IEEE Transactions on Industrial Electronics* **56**(4), pp. 913–925.

[43] DeGroot, M. H. (1986): *Probability and Statistics*.

[44] Dellnitz, M. et al. (2005): Transport of mars-crossing asteroids from the quasi-hilda region. *Physical Review Letters* **94**, p. 231102.

[45] Devore, J. L. and K. N. Berk (2012): *Modern Mathematical Statistics with Applications*. 2nd ed. Springer Texts in Statistics. Springer New York, NY.

[46] Dias, R., E. Cretu, and R. Wolffenbuttel (2011): Pull-in-based g-resolution accelerometer: Characterization and noise analysis. *Sensors and Actuators A: Physical*, pp. 47–53.

[47] Duan, J. and R. Rach (2013): A pull-in parameter analysis for the cantilever NEMS actuator model including surface energy, fringing field and Casimir effects. *International Journal of Solids and Structures* **50**, pp. 3511–3518.

[48] Duan, J., R. Rach, and A. Wazwaz (2013): Solution of the model of beam-type micro and nano-scale electrostatic actuators by a new modified Adomian decomposition method for nonlinear boundary value problems. *International Journal of Nonlinear Mechanics* **49**, pp. 159–169.

[49] Elata, D. and H. Bamberger (2006): On the dynamic pull-in of electrostatic actuators with multiple degrees of freedom and multiple voltage sources. *Journal of Microelectromechanical Systems* **15**, pp. 131–140.

[50] Engel, A., T. Ezra, O. V. Gendelman, and A. Fidlin (2023): Escape of two-DOF dynamical system from the potential well. *Nonlinear Dynamics* **111**, pp. 3019–3034.

[51] Engel, A., O. V. Gendelman, and A. Fidlin (2023): Escape of a particle from two-dimensional potential well. *Nonlinear Dynamics*.

[52] Eom, K., H. Park, D. Yoon, and T. Kwon (2011): Nanomechanical resonators and their applications in biological/chemical detection: Nanomechanics principles. *Physics Reports* **503**(4), pp. 115–163.

[53] Fakhrabadi, M., P. Khorasani, A. Rastgoo, and M. Ahmadian (2013): Molecular dynamics simulation of pull-in phenomena in carbon nanotubes with Stone–Wales defects. *Solid State Communications* **157**, pp. 38–44.

[54] Fang, Y. and P. Li (2013): A new approach and model for accurate determination of the dynamic pull-in parameters of microbeams actuated by a step voltage. *Journal of Micromechanics and Microengineering* **23**, p. 045010.

[55] Farid, M. (2020): Escape of a harmonically forced classical particle from asymmetric potential well. *Commun. Nonlinear Sci. Numer. Simul.* **84**, pp. 1–14.

[56] Farid, M. and O. Gendelman (2021): Escape of a forced-damped particle from weakly nonlinear truncated potential well. *Nonlinear Dyn.* **103**, pp. 63–78.

[57] Farid, M. (2023): Escape dynamics of a particle from a purely nonlinear truncated quartic potential well under harmonic excitation. *Nonlinear Dynamics* **111**(4), pp. 3035–3051.

[58] Farrokhabadi, A., R. Rach, and M. Abadyan (2013): Modeling the static response and pull-in instability of CNT nanotweezers under the Coulomb and van der Waals attractions. *Physica E* **53**, pp. 137–145.

[59] Fennimore, A., T. Yuzvinsky, W. Han, M. Fuhrer, J. Cumings, and A. Zettl (2003): Rotational actuators based on carbon nanotubes. *Nature* **424**, pp. 408–410.

[60] Fidlin, A. (2006): *Nonlinear Oscillations in Mechanical Engineering*. Springer-Verlag Berlin Heidelberg.

[61] Fidlin, A. and J. Thomsen (2008): Non-trivial effects of high-frequency excitation for strongly damped mechanical systems. *International Journal of Non-Linear Mechanics* **43**, pp. 569–578.

[62] Fidlin, A. and O. Drozdetskaya (2016): On the Averaging in Strongly Damped Systems: The General Approach and its Application to Asymptotic Analysis of the Sommerfeld Effect. *Procedia IUTAM* **19**, pp. 43–52.

[63] Fleming, G. and P. Hanggi (1993): *Activated Barrier Crossing*. Singapore: World Scientific.

[64] Fonseca, Grigolini, and Lombardo (1986): Diffusional effects of the processes of escape from a potential well. *Physical Review A* **33**(5), p. 3404.

[65] Fraser, W. B. (1965): *Buckling of a Structure with Random Imperfections*. PhD thesis. Harvard University.

[66] Fu, Y. and J. Zhang (2011): Size-dependent pull-in phenomena in electrically actuated nanobeams incorporating surface energies. *Applied Mathematics and Modeling* **35**, pp. 941–951.

[67] Gendelman, O. (2018): Escape of a harmonically forced particle from an infinite-range potential well: a transient resonance. *Nonlinear Dyn* **93**, pp. 79–88.

[68] Gendelman, O. and G. Karmi (2019): Basic mechanisms of escape of a harmonically forced classical particle from a potential well. *Nonlinear Dyn* **98**, pp. 2775–2792.

[69] Gilmore, R. and M. Steer (1991): Nonlinear circuit analysis using the method of harmonic balance—a review of the art. Part I. Introductory concepts. *Int. J. Microw. Millimeter-Wave Comput. Aided Eng.* **1**(1), pp. 22–37.

[70] Goldstein, H. (1980): *Classical Mechanics*. 2nd ed. Addison-Wesley.

[71] Goodier, J. N. and I. K. McIvor (1964): The elastic cylindrical shell under nearly uniform radial impulse. *J. Appl. Mech.* **31**(2).

[72] Gottwald, J., L. Virgin, and E. Dowell (1992): Experimental mimicry of Duffing's equation. *Journal of Sound and Vibration* **158** (3), pp. 447–467.

[73] Guckenheimer, J. and P. Holmes (1983): *Nonlinear oscillations, dynamical systems, and bifurcations of vector fields*. New York: Springer-Verlag.

[74] Hall, K., J. Thomas, and W. Clark (2002): Computation of unsteady nonlinear flows in cascades using a harmonic balance technique. *AIAA J.* **40**(5), pp. 879–886.

[75] Hamel, G. (1922): Über erzwungene Schwingungen bei endlichen Amplituden. Deutsch. *Mathematische Annalen*. Digitalisiert am: 2000-05-18.

[76] He, X., H. Yong, and Y. Zhou (2011): The characteristics and stability of a dielectric elastomer spherical shell with a thick wall. *Smart Materials and Structures* **20**, p. 055016.

[77] Hoff, N. J. and V. G. Bruce (1954): Dynamic analyses of the buckling of laterally loaded flat arches. *J. Math. and Physics* **32**(4).

[78] Holmes, P. (1979): A nonlinear oscillator with a strange attractor. *Phil. Trans. R. Soc. Lond. A* **292**(1394), pp. 419–448.

[79] Hubbard, J. (1999): The Forced Damped Pendulum: Chaos, Complication and Control. *American Mathematical Monthly* **106**(8), pp. 741–758.

[80] Humphreys, J. S. (1966): A note on the adequacy of energy criteria for dynamic buckling of arches. *AIAA Journal* **4**(5).

[81] Hung, E. and S. Senturia (1999): Extending the travel range of analog-tuned electrostatic actuators. *Journal of Microelectromechanical Systems* **8**, pp. 497–505.

[82] Hutchinson, J. W. and B. Budiansky (1966): Dynamic buckling estimates. *AIAA Journal* **4**(3).

[83] Ibrahim, M. and M. Younis (2010): The dynamic response of electrostatically driven resonators under mechanical shock. *Journal of Micromechanics and Microengineering* **20**, p. 025006.

[84] Institut für Technische Mechanik – Bereich Dynamik/Mechatronik (2023): Übungsblatt Nr. 5: Harmonische Balance. Einführung in Nichtlineare Schwingungen, Winter Semester 2023/24.

[85] Jaibir, S., K. Nagendra, and D. Amitava (2012): Fabrication of low pull-in voltage RF MEMS switches on glass substrate in recessed CPW configuration for V-band application. *Journal of Micromechanics and Microengineering* **22**(2), p. 025001.

[86] Jr., W. B. (1963): Thermal fluctuations of a single-domain particle. *Physical Review*.

[87] Kalmykov, Y., W. Coffey, and S. V. Titov (2006): Thermally activated escape rate for a Brownian particle in a double-well potential for all values of the dissipation. *Journal of Chemical Physics* **124**(1), p. 014503.

[88] Karmi, G., P. Kravetc, and O. Gendelman (2021): Analytic exploration of safe basins in a benchmark problem of forced escape. *Nonlinear Dynamics* **106**, pp. 1573–1589.

[89] Karmi, G. (2022): *Analytic Exploration of Safe Basins in a Benchmark Problem of Forced Escape*. Access restricted. PhD thesis. Technion - Israel Institute of Technology. url: https://www.graduate.technion.ac.il/Theses/Abstracts.asp?Id=33683.

[90] Kawaguchi, M., K. Yamano, K. Okuda, T. Jimbo, and N. Ishii (2007): The characteristics evaluation of stacked-type electrostatic actuators by the neural network. In: *Lecture Notes in Computer Science*. Vol. 4693, pp. 1059–1065.

[91] Keplinger, C., M. Kaltenbrunner, N. Arnold, and S. Bauer (2010): Rontgen's electrode-free elastomer actuators without electromechanical pull-in instability. *Proceedings of the National Academy of Sciences* **107**(10), pp. 4505–4510.

[92] Koiter, W. T. (1945): *On the Stability of Elastic Equilibrium*. Thesis (in Dutch). Amsterdam: H. J. Paris.

[93] Krack, M. and J. Gross (2019): *Harmonic Balance for Nonlinear Vibration Problems*. 1st ed. Mathematical Engineering. Number of Pages: XII, 159. Number of Illustrations: 21 b/w illustrations, 35 illustrations in colour. Topics: Engineering Mathematics, Solid Mechanics, Fourier Analysis, Multibody Systems and Mechanical Vibrations. Cham: Springer Cham.

[94] Kramers, H. (1940): Brownian motion in a field of force and the diffusion model of chemical reactions. *Physica (Utrecht)* **7**, pp. 284–304.

[95] Kravetc, P. and O. Gendelman (2022): Approximation of potential function in the problem of forced escape. *Journal of Sound and Vibration* **526**, p. 116765.

[96] Kravetc, P., O. Gendelman, and A. Fidlin (2023): Resonant escape induced by a finite time harmonic excitation. *Chaos: An Interdisciplinary Journal of Nonlinear Science* **33**(6), p. 063116.

[97] Kravetc, P., O. Gendelman, and A. Fidlin (2024): *Dynamical integrity of the safe basins in a problem of forced escape*. arXiv: 2401.13091 [math.DS].

[98] Krylov, N. and N. Bogoliubov (1934): *New Methods of Nonlinear Mechanics in their Application to the Investigation of the Operation of Electronic Generators, I (in Russian)*. Moscow: United Scientific and Technical Press.

[99] Krylov, S. and R. Maimon (2004): Pull-in dynamics of an elastic beam actuated by continuously distributed electrostatic force. *Journal of Vibration and Acoustics* **126**, pp. 332–342.

[100] Krylov, S. (2007): Lyapunov exponents as a criterion for the dynamic pull-in instability of electrostatically actuated microstructures. *International Journal of Non-Linear Mechanics* **42**, pp. 626–642.

[101] Lakrad, F. and M. Belhaq (2010): Suppression of pull-in instability in MEMS using a high-frequency actuation. *Communications in Nonlinear Science and Numerical Simulation* **15**, pp. 3640–3646.

[102] Lakrad, F. and M. Belhaq (2011): Suppression of pull-in in a microstructure actuated by mechanical shocks and electrostatic forces. *International Journal of Non-Linear Mechanics* **46**, pp. 407–414.

[103] Landau, L. and E. Lifshitz (1976): *Mechanics*. 3rd ed. Butterworth, Herrmann.

[104] Lansbury, A. N., J. M. T. Thompson, and H. B. Stewart (1992): Basin erosion in the twin-well Duffing oscillator: Two distinct bifurcation scenarios. *International Journal of Bifurcation and Chaos* **2**, pp. 505–532.

[105] Lee, K. (2007): Closed-form expressions for pull-in parameters of two-degree-of-freedom torsional microactuators. *Journal of Micromechanics and Microengineering* **17**(9), pp. 1853–1862.

[106] Lee, K. (2008): Design methodology for variable capacitors. *Journal of Micromechanics and Microengineering* **18**, p. 025016.

[107] Legrand, B., A. Rollier, D. Collard, and L. Buchaillot (2006): Suppression of the pull-in instability for parallel-plate electrostatic actuators operated in dielectric liquids. *Applied Physics Letters* **88**, p. 034105.

[108] Legtenberg, R., A. Groeneveld, and M. Elwenspoek (1996): Comb-drive actuators for large displacements. *Journal of Micromechanics and Microengineering* **6**(3), pp. 320–329.

[109] Lenci, S. and G. Rega (1998): Controlling nonlinear dynamics in a two-well impact system. Parts I and II. *International Journal of Bifurcation and Chaos* **8**, pp. 2387–2424.

[110] Lenci, S. and G. Rega (2003): Optimal control of homoclinic bifurcation: theoretical treatment and practical reduction of safe basin erosion in the Helmholtz oscillator. *Journal of Vibration and Control* **9**, pp. 281–316.

[111] Lenci, S. and G. Rega (2003): Optimal control of nonregular dynamics in a Duffing oscillator. *Nonlinear Dynamics* **33**, pp. 71–86.

[112] Lenci, S. and G. Rega (2003): Optimal numerical control of single-well to cross-well chaos transition in mechanical systems. *Chaos, Solitons and Fractals* **15**, pp. 173–186.

[113] Lenci, S. and G. Rega (2004): A unified control framework of the nonregular dynamics of mechanical oscillators. *Journal of Sound and Vibration* **278**, pp. 1051–1080.

[114] Lenci, S. and G. Rega (2004): Global optimal control and system-dependent solutions in the hardening Helmholtz–Duffing oscillator. *Chaos, Solitons and Fractals* **21**, pp. 1031–1046.

[115] Lenci, S. and G. Rega (2005): Computational nonlinear dynamics and optimal control/anti-control of a rocking block. In: *Multibody Dynamics 2005, ECCOMAS Thematic Conference*. J. M. Goicolea, J. Cuadrado, and J. C. García Orden eds. Madrid, Spain, pp. 21–24.

[116] Lenci, S. and G. Rega (2005): Heteroclinic bifurcations and optimal control in the nonlinear rocking dynamics of generic and slender rigid blocks. *International Journal of Bifurcation and Chaos* **15**, pp. 1901–1918.

[117] Lenci, S. and G. Rega (2006): Control of pull-in dynamics in a nonlinear thermoelastic electrically actuated microbeam. *Journal of Micromechanics and Microengineering* **16**, pp. 390–401.

[118] Lenci, S. and G. Rega (2007): Control of the homoclinic bifurcation in buckled beams: infinite-dimensional vs reduced order modeling. *International Journal of Non-Linear Mechanics*.

[119] Li, P., R. Hu, and Y. Fang (2007): A new model for squeeze-film damping of electrically actuated microbeams under the effect of a static deflection. *Journal of Micromechanics and Microengineering* **17**, pp. 1242–1251.

[120] Lin, R. and W. Wang (2006): Structural dynamics of microsystems-current state of research and future directions. *Mechanical Systems and Signal Processing* **20**, pp. 1015–1043.

[121] Liu, D., K.-C. Friend, and J. Yeo (2010): A brief review of actuation at the micro-scale using electrostatics, electromagnetics and piezoelectric ultrasonics. *Acoustical Science and Technology* **31**(2), pp. 115–123.

[122] Liu, H., Z. Zhou, W. Li, and Q.-A. Huang (2012): An online test structure for the thermal expansion coefficient of surface micromachined polysilicon beams by a pull-in approach. *Journal of Micromechanics and Microengineering* **22**, p. 055017.

[123] Liu, X., N. Boddeti, M. Szpunar, L. Wang, M. Rodriguez, R. Long, J. Xiao, M. Dunn, and J. Bunch (2013): Observation of pull-in instability in graphene membranes under interfacial forces. *Nano Letters* **13**, pp. 2309–2313.

[124] Loh, O., X. Wei, C. Ke, J. Sullivan, and H. Espinosa (2011): Robust carbon nanotube-based nanoelectromechanical devices: Understanding and eliminating prevalent failure modes using alternative electrode materials. *Small* **7**, pp. 79–86.

[125] Loh, O. and H. Espinosa (2012): Nanoelectromechanical contact switches. *Nature Nanotechnology* **7**(4), pp. 283–295.

[126] Luo, A. and F. Wang (2002): Chaotic motion in a Micro-Electro-Mechanical System with non-linearity from capacitors. *Communications in Nonlinear Science and Numerical Simulation* **7**, pp. 31–49.

[127] Ma, J., L. Jiang, and S. Asokanthan (2010): Influence of surface effects on the pull-in instability of NEMS electrostatic switches. *Nanotechnology* **21**(50), p. 505708.

[128] Ma, Z., A. Holle, K. Melde, T. Qiu, K. Poeppel, V. Kadiri, and P. Fischer (2020): Acoustic holographic cell patterning in a biocompatible hydrogel. *Adv. Mater.* **32**, p. 1904181.

[129] Magnus, K., K. Popp, and W. Sextro (2008): *Schwingungen: Eine Einführung in die physikalischen Grundlagen und die theoretische Behandlung von Schwingungsprobleme*n. 8th ed. Wiesbaden: Vieweg+Teubner Verlag, pp. XII, 298.

[130] Magnus, W. and S. Winkler (2004): *Hill's Equation*. English. Dover Books on Mathematics. Dover Publications, p. 138.

[131] Maithripala, D., J. Berg, and W. Dayawansa (2005): Control of an electrostatic MEMS using static and dynamic output feedback. *ASME Journal of Dynamic Systems, Measurement, and Control* **127**, pp. 443–450.

[132] Manevitch, L. (2007): New approach to beating phenomenon in coupled nonlinear oscillatory chains. *Arch. Appl. Mech.* **77**, pp. 301–312.

[133] Manevitch, L. and O. Gendelman (2011): *Tractable Modes in Solid Mechanics*. Berlin: Springer.

[134] Melde, K., E. Choi, Z. Wu, S. Palagi, T. Qiu, and P. Fischer (2018): Acoustic fabrication via the assembly and fusion of particles. *Adv. Mater.* **30**, p. 1704507.

[135] Moon, F. and G. Li (1985): Fractal basin boundaries and homoclinic orbits for periodic motions in a two-well potential. *Physical Review Letters* **55**, pp. 1439–1442.

[136] Moscardo, M., X. Zhao, Z. Suo, and Y. Lapusta (2008): On designing dielectric elastomers. *Journal of Applied Physics* **104**, p. 093503.

[137] Naiger, D. and O. Gendelman (2019): Escape dynamics of a forced-damped classical particle in an infinite-range potential well. *ZAMM - Journal of Applied Mathematics and Mechanics* **101** (7).

[138] Nathanson, H., W. Newell, R. Wickstrom, and J. Davis (1967): The resonant gate transistor. *IEEE Transactions on Electron Devices* **14**, pp. 117–133.

[139] Nayfeh, A. and D. Mook (1979): *Nonlinear Oscillations*. Vol. 1979. New York: Wiley.

[140] Nayfeh, A. H. and N. E. Sanchez (1989): Bifurcations in a forced softening Duffing oscillator. *International Journal of Non-Linear Mechanics* **24**, p. 483.

[141] Nayfeh, A. H. (1993): *Introduction to Perturbation Techniques*. New York: John Wiley & Sons.

[142] Nayfeh, A. H. (2004): *Perturbation Methods*. Wiley–VCH Verlag.

[143] Nayfeh, A., M. Younis, and E. Abdel-Rahman (2005): Reduced-order models for MEMS applications. *Nonlinear Dynamics* **41**, pp. 211–236.

[144] Nayfeh, A. and M. Younis (2005): Dynamics of MEMS resonators under superharmonic and subharmonic excitations. *Journal of Micromechanics and Microengineering* **15**, pp. 1840–1847.

[145] Neishtadt, A. (1991): Probability phenomena due to separatrix crossing. *Chaos* **1**, pp. 42–48.

[146] Nemirovsky, Y., I. Zelniker, O. Degani, and G. Sarusi (2005): A methodology and model for the pull-in parameters of magnetostatic actuators. *Journal of Microelectromechanical Systems* **14**, pp. 1253–1264.

[147] Nie, M., Q.-A. Huang, and W. Li (2009): Pull-in characterization of doubly-clamped composite beams. *Sensors and Actuators A: Physical* **151**, pp. 118–126.

[148] Nielson, G. and G. Barbastathis (2006): Dynamic pull-in of parallel-plate and torsional electrostatic MEMS actuators. *Journal of Microelectromechanical Systems* **15**, pp. 811–821.

[149] Nisar, A., N. Afzulpurkar, B. Mahaisavariya, and A. Tuantranont (2008): MEMS-based micropumps in drug delivery and biomedical applications. *Sensors and Actuators B: Chemical* **130**(1), pp. 917–942.

[150] Oh, K. and C. Ahn (2006): A review of microvalves. *Journal of Micromechanics and Microengineering* **16**(5), R13–R39.

[151] de Oliveira, H. P., A. M. Ozorio de Almeida, I. Damião Soares, and E. V. Tonini (2002): Homoclinic chaos in the dynamics of a general bianchi type-ix model. *Physical Review D* **65**, p. 083511.

[152] Osterberg, P. and S. Senturia (1997): M-Test: A test chip for MEMS material property measurement using electrostatically actuated test structures. *Journal of Microelectromechanical Systems* **6**, pp. 107–118.

[153] Ouakad, H., M. Younis, and F. Alsaleem (2012): Dynamic response of an electrostatically actuated microbeam to drop-table test. *Journal of Micromechanics and Microengineering* **22**, p. 095003.

[154] Pamidighantam, S., R. Puers, K. Baert, and H. Tilmans (2002): Pull-in voltage analysis of electrostatically actuated beam structures with fixed-fixed and fixed-free end conditions. *Journal of Micromechanics and Microengineering* **12**, pp. 458–464.

[155] Pandey, A. (2013): Effect of coupled modes on pull-in voltage and frequency tuning of a NEMS device. *Journal of Micromechanics and Microengineering* **23**, p. 085015.

[156] Pelesko, J. and D. Bernstein (2002): *Modeling MEMS and NEMS*. Chapman, Hall, and CRC Press.

[157] Pescini, L., H. Lorenz, and R. Blick (2003): Mechanical gating of coupled nanoelectromechanical resonators operating at radio frequency. *Applied Physics Letters* **82**(3), pp. 352–354.

[158] Pierre, C., J. Gilli, M. Monticelli, and N. Vanderberghe (2005): A damped pendulum forced with a constant torque. *American Journal of Physics* **73**.

[159] Previato, E. (2003): *Dictionary of Applied Math for Engineers and Scientists*. CRC Press.

[160] Pryputniewicz, R. (2007): Progress in microelectromechanical systems. *Strain* **43**(1), pp. 13–25.

[161] Qian, Y., L. Lou, M. Tsai, and C. Lee (2012): A dual-silicon-nanowires based U-shape nanoelectromechanical switch with low pull-in voltage. *Applied Physics Letters* **100**(11), p. 113102.

[162] Quinn, D. (1997): Transition to escape in a system of coupled oscillators. *Int. J. Non-Linear Mech.* **32**, pp. 1193–1206.

[163] Rega, G. and S. Lenci (2008): Dynamical integrity and control of nonlinear mechanical oscillators. *J. Vib. Control* **14**, pp. 159–179.

[164] Ren, H., F. Tao, W. Wang, and J. Yao (2011): An out-of-plane electrostatic actuator based on the lever principle. *Journal of Micromechanics and Microengineering* **21**, p. 045019.

[165] Rezazadeh, G., M. Fathalilou, R. Shabani, S. Tarverdilou, and S. Talebian (2009): Dynamic characteristics and forced response of an electrostatically-actuated microbeam subjected to fluid loading. *Microsystem Technologies* **15**, pp. 1355–1363.

[166] Robinett, R. (1995): Quantum and classical probability distributions for position and momentum. *American Journal of Physics* **63**(9), pp. 823–832.

[167] Rocha, L., E. Cretu, and R. Wolffenbuttel (2006): Using dynamic voltage drive in a parallel-plate electrostatic actuator for full-gap travel range and positioning. *Journal of Microelectromechanical Systems* **15**, pp. 69–83.

[168] Rocha, L., R. Dias, E. Cretu, and R. Wolffenbuttel (2011): Auto-calibration of capacitive MEMS accelerometers based on pull-in voltage. *Microsystem Technologies* **17**, pp. 429–436.

[169] Rokni, H. and W. Lu (2013): A continuum model for the static pull-in behavior of graphene nanoribbon electrostatic actuators with interlayer shear and surface energy effects. *Journal of Applied Physics* **113**, p. 153512.

[170] Rong, H., Q.-A. Huang, M. Nie, and W. Li (2004): An analytical model for pull-in voltage of clamped-clamped multilayer beams. *Sensors and Actuators A: Physical* **116**, pp. 15–21.

[171] Sadeghian, H., C. Yang, J. Goosen, E. van der Drift, A. Bossche, P. French, and F. van Keulen (2009): Characterizing size-dependent effective elastic modulus of silicon nanocantilevers using electrostatic pull-in instability. *Applied Physics Letters* **94**, p. 221903.

[172] Sadighi, A., A. Eyvazian, M. Asgari, and A. M. Hamouda (2019): A novel axially half corrugated thin-walled tube for energy absorption under axial loading. *Thin-Walled Structures* **145**, p. 106418.

[173] Salas, A., M. Abu Hammad, B. M. Alotaibi, L. El-Sherif, and S. El-Tantawy (2022): Closed-Form Solutions to a Forced Damped Rotational Pendulum Oscillator. *Mathematics* **10**(21), p. 4000.

[174] Sanders, J. A., F. Verhulst, and J. Murdock (2007): *Averaging Methods in Nonlinear Dynamical Systems*. 2nd ed. Applied Mathematical Sciences. Springer New York, NY, pp. XXIV, 434.

[175] Sanjuan, M. (1999): The effect of nonlinear damping on the universal escape oscillator. *Int. J. Bifurc. Chaos* **9**, pp. 735–744.

[176] Sardanashvily, G. (2015): *Handbook of Integrable Hamiltonian Systems*. URSS.

[177] Sarrouy, E. and J. Sinou (2011): Non-linear periodic and quasi-periodic vibrations in mechanical systems-on the use of the harmonic balance methods. In: *Adv. Vibr. Anal. Res.* Intech.

[178] Sasaki, H., M. Shikida, and K. Sato (2006): A force transmission system based on a tulip-shaped electrostatic clutch for haptic display devices. *Journal of Micromechanics and Microengineering* **16**, pp. 2673–2683.

[179] Seeger, J. and B. Boser (2003): Charge control of parallel-plate, electrostatic actuators and the tip-in instability. *Journal of Microelectromechanical Systems* **12**, pp. 656–671.

[180] Sharafkhani, N., R. Shabani, S. Tariverdilo, and G. Rezazadeh (2013): Stability analysis and transient response of electrostatically actuated microbeam interacting with bounded compressible fluids. *ASME Journal of Applied Mechanics* **80**, p. 011024.

[181] Shirazi, F., J. Velni, and K. Grigoriadis (2011): An LPV design approach for voltage control of an electrostatic MEMS actuator. *Journal of Microelectromechanical Systems* **20**, pp. 302–311.

[182] Simitses, G. and D. H. Hodges (2006): *Fundamentals of structural stability*. Butterworth-Heinemann.

[183] Soliman, M. and J. Thompson (1989): Integrity measures quantifying the erosion of smooth and fractal basins of attraction. *Journal of Sound and Vibration* **135** (3), pp. 453–475.

[184] Soliman, M. and J. Thompson (1990): Stochastic penetration of smooth and fractal basin boundaries under noise excitation. *Dynamics and Stability of Systems* **5**(4), pp. 281–298.

[185] Sousa, P., V. Chu, and J. Conde (2012): Reliability and stability of thin-film amorphous silicon MEMS resonators. *Journal of Micromechanics and Microengineering* **22**, p. 065030.

[186] Spyrou, K. and J. Thompson (2000): The nonlinear dynamics of ship motions: A field overview and some recent developments. *Philosophical Transactions of the Royal Society A: Mathematical, Physical and Engineering Sciences* **358**, pp. 1735–1760.

[187] Stemme, S. (2004): Design and fabrication aspects of an S-shaped film actuator based DC to RF MEMS switch. *Journal of Microelectromechanical Systems* **13**, pp. 421–428.

[188] Subramanian, R. (1970): *Escape from a potential well*. Ph.D. Dissertation. Cambridge, Mass.: Harvard University.

[189] SunY, D. Piyabongkarn, A. Sezen, B. Nelson, and R. Rajamani (2002): A high-aspect-ratio two axis electrostatic microactuator with extended travel range. *Sensors and Actuators A: Physical* **102**, pp. 49–60.

[190] Szemplinska-Stupnicka, W. (1992): Cross-well chaos and escape phenomena in driven oscillators. *Nonlinear Dynamics* **3**, pp. 225–243.

[191] Taghavi, N. and H. Nahvi (2013): Pull-in instability of cantilever and fixed–fixed nano-switches. *European Journal of Mechanics-A/Solids* **41**, pp. 123–133.

[192] Talebian, S., G. Rezazadeh, M. Fathalilou, and B. Toosi (2010): Effect of temperature on pull-in voltage and natural frequency of an electrostatically actuated microplate. *Mechatronics* **20**, pp. 666–673.

[193] Talkner, P. and P. Hanggi, eds. (1995): *New Trends in Kramers' Reaction Rate Theory*. Berlin: Springer.

[194] Tang, W., T.-C. Nguyen, and R. Howe (1989): Laterally driven polysilicon resonant microstructures. *Sensors and Actuators* **20**(1-2), pp. 25–32.

[195] Taylor, G. (1968): The coalescence of closely spaced drops when they are at different electric potentials. *Proceedings of the Royal Society A* **306**, pp. 423–434.

[196] Thompson, J., G. Hunt, and V. Tvergaard (1985): Elastic Instability Phenomena. *Journal of Applied Mechanics* **52** (1), pp. 241–242.

[197] Thompson, J., S. Bishop, and L. Leung (1987): Fractal basins and chaotic bifurcations prior to escape from a potential well. *Physics Letters A* **121**(3), pp. 116–120.

[198] Thompson, J. M. T. (1989): Chaotic phenomena triggering the escape from a potential well. *Proceedings of the Royal Society of London A* **421**, pp. 195–225.

[199] Thompson, J. M. T. (1990): Loss of Engineering Integrity due to the Erosion of Absolute and Transient Basin Boundaries. In: *Nonlinear Dynamics in Engineering Systems*. W. Schiehlen ed. Berlin, Heidelberg: Springer Berlin Heidelberg, pp. 313–320.

[200] Thompson, J. (1991): Chaotic phenomena triggering the escape from a potential well. In: *Engineering Applications of Dynamics of Chaos*. W. Szemplinska-Stupnicka and H. Troger eds. Vol. 139. CISM Courses and Lectures. Berlin: Springer, pp. 279–309.

[201] Thompson, J. M. T., R. C. T. Rainey, and M. S. Soliman (1992): Mechanics of ship capsize under direct and parametric wave excitation. *Philosophical Transactions of the Royal Society of London. Series A: Physical and Engineering Sciences* **428**, pp. 1–13.

[202] Thompson, J. and H. Stewart (2002): *Nonlinear Dynamics and Chaos (second edition)*.

[203] Ueda, Y., H. Nakajima, T. Hikihara, and H. Stewart (1987): Forced two-well potential Duffing's oscillator. In: *Proceedings of the Conference on Qualitative Methods for the Analysis of Nonlinear Dynamics*. Henniker, New Hampshire: SIAM.

[204] Vasilikis, D. and S. Karamanos (2014): Mechanics of confined thin-walled cylinders subjected to external pressure. *Applied Mechanics*. Cited by 53.

[205] Virgin, L. (1987): The nonlinear rolling response of a vessel including chaotic motions leading to capsize in regular seas. *Applied Ocean Research* **9**(2), pp. 89–95.

[206] Virgin, L. (1989): Approximate criterion for capsize based on deterministic dynamics. *Dyn. Stab. Syst.* **4**, pp. 56–70.

[207] Virgin, L. and L. Cartee (1991): A note on the escape from a potential well. *International Journal of Nonlinear Mechanics* **26**, pp. 449–452.

[208] Virgin, L. N., R. H. Plaut, and C.-C. Cheng (1992): Prediction of escape from a potential well under harmonic excitation. *International Journal of Non-Linear Mechanics* **27**(3), pp. 357–365.

[209] Wang, M. and G. Uhlenbeck (1945): On the theory of the Brownian motion II. *Reviews of Modern Physics*.

[210] Weyl, H. (1916): Uber die gleichverteilung von zahlen mod. eins. *Mathematische Annalen* **77**(3), pp. 313–352.

[211] Xiang, W. and C. Lee (2010): Nanoelectromechanical torsion switch of low operation voltage for nonvolatile memory application. *Applied Physics Letters* **96**(19), p. 193113.

[212] Yang, B., C. Lee, R. Kotlanka, J. Xie, and S. Lim (2010): A MEMS rotary comb mechanism for harvesting the kinetic energy of planar vibrations. *Journal of Micromechanics and Microengineering* **20**, p. 065017.

[213] Yang, Z., G. Ding, H. Cai, X. Xu, H. Wang, and X. Zhao (2009): Analysis and elimination of the 'skip contact' phenomenon in an inertial micro-switch for prolonging its contact time. *Journal of Micromechanics and Microengineering* **19**(4), p. 045017.

[214] Yong, Z. and H. Espinosa (2004): Effect of temperature on capacitive RF MEMS switch performance—a coupled field analysis. *Journal of Micromechanics and Microengineering* **14**, pp. 1270–1279.

[215] Younis, M., E. Abdel-Rahman, and A. Nayfeh (2003): A reduced-order model for electrically actuated microbeam-based MEMS. *Journal of Microelectromechanical Systems* **12**, pp. 672–680.

[216] Younis, M., R. Miles, and D. Jordy (2006): Investigation of the response of microstructures under the combined effect of mechanical shock and electrostatic forces. *Journal of Micromechanics and Microengineering* **16**, pp. 2463–2474.

[217] Zhang, W. and G. Meng (2005): Nonlinear dynamical system of micro-cantilever under combined parametric and forcing excitations in MEMS. *Sensors and Actuators A: Physical* **119**, pp. 291–299.

[218] Zhang, W., G. Meng, and D. Chen (2007): Stability, nonlinearity and reliability of electrostatically actuated MEMS devices. *Sensors* **7**, pp. 760–796.

[219] Zhang, W., O. Tabata, T. Tsuchiya, and G. Meng (2011): Noise-induced chaos in the electrostatically actuated MEMS resonators. *Physics Letters A* **375**, pp. 2903–2910.

[220] Zhang, W.-M., H. Yan, Z.-K. Peng, and G. Meng (2014): Electrostatic pull-in instability in MEMS/NEMS: a review. *Sens. Actuators A Phys.* **214**, pp. 187–218.

Publications

[221] Genda, A., A. Fidlin, and O. Gendelman (2021): On the escape of a resonantly excited couple of particles from a potential well. *Nonlinear Dynamics* **104** (1), pp. 91–102.

[222] Genda, A., A. Fidlin, and O. Gendelman (2022): On the Escape of a Resonantly Excited Couple of Colliding Particles from a Potential Well under Bi-harmonic Excitation. In: *European Nonlinear Dynamics Conferences, ENOC*. Lyon, sciencesconf.

[223] Genda, A., A. Fidlin, and O. Gendelman (2023): *Bias of the Steady-State Averaged Solutions of a Strongly Overdamped Particle in a Cosine Potential Under Harmonic Excitation*. Springer Preprint.

[224] Genda, A., A. Fidlin, and O. Gendelman (2023): Dynamics of forced escape from asymmetric truncated parabolic well. *ZAMM - Journal of Applied Mathematics and Mechanics / Zeitschrift für Angewandte Mathematik und Mechanik*.

[225] Genda, A., A. Fidlin, and O. Gendelman (2023): The level-crossing problem of a weakly damped particle in quadratic potential well under harmonic excitation. *Nonlinear Dynamics* **111**, pp. 20563–20578.

[226] Genda, A. and G. Stepan (2023): On the stability of bodies suspended asymmetrically with an inelastic rope. *Acta Mechanica* **234**, pp. 3009–3018.

[227] Genda, A., A. Fidlin, and O. Gendelman (2024): An alternative approach to averaging in nonlinear systems using classical probability density. *ZAMM - Journal of Applied Mathematics and Mechanics / Zeitschrift für Angewandte Mathematik und Mechanik*.

[228] Genda, A., A. Fidlin, and O. Gendelman (2024): Model reduction for an internally damped n-particle chain in a potential well under polyharmonic excitation. *Acta Mechanica*.

Supervised theses

[229] Bader, M. (2024): *Flucht eines harmonisch angeregten Teilchens aus einem abgeschnittenen, quadratischen Potential mit Coulombscher Reibung*. Betreuer: M. Sc. Attila Genda, Prof. Dr.-Ing. habil. Alexander Fidlin. Not published online. Bachelor's Thesis. Karlsruhe Institute of Technology.